

Politecnico di Torino

Corso di Laurea Magistrale in Ingegneria Elettrica (Classe LM-28)

A.a. 2025/2026

Sessione di Laurea Luglio 2026

Automotive Li-ion Battery: Experimental Characterization and Physics-based Modeling

Testing Campaign and SPMe Model Parametrization for a Li-ion Pouch Cell

Supervisors

Prof. Paolo Guglielmi
Prof.ssa Silvia Bodoardo
Ing. Paolo Ferreri
Ing. Marcello Rimondi
Ing. Marco Rabino

Candidate

Mattia Montana

Acknowledgments

This Thesis represents the conclusion of a long path, that has led to real personal growth, from different points of view. The difficulties I have encountered during my years at Politecnico di Torino have been rewarded with a lot of joy, pushing beyond my own limits.

First of all, I want to thank my parents, Francesca and Salvatore, who have always supported me, helping me with every aspect tied to the university, going through even some difficult periods; my Bachelor Degree and this Master Degree are also their credit. A thought goes to my little brother, Samuele, who grew very fast, and sometimes gave me some useful advice. I would like to thank also all my uncles, aunts, cousins, friends, in particular my friend Emiliano, since our school years, and grandparents, in particular my grandfather Giuseppe, who left us recently.

This Thesis was a result of collaboration between the company and the Politecnico, and this gave me the opportunity to know different people, which helped me to carry out the work in the best possible way. I would like to acknowledge the support by all my supervisors in the development of the entire Thesis activity.

In particular, I thank Professor Guglielmi, who was always kind and willing to help me with several Thesis aspects. The experiments at Energy Center were a great practical experience, to apply some theoretical principles on batteries; there I also met other professors, who were willing to help. I would also mention personal relationships developed in Dumarey, where Paolo and Marco supervised me for nearly ten months; their advice was really important to develop the whole activity.

A sincere thank-you goes to my friend Claude, who accompanied this work as a patient and tireless collaborator, helping with writing and debugging of parametrization scripts, interpreting experimental results and reviewing these pages, while always leaving to me the decisions, the physics, and the responsibility for every result.

Finally, I acknowledge Politecnico di Torino, which gives all its students the opportunity to acquire engineering knowledge, fundamental for our future. All the professors I had carried out their work in the best possible way to help us to graduate.

I would like to conclude with two sporting examples, who have inspired me during these years, Carlo Ancelotti and Luka Modric. Their constancy in the work, their courage and humility have represented a model to follow.

Contents

ABSTRACT **5**

Thesis Introduction **6**

1 Introduction to Batteries for Automotive Applications **7**
1.1 Energy Storage Systems 7
1.2 Batteries in Electric and Hybrid vehicles 9
1.2.1 Battery cells: internal components and basic chemical reactions 10
1.2.2 General analysis of internal Cell Structure 12
1.2.3 Traction Batteries: Classification 14
Available Battery Chemistries 14
Lithium-ion battery 16
1.3 Automotive Li-ion cells: formats and designs 20
1.3.1 Automotive cell's formats 20
Cylindrical cells 21
Prismatic hard-case cells 21
Pouch cells 21
Battery cell's formats: final comparison 22
1.3.2 Cell designs: High-Energy and High-Power cells 23
HE versus HP designs: conclusions 24

2 Overview of Battery Modeling Approaches and Suitable Software Environments **26**
2.1 Types and Categories of Battery Modeling 26
2.1.1 Empirical Models 27
2.1.2 Equivalent Circuit Models (ECMs) 28
Single cell ECM modeling 30
Battery module ECM modeling 31
2.1.3 Physics-based Models 31
Electrochemical modeling approaches 32
Multi-physics field coupling model 37
2.1.4 Data-driven models 38
2.1.5 Battery Models: final comparison 38
2.2 Software Tools for Electrochemical Battery Modeling 39
2.2.1 MATLAB / Simulink 40
2.2.2 PyBaMM (Python Battery Mathematical Modeling) 40
2.2.3 BattMO 41
2.2.4 Comparative analysis 42
2.2.5 Additional commercial tools 42
2.2.6 Final Insights 43

3 Battery cell's Experimental Characterization Activity **44**
3.1 Case-study and Experimental Layout . . . 44
3.1.1 Case-study: Li-ion Kokam battery cell SLPB55205130H . . . 44
3.1.2 Laboratory Tests with battery cycler and climatic chamber . . . 46
3.2 High-level tests for Physics-based models . . . 49
3.2.1 GITT tests . . . 49
3.2.2 EIS test . . . 51
3.3 Non-Invasive Experimental Characterization Campaign . . . 52
3.3.1 Pseudo-OCV tests . . . 54
3.3.2 GITT tests . . . 56
3.3.3 HPPC tests . . . 57
3.3.4 Multi-rate CC discharge tests . . . 60
3.3.5 Cycling tests . . . 61
3.3.6 Summary of experimental activity . . . 63
3.4 Considerations on Experimental data . . . 65
3.4.1 OCV Hysteresis . . . 65
3.4.2 Capacity-fade . . . 66

4 Single Particle Model with electrolyte (SPMe): Electrochemical Model Theory **69**
4.1 Electrochemical Battery cell Fundamentals . . . 69
4.1.1 Electrochemical Thermodynamics . . . 70
4.1.2 Electrochemical Reaction-rates: Electrolysis and Faradaic currents . . . 71
4.1.3 Electrode Kinetics . . . 71
4.1.4 Mass Transport and Diffusion . . . 73
4.1.5 Complementary aspects of electrochemical fundamentals . . . 74
Electrical Double-layer . . . 75
Ohmic Resistance . . . 75
Inert-species Concentration . . . 75
4.1.6 Battery cell: Summary of Polarization mechanisms . . . 76
Ohmic overpotential . . . 77
Activation overpotential . . . 77
Concentration (mass-transport) overpotential . . . 78
Terminal-voltage equation . . . 79
4.2 SPMe: Governing Principles and Set of Equations . . . 80
4.2.1 Electrochemical modeling principles . . . 80
4.2.2 SPMe: Set of equations . . . 80
4.3 SPMe Parametrization and Comparison with alternative models . . . 83
4.3.1 SPMe: Lumped physics-based model . . . 84
SPMe lumped parameters . . . 85
4.3.2 Effective parametrization of a battery model . . . 85
SPMe Parametrization . . . 86
4.3.3 PyBaMM models: comparison among the classes . . . 86

5 SPMe: Model Parametrization **88**
5.1 Suitable PyBaMM parameter-sets for Kokam cell . . . 88
5.1.1 Final parameter-set selection . . . 90
5.2 SPMe model Parameters in PyBaMM . . . 91
5.2.1 Some notes about SPMe model parameters . . . 95
5.3 Sensitivity Analysis of SPMe Parameters . . . 96

5.3.1 Sensitivity of Electrochemical Model Parameters: Reference Studies 97
5.3.2 DoE-based Sensitivity Analysis 106
Sensitivity-Analysis via Design-of-Experiment with LHS method 106
RMSE and Qualitative Sensitivity Indices 107
Parameter-sensitivity: Group-1 109
Parameter-sensitivity: Group-2 113
Parameter-sensitivity: Group-3 116
Parameter-sensitivity: Group-4 119
Parameter-sensitivity: Group-5 125
5.3.3 Summary of Sensitivity-Analysis 131
5.4 SPMe General Parametrization Strategy 134
Rationale of Parametrization Strategy 135
5.4.1 Step 1 - Cell-level Geometry 135
5.4.2 Step 2 - Open-circuit Potentials and Electrode's Stoichiometries 135
5.4.3 Step 3 - Electrolyte and Separator Properties 136
5.4.4 Step 4 - Electrode's Microstructure Properties 136
5.4.5 Step 5 - Transport, Kinetics, and Global Voltage Fitting 136
Step 5a - Solid diffusivity of positive electrode from GITT 136
Step 5b - Film and SEI resistance from HPPC 137
Step 5c - Electrode's conductivities and charge-transfer coefficients 137
Step 5d - Reaction-rate constants from constant-voltage (CV) holds 137
Step 5e - Cathode OCP correction from averaged C/50 data 137
Step 5f - Global Optimization 138
Step 5g - Diagnostic verification 138
5.4.6 Step 6 - Thermal Parameters (optional) 138
5.4.7 Step 7 - Validation of the Canonical Parameter-Set 139
5.4.8 Conclusions of SPMe Parametrization 139
5.4.9 Summary of the adopted Parametrization Procedure 139
Estimation methods for model's parameters 139
Step-by-step model's parametrization 140
5.5 Results from SPMe Parametrization Workflow 143
5.5.1 Step 1: Cell-level geometry and capacity-scaling 144
5.5.2 Step 2: OCP functions and stoichiometric window identification 146
Step 2b: Capacity-recalibration 149
5.5.3 Step 3: Electrolyte and Separator parameters 150
5.5.4 Step 4: Micro-structural properties of Electrodes 153
5.5.5 Step 5: Transport, Kinetics, and global (experimental-based) optimization . 156
Sub-step 5a: GITT pre-estimation of positive-particle diffusivity 157
Sub-step 5b: HPPC pre-estimation of SEI resistivity 160
Sub-step 5c: Electrode's conductivities and charge-transfer coefficients . . 161
Sub-step 5d: Pre-estimation of reaction-rate coefficients 163
Sub-step 5e: Cathode OCP function correction with Pseudo-OCV 165
Sub-step 5f: Global Optimization with three-stage architecture 169
Sub-step 5g: Diagnostic verification 176
5.5.6 Step 7: Final validation of model's parameter-set 179
5.6 Summary of SPMe Parametrization: Parameter-set and Workflow 186
5.7 Step 6 further development: Thermal models 190

Final notes and Conclusions **192**

ABSTRACT

In the context of a progressive electrification of the modern society, aimed at reducing the consumption and at increasing the efficiency of power systems, from mobility to home applications, batteries represent key components.

In this Master Thesis, result of a collaboration between Politecnico di Torino and Dumarey Automotive Italia S.p.A., an experimental characterization of a Li-ion battery cell for automotive applications is first performed, and the collected data-set is then exploited for the subsequent development of a physics-based (or electrochemical) model. This model is capable of capturing the main physical quantities associated with the cell's behavior (terminal-voltage, current, efficiency, thermal effects), as a function of the operating conditions (external temperature, charge/discharge patterns). The case-study focuses on a Lithium-ion High-Power NMC/graphite pouch cell, manufactured by Kokam, with $11\ Ah$ of nominal capacity, and $3.7\ V$ of nominal voltage.

On the modeling side, available options are reviewed, including physics-based, empirical, equivalent-circuit and data-driven models. In order to align with the activity's required physics-based approach, the Single Particle Model with electrolyte (SPMe) is selected. A review of five common simulation environments, suitable for electrochemical battery modeling, is also conducted; PyBaMM, a Python-based open-source tool, dedicated to the creation of physics-based models for battery cells, is chosen as the simulation framework. Different parameter-sets are analyzed according to the chemistry of the cell, finally selecting "Mohtat2020"; it is exploited as a basis for further model's parametrization.

A thorough experimental campaign, performed over a period of several months, is used to explore different aspects of the cell. This testing activity is designed to characterize the battery cell terminal-voltage behavior, during charging and discharging phases, and comprises several non-invasive tests, such as Pseudo-OCV, GITT (Galvanostatic Intermittent Titration Technique), or HPPC (Hybrid Pulse Power Characterization).

Model parametrization is the core activity of the entire work, requiring the most time-intensive tasks. The parametrization workflow comprises two different main steps: (i) first, a preliminary sensitivity-analysis (based on Design-of-Experiments) is performed to determine how the variations of a certain parameter group, inside plausible physical ranges (taken from literature), could affect the shape of terminal-voltage curve; (ii) second, a well-established fine-tuning procedure is performed to identify/estimate the highly sensitive model's parameters, involving some optimization techniques, aiming to minimize the discrepancies between simulations and experiments. Each step of model parameterization is further decomposed into several sub-steps, in order to manage the problem's complexity.

The achieved results from model parametrization allow one to construct a reliable parameter-set for the Kokam cell. Thus, the obtained model is finally validated using all the available experimental data (including training and unseen tests), demonstrating its good capability of capturing the cell response, in terms of terminal-voltage in both slow and fast transients.

Thesis Introduction

The idea underlying the Thesis was to analyze the deepest physical aspects of the battery, therefore the choice of the most complex model category, i.e. physics-based model, rather than simpler Equivalent-circuit model (ECM), was well motivated.

The primary objective was a comprehensive training/education, between university and company, with new competencies about the emerging field of battery applications for automotive. The growing demand for more efficient systems, that can couple the positive aspects of traditional ICE vehicles with electrical systems, inside HEVs (Hybrid Electric Vehicles), is a current topic. The batteries represent the core of modern electrified vehicles. In this context, the battery models assume a central role for the BMS (Battery-Management-Systems). The most commonly used models in BMS are, for simplicity, ECMs, although even simple electrochemical models, such as SPMe, are increasingly employed; this is an example of practical application of the models in the real world.

In order to parametrize an SPMe, a proper experimental activity was necessary to extract useful information for battery parameters. The experiments were carried out using a battery cycler and a suitable climatic chamber. This represented a great experience in laboratory, which allowed one to acquire knowledge about sophisticated instruments for battery cell tests, going into the academic research world.

Another objective was the willingness to understand the physical inner mechanisms inside the batteries. Indeed, the study of electrochemical aspects (e.g., thermodynamics, diffusion, kinetics), regulated by specific physical laws, was really important to acquire a deep knowledge of how the battery really works. In addition, the adoption of physics-based models, rather than empirical or data-driven models, is a strong point of this Thesis, with the purpose of obtaining a reliable physically-grounded parametrization.

The most important objective was to obtain reasonable results, considering a trade-off in the error minimization between the SPMe simulations and the real experiments. The final chapter summarizes the model evolution, showing the optimal set of parameters, which is coherent with the sets obtained for similar chemistries in several literature studies.

In conclusion, the Thesis chapters will be briefly exposed for a general introduction. The first chapter deals with the fundamental concepts underlying batteries, in terms of designs, chemistries, and basic operating principles. The second chapter classifies and analyzes the several types of battery modeling and the corresponding software-tools (such as: PyBaMM). The third chapter focuses on the experimental campaign, showing the laboratory instruments and the major tests used to characterize the Kokam battery cell. The fourth chapter is dedicated to fundamental electrochemical laws and it explains the basic equations for SPMe models. The fifth and final chapter introduces battery parametrization, analyzing the PyBaMM's parameters and their suitable sets, and develops the crucial Sensitivity-Analysis, to get a framework of the most impactful parameters on the model's response, followed by the step-by-step fine-tuning procedure, to construct a reliable parameter-set for the SPMe of the analyzed battery cell.

Chapter 1

Introduction to Batteries for Automotive Applications

This chapter focuses on the general aspects of energy storage systems, in particular on electrochemical devices, i.e. batteries. The fundamental units of batteries, electrochemical cells, are deeply investigated, considering the case-study: lithium-ion battery cells. A brief part regarding the electrochemical systems, compared with other forms of energy storage, is described in the first section. Meanwhile, the second section deeply analyzes the battery cells from structural, chemical, and physical points of view. A further analysis related to cell's formats and designs is depicted in the third section to introduce the real case-study.

1.1 Energy Storage Systems

Energy is the basis of contemporary societies. In particular, the form of energy that is available in nature, for conversion and usage by people, is known as primary energy. The sources of primary energy can be found in oil wells or in other natural environments such as in the wind or in the sun. Examples of primary energy sources are: fossil fuels, wind, solar, hydro, wave, nuclear, geothermal and biomass. Energy is produced from a certain primary source either by burning it or by transforming the source energy through a conversion system. When primary energy is transformed through the use of energy conversion devices, a new type of energy is obtained: secondary energy. Additional energy conversion systems use the secondary energy to deliver useful work (as described in [1]).

In general, primary sources have energy stored in chemical, heat, kinetic or some other alternative forms. Energy is stored in fossil fuels in chemical form: energy is extracted from them through an Internal Combustion Engine (ICE) vehicle by burning it in a heat engine. Electrical energy is an example of secondary energy (it is an energy vector), that can be typically converted into mechanical work by an electric machine (e.g., asynchronous or synchronous motors). Therefore, electrical energy can be obtained from the primary source by burning fossil fuels in thermal power plants, or from renewable primary sources of water, wind or sun. Electrochemical devices (e.g., batteries) convert chemical energy into electrical energy through a high-efficiency process. This Thesis focuses on rechargeable batteries, or secondary batteries, which store the electrical energy through a conversion into chemical energy, before releasing it during battery discharge ([1]).

Energy content of various raw fuels or materials refers to the energy that can be extracted from it for useful work. The parameters for energy content evaluation are specific energy and energy density. The first parameter is related to mass of the energy source, and is measured in Wh/kg, the other one is related to the total volume occupied by it and is measured in Wh/m^3. In order to make a comparison, the values for specific energy sources are given in Table 1.1([1]).

Energy source	**Nominal Specific Energy** (Wh/kg)
Gasoline	12500
Diesel	12000
Bio-Diesel	10900
Natural Gas	9350
Ethanol	8300
Methanol	6050
Hydrogen	33000
Coal (bituminous)	8200
Lead-acid battery	35
Lithium-polymer battery	200
Flywheel	200

Table 1.1: Nominal Specific Energy of several Sources

One of the problems of energy is to store it in a convenient form, so that it can be utilized when needed. In terms of storage, fossil fuels have the biggest advantage because they can be conveniently stored in a container. On the other hand, electrical energy is very useful to deliver work on demand using a highly efficient electrochemical device. The mechanism for energy delivery must also be considered for the system under consideration. The energy transportation system has to be secure, efficient and environmentally friendly. A big advantage for electricity is relative to energy transportation over long distances: electrical transmission and distribution systems are highly efficient. Once an infrastructure is in place, energy converted to the electrical form (at the generation side) can be delivered to industrial and residential units through transmission and distribution systems. Instead, fossil fuels are transported for long distances using pipelines, ocean liners and land transportation, before being finally stored in gas stations ([1]).

The electrochemical devices represent the most promising alternative technology to the conventional fossil fuels as energy storage. The electrochemical energy conversion processes have the advantages of high energy efficiency, large power output and the availability of a wide selection of chemistries. Batteries and fuel-cells are considered as energy storage and power generating devices, that are suitable for both hybrid & electric vehicles or stationary applications. A typical battery pack for automotive applications is shown in Figure 1.1.

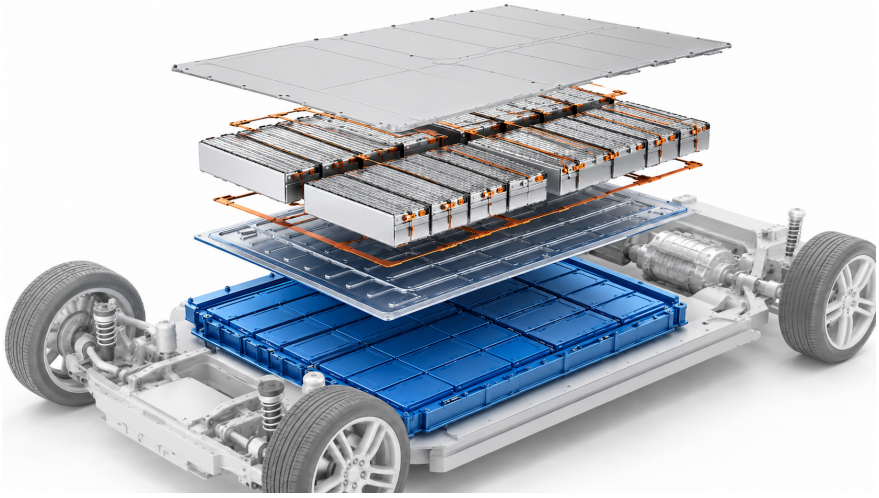


Figure 1.1: Typical automotive battery pack

In general, Electrochemical Storage Systems (ESS) convert electrical energy into chemical

energy for storage and release it as needed through controlled electrochemical reactions. They are the pillar to supply portable electronic devices, electric vehicles and renewable energy integration systems. Primary batteries are for a single-use, while secondary batteries are rechargeable for multiple usages. Batteries can be made of different materials, with lithium being the most widely used. Other storage technologies are super-capacitors and flow batteries; they provide high-power and large scale energy storage solutions.

1.2 Batteries in Electric and Hybrid vehicles

The basic requirement for purely electric vehicles is a portable supply of electrical energy, which is converted to mechanical energy in the electric motor for the vehicle propulsion. Batteries carry out a fundamental role: they transform chemical energy into electrical energy available for the electric motors, passing first through power converters (inverters) in a typical current DC/AC conversion. The main features of automotive batteries can be summarized in some crucial points ([1]):

- High specific power;
- High specific energy;
- High charge acceptance rate for both recharging and regenerative braking;
- Long calendar and cycle life.

In addition to these features, other elements must be considered for a vehicle: battery packaging, cell balancing, accurate state-of-charge (SoC) measurement, and recycling facilities to recover battery components.

In general, all the batteries implemented inside battery electric vehicles and hybrid electric vehicles (BEVs and HEVs) are secondary batteries, because they are the object of multiple charge-discharge cycles during their lifetime. The first type of batteries was represented by lead-acid batteries. However, the power and energy delivered by lead-acid batteries are lower than several other battery technologies. The research and development in this field led to the discovery of alternative chemistries in the last years of the 1960s and early years of the 1970s. There was an important interest in the 1980s for sodium-sulfur batteries for their high energy and power densities, but safety and manufacturing difficulties led to the abandoning of this technology. Finally, starting from the 1990s, a deep interest for batteries, useful for low-power applications, led to the developments of alternative chemistries: nickel-based (at the beginning, with the toxic nickel-cadmium chemistry) and lithium-based (mainly lithium-ion batteries). Currently, the major types of rechargeable batteries used or being considered for BEVs and HEVs are, in order of application ([1]):

1. Lithium-ion (Li-ion);
2. Nickel-Metal Hydride (NiMH);
3. Lithium-polymer (Li-poly);
4. Sodium-sulfur.

Surely, the Li-ion battery technology is the most applied and used among the mentioned four categories. There are several types of Li-ion battery technologies available on the market, including Li-iron phosphate, Li-titanate, Li-Manganese and Li-Cobalt. The choice of one specific chemistry depends on the type of vehicle (BEV or HEV or PHEV).

The specific chemistries adopted for the automotive field will be analyzed in the following sub-sections, with a particular focus on the predominant Lithium-ion batteries.

1.2.1 Battery cells: internal components and basic chemical reactions

The elemental unit of an automotive battery pack is called "cell". A cell is made by the presence of a single layer or by the aggregation of multiple layers (typical case). In general, the cells contain the stored chemical energy, that can be transformed into electrical energy. Different grouped cells, connected in series or in parallel are enclosed in a casing to form a module. More modules, typically connected in series, constitute a battery pack, that can deliver the desired voltage and energy to the power electronic drive system.

The chemical reactions at the two electrodes of a battery cell are redox reactions: oxidation at the anode and reduction at the cathode.

In general, for rechargeable lithium-ion cells, the terms anode and cathode must be used carefully, since their meaning may depend on the adopted convention. From a strict electrochemical point of view, the anode is always the electrode at which oxidation occurs, whereas the cathode is always the electrode at which reduction occurs.

Practically, the ions-flow always follows this pathway:

- During charging process, the ions move inside the electrolyte and pass from positive electrode, through the separator, to negative electrode.
- During discharging process, the ions move inside the electrolyte and pass from negative electrode, through the electrolyte, to positive electrode.

The electrolyte provides a suitable solvation environment for lithium-ions diffusion phenomena. Indeed the ions in lithium-graphite batteries are driven by concentration gradients to be moved from one electrode to the other one, depending on the adopted operation mode (charge or discharge). Originally, the majority of the lithium content of the cell is stored, in a complete discharged battery, inside the cathode structure.

The available chemical energy, represented by the flow of ions, is converted into electrical energy through the basic components inside a unit cell. The electrochemically active material inside electrodes are generally called active materials, while the inactive parts are called "binder".

Electrodes must be electronically conductive, and they are interconnected to other components, current collectors. These allow the passage of electrons to the external circuit of the load.

Thereby, in order to better understand the real structure of a single-unit cell, a general description of its fundamental components can be summarized as follows:

- Negative electrode: The electrode where oxidation occurs, releasing electrons during discharge; it is typically made of graphite or lithium metal in Li-ion batteries.
- Positive electrode: The electrode where the reduction occurs, accepting electrons during discharge; it determines battery voltage and capacity, often made of lithium metal oxides.
- Electrolyte: A medium, that allows ion transport between the two electrodes, preventing direct electron flow; it can be typically liquid, solid or gel-based.
- Separator: A porous membrane that physically separates the two electrodes to prevent short circuits, while allowing ion exchange; it is made of polyethylene or polypropylene in Li-ion batteries.
- Current Collectors: Metal foils (typically, copper for anode and aluminum for cathode) that transfer electrons between electrodes and external circuit.

In Figure 1.2, a typical cylindrical Li-ion battery is represented, with highlighted all its internal components.

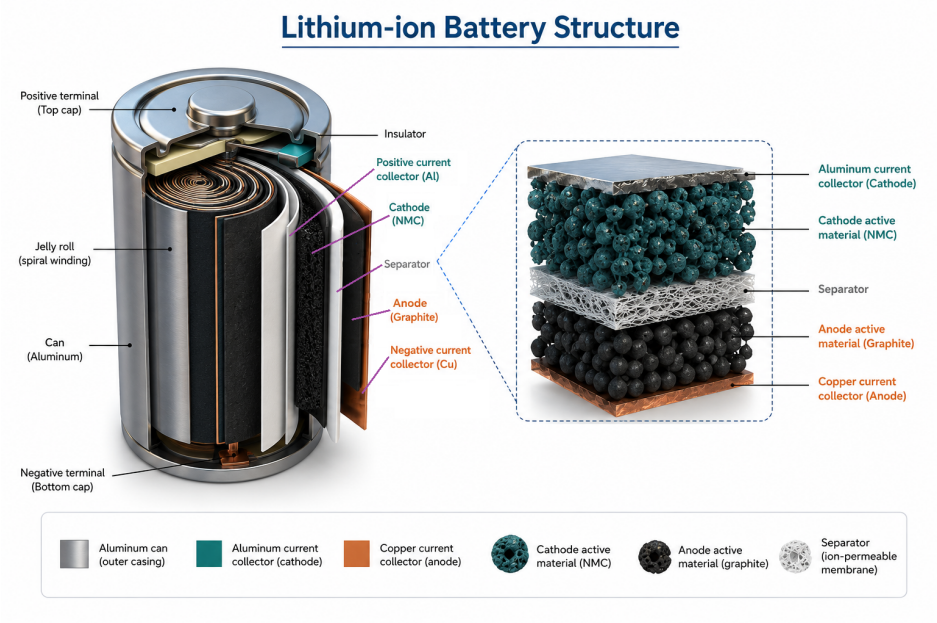


Figure 1.2: Typical lithium-ion battery: Internal components

To measure the actual value of charge for the battery, a term is employed: SoC (as said before, "State-of-Charge"). A practical view of the two mechanisms of charge/discharge for a single Li-ion battery cell is illustrated in Figure 1.3.

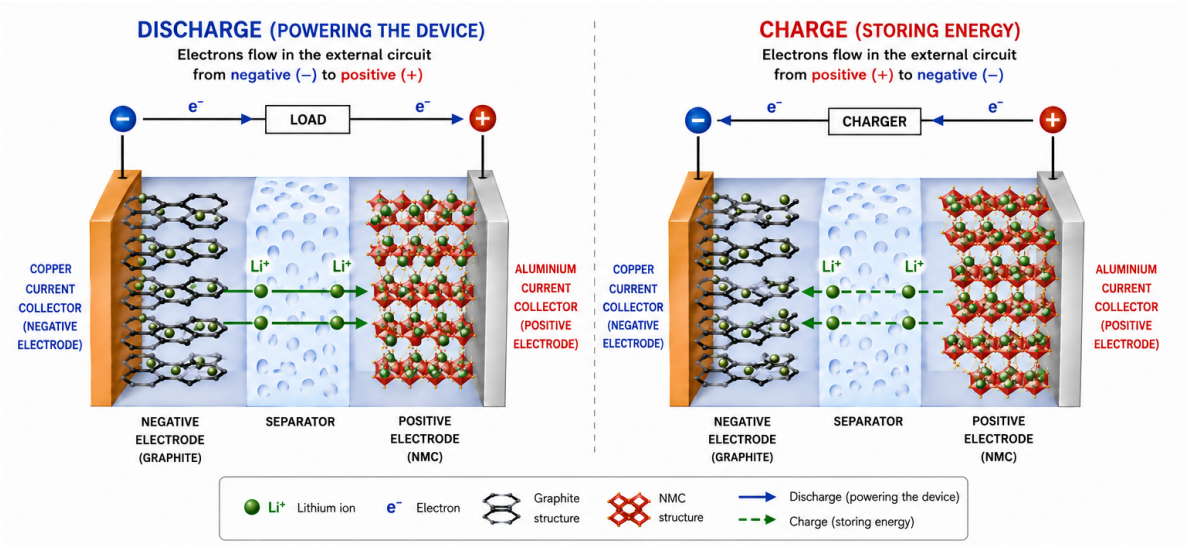


Figure 1.3: Charge and Discharge mechanisms for a Li-ion battery cell

Charging means to impose an external DC power source in order to bring the ions from the positive electrode structure to the negative electrode structure, passing from 0% of SoC to 100% of SoC. In this first case, electrons are released at the positive electrode and consumed at the negative electrode; consequently, the positive electrode is oxidized and the negative electrode is reduced. During charging process, the phenomenon that characterizes the migration of ions inside the cell is called "de-intercalation" (or equivalently de-lithiation), for the positive electrode material, while there is the inverse intercalation process for negative electrode material.

Discharging means to connect an electrical load to the cell, with a consequent internal passage of ions from the negative electrode to the positive electrode, going from 100% of SoC to 0% of SoC. In this second case, the positive electrode gets chemically reduced as it absorbs electrons from the

external circuit; the negative electrode gets oxidized as it releases electrons to the external circuit. During discharging process, the phenomenon that involves the migration of ions inside the cell is called "intercalation" (or equivalently lithiation), for the positive electrode material, while the other electrode undergoes the opposite de-intercalation phenomenon.

In order to avoid ambiguity between charge and discharge conditions, in battery modeling and technical discussions, it is often preferable to refer to the electrodes as "negative electrode" and "positive electrode", rather than anode and cathode. More generally, the electrochemical operation of lithium-ion cells is governed by the reversible transfer of lithium-ions through the electrolyte, and electrons through the external circuit, with the host electrode materials accommodating the corresponding redox processes.

1.2.2 General analysis of internal Cell Structure

In this sub-section, an in-depth analysis of the internal cell-structure is presented. The objective is to view: (i) internal double-sided layers; (ii) single-layer cell; (iii) single-electrode. In this way, it is possible to analyze a battery passing from basic structure to inner microscopic compounds.

A lithium-ion battery cell can be described as a multi-layer electrochemical system, obtained from the repetition of elementary laminated units (layers, as described in 1.2.1). Figure 1.4 illustrates the typical configuration of Li-ion battery cells. Indeed, in practical cell manufacturing, this arrangement is often realized through a "bi-unit" cell structure, in which double-sided coated electrodes are used: the positive active-material is deposited on both sides of an aluminum current-collector, while the negative active-material is deposited on both sides of a copper current-collector. The separator prevents direct electronic contact between the two parts of the cell, while its electrolyte-filled porosity enables lithium-ion transport across the cell thickness.

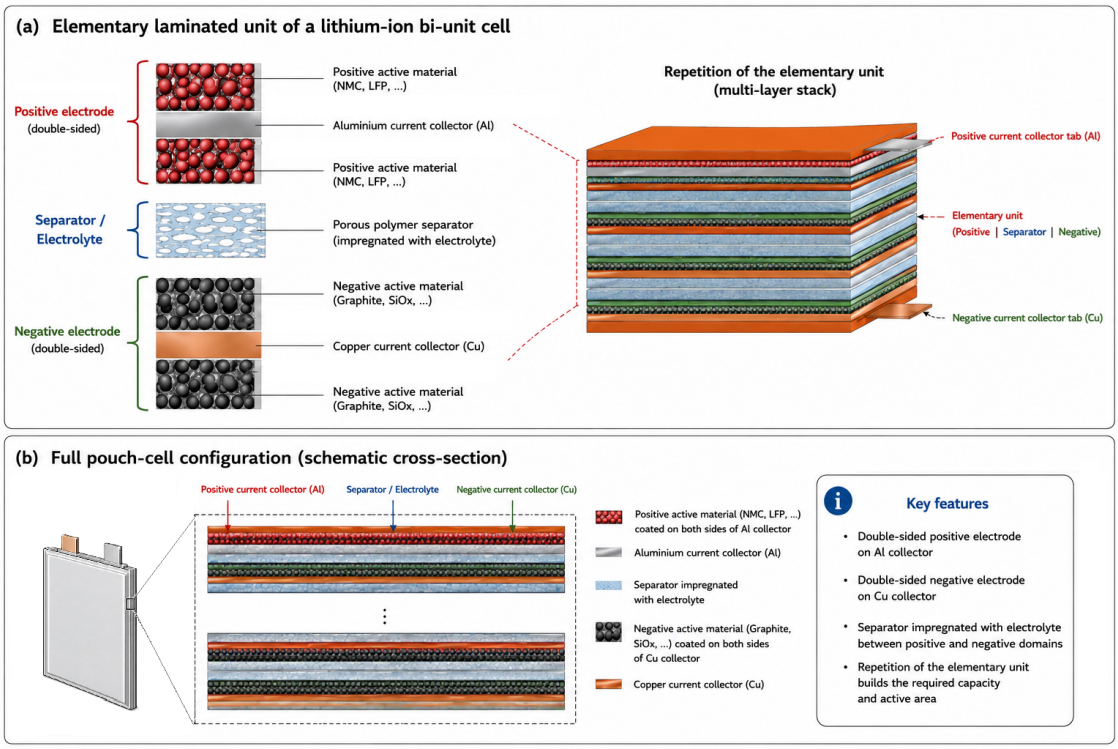


Figure 1.4: Cell structure: Bi-unit Configuration

This bi-unit configuration is widely adopted, because it provides an efficient compromise between electrochemical performance, compactness, and manufacturability. In particular, double-sided

coating increases the amount of active-material per current-collector, reduces the corresponding fraction of inactive components, and allows the total cell capacity to be scaled, by repeating the same elementary structure in a stacked, wound or Z-folded architecture.

In Figure 1.5, the different cell components are analyzed with more details. Each unit is composed of two electrodes, a separator impregnated with electrolyte and metallic current-collectors. The positive active material is typically made of NMC or LFP or NCA (automotive cases), whereas the negative active material is commonly graphite or graphite-SiO_x. This typical architecture is repeated to form more complex structures, as introduced before, aiming to increase the active area and the deliverable capacity.

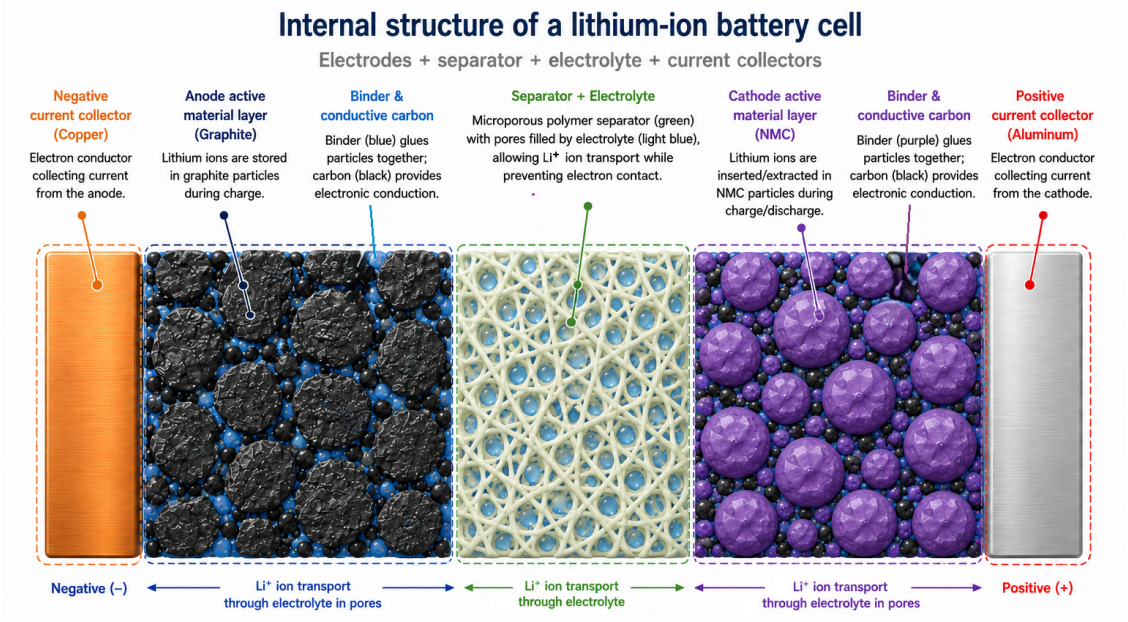


Figure 1.5: Fundamental inner Cell components

At the microscopic scale, as shown in both Figures 1.5 and 1.6, each porous electrode is a composite medium made of active-material particles, binder with conductive carbon, and electrolyte-filled pores.

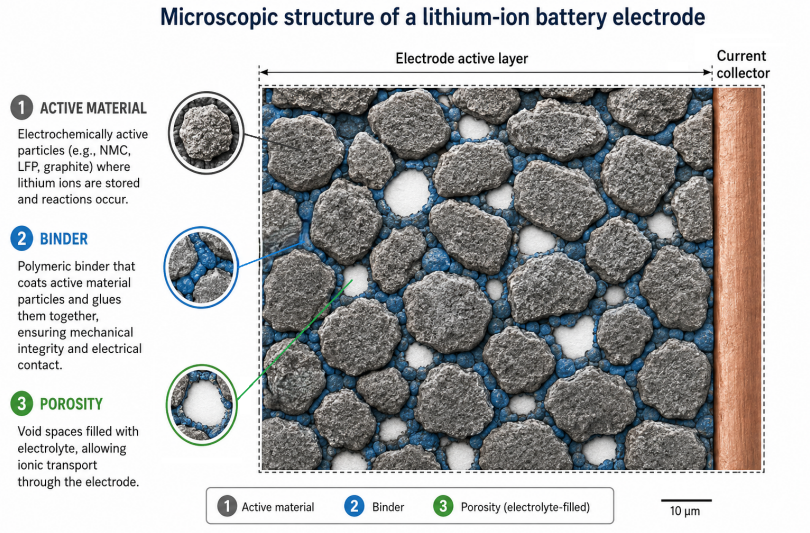


Figure 1.6: Typical Electrode-structure compounds

Overall, the active particles store lithium by intercalation/de-intercalation, the conductive additive and current collectors provide electronic pathways, the binder ensures mechanical cohesion, and the porosity allows ionic transport through the electrolyte. Therefore, its morphology directly affects lithium-diffusion, electronic conduction, ionic transport, and the main geometrical and micro-structural parameters, required in physics-based battery models.

This general description of commercial Li-ion cells as commonly formed by multiple layers of cathodes, anodes, and separators infused with electrolyte, and arranged in different ways, is the starting point of future modeling.

1.2.3 Traction Batteries: Classification

This Thesis focuses on secondary batteries, considering that they are rechargeable and so typically used in automotive for hybrid and electric vehicles. In general, secondary batteries are designed to sustain multiple processes of charge-discharge cycles, offering an alternative to primary batteries. This key difference between primary and secondary systems reduces wastes and long-term costs of possible substitutions. A fundamental feature of secondary batteries is the electrochemical reversibility: chemical reactions are reversible, allowing them to restore energy through recharging.

The available battery types on the market were already introduced before. This sub-section has the aim of making a clearer classification of the possible types that have evolved across the time, starting with first automotive applications employing lead-acid batteries, passing through Nickel-based batteries (toxic Nickel-Cadmium was progressively abandoned, in favor of Nickel-Metal-Hydride (NiMH)) or Sodium-Sulfur batteries, and arriving at the latest lithium-based chemistries, largely used nowadays by the main companies (above all: Tesla, BYD, Volvo, Volkswagen, Stellantis).

The whole treatment of this sub-section is based on two sources: the book of I. Husain [1] and the article written by Sciatti et al. (2026) [2].

Available Battery Chemistries

The available battery chemistries for automotive applications are presented in this part, leaving the description of the most employed battery chemistry (Lithium-ion batteries) at the end, with more details.

Lead-acid battery Lead-acid batteries have been the most popular choice of batteries for electric vehicles during the initial development stages, with the production that largely increased in the early 1980s. The long existence of the lead-acid battery is mainly due to: (i) relatively low cost; (ii) easy availability of raw materials; (iii) ease of manufacture; (iv) favorable electromechanical characteristics.

Therefore, these batteries can be designed for applications that demand high-power and essentially they are cheap, safe and reliable. Moreover, many recycling infrastructures are already in place for them. However, their typical drawbacks, given by low specific energy, poor performance at cold temperatures, short calendar and cycle life were the main obstacles to their use for hybrid and electric vehicles.

Nickel-Cadmium battery Nickel-Cadmium batteries present superior performance with respect to lead-acid batteries. More specifically, they provide good low-temperature performance, flat discharge voltage shape (low variability across voltage range), long cycle-life, and excellent reliability with easy possible maintenance. However, the lower practical cell voltage implies that more cells have to be connected in series to reach the final desired voltage of the pack. Moreover, the specific energy of $NiCd$ batteries is similar to that of lead-acid batteries.

Decisive drawbacks that have limited the diffusion of this battery chemistry are: (i) high costs; (ii) toxicity contained in cadmium; (iii) insufficient delivered power. The strong environmental concerns about this battery type have practically stopped their use on the market.

Nickel-Metal-Hydride ($NiMH$) battery Nickel-Metal-Hydride batteries are the successors of nickel-hydrogen batteries, and they are largely used for hybrid electric vehicles. A $NiMH$ battery contemplates a positive electrode made of nickel hydroxide and a negative electrode made of metal hydride.

The positive electrode shows the same composition of nickel-cadmium batteries, while the big difference is given by negative electrode: it consists of a certain metallic alloy, that can absorb a large number of hydrogen molecules (under certain temperature and pressure) to form metal hydride.

$NiMH$ batteries are characterized by high lifetime in terms of number of admitted typical cycles. This enables their adoption in hybrid electric vehicles (HEVs), for which battery pack must comply with a durability requirement of at least $100,000$ vehicle miles.

Finally, $NiMH$ batteries provide high-power density, although with high manufacturing costs; they are recyclable, safe and usually abuse-tolerant with respect to other types. The biggest drawbacks are high costs, high self-discharge rates, poor performance at elevated temperature and a relatively low efficiency.

Sodium-Sulfur Battery Sodium-Sulfur batteries emerged as a promising chemistry in the middle of 1960s. This battery type has different advantages in terms of chemical composition: sodium for negative electrode and sulfur for positive electrode.

The big difference with respect to other battery types is the solid electrolyte, i.e. beta-alumina, that is a sodium aluminum oxide with a complex crystal structure.

Despite these attractive features, NaS batteries have several practical limitations. In more detail, their operating temperature is around $300\ ^{\circ}C$, that implies the necessity of adequate insulation and a thermal control unit. These requirements forces to have a certain minimum size for the battery, limiting the application of sodium-sulfur batteries for electric vehicles. Other important disadvantages are: (i) absence of an over-charge mechanism; (ii) safety issues, in case of excessive produced heat or explosion due to possible accidents.

Sodium-Metal-Chloride Battery Sodium-metal-chloride batteries are a derivative of sodium-sulfur batteries, since they provide mechanisms of over-charge and over-discharge. The internal chemical composition of this battery type is similar to that of NaS batteries, with the difference that positive sulfur electrode is replaced by nickel-chloride ($NiCl_2$) or a mixture of nickel-chloride and ferrous-chloride ($FeCl_2$). Negative electrode and electrolyte chemistries are the same as those of sodium-sulfur batteries.

The sodium-metal-chloride batteries are commonly known as ZEBRA batteries. In general, they showed to be safe under all conditions of usage, with high potentials for being applied as batteries for hybrid and electric vehicles.

Lithium-polymer battery Lithium-polymer batteries evolved out of the development of solid-state electrolytes. As for sodium-sulfur batteries, they employ solids capable of conducting ions and that are also electron insulators. For this reason, Li-polymer batteries are considered as solid-state batteries. The most common polymer electrolyte is the polyethylene oxide compounded with an appropriate electrolyte salt.

The use of solid-polymers has a decisive safety advantage in cases of accidents for hybrid and electric vehicles. Another strong point is represented by the flexibility of this cell chemistry to form

a battery of any size or shape within the chassis of the vehicles. However, the biggest drawback of Li-polymer batteries is the need to operate at a high temperature range $(80 - 120)\ ^{\circ}C$, in order to have good performance; this represents the main limitation for this promising battery chemistry.

Zinc-Air battery Zinc-air batteries are the only primary-battery chemistry in this overview that can be considered for automotive applications. Indeed, zinc-air battery is only mechanically rechargeable by replacing the discharged product (zinc-hydroxide) with fresh zinc electrodes. This battery type has a gaseous positive electrode of oxygen and a negative electrode made of pure metallic zinc.

Lithium-ion battery

Lithium-ion batteries began to spread in 1970s, when much research led to the discovery of different materials (e.g. Cobalt or Nickel) that could intercalate lithium inside their crystal lattice structures. They have become the basis of the positive electrode structure. Meanwhile, the use of graphite that can host lithium-ions within its layered structure, in alternative to pure metallic lithium that proved unstable, was a credible basis for this battery chemistry.

Indeed, the lithium-ion batteries are essentially based on the two opposite mechanisms of intercalation & de-intercalation of lithium inside the particles of anode or cathode (depending on the operation mode: charge or discharge). As explained in 1.2.1, the intercalation or de-intercalation processes liberate the electrons obtained from redox reactions, to establish a current flow toward external circuits.

In general, lithium metal has the most negative standard reduction potential (E^0), with respect to hydrogen ($-3.045\ V$ vs. SHE), and a low atomic mass (6.94). These features allow the Li-ion cells to have higher voltage range, compared to other chemistries, and lower total weight.

The majority of lithium-ion batteries use either a layered oxides or iron-phosphates of lithium as the positive electrode. Layered positive electrodes with cobalt oxide are expensive, but more complete, in terms of performance, with respect to other chemistries. Nickel oxide, which costs less with respect to the previous case, is structurally more complex, but with a similar performance to that of cobalt oxide electrodes. Manganese oxide-based is also used (mainly for portable electronics) since manganese is cheaper, widely available and less toxic. Alternative and widespread chemistry for positive electrode materials is the lithium-iron phosphate ($LiFePO_4$), which can deliver stable and good performance at lower costs. Finally, a hybrid chemistry is the mixture of nickel, cobalt and aluminum, that can perform well, although it exhibits more thermal instability than the other cases.

The anode structure is practically made of graphite (LiC_6), in the majority of cases or with some variant, avoiding pure lithium, due to possible formation of dendrites during the operations of the battery.

In general, the typical nominal cell voltage for a lithium-ion cell is $(3.6 - 3.7)\ V$, almost equivalent to 3 $NiMH$ or $NiCd$ cells connected in series.

The components of Li-ion batteries are also recyclable, even though suitable infrastructure is yet to be developed. In terms of costs, this battery chemistry is now more convenient than other battery types, e.g. Nickel-Metal-Hydride batteries, for automotive purposes. However, the lower material costs do not reflect directly on the total cost of battery packs, since expensive management systems (i.e. Battery-Management-Systems (BMS)) are necessary in lithium-ion packs to avoid several safety problems.

The main drawback of Li-ion batteries is represented by their high sensitivity to over-voltages and over-discharges. Over-voltage of Li-ion cells can cause, in the positive electrode, a solvent oxidation and an exothermic decomposition of the active material. The combination of over-voltage

and over-discharge events can result in irreversible cell damage, and in most of the cases, even in cell ignition.

Overall, automotive industry has essentially settled the use of layered cathode and graphite anode for common Li-ion cells for all the types of hybrid and electric vehicles. Specifically, Li-ion battery packs for BEVs vary with the possible choices of: NMC, NCA, LFP, for cathodes, and graphite/LTO, for anodes. The highest performance is offered by NMC or NCA battery chemistry, whereas LFP chemistry is becoming widespread in the automotive market.

Lithium-ion battery chemistries In electric-vehicle applications, the choice of chemistry directly affects energy density, power capability, cost, safety, aging behavior and recyclability; therefore, it represents a central element both for cell selection and for electrochemical model parametrization.

The following description of Li-ion batteries (LIB) state-of-art, related to electrode's chemistries is based on the work of Sciatti et al. (2026) [2].

Lithium-iron phosphate (LFP, $LiFePO_4$) is a cathode chemistry characterized by excellent safety, high thermal stability and long cycle life. The internal strong P-O bonds reduce the tendency of the cell toward thermal runaway. LFP typically operates at lower voltage than layered oxides, with an average operating voltage around $(3.2 - 3.5)\ V$ and a common operating voltage window of about $(2.5 - 3.65)\ V$, both measured with respect to Li/Li^+. Its practical specific capacity is about $(150 - 160)\ mAh/g$, while the lower voltage and moderate energy density are drawbacks with respect to other chemistries, NMC or NCA above all. Generally, LFP is attractive in applications, where cost, safety and durability are more important than maximum driving range, such as stationary storage, buses, medium-cost EVs and high-cycle life systems. Their usage in automotive applications has grown rapidly in recent years, with new enhanced LFP versions available on the market for modern EVs.

Lithium Nickel-Manganese-Cobalt Oxide (NMC, $LiNi_xMn_yCo_zO_2$) is one of the most relevant layered-oxide cathodes for automotive applications. Nickel mainly increases capacity and energy density, Manganese improves structural stability and lowers cost, while Cobalt contributes to electronic conductivity and structural stabilization. Different stoichiometries can be employed, such as NMC111 (or NMC333), NMC532, NMC622, and NMC811; the nickel content is directly correlated with the value of specific capacity, but it may reduce thermal stability and accelerate degradation if not properly stabilized. NMC typically operates in graphite-based cells with an average operating voltage of about $(3.7 - 4.1)\ V$, and a usual voltage window around $(3.0 - 4.2)\ V$, both with respect to Li/Li^+. Its practical cathode capacity is commonly about $(150 - 210)\ mAh/g$. This balanced combination of energy density, power capability and acceptable lifetime explains its wide use in EVs, PHEVs, e-bikes, power tools, and other industrial applications.

Lithium Nickel-Cobalt-Aluminum Oxide (NCA, commonly $LiNi_xCo_yAl_zO_2$) is another layered oxide, closely related to nickel-rich NMC. It offers very high specific energy, because of its high nickel content, while aluminum improves structural and thermal stability compared to pure $LiNiO_2$. Typical full-cell voltages are similar to NMC, with an average operating voltage around $(3.7 - 4.0)\ V$, and an operating voltage window of approximately $(3.0 - 4.2)\ V$, both against Li/Li^+. The practical cathode capacity is often in the range $(140 - 230)\ mAh/g$, and the corresponding commercial cell-level specific energy can be higher than that of many NMC battery systems. Its main limitations are higher costs, stronger safety-management requirements and sensitivity to high SoCs. Therefore, NCA is mainly used in high-energy EV cells and for selected industrial applications, that require high energy-density.

Lithium-cobalt Oxide (LCO, $LiCoO_2$) is the historical layered cathode used in the very first commercial lithium-ion batteries. It provides high-specific energy density and stable voltage

behavior, which made it very successful for portable electronic devices. Typical graphite-based cells have an average operating voltage of about $(3.6 - 3.9)\ V$, and operating voltage window of $(3.0 - 4.2)\ V$, both against Li/Li^+. Its practical cathode capacity is around $(120 - 160\ mAh/g)$, lower than previous chemistries. The main drawbacks are high costs and critical availability of cobalt, limited thermal stability and relatively poor high-power capability. Consequently, LCO is now mainly associated with consumer electronics.

Lithium-Manganese Oxide ($LMO, LiMn_2O_4$) provides a structure with low internal resistance and good power capability. Its average operating voltage is generally about $(4.0 - 4.2)\ V$, with typical operating range of $(3.2 - 4.4)\ V$, both versus Li/Li^+. However, the practical cathode capacity is very limited to around $(90 - 120)\ mAh/g$, and the material can suffer from manganese dissolution, especially at elevated temperatures. Pure LMO is never used in modern high-energy EVs, but it has been widely used in power tools, medical devices, in some hybrid-vehicles and blended cathodes with LMO/NMC mixtures.

Graphite (C/LiC_6) is the dominant anode material in commercial lithium-ion cells. It is a layered carbon material in which lithium intercalates to form LiC_6 at full lithiation. Its theoretical specific capacity is $372\ mAh/g$, and its average operating potential is very low, around $(0.1 - 0.2)\ V$ against Li/Li^+. This low potential is beneficial for full-cell voltage and energy density, which explains why graphite remains the reference anode for most of NMC, NCA or LFP cells for automotive purposes. Its advantages include low cost, good electrical conductivity, acceptable volume variation and mature manufacturing. Its main limitations are related to some degradation mechanisms (lithium-plating risk or SEI layer growth), contributing to aging of the cell. Some chemistry variants include graphite combined with silicon oxide (SiO_x), which provides several benefits in terms of overall cell performance.

Lithium titanate (LTO, $Li_4Ti_5O_{12}$) is a classical alternative anode chemistry. Its key feature is the correspondingly high operating potential, about $1.55\ V$ against Li/Li^+, which strongly reduces lithium-plating risks and improves safety during fast charge. Moreover, LTO has a limited volume change during charge/discharge of cell than other materials, and this gives excellent cycle life and rate capability. However, the higher anode potential lowers the full-cell voltage: commercial LTO cells typically have a nominal voltage around $2.4\ V$, operating voltage approximately between $1.8\ V$ and $2.85\ V$. Its theoretical capacity is only about $175\ mAh/g$, so LTO cells have much lower energy density than graphite-based cells. For these reasons, LTO is used mainly in applications that require extreme safety, fast charging and long lifetime, such as buses or industrial storage systems.

Comparisons among battery chemistries A summary of the main indicative properties of the battery chemistries for automotive is presented in the following Table 1.2 ([1]). The overall performance of each battery type depends on the combination of several parameters, considering also the field of application.

Battery Chemistry	Specific Energy $[Wh/kg]$	Specific Power [W/kg]	Energy Efficiency [%]	Life-cycle
Lead-acid	35 - 50	150 - 400	80	500 - 1000
Nickel-Cadmium	30 - 50	100 - 150	75	1000 - 2000
Nickel-Metal-Hydride	60 - 80	200 - 400	70	1000
Sodium-Sulfur	150 - 240	230	85	1000
Sodium-Nickel Chloride	90 - 120	130 - 160	80	1000
Lithium-polymer	150 - 200	350	-	1000
Zinc-air	100 - 220	30 - 80	60	500
Lithium-ion	90 - 160	200 - 350	> 90	> 1000

Table 1.2: Battery chemistries: Summary of main properties

Finally, a summary of all the main chemistries typically adopted for anode and cathode of Lithium-ion batteries (LIB) is reported in Table 1.3 ([2]). It is worth highlighting that in LIB, the selected battery chemistry is the primary driver of EV performance, safety, and sustainability.

Active material	Avg. Potential vs. Li/Li^+ [V]	Theor. Specific Capacity [mAh/g]
LFP (Cathode)	3.2 - 3.5	170
NMC (Cathode)	3.7 - 4.1	275 - 280
NCA (Cathode)	3.7 - 4.0	275 - 280
LCO (Cathode)	3.6 - 3.9	274
LMO (Cathode)	4.0 - 4.2	149
Graphite (Anode)	0.1 - 0.2	372
LTO (Anode)	1.55	175

Table 1.3: Lithium-ion batteries: chemistries comparison

Electrolytes and Separators in Lithium-ion batteries In order to complete the description of Li-ion batteries, the other elements to be taken into account are electrolytes and separators.

Electrolytes enable the transport of lithium-ions between the anode and the cathode. Organic solvents combined with lithium salts are the most common choice. In general, electrolyte must have high ionic conductivity (transport property) and thermal stability to maintain performance under varying conditions. Possible electrolytes to be used in Li-ion batteries are:

- **Classic Electrolytes**: Liquid Electrolytes, typically composed of conventional Organic Solvents + Lithium Salts.
- **Emerging Trends**: Solid-state Electrolytes or Polymer Electrolytes (typical in lithium-polymer batteries).

Considering the most common choice, i.e. liquid electrolytes, a brief description of their components is made:

- **Organic Solvents** They play a crucial role in lithium-ion battery electrolytes, by dissolving lithium salts and enabling ions transport between the anode and the cathode. The most commonly used solvents are carbonate-based, as they provide high dielectric constants and good lithium-ion solubility. Popular solution as organic solvent is: Ethylene Carbonate (EC); it is frequently mixed with Propylene Carbonate (PC), Di-Methyl-Carbonate (DMC), Di-Ethyl-Carbonate (DEC) or Ethyl-Methyl-Carbonate (EMC), to improve fluidity.
- **Lithium Salts** They are dissolved in organic solvents to create ionic conductivity, allowing lithium-ions to travel between electrodes during battery cycles. The salt choice can impact on battery performance, lifespan and safety. Typical solutions as lithium salts can be: $LiPF_6$ (Lithium Hexa-fluoro-phosphate), that is commonly used in commercial batteries; $LiBF_4$ or $LiClO_4$ are valid alternatives.

Regarding the separators material, different options can be adopted for Li-ion batteries:

- **Polyethylene**;
- **Ceramic Separators**;
- **Glass fiber**;
- **Solid State separator**.

The classic functions of separator are: (i) to be a permeable membrane for lithium-ion flows; (ii) to avoid short-circuits, that can be produced by accidental contact between the two electrode's structures.

The separator porosity plays a fundamental role in battery dynamics: it allows electrolyte to fill the separator's pores, useful for the diffusion of Li^+ between the electrodes; it also affects internal resistance of the cell, hence the battery response to inputs.

1.3 Automotive Li-ion cells: formats and designs

The case-study is a Li-ion battery cell, Kokam SLPB55205130H ([3]), that is a pouch cell with a High-Power design. That means significant design choices, that impact severely on the electrochemical battery characterization.

In general, the key features and some physical aspects are clearly affected by the adopted format: cylindrical, prismatic or pouch. In addition, the micro-structural properties of electrodes are clearly influenced by the cell purpose: high energy density or high power density.

This section introduces a general study of Li-ion battery cell formats and designs, as premise of further modeling activity.

1.3.1 Automotive cell's formats

In automotive battery systems, lithium-ion cells are not used as isolated electrochemical devices, but they are assembled into modules and packs, in order to meet the required voltage, power and energy levels (1.2.1). A typical BEV battery pack may contain from tens to thousands of individual cells, depending on the selected cell format and pack architecture. The most common cell formats used in electric and hybrid vehicles are essentially three: cylindrical, prismatic hard-case, and pouch cells. Their main differences are related to the external enclosure, the internal arrangement of electrodes and separators, the mechanical behavior during cycling, the thermal-management strategy, and the manufacturing process.

Cylindrical cells

Cylindrical cells are one of the most mature lithium-ion format types. Their internal structure is generally based on a jelly-roll configuration, obtained by winding long strips of anode, separator and cathode into a spiral assembly, which is then inserted into a metallic cylindrical can. The rigid housing, typically made of steel or aluminum, provides good mechanical protection and allows the integration of safety devices, such as pressure vents. This format is highly standardized, for example there are many types (also cited in literature, e.g. Chen et al. (2020) analyzed cell [4]), such as 18650 ($18\ mm$ diameter, $65\ mm$ length), 21700 and 4680 cells, and it benefits from high-throughput manufacturing process.

Overall, cylindrical cells are well-known for their robust stability and safety. From an automotive perspective, cylindrical cells offer high manufacturing maturity, good mechanical robustness, and relatively effective heat dissipation at cell level, especially because each cell is small and has a high surface-to-volume ratio. These characteristics make them attractive for applications that require high reliability and modularity. However, the cylindrical geometry introduces packaging inefficiencies because empty spaces remain between adjacent cells. In addition, large battery packs require a high number of cells and many electrical interconnections, which increases the complexity of pack assembly, monitoring and thermal management.

Prismatic hard-case cells

Prismatic cells are characterized by a rectangular metallic enclosure, usually made of aluminum. Their internal electrode assembly can be based on a flattened jelly-roll or, in some designs, on stacked electrode sheets. These cells are widely used in electric vehicles due to their exceptional stability, high power output, and durability.

Compared with cylindrical cells, the rectangular geometry enables better space utilization at module and pack level, reducing unused volume and simplifying mechanical integration. Moreover, these cells feature built-in safety valves to prevent over-charging, ensuring safer operations.

The main advantages of prismatic cells are their good packaging efficiency, structural stability, and suitability for compact automotive modules. They are widely used in electric vehicles and plug-in hybrid vehicles, where high energy content and simplified pack architecture are required. Nevertheless, the rigid case increases inactive material mass, and large-format cells may present more severe thermal gradients and safety-propagation issues. Moreover, during the operations, the cell may undergo moderate expansion, so mechanical compression and careful thermal design are required to guarantee long-term reliability.

Pouch cells

Pouch cells use typically a flexible multilayer aluminum-polymer laminate instead of a rigid metallic case. Internally, the electrodes and separators are generally stacked, semi-wound, or arranged through Z-folding, and the tabs are welded to collect current from the electrodes stack. The absence of a heavy rigid case allows a reduction in inactive mass and gives the cell a thin, light-weight and highly flexible geometry. For this reason, pouch cells are particularly attractive and widespread when high packaging efficiency, low weight and large contact surfaces for cooling are required.

In automotive battery packs, pouch cells can provide high volumetric efficiency and good thermal characteristics, because their large flat surfaces can be coupled effectively with cooling pastes or heat spreaders. That is relevant for high-power applications, such as the Li-ion Kokam NMC/graphite pouch cell considered in this Thesis. However, pouch cells are mechanically less robust than hard-case cells (prismatic ones). They require external support, controlled compression,

and space for swelling. Gas generation, electrolyte leakage and less predictable pressure release are among the main limitations, especially if manufacturing, drying, formation or operating conditions are not properly controlled. Due to their technical complexity, pouch cells require careful handling and precise manufacturing to ensure safety and performance.

Construction methods for Pouch cells Considering that the Thesis focuses on the analysis of a pouch cell, it could be useful to make a brief description of the possible methods of construction for this cell format.

In general, a pouch cell can be manufactured using different internal electrode arrangements. The selected architecture affects manufacturing cost, production speed, thermal behavior, mechanical stability and electrochemical homogeneity.

Stacking method consists of placing individual anode, separator and cathode sheets one above the other to form a multi-layer electrode stack. This configuration is well-suited to large-format pouch cells because it provides a flat geometry, good dimensional control and relatively homogeneous current distribution. It also facilitates efficient thermal contact through the large cell faces. However, the process requires accurate cutting and alignment of many electrode sheets, which can increase manufacturing time and the risk of defects at the electrode edges.

Winding method, or flat-wound construction, uses continuous electrode and separator strips wound into a flattened jelly-roll configuration. Compared with pure-stacking, this method can benefit from faster automated manufacturing, since winding is a high-throughput process. Nevertheless, the resulting structure may show non-uniform mechanical stresses, especially near curved regions, and electrolyte wetting can be more difficult than in a loosely stacked arrangement. For this reason, flat-wound pouch designs must balance productivity with mechanical and electrochemical uniformity.

Z-folding method is an intermediate approach in which the separator is folded in a zig-zag shape, while individual electrode sheets are inserted into the separator pockets. This configuration improves separator continuity around the electrodes and it can reduce the risk of direct electrode contact. Therefore, Z-folding is widely used for pouch cells, because it combines good stack regularity with improved electrical insulation. However, it still requires accurate placement of electrode sheets and careful control of folding tension, alignment and edge quality.

Battery cell's formats: final comparison

In order to summarize the main features of this part about battery cells, the following Table 1.4 reports a quick description of automotive cell formats.

Cell format	Typical construction	Automotive applications
Cylindrical cell	Wound jelly-roll electrode assembly inside a rigid cylindrical metal can	Widely used in EV packs requiring modularity, high manufacturing maturity and scalable production
Prismatic hard-case cell	Rectangular metallic case containing a flat jelly-roll or stacked electrodes	Common in BEV and PHEV packs where compact packaging and high-cell capacity are required
Pouch cell	Stacked, semi-wound or Z-folded electrode assembly sealed in aluminum-polymer laminate foil	Used in high-energy and high-power automotive packs where low mass, compactness and efficient thermal coupling are priorities

Table 1.4: Summary features for automotive cell formats

Overall, pouch cells are particularly attractive for automotive applications, because their thin geometry and large surface area support compact packaging and efficient cooling. At the same time, their flexible enclosure makes them more dependent on pack-level mechanical design than cylindrical or prismatic hard-case cells. Consequently, when pouch cells are selected, the module must provide controlled compression, swelling accommodation, protection against puncture, and a reliable thermal interface.

To conclude, cylindrical cells offer stability, prismatic cells deliver automotive-grade power, and pouch cells provide flexibility with added caution.

Finally, Figures 1.7, 1.8, 1.9 show the three automotive shape cell-categories, respectively: cylindrical cell, prismatic cell and pouch cell.

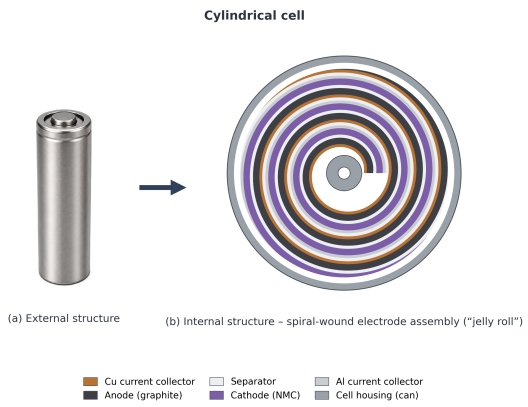


Figure 1.7: Cylindrical cell

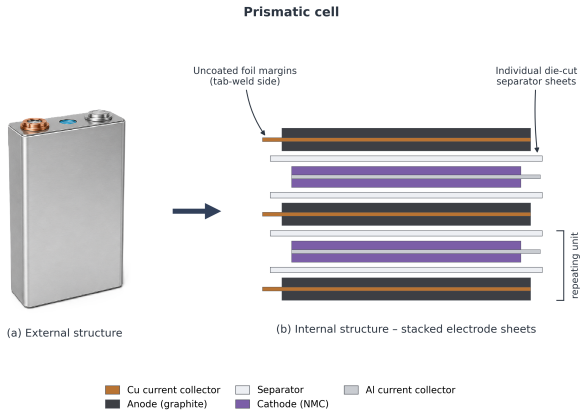


Figure 1.8: Prismatic cell

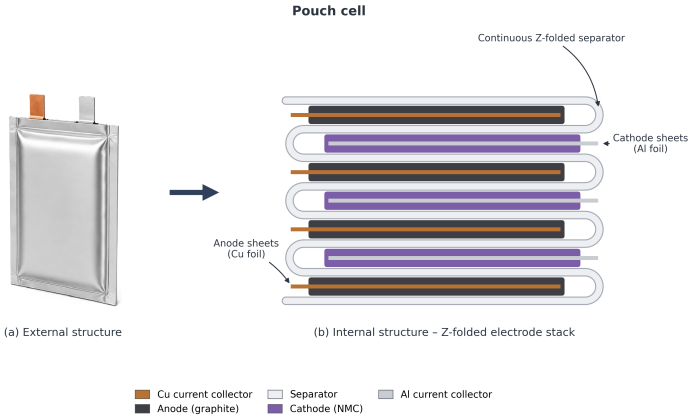


Figure 1.9: Pouch cell

1.3.2 Cell designs: High-Energy and High-Power cells

Considering the evolution of lithium-ion battery (LIB) technologies in recent years, two different approaches were used by manufacturers to optimize their cells: high energy density or high power density. The cell design varies significantly between these two options (HP or HE), depending on the type of applications. More specifically, the design is driven by specific requirements (e.g., performance, safety, recyclability, and cost), involving different cell's features. In both the cell designs, regarding the internal active materials composition, there is a certain trade-off between power and energy requirements.

The design of a lithium-ion cell is decided through a series of key decisions. In general, the manufacturers try to optimize several parameters, following one of the two choices (HP or HE): electrode compositions, coat weights, porosities, current collectors, electrolyte, separator; the main objective is to obtain the maximum cell safety and performance (from Sciatti et al. (2026) [2]).

Overall, High-Energy Li-ion batteries provide high energy densities but low power densities. As a result, among the different types of electric vehicles, they are suitable for BEVs, for which the driving range is a key factor. Meanwhile, High-Power Li-ion batteries offer high power densities and can deliver high charging/discharging currents, making them ideal for HEVs, which require rapid energy delivery (in acceleration), and fast energy storage (during braking or recharging).

In terms of specific/areal capacity, the typical values assumed by the two possible cell designs are:

- High-Energy cells $\rightarrow$ 20-50 Ah/m^2.
- High-Power cells $\rightarrow$ 10-20 Ah/m^2.

According to Sciatti et al. (2026) [2], the two cell designs affect the cell internal characteristics. Typically, High-Power Li-ion batteries require the minimization of the cell components (electrodes and separator), and this is obtained through thin coatings, large current-collectors, high electrode porosity, and use of robust conductive materials. On the other side, High-Energy Li-ion batteries aim to optimize the ratio between active material and total electrode volume, needing of thicker coatings, smaller current-collectors, and lower electrode porosity.

Considering the study of [5], performing several invasive experiments on 9 different lithium-ion cells with various power/energy ratios, High-Power cells result to exhibit low areal capacities and low coat weights. This is the physical case of the cell analyzed in this Thesis.

Actually, a clear distinction in terms of areal capacity is not possible, but the indicated ranges are an important indication of which purpose the cell has: lower specific capacity is used to realize a more porous structure of electrodes (High-Power oriented), while higher specific capacity is used to build electrodes with high percentage of active materials (High-Energy oriented).

Furthermore, it is worth citing the paper of Yao et al. (2025) [6], which presents a comparative study between two Samsung 21700 cylindrical cells, of which one with High-Power design and the other one with High-Energy design. The HP cell is characterized by superior power capability through its design features, including higher porosity, thicker current-collectors, dual electrode tabs, and thinner electrode coatings. Meanwhile, the HE cell shows higher energy density (with a certain percentage of silicon-oxide SiO_x in the anode), using thicker electrodes, and reduced binder and other inactive materials.

Generally, the active materials dictate the choice of binder and type of conductive carbon. Subsequent decisions are made regarding the electrode loading, thickness and porosity, to guide the design of the cells.

HE versus HP designs: conclusions

With reference to the three analyzed articles ([5], [2] and [6]), the following considerations can be finally made:

- High-Power cells use typically smaller particles for the active material in both anodes and cathodes.
- The cathodes of High-Power cells have typically higher porosities, with a similar trend presented for the anodes.
- High-Power cells typically present lower coat weights and areal capacities.

- High-Energy cells generally provide slightly thicker anodes and cathodes to improve their energy density, with respect to High-Power cells.
- The separators use the best thinnest materials in both cases.
- High-Power cells provide a minimized internal resistance for each component, with minimized lithium-ion diffusion path leading to low losses.

The following Table 1.5 summarizes the key features of High-Energy and High-Power cells (according to [5]).

Component	**High-Energy cells**	**High-Power cells**
Electrodes	High coat weights Low coating porosity Medium + large particle sizes Low conductive carbon content Minimum possible binder content	Low coat weights High coating porosity Small + medium particle sizes High conductive carbon content
Current collectors	Thinner Coated to improve adhesion	Thicker Coated to reduce resistance
Separator	Thin	Thin
Electrolyte	High conductivity	High conductivity

Table 1.5: Cell Design choices: High-Power vs. High-Energy

The requirements for maximum energy density of a cell are typically the opposite ones with respect to those for a high-power density. Therefore, a classic trade-off must be made by manufacturers. The electrodes generally follow a different design and composition in the two cases (High-Power and High-Energy), as described previously. Meanwhile, the separator features and thickness are typically based on safety or manufacturability. Regarding the electrolyte, assuming that the cell uses liquid electrolyte as classic case, there are some choices available in terms of the lithium-salt and concentration, the organic carbonate solvent mixture, and the additives. So, the electrolyte composition depends on the target operating temperature range of the cells, and the additives are selected to improve the performance of the active materials inside the electrodes.

In conclusion, high-power density of the cells (for High-Power design) requires the minimization of every component of the overall cell in terms of resistance, based on lower electrode coat weights, thinner separators with lower tortuosity and thicker current collectors. A common option is that the electrode resistances and lithium-ion diffusion path lengths can be reduced by using smaller particle sizes for the active materials (to be investigated with SEM or EDS techniques), and higher percentages of conductive additives.

The choice of a certain cell design significantly affects the further electrochemical battery modeling, showing completely different physical quantities, especially at high C-rates, as demonstrated by Yao et al. [6].

Chapter 2

Overview of Battery Modeling Approaches and Suitable Software Environments

This chapter analyzes the various model categories available for Li-ion battery cells or modules, mainly focusing on two viable options: Equivalent-circuit models and Physics-based models. A high-level description of four modeling approaches is reported, including final comparisons which highlight strength and weakness of each one. For the Thesis purposes, Physics-based models are preferred over the other possibilities. Then, a complete review of five tool options to construct an electrochemical model is presented, exposing open-source and commercial software environments.

2.1 Types and Categories of Battery Modeling

Lithium-ion battery, as the core of energy storage units, is essentially highly dependent on accurate battery modeling, to improve its performance and to assure safety management.

In general, batteries can be modeled at various levels, depending on the use of the model. The possible purposes of battery models are wide: battery design, performance evaluation, safety diagnostics, control and system simulation at the application level. Therefore, modeling is essential for: (i) helping with the research of device design, construction and materials, through understanding the factors that influence energy conversion process; (ii) enhancing the research on the performance of the device in a certain application, in order to obtain improved design and better utilization.

Battery models can be classified, according to the degree of physical detail they represent and the intended use in typical application fields. A general classification of the main types of battery modeling is illustrated in the scheme, shown in Figure 2.1. Each category presents different characteristics and methodology approaches, so the final choice of one of them depends on the objective of the case-study.

In general, the different kinds of battery models can be classified into four main categories:

- **Empirical (or analytical) models**: Battery terminal-voltage is a mathematical function of SoC and other parameters.
- **Equivalent-circuit models (ECMs)**: An equivalent circuit mimics the battery behavior; battery voltage is calculated from the solution of the circuit.
- **Physics-based models**: Based on equations describing the physics of the electrochemical phenomena, occurring inside the battery; solving systems of partial-differential equations is needed.
- **Data-driven models**: Direct relation between measured battery parameters, SoC and the terminal-voltage is established by training the model.

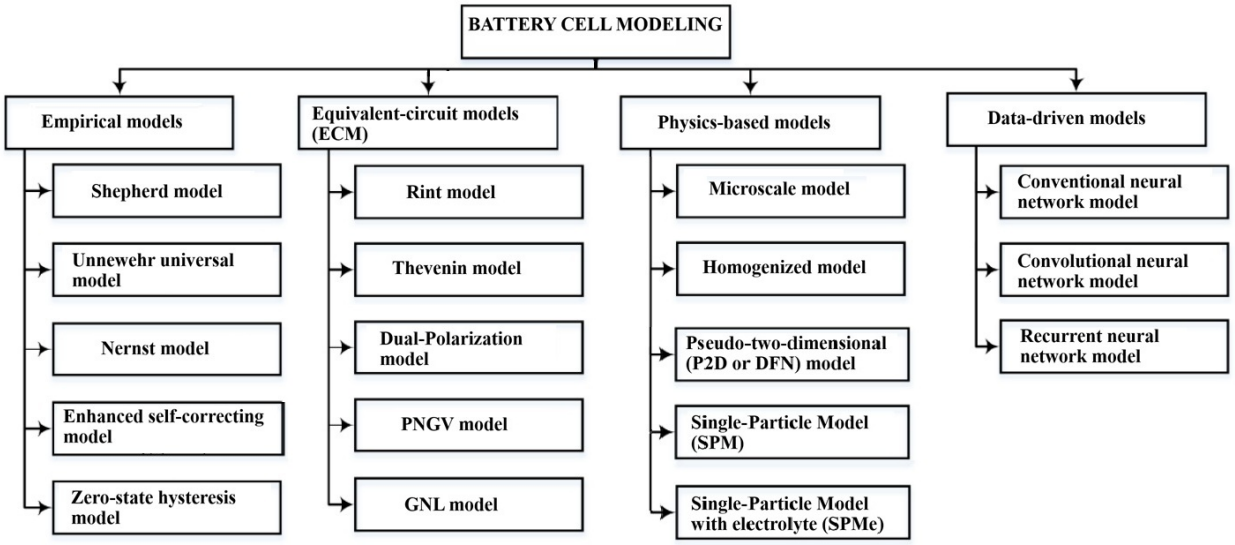


Figure 2.1: Classification of main groups of Battery Modeling

At the most complex levels, the fundamental physics and chemistry-based theories are exploited to develop theoretical models (e.g. physics-based models) of battery cells. In this modeling approach, the fundamental mechanisms of battery are analyzed from two points of view: (i) macroscopic behavior (terminal-voltage and current) and microscopic information (internal materials and reaction processes). These models are very useful to perform a complete analysis in terms of design and performance evaluation of a certain type of battery (high dependent on its chemistry and design).

Simpler battery models (e.g., empirical and equivalent-circuit models) are capable of emphasizing the macroscopic behavior of batteries, and they are more useful for a global performance evaluation (at system-level) and for the corresponding design. Therefore, they are typically applied in Battery Management Systems (BMS) for BEV and HEV (Battery and Hybrid Electric vehicles).

An alternative is represented by data-driven models, that rely on availability of wide data-sets to approximate the relationship between the system response and its inputs. Therefore, they are clearly dependent on the quality of data.

This classification is not only by model type, but also reflects the typical trade-off between interpretability and generalization (higher in physics-based models) against simplicity and computational efficiency (higher in empirical / ECM models).

An extensive review of the most popular battery modeling approaches is provided in: the paper of B. Zheng et al. (2025) [7], the article of F. Brosa-Planella et al. (2022) [8], the book written by Iqbal Husain (2021) [1].

2.1.1 Empirical Models

Empirical models are one of the simplest battery models developed primarily for input-output relationships in lithium-ion battery cells. Typically, these models can describe the overall performance of the battery by using a mathematical relationship matched with theoretical or experimental model data.

Therefore, their main objective is to reproduce the externally observable electrical behavior of the cell, especially the terminal-voltage, by means of mathematical equations. In this modeling approach, the battery is not described through specific physical phenomena, but through direct

correlations between measurable quantities, such as current, voltage, state-of-charge (SoC), and sometimes temperature. In literature, classical empirical formulations include: (1) Shepherd model, (2) Unnewehr universal model, (3) Nernst model. In these models, typically, the terminal-voltage is expressed as a non-linear function of SoC and current.

More precisely, mathematical or empirical relationships are established by curve fitting against experimental data. This is a clear difference with theoretical models: empirical models do not consider the real physical mechanisms inside the cells.

From a functional point of view, empirical models are generally based on algebraic equations or low-order dynamic relations. Their parameters are obtained by fitting experimental charge/discharge curves, pulse tests, or manufacturer datasheet information.

Specifically, these simplified generic empirical models can be parametrized using only a limited number of characteristic points, extracted from a steady-state discharge curve, making them relatively easy to be implemented, when detailed physical information about the cell is not available.

Instead, more advanced empirical or semi-empirical models, such as Enhanced-Self-correcting (ESC) model or Zero-state hysteresis model, introduce additional terms to account for dynamic voltage relaxation and hysteresis effects. In particular, zero-state hysteresis models include a direct correction term associated with charge/discharge direction, while ESC-type formulations extend the equivalent voltage representation by adding hysteresis and low-pass dynamic components.

The main advantage of empirical models is their low computational cost. Since they avoid the solution of partial-differential equations, they are particularly suitable for real-time applications, system-level simulations, preliminary design studies, and Battery-Management-Systems (BMS) algorithms. This is especially relevant in automotive applications, where the model must often be executed repeatedly under dynamic current profiles with limited computational resources.

However, these models also present important limitations. Since their parameters do not generally correspond to physical quantities, such as diffusion coefficients, reaction-rate constants, porosity, or electrode stoichiometry, empirical models have limited interpretability. Their predictive capability is strongly dependent on the quality and representativeness of the experimental data-set used for calibration. Consequently, extrapolation outside the identified range of SoC, temperature, current-rate, or aging conditions may lead to significant errors. This limitation becomes particularly relevant for fast charging, low temperature operations, high power pulses, or aged cells, where internal transport limitations and degradation mechanisms strongly influence the voltage response.

Nevertheless, empirical models can provide acceptable voltage predictions when they are calibrated within the same operating range used for identification, especially under moderate current rates and controlled temperature conditions.

To summarize, empirical models are the most appropriate model category to be chosen when the main objective is fast voltage estimation or SoC-oriented control, rather than the analysis of internal cell-states or degradation mechanisms.

2.1.2 Equivalent Circuit Models (ECMs)

Equivalent circuit model (ECM) is a semi-empirical simulation approach based on circuit theory, that utilizes system identification techniques to obtain the necessary parameters; in particular, by recording input-output data of battery, they are able to simulate the non-linear characteristics of Li-ion batteries.

This modeling approach is based on simple structure, a limited number of parameters, and a high simulation accuracy (compared to required effort). Therefore, this approach effectively reduces computational complexity and enables the derivation of analytical mathematical equations. The fundamental components of ECM models are: resistors, capacitors, and voltage sources in specific configurations. An ECM is capable of catching, in a simplified way, complex electrochemical

reactions and physical processes within the battery, with an effective capture of battery dynamic characteristics during charging or discharging operations.

ECM models are suitable for making an analysis of the battery across all the SoC range, ideal for battery modules or packs. In comparison with other modeling approaches, the ECM provides superior advantages from computational efficiency and ease of parameter acquisition/estimation points of view.

A generic ECM model computes voltage response as follows:

$$V(t) = U_{OCV}(SoC, T) - I(t) \cdot R_0(SoC, T) - \sum_k V_{RC,k}(t)$$

$$\frac{dV_{RC,k}(t)}{dt} = -\frac{1}{R_k \cdot C_k} \cdot V_{RC,k}(t) + \frac{1}{C_k} \cdot I(t) \ , \ \ k = 1, 2, ..., n$$

where:

- U_{OCV} is the open-circuit-voltage of the cell (related to thermodynamics), strictly dependent on SoC and temperature;
- I is the current applied at a certain time to the cell (positive ($I > 0$) in case of discharge);
- R_0 is a lumped resistance capturing instantaneous ohmic losses (electronic, ionic and contact resistances);
- R_k and C_k are respectively resistance and capacitance of a certain RC group, representing different kinds of electrochemical losses;
- $V_{RC,k}$ is the state-voltage produced by each RC group, governed by a first order Ordinary-Differential Equation (ODE).

Figure 2.2 shows a typical scheme for a generic Equivalent-circuit Model.

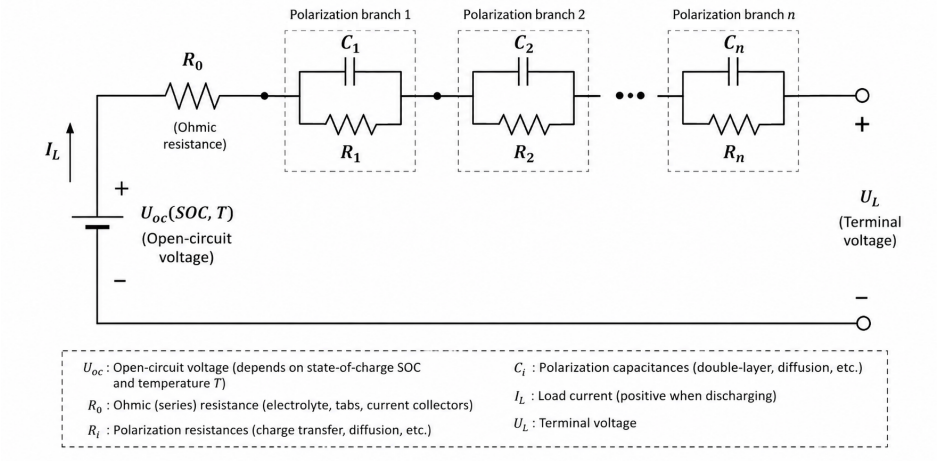


Figure 2.2: Equivalent-circuit model (ECM)

Moreover, considering the structural hierarchy and connection methods of the internal components, ECM can be divided into two main categories:

- Single cell models;
- Battery module models.

Main applications of ECM approach are: (i) real-time monitoring, and (ii) control within BMS. Indeed, this model category provides rapid and precise battery SoC estimations, in order to ensure reliable and efficient battery operations.

Single cell ECM modeling

The selection of a certain single cell ECM depends on the specific case.

Rint model is a basic ECM model; it simplifies the equivalent circuit model of a lithium-ion battery considering an ideal voltage source connected in series with some ohmic resistances. They practically represent the internal resistance of the model. Hence, Rint model is structured with simple components, so it avoids complex parameter calibration, with a straightforward parameter identification. Moreover, for these reasons, it is suitable for models that require low computational costs and low complexity, with a consequent rapid terminal-voltage estimation in resource-constrained systems (e.g., low-power BMS).

Thevenin model (first-order RC model) is based on the previous Rint model. Essentially, this new model adds to the basic Rint model architecture an RC parallel circuit composed of a charge-transfer resistance (R_e) and capacitance (C_e). The scope of the RC group is to simulate the electrochemical polarization phenomena during battery charging or discharging modes. Basically, Thevenin model adds to the ohmic polarization the concepts related to electrochemical non-linear polarization, significantly improving the quality of the model at the cost of a slight increasing complexity. Considering certain operating conditions, i.e. normal battery health and constant current/temperature, a Thevenin model can reproduce with a reasonable fidelity grade the real battery behavior. However, when other elements come into play, such as battery aging or operations in environment with fluctuations of temperature, the internal impedance and capacitance characteristics become not appropriate to describe the battery voltage output.

Dual Polarization (DP) model (second-order RC model) improves the previous Thevenin model, by adding a second RC group to the equivalent-circuit. This makes it possible to separate the simulations of electrochemical polarization and concentration polarization, during battery charging or discharging modes. DP models provide a more precise equivalent-circuit architecture, to reflect the non-linear characteristics of Li-ion batteries. The first RC group focuses on the purely kinetic polarization phenomena, while the added second RC group is used to reflect the concentration polarization. This new model is suitable for more complex scenarios, with better estimation of voltage during high-rate currents, rapid SoC changes, or complex operating conditions. Therefore, the DP model can provide high-precision support for high-level BMS control. The main drawbacks are related to extreme model complexity (compared to the previous ones) and parameter quantities, requiring more experimental data or advanced identification algorithms.

PNGV model is a variant of Thevenin model. Indeed, it adds to basic Thevenin equivalent-circuit a series capacitance C_Q, to better describe the evolution of the open-circuit voltage with charge/discharge time. It is still a first-order model, since it uses only an RC group. The improvement with respect to the Thevenin model allows not only an effective SoC estimation, but also SOP (State-of-Power) and SOH (State-of-Health) assessments. However, exactly like Thevenin model, PNGV model can struggle in more complex operating conditions, and the introduction of capacitance C_Q increases the parameter identification difficulty, with the necessity to rely on more accurate Hybrid Pulse Power Characterization (HPPC) tests.

GNL model is a mixture of the previous four ECM modeling approaches. It can reproduce well the internal mechanisms of lithium-ion batteries and introduces self-discharge factors. Therefore, it is able to describe the battery charging and discharging modes separately, effectively reproducing: ohmic polarization, electrochemical (kinetic) polarization, concentration polarization, and self-discharge phenomenon. Its architecture aligns very well with the effective internal mechanisms of the batteries, demonstrating optimal performance in simulating a high-fidelity battery response at widely different current-rates. Its major advantages are wide applicability for various conditions and

high simulation accuracy. Therefore, GNL models are employed to simulate at a high-level battery charging/discharging operations, achieving precise estimations of state-of-power and state-of-health.

Other ECM variants for single cells can implement different multi-resistor-capacitor (RC) groups, in order to better simulate the battery cell dynamics than other models. However, they can require more intricate computations, with the need of substantial computational resources and advanced algorithms.

Battery module ECM modeling

In general, lithium-ion cells are employed in more complex configurations, such as they can be aggregated within battery modules.

The battery module models are particularly useful to support BMS of single module and to ensure safe operations among the modules.

Battery module ECMs include two main categories as possible approaches:

- Modeling based on different series-parallel mode
- Mean-difference modeling

The first category typically focuses on battery modules that adopt a series-parallel hybrid structure, to balance voltage, capacity and reliability. A pure series or parallel construction with individual cells for a battery module can present different issues to be solved. Therefore, a hybrid series-parallel module's model can integrate the advantages of both series and parallel configurations, compensating the limitations of a pure-series or pure-parallel architecture approaches, thereby offering high-voltage and high-capacity simultaneously. In this case, the modeling approach is practically based on the design of series and parallel circuits, adopting resistances and capacitances to represent the possible configurations of a real hybrid series-parallel module. Such modules are widely employed in high-performance battery systems, with configurations called: NSMP and MPNS.

The second category is typically used for battery modules composed of a large number of individual cells connected with series/parallel configurations. However, due to manufacturing differences and uneven aging, the performance disparities among individual cells tend to increase over the time, resulting in increased management complexity, elevated risks of over-charging or over-discharging and potential safety hazards. In order to face these problems, Mean-Difference model (MDM) can be adopted, decoupling average dynamics and individual differences inside the module. It emerges as a key technique that balances efficiency and precision. MDM combines average model (mean-model, MM) features, to describe common characteristics of the battery, with the difference model (DM), to establish individual differences among the cells.

2.1.3 Physics-based Models

Physics-based models depend on the electrochemical theory and multi-physical coupling mechanisms, and utilize systems of partial-differential equations, in order to analyze the internal microscopic transport processes of the lithium-ion batteries. Therefore, these models are capable of capturing fundamental physical phenomena, including different interaction mechanisms, such as lithium-ion diffusion and kinetics (in solid and liquid phases), electrochemical reaction thermodynamics, and interfacial material properties. Another important feature of electrochemical model consists of their ability to make observations of main internal state variables of the battery, such as solid-phase concentration distributions (related to diffusion phenomenon) or interfacial reaction-current densities (related to kinetic aspects).

Generally, physics-based models have an excellent prediction accuracy of battery response in various operating conditions, such as high-rate cycling or variable external temperatures. Therefore, they are more suitable for high-level applications, requiring microscopic mechanistic insights, such as: (1) long performance evolution analysis, (2) electrode material optimization design, (3) multi-physics coupled mechanisms for research.

Electrochemical modeling approaches

Electrochemical models rely on the physical understanding of the processes occurring within the batteries and their mathematical formulation. The theoretical foundation of modern electrochemical models is commonly associated with the combination of two fundamental theories:

- Porous electrode theory (PET);
- Concentrated solution theory.

Porous Electrode Theory provides a macroscopic description of composite electrodes, by representing the complex microstructure as an overlapping continuum, made of the electronically conductive solid matrix and the electrolyte-filled pore phase. Through this homogenized description, the effects of some properties of electrodes, seen in 1.2.1 (i.e., porosity, tortuosity, active surface area, and effective transport properties) can be incorporated without explicitly resolving the microscopic geometry of the electrode.

Concentrated Solution Theory complements this framework, by describing ion-transport in the electrolyte under non-dilute conditions, where interactions among charged species and solvent molecules cannot be neglected. Therefore, electrolyte diffusion, migration, ionic conductivity, and transference effects are treated in a more rigorous manner than in dilute-solution approximations.

The integration of these two theories enables electrochemical models to describe the coupled evolution of lithium-concentration in the solid particles, electrolyte concentration, electric potentials, and interfacial charge-transfer reactions, thereby providing a physics-based representation of lithium-ion battery operation.

In general, electrochemical models are based on a system of partial-differential equations (PDEs), exploiting basic physical principles tied to mass conservation and charge conservation.

Brosa-Planella et al. (2022) [8] performed a complete review of the physics-based models, starting from a high-fidelity microscale model and reducing it to a Single-Particle Model, deriving, during the process, other common models, such as Doyle-Fuller-Newman model (equivalently called Pseudo-two-Dimensional model).

The starting point for electrochemical modeling is represented by Microscale Model, which provides the highest spatial resolution, with an elevated grade of complexity. Thus, all the subsequent electrochemical models can be derived, in order of increased simplifications: (i) Homogenized model, (ii) DFN model, (iii) Single Particle Model with electrolyte (SPMe), (iv) Single Particle Model (SPM).

In general, physics-based battery models are built around conservation laws for lithium-ions inside the electrolyte, and for lithium-ions intercalated or de-intercalated inside/outside the active electrode particles. These conservation laws are supplemented by suitable transport laws (equivalently defined as constitutive equations), which are driven by concentration and potential gradients of the ion species.

Microscale Model is the basic framework to develop all the most known electrochemical models. Essentially, it provides a detailed continuum description of the mechanism of charge transport at the microscopic scale of single electrode particles. Considering that the microscale model relies on resolving electrode geometry through a microscopic representation, an accurate

reproduction of internal cell microstructure is required for model utilization. The high complexity of this electrochemical model, based on a complete set of partial-differential equations, related to conservation and transport laws, is a clear limitation to its applicability in real cases. In general, a microscale model is computationally very expensive, because of the detailed framework required by the geometry of the electrodes.

Homogenized Model is the first derived model from the microscale model. The key property of a homogenized model is its capability of treating the electrode's porous material and its pore space as a continuum, thereby modifying the equations of previous model, to account for the effects that this assumption has on the electrode's microstructure. The main advantage of this model is its dependence upon only macroscopic spatial variables (i.e., a spatial-vector), solving the equations-set through a much simpler homogeneous geometry. In addition, the homogenized model retains a microscale variable, in order to model the lithium-ion transport phenomena within the cell. Substantially, the fundamental model's feature of coupling macroscale and microscale equations enables deriving the classical formulation of simplified porous electrode models (e.g., DFN model).

Therefore, the most commonly used electrochemical models can be categorized in the following three types:

1. Pseudo-two-Dimensional (P2D) model;
2. Single Particle Model (SPM);
3. Single Particle Model with electrolyte (SPMe).

Pseudo-two-Dimensional (P2D) Model Pseudo-two-Dimensional models were developed starting from homogenized models. More specifically, P2D models are based on knowing the porous structure of lithium-ion battery electrodes and on optimizing electrochemical reaction kinetics through the expansion of the solid-liquid interfacial area.

During different years, there was a progressive improvement of lithium-ion electrochemical modeling, until 1990s. Indeed, the studies of Newman team led to the development of P2D model, which integrated concentrated solution theory with Butler-Volmer kinetics, achieving a first full-cell simulation and solidifying the fundamental role of PET (porous electrode theory).

The first P2D model, that is considered as a milestone of electrochemical modeling, has undergone continuous validations and expansions. The studies of Doyle et al. (1993) [9] and Fuller et al. (1994) [10] led to the birth of a complete P2D model, the so-called Doyle-Fuller-Newman model, from the names of main authors.

The power of a DFN model, which is substantially different with respect to a homogenized model, consists of a further simplification of internal cell geometry on which it is solved; in particular, the DFN model assumes that the electrode particles are spherical. It assumes a one-dimensional domain with spherical symmetry for the microscopic aspects of the cell. In addition, P2D models consider one-dimensional planar geometry for electrodes and separator, reducing the macroscopic aspects to a one-dimensional planar form. These features make pseudo-two-dimensional models more computationally affordable than homogenized models, retaining, at the same time, a reliable physics for an accurate prediction of battery behavior, capturing the evolution of its internal state-variables.

Basically, this model employs coupled multi-physics field partial-differential equations, in order to simulate the internal physical phenomena of Li-ion batteries, offering strong versatility and scalability. P2D model is capable of capturing the phenomena of ion-transport and relative kinetics at the solid-liquid interface (electrodes/electrolyte), with optimal predictions of battery performance and dynamic response characteristics.

Moreover, DFN model allows one to characterize the electrode's microstructure using relatively few parameters (e.g., porosity / active material fraction and particle radius).

This modeling approach is still heavy at the parametrization level, requiring a detailed experimental characterization of the cell, comprising physico-chemical tests on the battery (4.3). However, its capability to analyze, in a reliable way, the evolution of electrolyte/solid-phase variables, as a function of time and two space variables, significantly improves prediction accuracy of real battery behavior, with respect to more advanced ECMs.

The basic set of the governing equations underlying the P2D model comprises lithium-ion and charge conservation equations, with related transport equations.

Since the spread of this model across the years, there was a passage of P2D model from laboratory/research-level to industrial/engineering-level for high quality battery behavior estimations.

The following Figure 2.3 illustrates the main features of a DFN model, focusing on its double nature: it analyzes both the macroscopic cell's aspects (along thickness x-direction) and its inner microscopic mechanisms (along radial r-direction); from that, its classical P2D denomination.

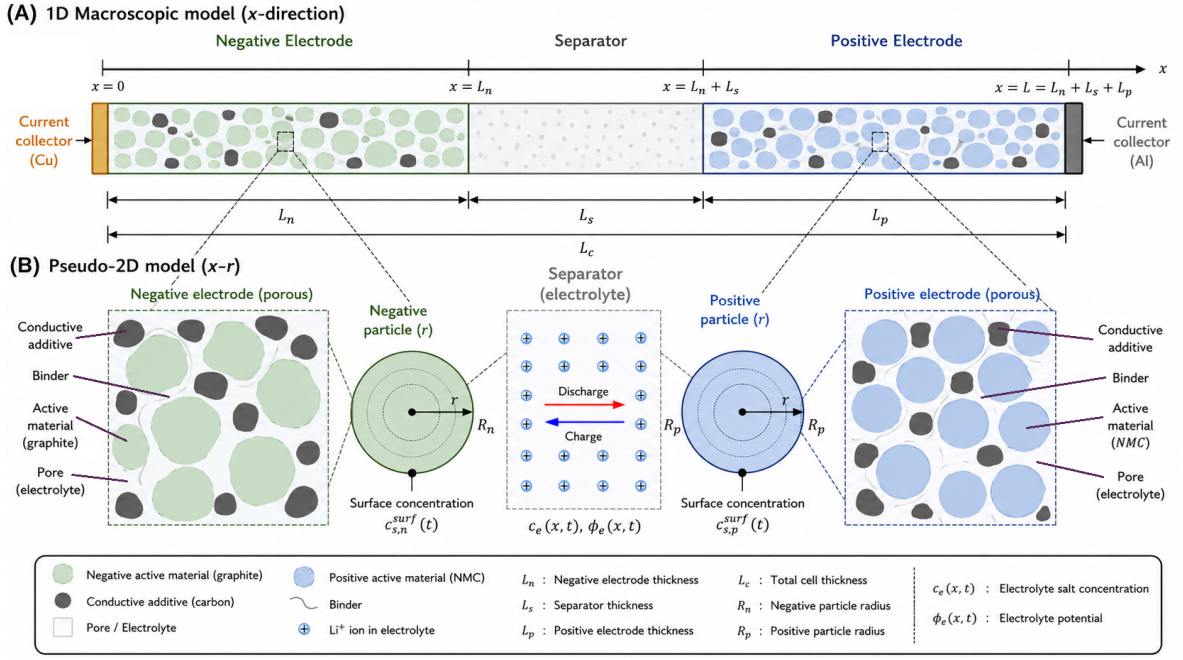


Figure 2.3: P2D (or DFN) model illustration

The P2D models are implemented in most simulation platforms, including both open-source tools (e.g., PyBaMM) and commercial software (e.g., COMSOL).

Single-Particle Model SPM modeling approach is a simplified version of P2D model. More precisely, the solution of a system of PDEs (partial-differential equations) for a P2D model can be, in some cases, computationally intensive and unusable for real-time BMS applications. Therefore, further studies of researchers led to the development of Single-Particle Models.

This reduced-order family, i.e. models that are simpler than DFN model, but retain most of its predictive capabilities, can improve the physical understanding of battery behavior and provide accurate solutions at a lower computational cost.

As a reduced-order version of P2D model, Single-Particle Model essentially introduces some physical simplifications; in particular, it assumes uniform current density in the electrolyte, obtaining a system of only two PDEs, enhancing significantly computational efficiency.

Differently from P2D models, SPM adopts a modeling approach that considers a uniform behavior of the particles within each electrode; therefore, this model assumes a single representative (or

average) particle for each electrode. This assumption is a fundamental feature of SPM, considering a spatially uniform electrode's composition, differently from typical particle distributions analyzed in P2D models.

For SPMs, the partial-differential equations (PDEs) decouple the microscopic spatial variable (r) from the macroscopic one (x); therefore, it is a real one-dimensional model (in space), maintaining only the dependence on the radial direction. This aspect is effectively responsible for their reduced computational complexity with respect to DFN models.

In more detail, the SPM framework includes two PDEs, related to two different diffusion equations, one for each representative particle of electrodes, and a closed-form expression for the terminal-voltage. This represents a crucial reduction of complexity, compared to DFN models, considering even the deleting of the differential-equation for the electrolyte concentration from the set of equations.

The decoupling between PDEs for potential and lithium concentration in the electrodes and electrolyte is a direct consequence of the SPM modeling approach. In many cases, due to their intrinsic simplifications, the equations for the potentials of electrodes and electrolyte can be solved analytically, leaving only the equations for lithium concentration to be solved numerically.

Typical SPMs neglect potential drops across the electrolyte; they are particularly useful for simulating the battery behavior at very low C-rates, when gradients in both the concentration and the potential of electrolyte are negligible.

The main reason for these assumptions is justified by the observation that in many circumstances the intercalation/de-intercalation reactions occur almost uniformly within both electrodes. So, during discharge, all negative electrode particles de-lithiate at the same rate, independently of the position inside the electrode, whereas all the positive electrode particles lithiate at the same rate, independently of their position inside the electrode. SPMs can be applied in specific scenarios, in which the cell behavior can be approximated by a single representative particle for each electrode, without losing its intrinsic electrochemical meaning.

Different versions of SPMs, which exploit other numerical algorithms, predominantly implemented in open-source tools, have produced reliable results with further reduction of computational times. This property was very important to fully meet the requirements of on-board BMS in electric-vehicles for online state-estimations.

Single Particle Model with electrolyte (SPMe) Single-Particle Model with electrolyte (SPMe) is capable of covering the distance, in terms of quality of modeling, between P2D model and SPM. As seen, SPM is based on assumptions of uniform current-density and other micro-structural simplifications, showing advantages of fast computational times; however, its evident limitations in representing complex transport phenomena inside the batteries, particularly regarding lithium-ion concentration polarization in electrolytes, under medium-to-high rate charge/discharge conditions, lead to the need of a more complete model: Single-particle-model with integration of electrolyte dynamics (SPMe).

Essentially, SPMe assumes, exactly as SPM, a single representative particle in each electrode. The key difference is the following: SPMe integrates electrolyte transport and kinetic equations (i.e. electrolyte dynamics) into SPM architecture, retaining the computational efficiency of SPM itself, while compensating for its known model limitations regarding electrolyte polarization effects.

In general, SPMe achieves an equilibrated balance between model accuracy and engineering applicability, particularly under medium-to-high rate charge/discharge operations of lithium-ion batteries.

SPMe belongs to the category of "Extended Single-Particle" models (ESP models), derived from previous SPM family (as declared by Zheng et al. (2025) [7]). They were deeply treated by

Marquis et al. (2019) [11], Richardson et al. (2020) [12], and Brosa-Planella et al. (2022) [8]. More specifically, the main differences inside this modeling category relate to the methods used to calculate terminal-voltage and other derived quantities, not in the differential equations to be solved, in order to determine the concentrations in the particles and in the electrolyte.

The study of Marquis et al. (2019) has established SPMe as the most famous derivation of ESP models, incorporating an electrolyte potential equation into general ESP framework. The researchers applied specific asymptotic methods to derive the SPMe from the P2D model. Therefore, their purpose was to mitigate the simplifications in the description of electrolyte transport (typical of SPMs), in order to achieve good results in terms of prediction of battery terminal-voltage response, reducing average errors under high-rate scenarios.

Moreover, it was proved that in different medium-to-high rate charge/discharge conditions (from 1C until 4C), a generic SPMe exhibits significantly lower maximum error, average error and root-mean-square error (RMSE) related to terminal-voltage prediction, with respect to a Single-Particle Model, thereby demonstrating a general superior performance.

The general performance of SPMe modeling is comparable to that of P2D models at low-medium rates, typically until 1C. The quality of results degrades substantially around 2C, showing clear limitations for fast charge/discharge applications.

The following Figure 2.4 illustrates the main features of SPMe, focusing on their one-dimensional approach, with a single-representative particle for each electrode (spatial uniformity across cell's thickness).

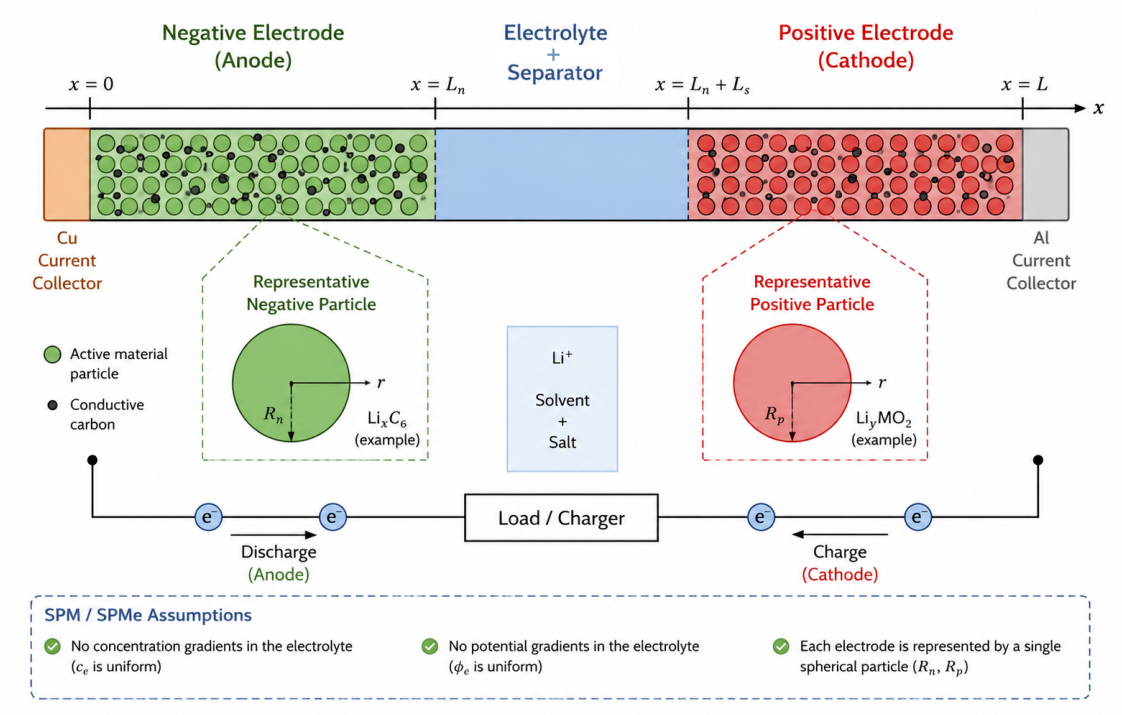


Figure 2.4: SPMe model illustration

In contrast to P2D model, the SPMe equation framework decouples the problems in the x and r coordinates, effectively making the SPMe a one-dimensional model.

Further details about SPMe theory, with the characteristic set of equations, derived from electrochemical laws, is provided in section 4.2.

Multi-physics field coupling model

A battery's multi-physical field coupling model is based on a complex modeling approach, which, considering the fundamental laws of porous electrode theory and conservation equations, couples the solution of different physical phenomena: electrochemical diffusion, heat conduction, and mechanical stress equilibrium equations. This model enables constructing a cross-scale electro-thermal-mechanical multi-physical field coupling system for a lithium-ion battery.

In general, this modeling approach is capable of describing well: (i) the lithium-ion transport and kinetic phenomena, (ii) the critical temperatures for thermal runaway, and (iii) the electrodes material expansion stresses. Therefore, it can provide a substantial theoretical support for advanced research directions, such as solid-state battery interface optimization or analysis of thermal runaway.

Moreover, thermal modeling of a battery can be characterized through two different approaches:

- Lumped model: it provides a general description of thermal battery behavior, without considering the spatial distribution of variables.
- Three-dimensional model: it makes a thermal description of battery from three-dimensional point of view (at single cell level or battery module level), using a spatially-resolved approach.

Lumped models are adopted to simplify the thermal analysis, with a high computational efficiency, although they have limited accuracy and adaptability.

Three-dimensional models are an optimal choice, when it is needed a more in-depth thermal analysis of the battery, obtaining high-precision modeling (both at cell or module levels), although at the cost of higher computational effort and an increased complexity in terms of thermal parameter calibration. A further analysis of thermal sub-models, coupled with electrochemical models, is presented in 5.7.

It is possible to distinguish several types of multi-physical coupling models:

- Electrochemical-thermal coupled model;
- Electrochemical-mechanical coupled model;
- Thermo-electrochemical-mechanical coupled model.

Electrochemical-thermal coupled model focuses on the interaction mechanisms between electrochemical reactions and thermal behaviors within the Li-ion battery, therefore it provides a solid theoretical basis for enhancing battery performance and ensuring operational safety.

Electrochemical-mechanical coupled model deeply analyzes the stress-strain phenomena during oxidation-reduction chemical reactions inside electrodes, considering an interaction between mechanical behaviors and overall electrochemical performance of the battery. Mohtat et al. (2020) [13] developed an MPMe (Multi-Particle Model with electrolyte), to simulate the mechanical response of its NMC/graphite battery cell to intercalation-induced expansion (swelling) during the charging phase.

Thermo-electrochemical-mechanical coupling model covers all the interrelated aspects of Li-ion batteries, thereby coupling thermal, mechanical and electrochemical fields in a unique modeling approach. Therefore, this model considers the interaction of electrochemical battery processes with temperature and stress-strain effects. Essentially, temperature rise or decrease can influence transport and kinetic processes inside the battery, with consequent different behaviors in charging/discharging performance; excessive temperature can trigger side reactions, such as electrolyte decomposition and electrode material structural phase changes, leading to capacity fading, increased internal resistance, and even thermal runaway. Meanwhile, lithium-ions insertion and extraction in electrodes can induce volume changes and stress-strain effects, and may lead the battery to issues of particle cracking and pulverization, with side effects on cycle-life and performance stability. Overall, the

complexity of thermo-electrochemical-mechanical model lies in comprehensively capturing the interaction, at different levels, among all the physical mechanisms within a Li-ion battery.

2.1.4 Data-driven models

Data-driven models adopt an approach essentially based on extensive experimental and real-world operational data, using machine learning and deep learning algorithms, in order to establish certain relationships between variables for battery performance prediction and analysis. These models are completely different from previous modeling approaches, because they do not require an in-depth analysis of electrical or multi-physical aspects of batteries. Instead, they employ advanced data mining and analytical techniques to extract key features and uncover latent patterns from wide data-sets.

A rapid classification of main categories of data-driven modeling is the following:

- Conventional Neural Network;
- Convolutional Neural Network;
- Recurrent Neural Network.

Conventional Neural Network models leverage their powerful non-linear mapping and adaptive learning capabilities to simulate the information processing mechanism of biological neural networks. In this way, they can achieve a precise modeling of the most complex physical and chemical aspects of lithium-ion batteries. Basically, the typical approach for conventional neural network models is Multi-layer perceptron modeling (MLP). It is also known as Artificial Neural Network (ANN), and basically is a feedforward neural network composed of an input layer, multiple hidden layers, and an output layer.

Time-space modeling category represents alternative data-driven modeling with respect to conventional methods. Basically, this kind of models can overcome the limitations of conventional models, that rely on manually crafted features, thereby demonstrating superior capabilities in modeling temporal dependencies and spatial distribution characteristics.

Convolutional Neural Network models, also called CNNs, belong to time-space modeling category. They have become a significant tool in lithium-ion modeling research, through their capabilities in image processing and feature extraction mechanisms. By exploiting their complex architecture, CNN models can efficiently extract local features from battery data.

Recurrent Neural Network models, also called RNNs, are part of time-space modeling category. Essentially, they focus on the analyses of several battery physical mechanisms through a time-series process with significant non-linear characteristics. However, they can suffer from some internal defects, resulting in model limitations in terms of training and prediction accuracy.

Regarding the emerging data-driven approaches, it is worth mentioning Physics Informed Neural Networks (PINN) models; they represent a sort of hybrid approach between machine learning and physical laws, leading to enhanced results with respect to the previous techniques.

2.1.5 Battery Models: final comparison

Lithium-ion battery modeling approaches can vary across several possibilities, as analyzed before; a comparative analysis of empirical models, equivalent-circuit models, physics-based models and data-driven models is useful to comprehensively understand the application fields, and respective advantages and limitations.

In the following Table 2.1, a general comparison, from different points of view, is reported for the four main categories of battery modeling ([7]).

Name & Type	Model computation	Model accuracy	Application fields
Empirical Model: Basic models	Very low-complexity parameters calibration	Low-to-medium	Basic voltage predictions, fast simulations of battery response
Empirical Model: Advanced models	Modest number of parameters, generally fast simulations	Medium	BMS-oriented design, applications requiring high computational efficiency
Equivalent-circuit Model: Single cell model	Few parameters, solution through milliseconds-level calculation	Medium (typical error in range $(1-10)\ \%$)	BMS real-time control (SoC/SoH estimation), preliminary system design
Equivalent-circuit Model: Battery module model	Linear growth with the number of series and parallel connections	Medium (system-level error in range $(5-15)\ \%$)	Electric vehicle battery packs, power tools, energy storage system architecture design
Physics-based Model: Pure Electrochemical Model	Solving partial-differential equations at minutes-level	Extremely high (typical error $< 2\%$)	Complex modeling with industrial (SPM or SPMe) or research-oriented (P2D model) for material developments or safety analyses
Physics-based Model: Multi-physics coupling model	Millions of grids, hourly-level simulation	Extremely high (cross-field coupling error in range $(1-3)\ \%$)	Thermal runaway criticality prediction, mechanical stress failure analysis, long-life structural design
Data-driven model: Traditional neural network modeling	Small-sample size, hour-level training	Medium (typical error in range $(3-8)\ \%$)	Rapid modeling of small sample scenarios and preliminary fault classification
Data-driven model: Timing and Spatial modeling	Complex network, daily-level training	High (error in complex conditions $< 5\%$)	Remaining useful life (RUL) prediction, fault diagnosis, multi-source data-fusion

Table 2.1: Final comparison features of main Battery Modeling categories

2.2 Software Tools for Electrochemical Battery Modeling

In this section, a deep analysis of the main software tools, suitable for electrochemical modeling, is made, considering either commercial or open-source software. In general, the implementation of physics-based battery models requires a software environment capable of representing coupled electrochemical, transport, and, when required, thermal phenomena. As seen for Li-ion battery modeling, the reference framework is derived from porous-electrode theory and concentrated-solution theory, and it includes Doyle-Fuller-Newman (or P2D) model, together with simplified reduced-order model, such as SPM or SPMe. Typically, the choice of the software tool is not only a numerical issue in terms of computations, but it is also a methodological decision that can affect model transparency, parametrization strategy and reproducibility (Sulzer et al. (2021) [14],

Brosa-Planella et al. (2022) [8]).

At the end of the software analysis, the final choice of PyBaMM tool will be explained, considering the preference for an open-source software, basically due to the wide availability of relative scientific literature, and its specific development for electrochemical modeling.

2.2.1 MATLAB / Simulink

MATLAB/Simulink represents one of the most established commercial environments for model-based designs. Its main strength is the integration between numerical scripting, block-diagram simulation, control design and automatic code-generation workflows.

In the battery field, MATLAB offers the possibility to directly implement the governing equations of P2D/DFN models at scripting level, whereas Simulink provides a package (Simscape-Battery) which is a convenient framework for cell, module and pack-level simulations. Simscape-Battery allows: (i) to study the battery cell's behavior on the basis of measured data, (ii) to execute virtual tests on different architectures of battery packs, (iii) to design Battery-Management-Systems, (iv) and to assess the battery system behavior in normal and fault conditions.

From a conceptual point of view, the electrochemical model can be coupled with thermal-management systems, power electronics, BMS algorithms and vehicle models, within the same environment. This makes MATLAB/Simulink particularly attractive for industrial applications, in which the battery model is part of a wider electrified powertrain or control architecture. Public case studies report its use in battery-management and thermal-management workflows by automotive companies, such as Dongfeng Electric Vehicle and Mahindra Electric.

2.2.2 PyBaMM (Python Battery Mathematical Modeling)

PyBaMM, acronym for Python Battery Mathematical Modeling, is an open-source software package specifically developed for physics-based battery modeling. It provides pre-built implementations of the main lithium-ion battery models, available in literature studies, including SPM, SPMe, and DFN model, together with parameter sets, experimental definitions, solvers and post-processing tools (Sulzer et al. (2021) [14], PyBaMM.org [15]).

In particular, PyBaMM consists of:

- A framework for writing and solving systems of differential equations;
- A library of battery models and parameter-sets;
- Specialized tools for simulating specific battery experiments and visualizing the results.

Its modeling philosophy is particularly suitable for academic work, because equations are organized in a modular structure: sub-models describe individual physical processes, such as solid-diffusion, electrolyte transport, interfacial kinetics, thermal behavior or degradation, and these components are assembled into a complete cell's model. The software gives also the possibility to manually modify physical assumptions, replace constitutive relations, introduce new parameters and compare model fidelity within a common framework. They are decisive advantages for deep studies of Li-ion modeling, for more advanced cases in which the objective could not be only to simulate terminal-voltage of a cell, but also to understand and calibrate the electrochemical equations governing the specific model.

The main advantages of PyBaMM are its openness, scientific framework for easy reproducibility, and high flexibility. Since the code is written in Python and distributed as an open-source project, simulations can be inspected, modified and shared, without dependence on proprietary solvers. Moreover, PyBaMM is well-aligned with a workflow based on experimental parametrization,

sensitivity analysis and model validation, since it allows systematic changes of geometrical, kinetic, and transport parameters. Its limitations are mainly related to the need of programming knowledge and to the fact that realistic parameter identification remains a difficult task for all electrochemical models (Chen et al. (2020) [4], Ecker et al. (2015) [16] [17], Schmalstieg et al. (2018) [18] [19]).

In addition, although PyBaMM can include thermal and degradation sub-models, full vehicle-level integration and certified control-code generation are not its primary purpose. For this reason, PyBaMM is particularly appropriate for research-oriented cell modeling, with great interest from scientific community to build a verified and wide knowledge on battery-modeling.

In Figure 2.5, the PyBaMM environment, with its more classical commands to run an SPMe simulation, is shown.

```python
import pybamm
import numpy as np
import matplotlib.pyplot as plt

# Setting up electrochemical model: SPMe or DFN model
model = pybamm.lithium_ion.SPMe()

# Load the "Mohtat2020" parameter-set
Parameter_set = pybamm.ParameterValues("Mohtat2020")

# Update of some parameter values (example)
Parameter_set.update({
   "Nominal cell capacity [A.h]": 11.0,
   "Initial concentration in negative electrode [mol.m-3]": 19462.27,
   "Initial concentration in positive electrode [mol.m-3]": 1183.22,
})

# Definition of the experiment steps (example: 1C discharge)
experiment = pybamm.Experiment(
    ["Discharge at 1C until 2.7 V"],
    period="10 seconds",
    )

# Simulation initialization (defining model, parameter-set and experiment)
simulation = pybamm.Simulation(model,
                               parameter_values=Parameter_set,
                               experiment=experiment)

# Running solver for solution
solution = simulation.solve(calc_esoh=False)

# Visualization of main output plots
simulation.plot()
```

Figure 2.5: PyBaMM tool: typical script

2.2.3 BattMO

BattMO, i.e. Battery Modeling Toolbox, is another open-source tool for continuum modeling of electrochemical devices. It was originally developed in the MATLAB ecosystem and is based on finite-volume discretizations and advanced numerical solvers. Its initial focus is a Pseudo-X-Dimensional framework for DFN model of lithium-ion cells, with the possibility of extending the approach toward electrochemical-thermal simulations and multi-dimensional geometries.

Compared with PyBaMM, BattMO is particularly attractive when the research focus is on spatially resolved continuum modeling, grid generation and extension from P2D modeling toward higher-dimensional representations. However, its user community and documentation ecosystem are more limited than those of PyBaMM, and the dependence on MATLAB Reservoir Simulation Toolbox (MRST) may reduce accessibility for users searching for a fully Python-based workflow.

2.2.4 Comparative analysis

In the context of this Thesis, PyBaMM is the most coherent choice for basic purposes of research, because of its direct SPMe implementation, extensive model library, active scientific community, and suitability for parameter calibration.

In Table 2.2, there is a summary of the main features for the three analyzed software-tools, useful for battery electrochemical modeling.

Feature	**MATLAB/Simulink**	**PyBaMM**	**BattMO**
Type of License	Commercial	Open-source	Open-source
Primary focus	System-level & control analyses	Electro-chemical modeling research	High-fidelity cell modeling
Modeling type	ECM + Basic P2D models	Advanced DFN / SPM / SPMe	Multi-dimensional PXD Models
Ease of Use	Medium (scripts + component-blocks)	Medium (required Python-coding)	Hard (advanced code-language)
Thermal sub-models	Included	Included	Limited (available extensions)
Degradation sub-models	Limited	Extensive	Limited
Real-time / HIL simulations	Excellent	Not included	Not included
Ease of customization	Medium	Very high	Medium

Table 2.2: Summary of main features of three software-tools for electrochemical modeling

2.2.5 Additional commercial tools

Two further commercial tools deserve brief mention.

GT-AutoLion, integrated within the GT-SUITE environment, is a high-fidelity electrochemical battery simulation-tool, designed for cell manufacturers and OEMs applications. It is oriented toward the prediction of performance, degradation and safety of lithium-ion cells and benefits from coupling with system-level thermal, electrical and vehicle simulations. Its main advantages are industrial validation and workflow integration.

COMSOL-Multiphysics, through the Battery-design module, provides a highly flexible finite-element environment for electrochemical and multi-physics modeling. It supports Newman-type lithium-ion models in 1D, 2D and 3D, and it can be coupled with heat-transfer, mechanical stress and other physical fields. Public material also documents the use of COMSOL by Porsche for electrochemical modeling of fast-charging automotive cells. Therefore, COMSOL-Multiphysics is the most powerful software for detailed multi-physical analysis, but it generally requires more modeling effort and computational resources than dedicated reduced-order battery libraries of the other cases.

2.2.6 Final Insights

Electrochemical battery modeling tools can be broadly classified into research-oriented frameworks (PyBaMM, BattMO), multi-physics design tools (COMSOL), and system-level industrial platforms (MATLAB/Simulink, GT-AutoLion).

The selection of PyBaMM is consistent with the objectives of the Thesis; it is focused on the implementation, interpretation and calibration of electrochemical model equations for a lithium-ion pouch cell, rather than on closed industrial deployment or full-vehicle control design. In this perspective, PyBaMM offers the most appropriate compromise between physical fidelity, computational efficiency, transparency of results and their easy reproducibility. Meanwhile, MATLAB/Simulink, BattMO, GT-AutoLion and COMSOL-Multiphysics remain relevant references, because they highlight alternative modeling philosophies: respectively, industrial control integration, open-continuum modeling, commercial cell-design workflows or high-fidelity multi-physics simulations.

For this Thesis, PyBaMM perfectly follows the main purposes, assumed at the beginning: use of an open-source software tool, supported by scientific community, with a practical and high-level approach in terms of electrochemical modeling. The advantage of built-in parameter-sets, assumed as a basis for initial analysis, and already integrated equations of models (i.e. DFN / SPM / SPMe), with the addition of the corresponding simplicity of Python coding are other motivations for this choice.

Finally, the possibilities of developing further thermal analysis and aging/degradation studies make PyBaMM an optimal tool for in-depth research.

The current software review for electrochemical modeling analyzed only five of the most known tools, although different other alternatives are available. Further details with more in-depth analyses regarding battery modeling tools (open-source or commercial ones) are available at website [20].

Chapter 3

Battery cell's Experimental Characterization Activity

This chapter deals with the analysis of the main non-intrusive characterization tests available for Li-ion battery cells. The first section introduces the case-study and the instruments used in laboratory during the experimental campaign. The second section focuses on the introduction of the crucial tests, frequently used in literature to characterize Li-ion batteries. The third section analyzes the entire experimental campaign carried out in laboratory; five categories of non-intrusive tests are described with details about execution (aimed to cell's characterization) and ambient conditions/applied rates. Some considerations about experimental data are made in the last section, considering the potential issues from OCV hysteresis and capacity-fading.

In general, the electrochemical model's parameters may need more specific characterization tests, in addition to the non-invasive procedures. In more detail, from literature studies, the future model's parametrization would typically require: (i) a complete teardown of the cell (to discover its internal physical structure), (ii) half-cell configurations (to analyze physical features of the single electrodes), and (iii) specific physico-chemical characterization tests (to analyze various micro-structural properties of the electrodes).

3.1 Case-study and Experimental Layout

In general, physics-based models (DFN / SPMe) need geometric, material properties, thermo-dynamic, transport, kinetic and thermal information, for the subsequent model parametrization activity.

To comply with this purpose, the experimental data are fundamental to characterize the cell's behavior in any real conditions. The great variety of experiments allows one to extract some specific information about the physical properties of the cell.

This section introduces the Thesis case-study, i.e. Kokam Li-ion NMC/graphite pouch cell (SLPB55205130H), and the tests and instruments used during the entire experimental campaign.

3.1.1 Case-study: Li-ion Kokam battery cell SLPB55205130H

The Li-ion battery cell studied in this Thesis, as anticipated, is manufactured by Kokam, belonging to the category SLPB (Superior Lithium Polymer Battery), dating from 2009, with model-name: SLPB55205130H.

As stated by Kokam, this Li-ion pouch cell provides different advantages, such as: longer cycle and calendar life, high safety, good recharge time, optimal power delivery and ability to operate at

extreme temperatures.

Furthermore, from Kokam catalogue [3], Kokam cell SLPB55205130H uses stacked technology, guaranteeing low internal resistance and high-efficiency.

Nowadays, the Li-ion NMC batteries have reached higher standards than the one of this case-study, but it is important to remember the purpose of the Thesis: experimental characterization and battery cell modeling, without necessarily using the most modern technologies.

From datasheet ([3]), this cell is High-Power NMC/graphite (respectively for cathode/anode compositions). The percentages of Nickel, Manganese and Cobalt are unknown (probably, it can be NMC111 or NMC532, considering the year of production). Furthermore, the internal cell's configuration, based on stacked electrode-sheets, is classical for old pouch cells.

The High-Power designation is reflected in the very low AC internal resistance ($1.6\ m\Omega$ at $1\ kHz$), and in the elevated continuous/pulsed discharge ratings (8C and 10C, respectively). As explained in sub-section 1.3.2, cells of this class are engineered with thin electrode coatings and high-porosity micro-structures, so as to minimize ohmic and transport losses, at the expense of gravimetric energy density.

The principal features of this SLPB pouch cell are summarized in the following Table 3.1.

Cell feature	
Manufacturer/model	Kokam SLPB55205130H
Form factor	SLPB Pouch
Positive/Negative electrode chemistry	NMC/graphite
Manufacturer classification	High-Power (HP) NMC
Rated (nominal) capacity	$11\ Ah$
Nominal voltage	$\sim 3.7\ V$
Operating voltage window	$(2.7 - 4.2)\ V$
AC internal resistance (at $1\ kHz$)	$1.6\ m\Omega$
Continuous/pulsed discharge rating	8C/10C
Dimensions (W x L x T)	207 x 137 x 5.6 mm
Mass	$\sim 280\ g$
Gravimetric energy density	$\sim 145\ Wh/kg$

Table 3.1: Main features of Kokam SLPB55205130H

Figure 3.1 shows one of the Kokam cells used during the experimental campaign.



Figure 3.1: Kokam Li-ion High-Power NMC/graphite pouch cell

3.1.2 Laboratory Tests with battery cycler and climatic chamber

The experimental activity was carried out at the Energy Center, an external facility of Politecnico di Torino. Thereby, it was possible to explore the cell's behavior under different charge/discharge patterns and temperatures. More specifically, tests belonging to the following main categories were performed:

- Pulsed charge & discharge tests (typically followed by relaxation periods).
- Continuous charge & discharge tests.

The first category is represented by GITT (Galvanostatic Intermittent Titration Technique) or HPPC (Hybrid Pulse Power Characterization) tests. The second category is represented by Pseudo-OCV (Open-circuit Voltage), multi-rate CC discharge, and cycling tests. The dynamic behavior of the cell can be studied analyzing the first category, that can contain some useful information on ohmic, transport and kinetic features of the cell. Meanwhile, the second category of tests may be useful to analyze thermodynamic (e.g. stoichiometry windows) and some specific geometric properties of the cell.

Overall, in order to get a good cell's characterization, it is important to consider the quality of data (how they are measured), and their influence on the subsequent model's parametrization. Therefore, a very rigorous approach was applied, including long CV-charge phases until $50\ mA$ (equivalently to C/220) and large rest periods until 2 hours; this protocol (commonly defined as "pre-conditioning step") was applied in all the experiments to chemically stabilize the cell (deleting the inner concentration gradients), before the execution of the tests.

The combined use of battery cycler and climatic chamber was a strength point for Thesis experimental activity. Indeed, its purpose was to vary the test types (more dynamic or static tests) with the available programs of the battery cycler, at the same temperature, in order to construct a reliable framework for battery cell's characterization. A note is important: temperature is a state-variable that can affect different parameters of the cell, so it can have a wide impact on the

model. The role of the climatic chamber was fundamental to maintain a controlled temperature environment during the entire experimental activity.

Figure 3.2 shows the battery cycler, manufactured by LCN Bitrode, used during the experimental campaign. Bitrode MCV is a test-system at low-medium DC currents, employed for research and development of several battery chemistries. It exploits a single CPU, and it is capable of managing the various channels separately, allowing one to run, at the same time, different tests.

The module provides 16 channels, having the following specific features:

1. Voltage range: $(0 - 18)\ V$;
2. Current range: $(1\ mA - 300\ A)$;
3. Number of circuits: up to 96;
4. Accuracy: $\pm 0.1\%$;
5. Sampling frequency: up to $10\ Hz$.



Figure 3.2: Battery cycler: Bitrode MCV

Figure 3.3 shows the climatic chamber used during experiments, manufactured by Binder. This climatic chamber can establish a temperature range, for the tests, between $-20\ °C$ and $+60\ °C$. It provides two main settings: (i) Temperature (it can be varied through programs or set as constant); (ii) Relative humidity (typically set at 25%). The majority of tests were made at ambient temperature of $25\ °C$, other few tests at $10\ °C$ and $40\ °C$.



Figure 3.3: Binder Climatic-chamber

Finally, Figures 3.4 and 3.5 show the Kokam SLPB55205130H cell under-test with its supports made of special glass-fibers (so-called "vetronite").



Figure 3.4: Kokam cell: operative conditions (1)

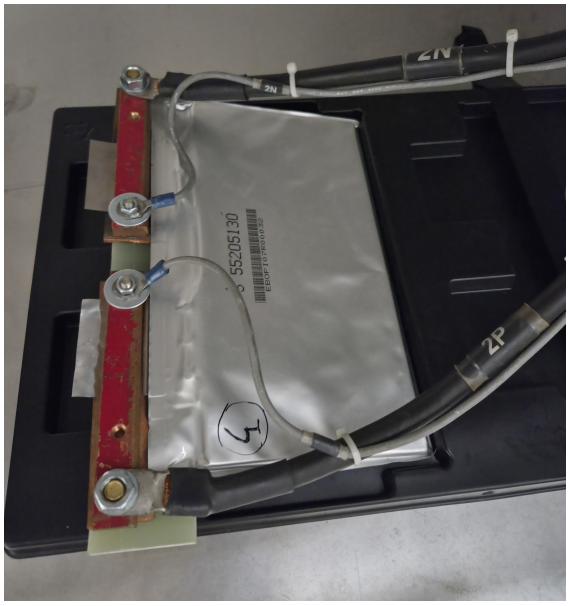


Figure 3.5: Kokam-cell: operative conditions (2)

3.2 High-level tests for Physics-based models

In different literature works, two high-level crucial tests are usually very useful to extract a great amount of information for the cell's characterization of an electrochemical model:

1. GITT (Galvanostatic Intermittent Titration Technique) test;
2. EIS (Electrochemical Impedance Spectroscopy) test.

In the two following sub-sections, these two tests were analyzed highlighting their most important aspects for the battery modeling and other future developments.

3.2.1 GITT tests

The Galvanostatic Intermittent Titration Technique (GITT) is an electrochemical characterization method based on the repetition of low-current galvanostatic pulses, each one followed by a relaxation period at open-circuit. During each current pulse, lithium-ions are extracted from some electrode particles and inserted into the opposite electrode particles. During the following rest period, the concentration gradients generated inside the active-material particles progressively relax by solid-state diffusion. For this reason, GITT is particularly useful for separating, at least approximately, resistive, kinetic and diffusive contributions to the measured voltage response.

The GITT test measures the transient voltage change and open-circuit voltage (OCV) change during the charging and discharging processes, using only a pulsed DC current and specified cut-off voltage intervals.

A typical GITT step contains three main voltage features. In Figure 3.6, a typical GITT step, in presence of a pulsed current (discharge case, with applied $I > 0$), is shown, considering three different phases; two phases during the current pulse and one phase during the relaxation.

First, when the current is applied, the voltage exhibits an instantaneous jump (ΔE_{IR}), associated mainly with ohmic resistance and fast charge-transfer polarization. Then, during the constant-current pulse, the voltage evolves more slowly because a lithium concentration gradient is formed inside the active particles; it leads to a second smoother voltage jump (i.e. a diffusion-driven voltage change during the pulse), termed ΔE_t. Finally, when the current is interrupted, the voltage shows an opposite instantaneous jump, and then it relaxes gradually toward an equilibrium value, as lithium redistributes inside the particles. The potential difference between the previous equilibrium state and the current equilibrium state (i.e., two successive rest-plateaus) is called ΔE_s. This interpretation is consistent with GITT description (Weppner-Huggins (1977) [21]). In fact, each pulse is followed by relaxation until the condition $dE/dt \simeq 0$ (to reach the equilibrium), and the open-circuit voltage is approached.

Typically this measurement can take weeks to perform, through slow C-rate pulses, a complete sweep against state-of-charge and temperature.

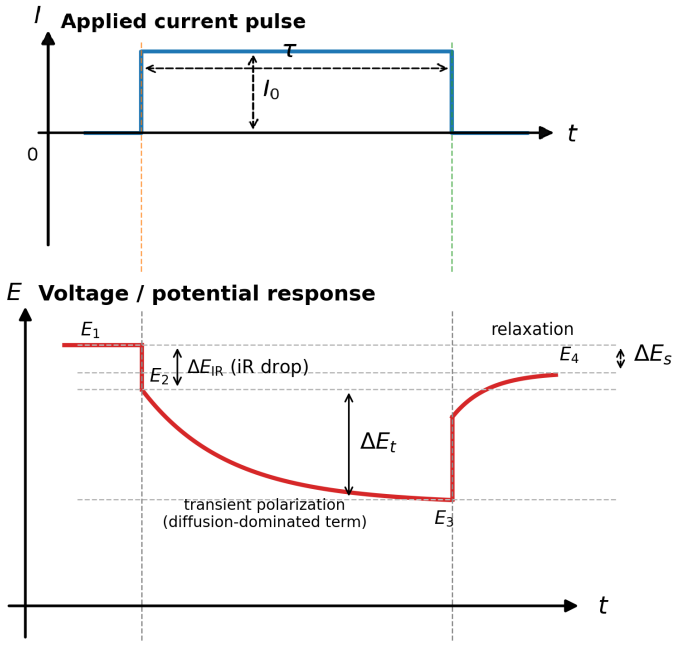


Figure 3.6: GITT discharge-pulse: analysis plot

From a modeling point of view, the slow part of the voltage transient is the most relevant for diffusivity estimation. After removing the instantaneous resistive (iR) contribution from this phase, the remaining voltage variation (ΔE_t) during the pulse is related to the change of lithium concentration at the particle surface. If the pulse is sufficiently short and the current sufficiently small, the early-time diffusion response can be approximated by the Sand-type relation, in which the surface concentration varies proportionally to $\sqrt{t}$. This is the physical reason for which GITT analysis often uses the slope of potential E (of anode or cathode) versus $\sqrt{t}$.

The Galvanostatic Intermittent Titration Technique is a standard method for determining the solid-phase diffusion coefficient of intercalation electrodes, together with their quasi-equilibrium open-circuit potential (OCP). The repetition of the classical pulse-relaxation sequence over the full stoichiometry range maps both the equilibrium potential and the diffusion coefficient as functions of the SoC.

The theoretical background of the method is based on the knowledge of the behavior of the solid-phase concentration under a constant interfacial Li-ion flux. For short pulse durations, with respect to the characteristic diffusion time, i.e. $\tau << R_p^2/D_s$, the diffusion field does not reach the center of active particles (assumed as spherical); in this case, the surface concentration evolves according to the constant Li-ion flux solution of the diffusion problem. Thereby, the corresponding Sand-type relation ([4]) is applied:

$$c_s^{surf}(t) = c_{s,0} + \frac{2I}{F \cdot S} \cdot \sqrt{\frac{t}{\pi D_s}}$$

where: I is the pulse current, F is the Faraday constant, S is the active electrode/electrolyte interfacial area, D_s is the solid-phase diffusion coefficient, and $c_{s,0}$ is the equilibrium surface concentration. The surface concentration, and so the diffusion over-potential, grows proportionally to $\sqrt{t}$, as anticipated before; this feature is exploited to extract D_s from a GITT test.

Because the open-circuit potential is a smooth function of surface concentration, the diffusion, controlling part of the voltage transient, inherits the same $\sqrt{t}$-dependence. Following the Weppner-Huggins formulation ([21]), the diffusion coefficient is obtained through the ratio between the

equilibrium voltage change ΔE_s and the diffusion-driven voltage change ΔE_t; thereby, the equation to evaluate D_s is:

$$D_s = \frac{4}{\pi \cdot \tau} \cdot \left(\frac{V_{act}}{S}\right)^2 \cdot \left(\frac{\Delta E_s}{\Delta E_t}\right)^2$$

where: V_{act} is the active-material volume, τ is the current-pulse duration. Using this equation, D_s can be recovered from purely geometric quantities and two directly measurable voltage differences.

Assuming spherical active particles, the volume-to-area ratio reduces to $V_{act}/S = R_p/3$ (R_p is the particle radius), which yields the last equation for the most commonly used form of D_s for porous battery electrodes:

$$D_s = \frac{4}{\pi \cdot \tau} \cdot \left(\frac{R_p}{3}\right)^2 \cdot \left(\frac{\Delta E_s}{\Delta E_t}\right)^2 \tag{3.1}$$

In practice, this equation allows one to discard the initial fraction of pulse-time, dominated by the ohmic drop and kinetic charge-transfer (for more details, see section 4.1), and the final fraction of pulse-time, where finite-particle effects begin to invalidate the previous assumptions on diffusion.

Finally, because solid-phase diffusion is a thermally activated process, the temperature dependence of the extracted D_s coefficient is commonly expressed through the Arrhenius relation:

$$D_s(T) = D_{s,ref} \cdot exp\left[-\frac{E_a}{R} \cdot \left(\frac{1}{T} - \frac{1}{T_{ref}}\right)\right] \tag{3.2}$$

where: E_a is the activation energy of solid-state lithium diffusion, R is the universal gas constant, and $D_{s,ref}$ is the solid-phase diffusion coefficient at the reference temperature T_{ref}.

In this Thesis, some GITT tests were performed at other temperatures (at $10\ ^\circ C$ and $40\ ^\circ C$), however they are not used to extract the D_s dependence on temperature.

3.2.2 EIS test

Electrochemical Impedance Spectroscopy, usually abbreviated as EIS, is a typical electrochemical technique widely used for the characterization of lithium-ion batteries and, more generally, of electrochemical systems. Its main purpose is to investigate the dynamic response of a cell around a given equilibrium or steady-state operating point. Differently from conventional charge and discharge tests, which are performed in DC (direct current), so in the time domain, EIS works in the frequency domain. A small sinusoidal perturbation, either in voltage or in current, is applied to the cell over a wide frequency range, and the corresponding current or voltage response is measured. If the perturbation amplitude is sufficiently small, the battery can be considered locally linear and time-invariant, so that the impedance can be interpreted as a transfer-function between the input and the output signals. That is one of the reasons for which EIS is particularly useful: it can separate electrochemical processes characterized by different time constants, such as ohmic conduction, charge transfer, double-layer charging, SEI-related effects and diffusion phenomena.

Therefore, it is a highly informative test. In literature, it is typically employed as a complementary test of GITT, allowing one to analyze specific kinetic aspects, rather than only diffusion-related ones. In the Thesis context, it is reported only as an advised characterization technique, suitable for a more detailed battery cell characterization (e.g., it is used by Chen et al. (2020) [4], Ecker et al. (2015) [16] [17]).

In the following Table 3.2, the most relevant parameters that can be extracted from an EIS test, for a subsequent electrochemical modeling, are listed.

EIS feature	Physical interpretation	Possible SPMe/P2D parameter relevance
High-frequency intercept	Lumped ohmic resistance from electrolyte, current collectors, tabs, contacts and electronic pathways	Electrolyte conductivity, solid-phase conductivity, contact resistance (if explicitly included)
High/intermediate frequency arcs	Interfacial film and charge-transfer processes	Exchange-current density i_0, reaction-rate constants ($k_{0,p}$ & $k_{0,n}$), charge-transfer resistance, SEI/film resistance (presented in SEI sub-model)
Capacity behavior / depressed semicircles	Double-layer and non-ideal interfacial capacitance	Double-layer capacitance C_{dl} (if present), CPE-like parameters (if impedance modeling is included)
Low-frequency Warburg-like response	Diffusion and concentration polarization	Solid-phase diffusion coefficients ($D_{s,p}$ & $D_{s,n}$), electrolyte transport parameters (although GITT is often more direct for these estimations)
SoC/Temperature dependence of spectra	Variation of kinetics and transport with lithiation and temperature	Activation energies for kinetic and transport parameters (if included with thermal sub-model)

Table 3.2: Possible parameter estimations by using an EIS test

In EIS tests, the perturbation amplitude on the cell must be sufficiently small, typically a few mV in potentiostatic mode, so that the cell response can be treated as logically linear around the selected operating point. The test is repeated over a wide frequency range, generally from kHz region, so that electrochemical processes with different characteristic time constants can be separated. Ecker et al. (2015), for example, performed EIS on Kokam-related electrode half-cells, in potentiostatic mode, with a maximum voltage amplitude of $5\ mV$ and a frequency range from $10\ kHz$ to $500\ \mu Hz$, while additional galvanostatic spectra with DC superposition were used to identify charge-transfer coefficients.

3.3 Non-Invasive Experimental Characterization Campaign

A reliable electrochemical description of a lithium-ion battery cell is based on a well-established experimental characterization campaign, which quantifies its three defining electrical signatures, i.e. capacity, open-circuit voltage (OCV), and internal resistance, together with their dependence on state-of-charge (SoC), current-rate and temperature (Barai et al. (2019) [22]). Considering that the cell, investigated in this work, is a commercial, sealed device, only non-invasive (i.e. non-destructive) techniques were employed: each test perturbs the cell with a controlled current and records the terminal-voltage response, without disassembly or any operation that would compromise the cell. This class of tests is favored because it preserves the cell for repeated and subsequent measurements and also because it furnishes the quantities, which are most directly required for an electrical and thermal description of the cell (Barai et al. (2019) [22], Broatch et al. (2022) [23]).

The device under tests is the Kokam SLPB55205130H pouch cell, described with its main

features in sub-section 3.1.1.

All tests were carried out on a Bitrode LCN battery cycler, within a controlled climatic chamber, (both instruments were already described in the sub-section 3.1.2). The cycler applies programmed current profiles to the cell terminals through dedicated power leads, while the terminal-voltage is acquired through separate sense leads; the climatic chamber fixes the ambient temperature for the entire duration of each test.

The entire campaign was conducted principally at $25\ ^{\circ}C$, which serves as the reference temperature for the cell description, while selected tests (only Pseudo-OCV and GITT) were repeated also at $10\ ^{\circ}C$ and $40\ ^{\circ}C$, in order to only qualitatively visualize the temperature dependence of capacity and resistance. Although the entire study is referred to the standard temperature of $25\ ^{\circ}C$, the temperature effects can affect the results in different way: (i) the reduced temperature probes the regime in which solid-state diffusion and ionic transport are hindered, raising overpotential and reducing the accessible capacity, whereas (ii) the elevated temperature probes the opposite trend (Barai et al. (2019) [22], and Broatch et al. (2022) [23]).

Two conventions are adopted across the experimental campaign. First, the C-rate convention expresses current relative to the rated capacity ($Q_{nom} = 11\ Ah$); so, a rate of nC denotes a constant current:

$$I = n \cdot \frac{Q_{nom}}{1\ h}$$

thereby, 1C corresponds to $11\ A$. Although the C-rate carries a certain intrinsic electrochemical meaning and is, strictly, an arbitrary normalization, it is retained here because the active electrode area of a commercial cell is not known "a priori", and the C-rate remains the conventional and most probable descriptor (from Barai et al. (2019) [22]). Second, SoC is reconstructed from the Coulomb counting (in a discharge case):

$$SoC(t) = SoC_0 - \frac{1}{Q_{[Ah]}} \cdot \int_{t_0}^{t} \eta \cdot I(t')dt'$$

where: $Q_{[Ah]}$ is the measured capacity and η is the coulombic efficiency (from Broatch et al. (2022) [23]). The 0% SoC reference is defined by the lower cut-off voltage, reached at the end of a low-rate discharge, and 100% SoC by the completion of a constant-current/constant-voltage (CC-CV) full-charge.

The experimental campaign includes five main classes of tests:

1. Pseudo-OCV (open-circuit voltage) tests;
2. GITT (Galvanostatic Intermittent Titration Technique) tests;
3. HPPC (Hybrid Pulse Power Characterization) tests;
4. Multi-rate CC discharge tests;
5. Charge/Discharge cycling tests.

In particular, the campaign is richer than the minimum data-set, typically required for a non-invasive cell characterization, because it combines low-rate equilibrium information, pulse-response information with medium-to-large relaxation periods, rate-capability data, and repeated cycling behavior, over a wide range of current rates.

In the following sub-sections, the individual procedures, objectives and possible limitations are detailed for every executed test of the experimental campaign.

3.3.1 Pseudo-OCV tests

The Pseudo-OCV test consists of a complete galvanostatic discharge followed by a complete galvanostatic charge, interspersed with a long relaxation period. This test is performed deliberately at low constant current, so that the kinetic, ohmic and concentration-polarization contributions to the terminal-voltage are minimized, and the recovered voltage approaches the equilibrium potential at every SoC. Two rates were employed, C/20 and C/50; the lower rate (C/50, corresponding to $0.22\ A$) approaches the equilibrium limit more closely, while the C/20 acquisition provides a faster cross-check. Before each test, the cell was brought to a defined initial state by a CC-CV full charge; the subsequent low-rate CC charge and CC discharge then sweep the full SoC window between the manufacturer voltage limits ($(2.7 - 4.2)\ V$). The single-valued OCV-SoC curve is obtained as the half-sum of the charge and discharge voltage branches at equal SoC (as explained by Truchot et al. (2014) [24] and Barai et al. (2019) [22]).

The principal aim of a Pseudo-OCV test is to obtain a continuous, high-resolution approximation of the OCV-SoC relationship, which defines the thermodynamic operating curve of the cell and constitutes the dominant term of its terminal-voltage response (Broatch et al. (2022) [23]). Because the data are acquired continuously rather than at discrete rest points, the resulting curve resolves fine features of the voltage signature far better than a discrete-step measurement; the same charge/discharge data-sets additionally supports electrochemical voltage spectroscopy (EVS), which comprises incremental-capacity and differential-voltage analysis. In EVS analysis, the derivatives dQ/dV and dV/dQ expose the phase-transition and solid-solution features of the electrodes (Barai et al. (2019)). The separation between the charge and discharge branches further provides a direct SoC-resolved measurement of the cell's voltage hysteresis.

However, even at C/50, the charge and discharge branches do not coincide: a residual hysteresis remains convoluted with the small but non-zero overpotential, being an intrinsic characteristic of cell also at null currents. Therefore, neither the single branch individually qualifies as a true OCV and the averaging procedure recovers the equilibrium curve only approximately, under the assumption that the charge and discharge deviations are symmetric (this will be further analyzed in section 3.4). The technique is also time-consuming, considering that a single C/50 half cycle requires of the order of $50\ h$, which limits the number of repeats and temperatures that can be economically explored. At such low currents, the voltage response is sensitive to measurement noise and to slow parasitic side reactions, accumulated over long test duration; the industrial-grade Bitrode cycler mitigates the signal-to noise concern, but the fundamental compromise between proximity to equilibrium and test duration remains (Barai et al. (2019)). Finally, the hysteresis observed in a low-rate cycle is partly path dependent and should not be conflated with the structural potential hysteresis of the active materials.

In Figures 3.7 and 3.8, the Pseudo-OCV tests in charge and discharge at slow C-rate (C/50) are shown in two plots: (i) the first one represents voltage as a function of time, (ii) the second one represents voltage as a function of SoC. From the second plot, a typical asymmetry between charge and discharge emerges: the deliverable capacity during charge is $11.27\ Ah$, whereas the deliverable capacity during discharge is $11.18\ Ah$. These tests are useful to analyze the thermodynamic aspects of the cell, due to the lower rates, reproducing similar equilibrium (open-circuit) conditions.

The following Table 3.3 summarizes the main features adopted for the Pseudo-OCV test protocol.

Test	Adopted protocol	C-rates
Pseudo-OCV discharge	CC discharge between $4.2\ V$ and $2.7\ V$	C/20, C/50
Pseudo-OCV charge	CC charge between $2.7\ V$ and $4.2\ V$	C/20, C/50

Table 3.3: Pseudo-OCV tests: main features

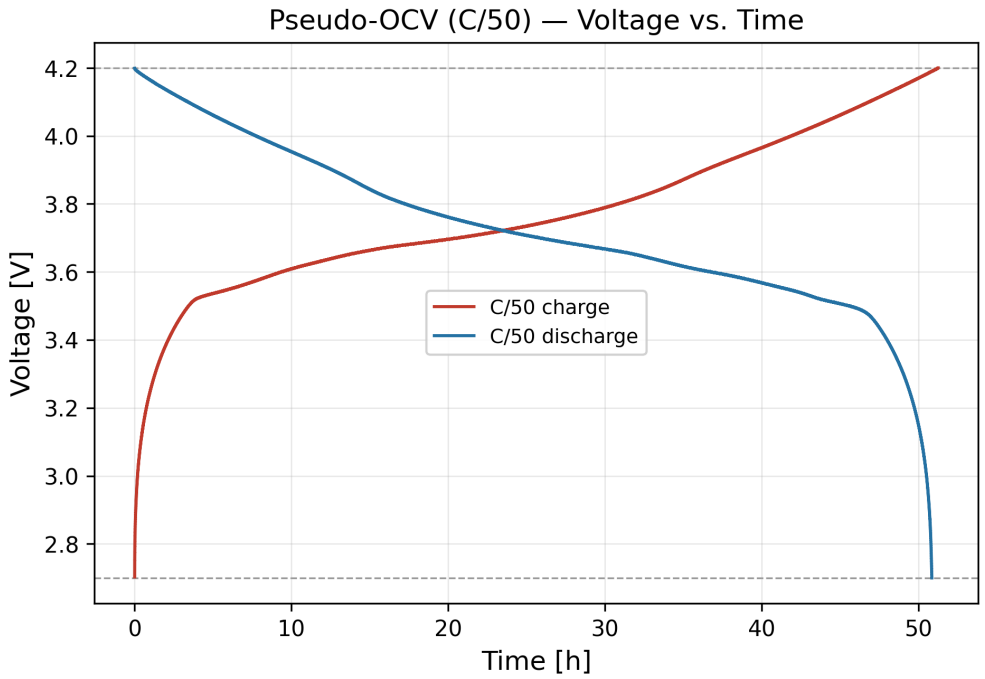


Figure 3.7: Pseudo-OCV tests (charge and discharge at C/50) - Voltage vs. Time

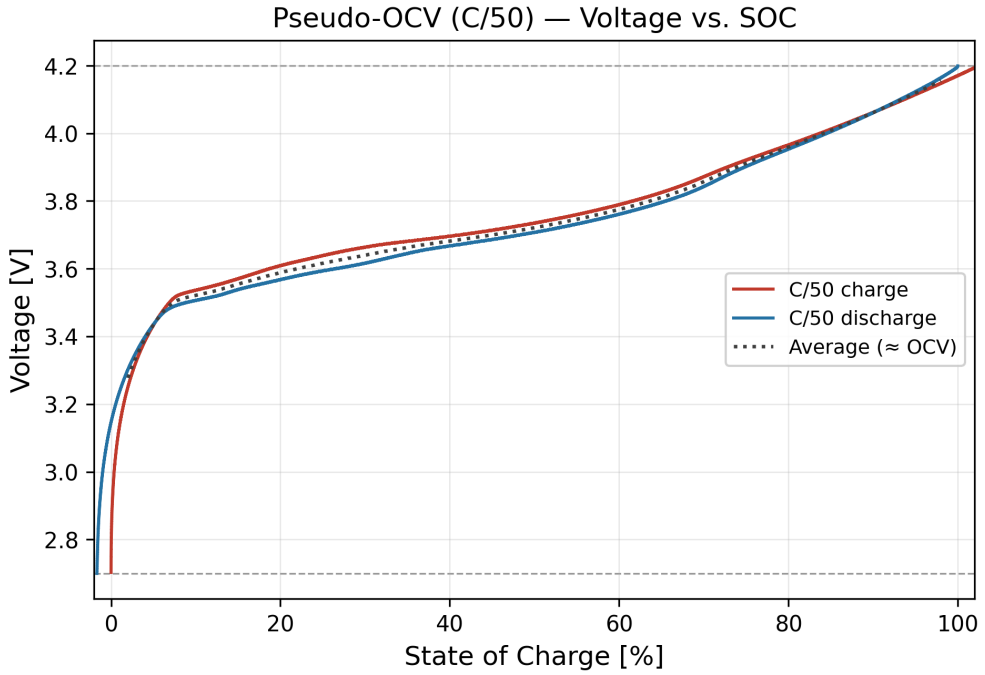


Figure 3.8: Pseudo-OCV tests (charge and discharge at C/50) - Voltage vs. SoC

3.3.2 GITT tests

GITT tests characterize the cell through a sequence of short galvanostatic pulses, each one followed by a prolonged open-circuit relaxation, thereby reconstructing the OCV-SoC curve point-by-point, while simultaneously exposing the cell's relaxation dynamics (Weppner & Huggins (1977) [21], and Barai et al. (2019) [22]). In the present experimental campaign, each pulse was applied at C/10 for $((8-10)\ min)$, incrementing the SoC by approximately $(1.3-1.7)\%$ per step, and was followed by a relaxation period of $40\ min$ to $1\ h$, during which the cell rests at open-circuit and the terminal-voltage relaxes towards its equilibrium value. The procedure was performed in both the charge and discharge directions, across the full SoC window. The voltage recorded at the end of each rest period can be taken as the near-equilibrium OCV point at the corresponding SoC (alternatively to Pseudo-OCV test).

The GITT yields the OCV-SoC relationship under conditions in which the kinetic contributions have been allowed to decay during the rest periods; therefore, these measurements are regarded as among the most accurate determinations of the equilibrium potential (Barai et al. (2019)). Performing the technique in both directions provides a rigorous measurement of the OCV hysteresis with correct SoC referencing at both extremes. The transient voltage evolution during and after each pulse additionally reflects the solid-state diffusion and redistribution processes within the active materials; the relaxation transients allow the apparent solid-phase diffusion coefficient to be estimated through the classical Weppner-Huggins analysis (Weppner & Huggins (1977)), making GITT a standard tool for probing the cell's transport behavior (as already explained in sub-section 3.2.1).

The central compromise of GITT concerns the adequacy of the relaxation period. A rest of one hour is generally accepted as sufficient for some chemistries, but may be insufficient for graphite/NMC cells to attain full electrochemical equilibrium, thereby a residual relaxation persists at the end of each rest, and the resulting OCV may slightly overestimate the true hysteresis (as explained by Petzl & Danzer (2013) [25], and Barai et al. (2019) [22]). The relaxation times adopted here $((40-60)\ min)$ thus represent a pragmatic balance between accuracy and test duration: a fully equilibrated GITT measurement with 1% SoC steps and $4\ h$ rests would require well over two weeks per direction, which is prohibitive for a campaign exploring multiple conditions. The discrete nature of the technique means that the OCV is sampled at finite SoC intervals rather than continuously, and, as for all OCV measurements, the long overall duration introduces a small contribution from parasitic side reactions (Barai et al. (2019)).

In Figure 3.9, the plot of the typical GITT tests in charge and discharge, at $25°C$, with C/10 pulses (lasting for $8\ min$), is shown. In particular, the relaxation periods are fixed at 1 hour, after each pulse, although they are not always sufficient to reach the necessary equilibrium, as highlighted from voltage shapes around nominal voltage ($3.7\ V$). The GITT test highlights the diffusion aspects during the second part of current pulse duration, and analogously during the relaxation periods.

Table 3.4 summarizes the adopted test protocol, specifying the charge/discharge pulses rate of GITT tests.

Test	Adopted protocol	Charge/Discharge pulses
GITT discharge	Discharge between $4.2\ V$ and $2.7\ V$ with pulses + relaxation periods of $1h$	At C/10
GITT charge	Charge between $2.7\ V$ and $4.2\ V$ with pulses + relaxation periods of $1h$	At C/10

Table 3.4: GITT tests: main features

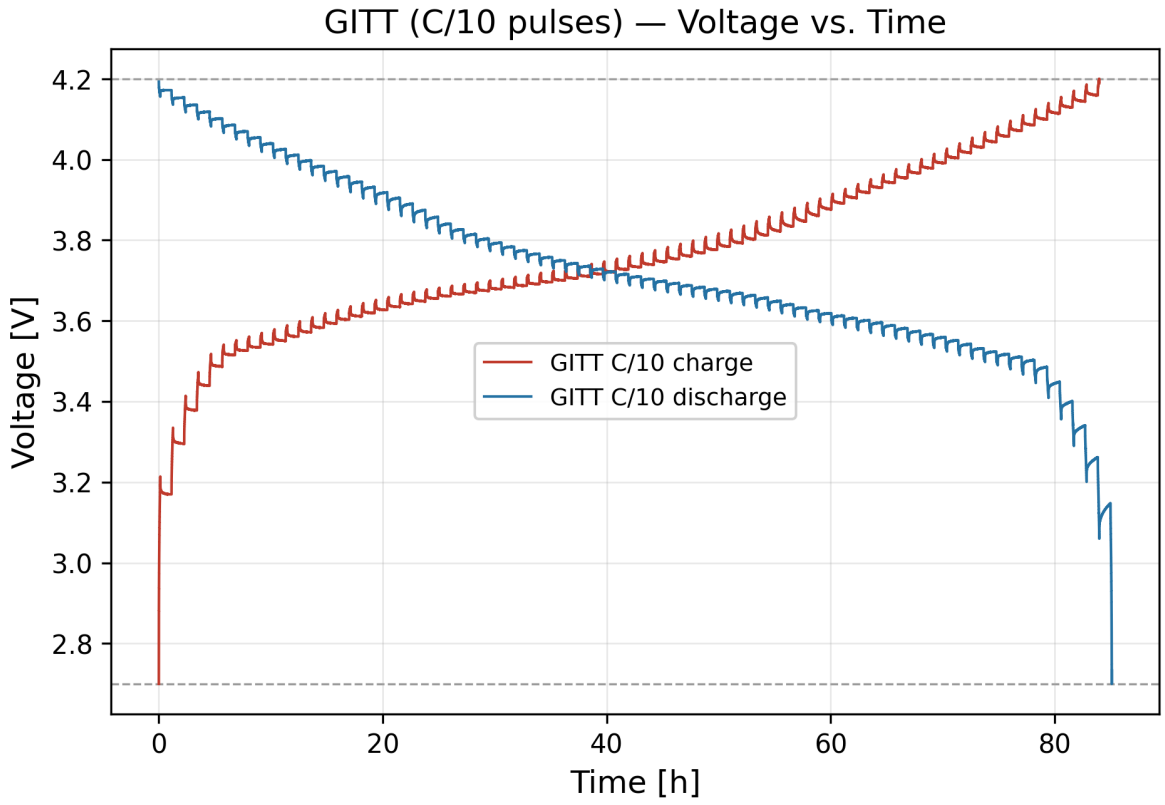


Figure 3.9: GITT tests (charge and discharge with C/10 pulses) - Voltage vs. Time

3.3.3 HPPC tests

The HPPC test, originally formalized within the "USABC/FreedomCAR programme" (Idaho National Laboratory, 2010 [26]), quantifies the internal resistance of the cell as a function of SoC, by superimposing short current pulses on a sequence of SoC set-points (Barai et al. (2019) [22]). In the adopted protocol for the campaign, the Kokam cell was discharged in steps to successive SoC levels and, at each level after an equilibration rest, subjected to a train of short ($90\ s$) charge and discharge pulses (interspersed with some rest periods of $((5-15)\ min$). Rather than the single 1C pulse of the standard procedure, an extended ladder of rates was applied (with pulses at C/5, C/3, C/2, 1C, 2C, supplemented by 0.25C, 0.75C, 1.25C and 1.5C), so as to resolve the dependence of the cell resistance on both current magnitude and current direction at each SoC. This multi-rate strategy follows the rationale of recent characterization methodologies, that argument the standard HPPC with additional pulse rates, to capture the non-linearity of the resistance (as explained by Broatch et al. (2022) [23]).

From each pulse, the cell resistance is estimated as the ratio of the voltage excursion to the applied current:

$$R_{pulse} = \frac{\Delta V}{\Delta I}$$

where the quasi-instantaneous voltage step at the onset of the pulse is associated predominantly with the ohmic resistance R_0, and the slower voltage evolution over the remainder of the pulse is affected by the charge-transfer and polarization (diffusion) contributions (Barai et al. (2019), Broatch et al. (2022)).

The HPPC campaign provides some indications of dependencies of internal resistance on SoC, rate and charge/discharge direction. It governs the cell's power capability and its ohmic heat generation, and constitutes the dissipative term of the terminal-voltage response. It is adopted here as the practical alternative to electrochemical impedance spectroscopy (EIS); indeed, EIS resolves the cell impedance across a frequency spectrum, requiring specialized, high-accuracy instrumentation and a sophisticated test set-up (as explained in section 3.2). Instead, HPPC delivers a robust, high-current resistance measurement using the standard cycler and pulse magnitudes, that more closely mimic real-world loads (Barai et al. (2019)). Additionally, the extended rate ladder allows the departure from ohmic behavior at higher currents to be quantified.

However, the pulse resistance is a lumped and bulk parameter: the ohmic, charge-transfer and polarization contributions are convoluted and cannot be cleanly separated from a single voltage transient, so any attribution of portions of R_{pulse} to individual physical processes is necessarily approximated (Barai et al. (2019)). Moreover, the measured resistance is sensitive to the pulse duration (a longer pulse drives the cell further into the solid-state diffusion regime and yields a larger apparent resistance), so the $90\ s$ value characterizes one specific measurement time-scale and is not a unique property of the SoC (Schweiger et al. (2010) [27], and Barai et al. (2019) [22]). Accurate isolation of the pure ohmic resistance is further limited by the data-acquisition bandwidth of commercial cyclers, which is typically too low (in this case, $10\ Hz$), to capture the instantaneous ohmic drop with the fidelity attainable by EIS. At the extremes of the SoC window, the pulses may be truncated by the voltage limits (discharge pulses cannot complete near the lower limit, nor charge pulses near the upper one), restricting the usable range; and, at long pulse lengths or high rates, the resistance can no longer be assigned to a single SoC, because the surface stoichiometry shifts appreciably during the pulse (Barai et al. (2019)). The extended rate ladder improves the resolution of the current dependence at the cost of a longer overall test.

In Figures 3.10, 3.11, and 3.12, the three performed HPPC tests, with different rate pulses are shown. The three plots represent the voltage against time, with a set of charge/discharge pulses, ranging from C/5 to 2C, progressively increasing, and interspersed with brief periods of relaxation (approximately $(5 - 15)\ min$). HPPC tests belong to category of the most dynamic tests of the entire experimental campaign, characterized by rapid variations of applied current, reproducing similar real driving-cycle conditions.

In the following Table 3.5, the details about HPPC protocol adopted for each test are summarized.

Test	Adopted protocol	Charge/Discharge pulses
HPPC 1	Reference discharge between $4.2\ V$ and $2.7\ V$ at C/10	At C/5, C/3, C/2, 1C, 2C
HPPC 2	Reference discharge between $4.2\ V$ and $2.7\ V$ at C/10	At 0.25C, 0.5C, 0.75C, 1C, 1.25C, 1.5C
HPPC 3	Reference discharge between $4.2\ V$ and $2.7\ V$ at 1C	At C/5, C/3, C/2, 1C, 2C

Table 3.5: HPPC tests: main features

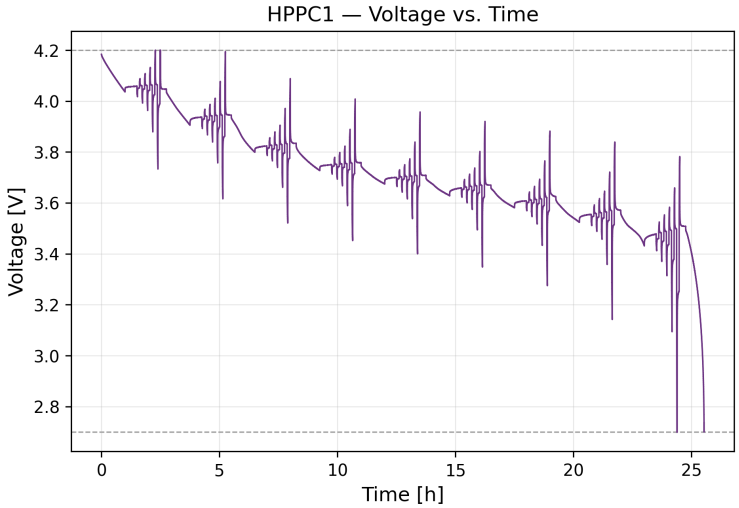


Figure 3.10: HPPC test 1 - Voltage vs. Time

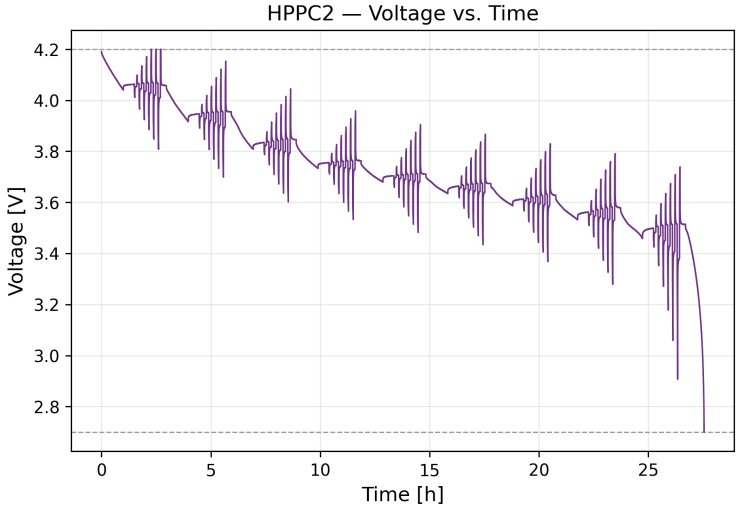


Figure 3.11: HPPC test 2 - Voltage vs. Time

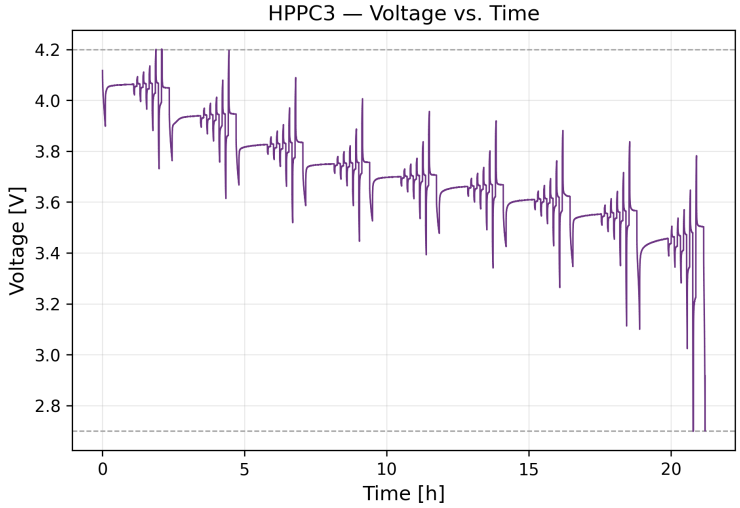


Figure 3.12: HPPC test 3 - Voltage vs. Time

3.3.4 Multi-rate CC discharge tests

The rate capability of the cell was assessed through a series of full constant-current discharges, performed at successively higher rates, i.e. C/10, C/5, C/2, 1C, 1.5C, and 2C. In each case, the cell was first brought to a fully charged state by the CC-CV protocol and allowed to rest, after which it was discharged at the prescribed constant-current to the lower cut-off voltage ($2.7\ V$); the delivered capacity was obtained by Coulomb counting, shown at the beginning of this section (Broatch et al. (2022) [23]). The sequence was conducted only at $25\ °C$.

These tests quantify the dependence of the accessible discharge capacity, and of the voltage discharge profile, on the C-rate, involving one of the defining performance characteristics of the cell and a primary input for any rate-dependent capacity description (Barai et al. (2019) [22]). The deliverable capacity decreases as the rate increases, because the larger current density raises the electrode overpotential and the ohmic drop, driving the cell to the lower voltage limit, before its full-charge has been extracted; this behavior is conventionally described by Peukert-type relations (as explained by Broatch et al. (2022)). The family of discharge curves, measured at different rates, provides the data against which rate-dependent capacity behavior is established and against which the cell's response under realistic loads can be assessed.

In general, at the higher rates, the measured capacity reflects a convoluted mixture of thermodynamic and kinetic effects, so that a high-rate capacity is not certainly representative of the cell's thermodynamic capacity. Self-heating compounds this difficulty: at elevated currents, the cell temperature rises above the chamber set-point, so that the effective temperature, during a high-rate discharge, differs from the nominal value. Therefore, rigorous high-rate testing calls for the active surface-temperature control, rather than reliance on the chamber alone, which represents a refinement beyond the scope of the present chamber-based set-up (Barai et al. (2019)). Consequently, the high-rate results are interpreted as effective, condition-dependent quantities rather than as intrinsic thermodynamic capacities.

In Figures 3.13 and 3.14, the multi-rate CC discharge tests are shown, representing voltage as a function of time (first plot) or SoC (second plot). More specifically, these figures highlight, as Pseudo-OCV tests, the smoothness of experimental discharge voltage curves of Kokam cell. Six C-rates are employed for this test, ranging from C/10 to 2C. These tests are suitable for analyzing common cell features through simple continuous discharges.

The following Table 3.6 summarizes the main protocol's features of multi-rate CC discharge tests.

Test	**Adopted protocol**	**C-rates**
Multi-rate CC discharge	CC discharge between $4.2\ V$ and $2.7\ V$	C/10, C/5, C/2, 1C, 1.5C, 2C

Table 3.6: Multi-rate CC discharge test: main features

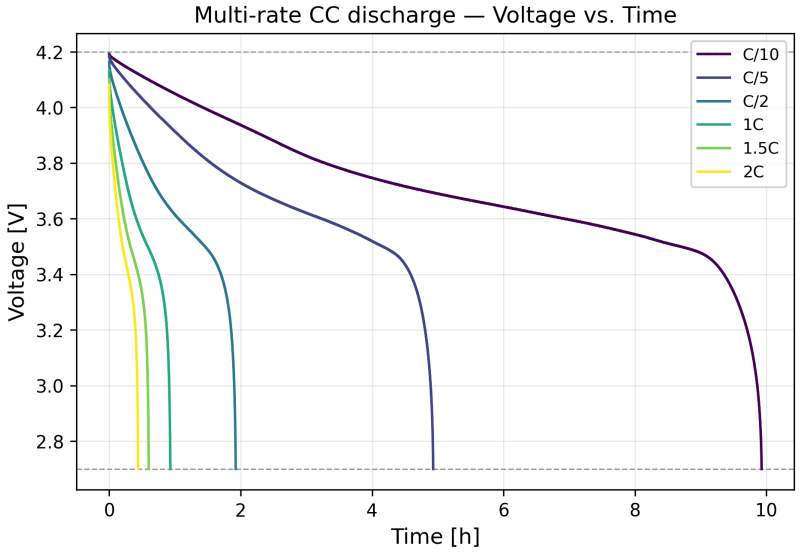


Figure 3.13: Multi-rate CC discharge tests - Voltage vs. Time

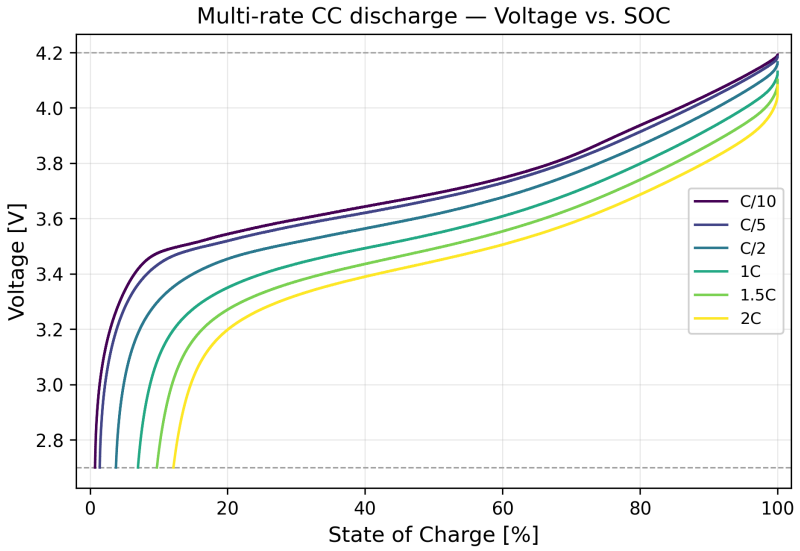


Figure 3.14: Multi-rate CC discharge tests - Voltage vs. SoC

3.3.5 Cycling tests

A cycling campaign was performed in order to have each cycle comprised of a CC-CV charge followed by a constant-current discharge, with the discharge conducted at one of eleven rates,

spanning 0.1C to 2C. The CC-CV charge (i.e. a constant-current charge to the upper voltage limit, followed by a constant-voltage hold until the current decays below a small cut-off) ensures that each discharge begins from a reproducible fully charged state, isolating the discharge rate as the variable of interest. The discharges to the lower cut-off voltage were Coulomb-counted to possibly extract the delivered capacity at each rate.

The cycling tests consolidate the rate-performance picture across a dense set of discharge rates and, by repeating charge/discharge cycles under controlled conditions, generate the framework of voltage-capacity data, required to characterize the cell over its operating envelope (in this case, the charge CV increases the cell's capacity at $4.2\ V$). The eleven-rate resolution provides a fine mapping of the capacity-rate and voltage-rate relationships, complementing the sparser multi-rate discharge series and furnishing reference data for the subsequent assessment of the cell under dynamic operating conditions (Barai et al. (2019) [22]).

Every charge/discharge cycle contributes incrementally to the cell's aging, so that an extended cycling campaign is itself a mild source of degradation, and particular care is required to distinguish genuine rate-dependent performance from any incipient capacity fade, accumulated over the whole campaign (Barai et al. (2019)). Because the charge step is CC-CV, while the discharge is purely constant-current, the constant-voltage tail of the charge differs in duration across cycles; therefore, the comparison is properly framed as one across discharge rates under a common charging protocol, rather than as a symmetric charge/discharge rate comparison. As with the multi-rate discharges, self-heating at the upper rates raises the cell temperature above the set-point and must be taken into consideration when interpreting the high-rate capacities.

In Figure 3.15, the 11 rates of various cycles, with CC-CV charge phases and CC discharge phases, are shown, with voltage as a function of time. The 11 C-rates are distinguished with progressive legend's colors, highlighting the passage from lower rate (e.g. C/10) to higher rate (e.g. 2C). It is worth noticing the duration of CV (constant-voltage) phase, which is dependent on some kinetic aspects, but is also influenced by Bitrode's internal control-system.

Table 3.7 shows the protocol adopted for the two phases (CC-CV charge and CC discharge) of cycling tests.

Test	**Adopted protocol**	**C-rates**
CC-CV charge phases	CC charge between $2.7\ V$ and $4.2\ V$ and CV until $50\ mA$	At 0.1C, 0.2C, 0.3C, 0.4C, 0.5C, 0.75C, 1C, 1.25C, 1.5C, 1.75C, 2C
CC discharge phases	CC discharge between $4.2\ V$ and $2.7\ V$	At 0.1C, 0.2C, 0.3C, 0.4C, 0.5C, 0.75C, 1C, 1.25C, 1.5C, 1.75C, 2C

Table 3.7: Cycling tests: main features

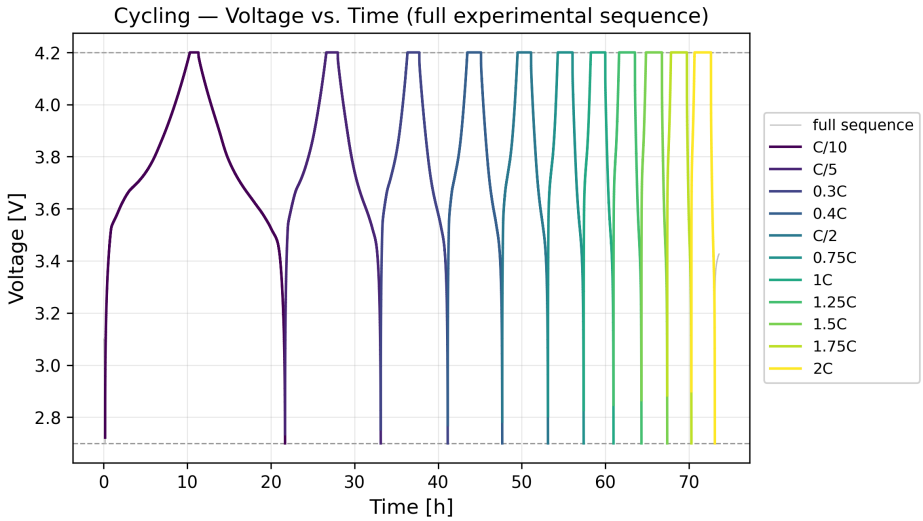


Figure 3.15: Cycling tests (CC-CV charge & CC discharge) - Voltage vs. Time

3.3.6 Summary of experimental activity

A summary of the entire experimental activity is made in this sub-section, in order to have a clear framework of the tests, used to characterize the cell. The campaign was developed in a period of four months, and only the tests of the last two months were used for further model's parametrization.

Overall, the characterization campaign combines complementary non-invasive techniques, each addressing a distinct kind of cell's behavior: the Pseudo-OCV and GITT tests establish the thermodynamic OCV-SoC relationship and its hysteresis (with GITT additionally probing the relaxation and diffusion dynamics); the HPPC tests map the internal resistance across SoC, rate and charge/discharge direction; and the multi-rate discharge and cycling tests characterize the rate-dependent capacity and voltage response.

As highlighted before, several specific physico-chemical characterization tests are invasive and they go beyond the scope of this Thesis; anyway, a complete description of these tests for electrochemical modeling is provided in the conference paper [28].

In the following Table 3.8, all the tests performed during the entire campaign are reported, exposing many details regarding ambient temperature, adopted C-rates, testing protocol and primary objective of characterization.

Test category	Ambient Temperature	Adopted C-rates	Protocol	Primary objective
Pseudo-OCV (charge & discharge)	$25\ °C$, $10\ °C$, $40\ °C$	C/20, C/50	Slow CC charge & discharge (full sweep)	Quasi-equilibrium OCV-SoC curve; hysteresis; differential-voltage-analysis (DVA)
GITT (charge & discharge)	$25\ °C$, $10\ °C$, $40\ °C$	C/10 (pulses)	Charge & Discharge with C/10 pulses $((8-10)\ min)$ + $(40-60)\ min$ of rest	Near-equilibrium OCV; hysteresis, relaxation/diffusion behavior
HPPC (charge & discharge)	$25\ °C$	0.2C, 0.25C, 0.33C, 0.5C, 0.75C, 1C, 1.25C, 1.5C, 2C (pulses)	$90\ s$ charge and discharge pulses at successive SoC, during reference discharge	Internal resistance versus SoC, dependent on rate and direction
Multi-rate CC discharge	$25\ °C$	C/10, C/5, C/2, 1C, 1.5C, 2C	Full constant-current discharges	Rate-capability, capacity-rate and voltage-rate dependence
Cycling (CC-CV charge & CC discharge)	$25\ °C$	0.1C, 0.2C, 0.3C, 0.4C, 0.5C, 0.75C, 1C, 1.25C, 1.5C, 1.75C, 2C	CC-CV charge phases + CC discharge phases	Dense rate-performance mapping; reference data for dynamic operation

Table 3.8: Test campaign details: temperatures, C-rates, protocol and primary objective

Mainly conducted at $25\ °C$, with some selected repetitions at $10\ °C$ and $40\ °C$, the campaign spans the SoC, current-rate, and in some cases, temperature dependencies, that together define the electrical signature of the High-Power Kokam pouch cell behavior. The limitations identified for each technique, i.e., residual hysteresis at finite rate, finite relaxation in GITT, the lumped and timescale-dependent nature of the pulse resistance, and the convolution of thermodynamic and kinetic effects (with addition of self-heating), at high rates, delimit the conditions under which the resulting data may be regarded as quantitatively reliable.

Finally, regarding the future modeling, it is crucial to choose a coherent data-set, for which the cell presents a certain internal degradation, that has to be similar during the whole campaign. This means that the first tests were very different from the last ones, in terms of deliverable capacity and battery efficiency.

Overall, as highlighted by the previous Table, the whole cell's characterization is mainly made at the same ambient temperature of $25\ °C$, thereby it is suitable for an isothermal modeling.

3.4 Considerations on Experimental data

The cell's characterization, developed in the previous sections, is based on the assumption that the experimental data describe a single, time-invariant cell, whose equilibrium thermodynamics is uniquely defined by its state-of-charge (SoC). Actually, two physical phenomena observed during the campaign violate this assumption and thereby set a lower bound on the fidelity that any SPMe can achieve for Kokam cell: (i) the open-circuit-voltage hysteresis of the active materials, and (ii) the capacity-fade accumulated by the cell, whose manufacturing date predates the campaign by more than fifteen years.

Both effects concern the same underlying quantity, i.e. the open-circuit voltage (OCV) versus SoC mapping, but they enter the work differently.

3.4.1 OCV Hysteresis

For an ideal battery cell, the equilibrium terminal-voltage is a single-valued function of SoC, defined by the difference of the two electrode equilibrium potentials (U_p for cathode OCP and U_n for anode OCP), assessed on a common SoC grid; this relation is expressed by:

$$U_{cell}(SoC) = U_p(y(SoC)) - U_n(x(SoC))$$

where: $U_{cell}(SoC)$ is the cell's OCV, whereas $x(SoC)$ and $y(SoC)$ are anode and cathode stoichiometries, respectively.

In a real cell, the quasi-equilibrium voltage reached at a given SoC depends on the direction from which that SoC was approached. The charge branch lies systematically above the discharge branch, with the following gap:

$$\Delta V_{hys}(SoC) = U_{ch}(SoC) - U_{dch}(SoC) \geq 0$$

where: ΔV_{hys} is the voltage variation due to hysteresis, U_{ch} is the OCV during charge, and U_{dch} is the OCV during discharge.

The hysteresis must be distinguished from over-potential (ohmic, charge-transfer, diffusion polarization, as explained later in 4.1.6), which is a voltage loss that scales with current and vanishes as current I goes to zero. Hysteresis is a thermodynamic/configurational property, which survives in the zero-current limit (Barai et al. (2019) [22]).

Several mechanisms contribute to hysteresis phenomenon, and their relative weight is highly chemistry-specific.

A first contribution is thermodynamic and arises in materials that are phase-separated. Some studies showed that an ensemble of intercalation particles does not fill homogeneously but particle-by-particle; typically, the sequence on lithiation inside active particles differs from that on de-lithiation, producing distinct voltage plateaus on charge and discharge, even at true equilibrium.

A second contribution is mechanical: the lattice parameters of lithiated and de-lithiated phases differ, so a moving phase boundary is loaded by elastic stress, and that stress shifts the equilibrium potential of the particle.

A third similar effect is graphite staging, consisting of intercalation/de-intercalation of negative-electrode's active material through a sequence of ordered stages; each of them carries its own charge/discharge asymmetry.

These three structural and mechanical effects are formalized more generally as path-dependence hysteresis causes.

For the studied Kokam cell, the majority of hysteresis is attributable to graphite negative-electrode (mainly tied to graphite staging), with only secondary effects added by NMC layered cathode.

Figure 3.16 shows the clear presence of hysteresis in the measured C/50 Pseudo-OCV test. This test comprises two branches, charge and discharge, at the same C-rates, and it makes the hysteresis directly visible.

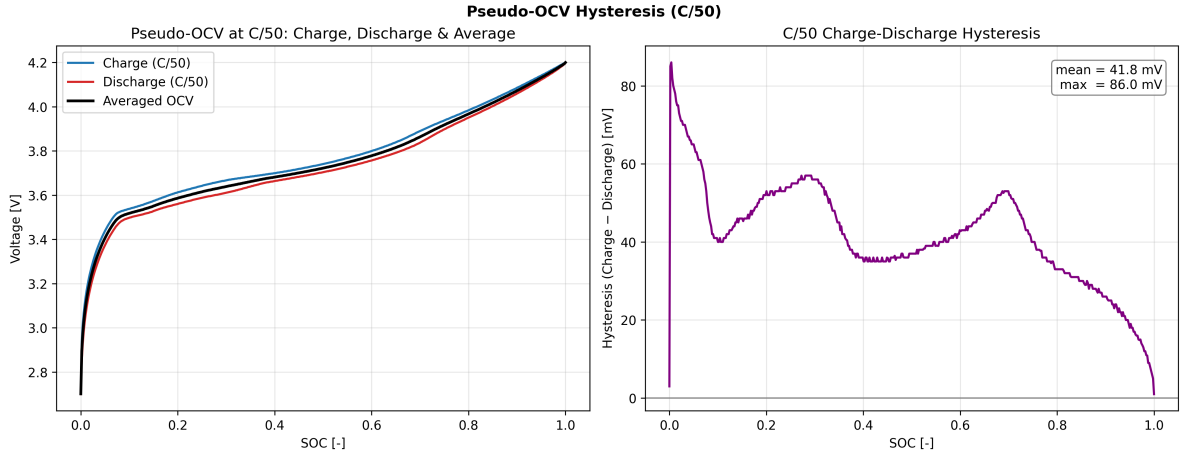


Figure 3.16: Hysteresis Quantification for cell's terminal-voltage

At C/50, the charge branch clearly lies above the discharge branch, with the difference between them defining the charge/discharge hysteresis. The charge-discharge gap, quantified on the canonical data-set, is approximately $41.8\ mV$, with peak value of $86\ mV$. The hysteresis profile is markedly non-monotonic: it peaks at the low-SoC knee ($86\ mV$), relaxes to a local minimum near 10% SoC, exhibits two intermediate maxima ($\sim 57\ mV$, near 28% SoC, and $\sim 53\ mV$ near 68% SoC), consistent with the graphite staging plateaus, and vanishes toward full charge.

Therefore, structured local maxima coincide with the regions, where the graphite staging plateaus and the NMC features are more pronounced, which is the expected case of a phase/stage-driven hysteresis, superimposed on a smooth background.

Finally, it must be considered two methodological cautions, both supported by the data and the literature. First, the C/50 gap is an upper bound on the true thermodynamic hysteresis, not the real hysteresis: at C/50, a residual kinetic polarization still survives, so the measured charge-discharge separation is characterized by genuine hysteresis, together with leftover overpotential and any imperfect alignment of 0% and 100% SoC references between the two steps. Second, this convolution is worst exactly where the gap is larger, i.e. at the low-SoC knee, where the OCV is steeper, so a small voltage error maps to a large apparent SoC error and vice-versa.

3.4.2 Capacity-fade

Capacity-fade in a graphite/NMC cell is conventionally decomposed into loss of lithium inventory (LLI) and loss of active material (LAM). In general, two aging pathways feed these modes: calendar aging and cycling aging.

Calendar aging proceeds even at rest and is dominated, for graphite electrode, by continued growth of the solid-electrolyte interphase (SEI) which irreversibly consumes cyclable lithium (LLI), and, to a lesser extent, by slow electrolyte decomposition that raises internal impedance. Diffusion-limited SEI growth follows an approximately parabolic law:

$$Q_{loss} \propto \sqrt{t}$$

where: Q_{loss} is the loss of capacity, and t is the time.

Most of the calendar loss of a fifteen year-old cell is already present before the campaign. The January-to-March comparison mainly captures the incremental fade, accrued during testing, on top of a substantially pre-aged baseline.

Cycling aging is incurred by the characterization itself. Each Pseudo-OCV measurement is a full-depth charge-discharge cycle, and a complete characterization matrix is known to remove a few percentage of capacity on its own; so, every cycle contributes to LLI and LAM (Barai et al. (2019) [22]). Another minimal cause of differences between Pseudo-OCV tests could due to C/50 protocol; it is extremely long, considering that half-cycle of 11 Ah cell takes around $50\ h$. Therefore, some parasitic side reactions can accumulate over the tests even at room temperature, where lithium-plating (a fast-charge, low temperature degradation mechanisms) is not expected to play any role.

Crucially, both Pseudo-OCV acquisitions were performed at the same temperature ($25\ ^{\circ}C$), which removes the most important test variable. Anyway, the accessible capacity is only weakly temperature-dependent, because polarization is minimal at C/50, and the lower voltage limit is reached close to full depletion, regardless of moderate temperature changes; only the tab temperatures were measured, ranging typically between $22^{\circ}C$ and $28^{\circ}C$, during both tests execution. The constant ambient temperature isolates the difference as a genuine loss of deliverable capacity rather than a thermally induced shift. Therefore, with an identical pre-conditioning protocol, identical SoC-window definition and identical ambient temperature, aging is the most reasonable and well-supported phenomenon for the deliverable capacity differences.

The same C/50 Pseudo-OCV protocol, applied to the same cell, at two different points of the experimental campaign, and the same ambient temperature ($25^{\circ}C$), returned different deliverable capacities: $\simeq 11.79\ Ah$ in January, against $\simeq 11.18\ Ah$ in March.

The capacity loss is quantified as:

$$\frac{Q_{Jan} - Q_{Mar}}{Q_{Jan}} = \frac{11.79 - 11.18}{11.79} \simeq 5.17\%$$

Figure 3.17 shows, in the same plot, the two Pseudo-OCV tests at C/50, both for a discharge process.

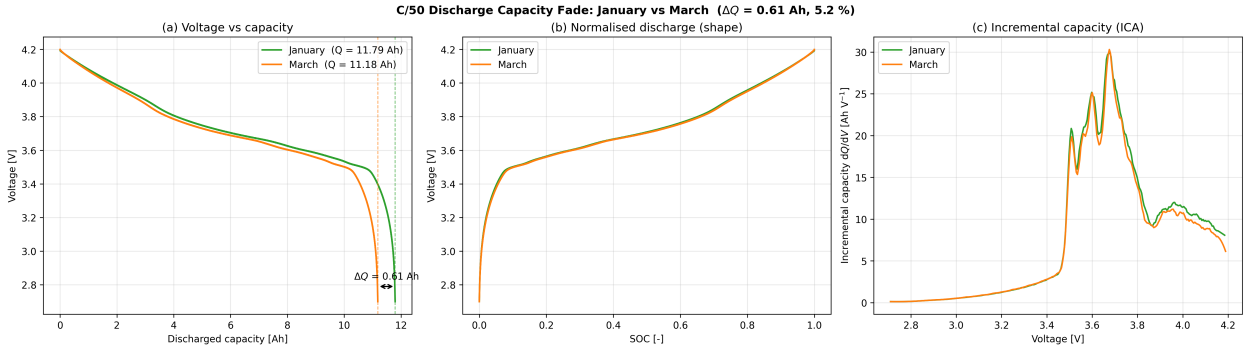


Figure 3.17: Capacity-fade: cell's terminal-voltage difference between January and March

The plot confirms the theoretical estimations: the deliverable capacity decreases by approximately 5.2%, falling from $11.79\ Ah$ to $11.18\ Ah$, in the period January-March, with a quantitative loss of $0.61\ Ah$. Considering that temperature, discharge protocol and voltage window were held fixed between these two dates, this difference is attributable to genuine aging, rather than to a change

in the accessible fraction of capacity. When the two discharge curves are re-expressed against their own normalized state-of-charge, they become almost indistinguishable (second sub-plot): the equilibrium voltage-SoC relationship is preserved, and the fade therefore manifests as a contraction of the deliverable capacity, rather than a distortion of the open-circuit voltage characteristic. This is methodologically reassuring, as it confirms that the March-anchored OCV remains shape-representative, and that the fade enters the cell characterization only through real discharge-capacity. The incremental capacity (dQ/dV) analysis refines this picture. The characteristic peaks, associated with the graphite staging transitions and the NMC features between roughly $3.45\ V$ and $3.75\ V$, retain their voltage positions across the time, indicating that the electrode equilibrium potentials, and hence the active-material structure, are essentially unchanged over this time-interval. The peak intensities are only marginally reduced, with the reduction being most visible at the high-voltage (at high SoC) end-of-discharge. The absence of any lateral peak shift argues against pronounced electrode slippage, while the slightly and broadly distributed attenuation of the peaks is consistent with a certain loss of active material (LAM) and/or lithium inventory (LLI).

This loss occurred over roughly two months of active testing. This is consistent with capacity-fade superimposed on a cell that, manufactured in 2009 and tested in 2026, has already accumulated of order fifteen years of calendar life before the campaign began.

Chapter 4

Single Particle Model with electrolyte (SPMe): Electrochemical Model Theory

This chapter frames a general analysis, from basic physical principles of electrochemical cells to specific features of electrochemical models. The first section analyzes the fundamentals of electrochemical cells, reporting the equations useful to describe the inner phenomena of battery cells. The second section focuses on the model adopted for the Thesis, i.e. Single Particle Model with electrolyte (SPMe), explaining the governing principles, the basic assumptions and the set of equations. The last section introduces the model's parametrization, with a general comparison between SPMe and two valid alternatives: DFN model and ECM.

4.1 Electrochemical Battery cell Fundamentals

As explained in 1.2.1, the electrochemical cells rely on the chemical reactions of oxidation-reduction for the flow of electric currents, known as faradaic currents. The electrochemical cells can be classified into two main categories:

- Galvanic cells: they are characterized by spontaneous chemical reactions occurring between the two electrodes, producing an electron flow directed to an external circuit.
- Electrolytic cells: they are characterized by forced chemical reactions occurring between the two electrodes, with imposition of an external voltage source.

In general, automotive batteries are considered both as galvanic cells when they are in discharge-phase, while they act as electrolytic cells when they are in a charge-phase. In general electrochemical cells are referred to secondary batteries, that, by definition, carry out multiple charge/discharge cycles in electric and hybrid vehicles.

Electrochemical fundamentals in battery cells are based on physical and chemical principles involved in the energy conversion process. This could be useful to develop a framework, that of electrochemical models (treated in chapter 3), useful not only for single-cells, but also to evaluate more complex systems from different points of view.

The fundamental governing principles and operations within battery cells basically are: (i) electrochemical thermodynamics, (ii) electrochemical reaction-rates, (iii) electrode kinetics, (iv) mass transport and diffusion. Each one of these mechanisms certainly influences the energy conversion from chemical to electrical energy and vice-versa in an electrochemical cell.

The electrochemical principles, expressed in the following sub-sections, are summarized from the book written by I. Husain (2021) [1].

4.1.1 Electrochemical Thermodynamics

Electrochemical thermodynamics is a fundamental mechanisms that determines the electrical potential difference between the electrode and the electrolyte of an electrochemical cell in the absence of current-flow produced or received by the battery.

Thermodynamics is capable of explaining the mechanism of electrode potential formation at the electrode-level (Open-circuit-potential, OCP), and it establishes the theoretical limits of energy conversion (related to potential of the cell) and global efficiency.

This electrochemical mechanism is based on the two principles of Thermodynamics, in fact from them it assumes its name. Starting from the two Thermodynamic Laws, it is possible to introduce a new concept: Gibbs free-energy.

This form of energy is correlated to two state-variables of a thermodynamic system: enthalpy H, and entropy S.

Therefore, Gibbs free-energy can be calculated from the enthalpy (H) and the entropy (S) variations between the products and the reactants in a chemical reaction as:

$$\Delta G = \Delta H^0 - T \cdot \Delta S^0$$

where:

$$\Delta H^0 = \sum H^0(products) - \sum H^0(reactants)$$

$$\Delta S^0 = \sum S^0(products) - \sum S^0(reactants)$$

These relations are referred to standard-state conditions, meaning: temperature at 25 °C and atmospheric pressure of $1\ atm$.

Gibbs-free energy determines if a chemical reaction is spontaneous or non-spontaneous:

1. $\Delta G < 0$: reaction is spontaneous;
2. $\Delta G > 0$: reaction is non-spontaneous.

Gibbs-free energy is even used to evaluate the maximum thermodynamic conversion efficiency of a galvanic cell, which is given by the ratio of Gibbs free-energy and the total amount of enthalpy change:

$$\eta_{EC} = \frac{\Delta G}{\Delta H} = 1 - \frac{T \cdot \Delta S}{\Delta H}$$

Finally, Gibbs free-energy, released during electrochemical processes of a battery cell, imposes the theoretical limit of the maximum amount of work that a cell is able to do. This work is calculated as the charge transferred per mole under the presence of a voltage, i.e. Open-circuit voltage (OCV) of the cell. Therefore, the relation between Gibbs free-energy and OCV assumes the following form:

$$\Delta G = -n \cdot F \cdot E^0$$

where: $-nF$ is the total transferred-charge, while E^0 is the cell's OCV.

The theoretical upper limit of a certain galvanic cell's OCV can be expressed through the following formula:

$$E^0 = -\frac{\Delta G}{n \cdot F}$$

This theoretical cell potential is never achievable in real conditions, due to various electrochemical phenomena occurring inside the cell, so it is only useful to provide a theoretical limit for the electrical potential of a certain battery cell chemistry.

Another concept is related to single electrode-potential, the so-called OCP (Open-circuit potential), obtained as difference between the electrode and the surrounding-electrolyte. The

electrode potential is always determined with respect to a reference electrode, assumed with null potential (typically hydrogen-electrode), since an absolute potential value cannot be measured. In general, the electrochemical processes contribute to the electrode's potential difference. The resultant potential for the two kinds of energy variation (chemical and electrical ones) is termed electrochemical potential, or simply electric potential.

4.1.2 Electrochemical Reaction-rates: Electrolysis and Faradaic currents

The process of electrolysis is practically the transfer of electrons between an electrode and a chemical species in a solution (e.g., in the electrolyte) with a consequent oxidation or reduction reaction. The flow of electrons generated by redox reactions at the electrodes of the electrochemical cell goes into current-collectors reaching the external circuit. The current in the external circuit is tied to the redox reactions by means of Faraday's law of electrolysis; evidently, there is a relation between charge and current.

In general, the chemical conversion rates are controlled or obtained by the electrical current passing through a given electrode.

Faraday's law of electrolysis establishes the mass-quantity of a certain substance at an electrode transformed into a certain electrical-charge quantity for that electrode. Therefore, the rate of electrolysis process is given by Faraday's law, expressed in terms of electrolyzed moles:

$$x = \frac{Q}{n \cdot F}$$

where: Q is the coulombic electric-charge, nF is the amount of total transferred charge (n is number of released electrons per ion at electrode, F is the Faraday constant), while x is the number of electrolyzed moles.

From common electrical processes, it is known that:

$$i = \frac{dQ}{dt}$$

where: i is properly called, in this case, Faradaic-current.

Combining the two equation, there is a direct relation between reaction-rate and faradaic current:

$$\frac{dx}{dt} = \frac{i}{n \cdot F}$$

where: dx/dt is properly the reaction rate, expressed in mol/s.

In alternative, the reaction-rate could be expressed in $mol/(s \cdot cm^2)$, since electrode reaction processes occur only at the electrode-electrolyte interface; so, the related relation is:

$$\frac{1}{A_s}\frac{dx}{dt} = \frac{i}{n \cdot F \cdot A_s} = \frac{j}{n \cdot F}$$

where: A_s is the interface area electrode-electrolyte, j is the current density in A/cm^2.

In conclusion, the various reaction-rates depend on the mass transfer to the electrodes and to other surface effects, in addition to other mechanism, i.e. electrode kinetics.

4.1.3 Electrode Kinetics

The study of Electrode-kinetics includes electrochemical processes that rule electrolysis or faradaic-currents in an electrochemical cell. Basically, electrode-kinetics is affected by various electrochemical processes, of which the two most common are:

- The electron transfer-rate between electrodes and species in solution (electrolyte) at the electrode surface (seen previously with the introduction of Faraday's law for electrolysis).
- The mass-transport phenomenon of some chemical species from bulk solution to the electrode interface.

Therefore, electrode-kinetics is fundamental to introduce some principles that can establish the terminal-voltage - current relationship, considering a normal redox reaction inside a common electrochemical cell.

In general, the critical cell-potential at which the electrode redox reactions occur is called standard-potential (E^0); it is different depending on the chemical substances in the battery-system. The real electrode potential deviates from the reference standard-potential in all the cases in which there is the flow of an external electrical current, produced or absorbed by the cell. The relationship that ties electric current and chemical reactions is very complicated for an electrochemical-cell, since they are basically heterogeneous processes.

Essentially, the electrode voltage-current relationship can be obtained through consideration of forward and reverse chemical reactions between electrodes and electrolyte. The current can be found by relating reaction-rates to the rate-constants (typical kinetic-constants) and the concentration of reactants.

In a general electrode reaction, the two rate-constants, related to oxidation and reduction, are typically indicated as k_f (forward reaction) and k_r (reverse reaction). These are the proportionality factors which link two quantities: concentration of the species and reaction-rates.

Therefore, the reaction-rates are obtained from the product between rate-constants and related species concentration at the electrode surfaces. Using the previous equation for reaction-rate formulation, a new relationship is established between species concentrations and faradaic currents:

$$k_f \cdot C_O(0,t) = \frac{i_f}{n \cdot F \cdot A_s}$$

$$k_r \cdot C_R(0,t) = \frac{i_r}{n \cdot F \cdot A_s}$$

where: $C_O(0,t)$ is the surface-concentration of species during oxidation process, and $C_R(0,t)$ is the surface-concentration of species during reduction process.

Thus, the net current-flow obtained from a redox reactions at electrodes is simply the difference between forward current and reverse current; thereby, the equation is:

$$i = i_f - i_r = n \cdot F \cdot A_s \cdot [k_f \cdot C_O(0,t) - k_r \cdot C_R(0,t)] \tag{4.1}$$

During chemical reactions at the electrode surfaces, assuming to have a single electron-transfer by chemical species (i.e., $n = 1$), the process is remarkably simplified. Indeed, it is possible to find a relation between rate-constants and electric potential of the cell (across electrode-electrolyte interfaces). In this case (with standard potential E^0), the two quantities k_f and k_r are equivalent, and indicated by using a constant, which is known as the standard rate-constant k^0. This is a crucial parameter of electrochemical model.

Finally, the rate-constants at other electric potentials are obtained as a function of standard rate-constant:

$$k_f = k^0 \cdot e^{(F/RT)\cdot(-\alpha)\cdot(E-E^0)}$$

$$k_r = k^0 \cdot e^{(F/RT)\cdot(1-\alpha)\cdot(E-E^0)}$$

where: α is the so-called charge-transfer coefficient, and E is the electrode potential in different conditions from standard ones.

Inserting these equations in Eq. 4.1 , it is possible to obtain the famous Butler-Volmer equation, a fundamental law of electrode kinetics for electrochemical cells, expressing the complete current-voltage characteristics at the electrode-electrolyte interface. The equation is:

$$i = F \cdot A_s \cdot k^0 \cdot [C_O(0,t) \cdot e^{(F/RT)\cdot(-\alpha)\cdot(E-E^0)} - C_R(0,t) \cdot e^{(F/RT)\cdot(1-\alpha)\cdot(E-E^0)}]$$

The Butler-Volmer equation is capable of describing accurately the electrode kinetics, however it is too complex to be applied in practical electrochemical cell reactions.

An alternative solution, that simplifies Butler-Volmer equation, and considers small-currents, which, as hypothesis, can be neglected, is the Nernst-equation. Nernst-equation is given by:

$$E = E^0 + \frac{R \cdot T}{n \cdot F} \cdot ln \frac{C_O(0,t)}{C_R(0,t)}$$

Another approach useful to estimate the terminal potential is the Tafel equation, which assumes large electric currents for charge or discharge of battery cell. This approximation makes possible that one of two exponential terms in Butler-Volmer equation is essentially negligible. Tafel-equation is given by:

$$E(t) = E^0 + \frac{R \cdot T}{\alpha \cdot n \cdot F} \cdot ln(i_0) - \frac{R \cdot T}{\alpha \cdot n \cdot F} \cdot ln(i(t))$$

where: i_0 is the exchange-current at electrode-electrolyte interface, obtained from equilibrium-conditions.

Both Nernst and Tafel equations can be derived in specific conditions from more general Butler-Volmer equation, that is the basic law of the entire electrode-kinetics treatment.

Overall, the reactant activities at the electrode-electrolyte interface cause the open-circuit voltage E to deviate from the standard-state voltage E^0. This means there is a voltage drop between equilibrium conditions and in presence of electric current flow due to charge-transfer at the electrode-electrolyte interface. This voltage difference is quantified as the activation or charge-transfer polarization overpotential.

4.1.4 Mass Transport and Diffusion

A classical electrochemical cell is composed of basic elements described in detail in the previous section: two porous electrodes immersed in the electrolyte, a separator in the middle, and two current collectors connected to the external circuit. Essentially, electrode reactions and mass transport are two fundamental mechanisms to support continuous electric-current flow through the external circuit; in particular the mass transport is related to the proper transport of ions through the electrolyte and inside the electrode particles.

The dominant process of the mass transport is the diffusion process, that causes the molecules (ions) transfer from a location with higher concentration to another one with lower concentration. Complementary methods for mass transport are convection (which is not present in an electrochemical cell) and migration. Migration is the ions-movement through electrolyte, caused by the influence of an external electric field, in two possible directions: positive-charged ions migrate toward negative electrode, while negative-charged ions migrate toward positive electrode.

Diffusion and migration are two fundamental mechanisms of mass transport inside electrochemical cells, with the first one that is clearly dominant on the second one. Migration can bring the molecules in the same direction of diffusion or in the opposite direction, but it is a secondary process in mass transport, so it can be neglected for a simplified analysis.

Therefore, the mass transport is described perfectly by the two Fick's laws.

Regarding the diffusion process for an active species in an electrochemical cell, the second Fick's law is applied:

$$\frac{\partial C(x,t)}{\partial t} = D \cdot \frac{\partial^2 C(x,t)}{\partial x^2}$$

where: $C(x,t)$ is the active-species concentration (ions), D is the diffusion coefficient (solid-phases or electrolyte) for an electrochemical cell, and x, t are, respectively, space and time variables.

The presence of continuous electric current flow in the external circuit is due to minimum concentration of active species established at the electrode for the redox reactions; it is called C_d. Typically, this concentration is lower than the bulk concentration of electrolyte C_{bulk}. Thus, a linear relationship, derived from Fick's law, between these two quantities is written as:

$$C_d(t) = C_{bulk} - \frac{\delta}{n \cdot F \cdot A_s \cdot D} \cdot i(t)$$

where: δ is the diffusion layer thickness and A_s is again the surface area.

A complication of diffusion mechanism derives from the porous structure of electrodes, used typically in lithium-ion cells, to decrease the activation potential (due to electrode kinetics). Basically, the active species penetrate into the pores of the electrodes to reach the reaction site. In this case, there is an increased surface due to the electrode's pores, and this results in parallel diffusion processes, known as "branched-diffusion process".

The physical behavior related to the branched-diffusion has been shown to follow the pattern given by the constant-phase-element (CPE). It is more appropriate for the description of porous electrodes than the Fick's second law. The fundamental property of a CPE is that the phase of the frequency response (output) is the same for all the frequencies. The CPE's transfer-function is used to represent the branched-diffusion process is given by:

$$H(s) = \frac{C_d(s)}{i(s)} = \frac{K}{s^q} \quad , \quad with\ 0 < q < 1$$

In the case of simple operations for a battery cell, such constant-current discharge, the time response of CPE is easy to be solved:

$$C_d(t) = C_{bulk} - K \cdot i(t)^q$$

In conclusion, from the last CPE analysis, the branched-diffusion process is capable of representing both the energy storage and the internal impedance of the electrochemical cell. Indeed, the energy within a battery is stored or partially distributed inside the electrodes and electrolyte in terms of concentration of active species. Thus, the movement of the active species is controlled, during the cell reactions, by the inherent electrolyte impedance. For this reason, CPE representation is very useful to couple the diffusion process and the internal impedance characterization for an effective description of mass-transport, mainly from an electrical perspective.

In practical cases, in presence of more complicated charge/discharge operations, it is difficult to obtain analytical solution of CPE-modeling, so often numerical solutions are required to solve it.

4.1.5 Complementary aspects of electrochemical fundamentals

In order to complete the treatment of fundamentals for electrochemical battery cells, other complementary physical concepts to the basic previous ones are briefly described; essentially, they are:

1. Electrical double-layer;
2. Ohmic resistance;
3. Concentration polarization.

Electrical Double-layer

The electrical potential difference between the electrode and the electrolyte is produced by the presence of an excess of charges locating at the electrode-electrolyte interface. Therefore, considering the surface of electrode, an excess of charges with a certain polarity must be counter-balanced by a certain amount of charges with opposite polarity in the electrolyte. This phenomenon, as a result of electrostatic field, is the basis for the formation of a structure similar to that of a capacitor; this electrode interface is properly called Electrical Double-layer.

Typically, electrical double layer is a thin layer, with usual thickness around few Angstroms; it is characterized by a strong electrostatic field at the surface, since there is not any dielectric material at the electrode-electrolyte interface.

The main properties of electrical double-layer are: its capacitance, the variations of electric potential and ions concentration within the batteries. From experiments, it is shown that the capacitance behavior of this layer is not linear with electrical field that causes its formation. Often, in the electrochemical models, the electrical double-layers are represented through a non-linear capacitor C_{dl}.

Although at battery level, this physical element in not as important as others, electrical double-layer is the basis for the use of non-faradaic electrochemical devices, termed super-capacitors or ultra-capacitors.

Ohmic Resistance

An important contribution to voltage drop is given by the total internal resistance of the electrochemical cell. A large part of that is due to the migration of active species in the electrolyte. Overall, the lumped electrical resistance is the addition of contributions from: electrode materials, bulk electrolyte, and electrode-electrolyte interface. They all contribute to the effective ohmic voltage drop related to Open-circuit voltage of the cell.

It can be considered the addition of another ohmic term, tied to contact-resistances, formed during operations of charge/discharge; contact-resistances gradually increase during the formation of non-conducting film layers (e.g., Solid electrolyte Interface (SEI) layer), during common cell reactions.

Usually, in order to reduce the effects of ohmic voltage drop due to active-species migration, a secondary electrolyte, known as supporting or inert electrolyte is added inside the cell. The main task of the supporting electrolyte is to increase the ion-conductivity of the cell. In this case, the collateral effects of diffusion or migration substantially decrease with the addition of the supporting electrolyte.

Inert-species Concentration

Generally, in an electrochemical cell, some molecules do not participate in chemical reactions, but they are useful for the conduction of electrons. These chemical species, that are inactive in current-flow formation, come substantially from primary electrolyte or, if present, from supporting electrolyte; practically, they do not never react with electrodes.

Typically, these species behave consistently with electrical field: positive ions accumulate near negative electrode, while negative ions accumulate near positive electrode. The result of this

accumulation or excess of these charged but unreacted particles at the two electrodes causes the formation of an additional electrical field across the cell.

This physical phenomenon is known as part of concentration-polarization. Basically, it is ruled by the Nernst equation applied for this specific case (considering to know the concentration of inert ions):

$$E_c = \frac{R \cdot T}{n \cdot F} \cdot ln \frac{C_{electrode,i}}{C_{bulk,i}}$$

where: $C_{electrode,i}$ and $C_{bulk,i}$ are respectively the concentration of inert ions at electrode and concentration of bulk-solution.

The presence of these inactive species leads partly to another type of voltage drop, summarized inside concentration-polarization phenomenon, affecting the Open-circuit voltage of the cell. Overall, concentration-polarization is mainly tied to the major contribution given by the limitations of mass-transport through electrolyte and inside the solid-phase electrodes of the cell.

4.1.6 Battery cell: Summary of Polarization mechanisms

Lithium-ion battery polarization refers to the deviation between a battery's actual operating voltage and its theoretical equilibrium voltage, during charge or discharge.

In general, when a battery cell is not connected to any load (discharging case) or charger (charging case), its terminal-voltage coincides with the open-circuit voltage (OCV). As described in a previous sub-section, the OCV is a purely thermodynamic quantity, set by the difference between the equilibrium potentials of the positive and negative electrodes, evaluated at their surface stoichiometries: x (or equivalently, θ_n) for anode, and y (or equivalently, θ_p) for cathode; so, the relationship is given by:

$$U_{OCV}(SoC, T) = U_p(\theta_p) - U_n(\theta_n)$$

Cell's OCV weakly depends on temperature, introduced through the entropic term $\partial U_{OCV}/\partial T$ (by Tardy et al. (2023) [29]).

When a current flows through an external circuit, the measured terminal-voltage departs from the OCV. This deviation is termed **Polarization**, seen in various forms before. The corresponding voltage losses are the "over-potentials" (η). Basically, they originate from the finite rates at which charge and mass are transported within the cell and at which the interfacial reactions proceed. So, to summarize, the voltage drops have different causes: internal resistance, ion-transport limitations, and reaction kinetics imbalance within the cell.

Following the macro-homogeneous porous-electrode framework (Doyle et al. (1993) [9], Fuller et al. (1994) [10]), it is common to resolve the total polarization into three contributions of distinct physical origin and characteristic time-scale. In order from fast-to slow time-scale, they are:

1. Ohmic over-potential;
2. Activation over-potential;
3. Concentration over-potential.

Considering a simple cell's discharge, the terminal-voltage is given by:

$$V_{cell}(t) = U_{OCV}(SoC) - [\eta_{ohm} + \eta_{act} + \eta_{conc}] \tag{4.2}$$

Therefore, the three over-potentials cause the decrease of terminal-voltage below OCV. Under cell's charge, the same losses act with revised sign and raise the terminal-voltage above OCV. Overall, battery polarization directly affects energy efficiency, power capability, fast-charging performance, and long-term durability. Now, the three polarization mechanisms are examined at turn below.

Ohmic overpotential

The ohmic over-potential arises from the resistive losses experienced by charge as it is transported through the cell. The main contributions are from: (i) electronic conduction through the solid electrode structure, (ii) ionic conduction through the electrolyte filling the pores of the electrodes and the separator, and (iii) the contact resistances and surface-film (SEI) resistances at the interfaces. Because these mechanisms obey Ohm's law, the ohmic loss is instantaneous and strictly proportional to the applied current; so, basically the relationship is:

$$\eta_{ohm} = I \cdot R_{ohm}$$

where: R_{ohm} is the lumped internal resistance of the cell.

Therefore, this phenomenon is effectively instantaneous, because it appears and vanishes on a sub-millisecond timescale, it is responsible for the immediate voltage step observed at the onset and removal of a current pulse, and for the linear portion of the discharge curve. The internal resistance is temperature-dependent, decreasing as the temperature rises, largely through the Arrhenius-type increase of the electrolyte's ionic conductivity (Hamed et al. (2024) [30]).

Activation overpotential

The activation over-potential η_{act} is the driving force required to sustain the charge-transfer (faradaic) reaction at the electrode/electrolyte interface with a finite current-rate (as seen in sub-section on "Electrode-kinetics"). When the electron transport rate exceeds the electrode reaction-rate barrier, a temporary accumulation of electrons or ions occurs on the electrode surface, leading to a change in electrode potential. Its variation is defined as the deviation of the local interfacial over-potential difference from its equilibrium value; this means that:

$$\eta_{act} = \phi_s - \phi_e - U_{eq}$$

where: ϕ_s and ϕ_e are the solid-phase and electrolyte potentials respectively, while U_{eq} is the local equilibrium potential. The relation between this over-potential and the reaction (in case of intercalation) current-density (j) is derived by the previously cited Butler-Volmer equation (Brosa-Planella et al. (2022) [8] , Ecker et al. (2015) [16] [17]). Thereby, the corresponding equation is

$$j = j_0 \cdot \left[exp\left(\frac{\alpha_a \cdot F}{R \cdot T} \cdot \eta_{act} \right) - exp\left(-\frac{\alpha_c \cdot F}{R \cdot T} \cdot \eta_{act} \right) \right] \tag{4.3}$$

in which: j_0 is the exchange-current density, α_a and α_c are separated charge-transfer coefficients for anodic and cathodic branches (commonly, it is assumed that: $\alpha_a = \alpha_c = \alpha = 0.5$), F is the Faraday constant, R is the universal gas constant, and T is the temperature (in K).

Essentially, the exchange-current density depends on the lithium concentrations available at the reacting interface, considering electrolyte concentration c_e and particle surface concentration $c_{s,surf}$ (this one is relative to maximum lithiation concentration $c_{s,max}$). So, exchange-current density is commonly written as:

$$j_0 = F \cdot k_0 \cdot (c_{s,max} - c_{s,surf})^{\alpha_a} \cdot c_{s,surf}^{\alpha_c} \cdot c_e^{\alpha_a}$$

In the case of symmetric charge-transfer phenomenon, it reduces to:

$$j_0 = F \cdot k_0 \cdot \sqrt{c_e \cdot (c_{s,max} - c_{s,surf} \cdot c_{s,surf})}$$

Two limiting regimes are of practical interest. In case of small over-potentials, the exponentials of the equation may be linearized (with $\alpha_a + \alpha_c = 1$), yielding an ohmic-like response that defines the charge-transfer resistance; that results in:

$$\eta_{act} \simeq \frac{R \cdot T}{F \cdot j_0} \cdot j \quad , \quad R_{ct} = \frac{R \cdot T}{F \cdot j_0 \cdot A_s}$$

where: A_s is the already encountered interfacial active area. This relation was verified by Chen et al. (2020) through small-signal electrochemical-impedance-spectroscopy (EIS).

For large over-potentials, the Tafel equation is recovered, obtaining the following formula to express η_{act}:

$$\eta_{act} \simeq \frac{R \cdot T}{\alpha_a \cdot F} \cdot ln \frac{j}{j_0}$$

Usually, activation phenomenon is influenced by Arrhenius equation, i.e. lower temperatures mean higher activation energies, obtaining more severe polarization.

In conclusion, charge-transfer is fast relative to solid-state diffusion, so the activation overpotential is responsible for the sharp, quasi-exponential voltage drop, immediately following the application of a current (time-scale in the order between microseconds and milliseconds).

Concentration (mass-transport) overpotential

The concentration over-potential (η_{conc}) reflects the limitation imposed by mass-transport (dominated by diffusion). In general, when the interfacial reactions consume (or release) lithium faster than diffusion and/or migration of ions can supply (or remove) it, some concentration gradients develop both in the electrolyte (either across the separator or through the porous electrodes) and within the solid-active particles, where the surface concentration differs from the particle-averaged value.

These gradients displace the lithium concentrations, that enter the equilibrium potential and move the kinetics away from their bulk values; the resulting loss is evaluated through Nernst equation, as:

$$\eta_{conc} \sim \frac{R \cdot T}{F} \cdot ln \frac{c_{s,surf}}{c_{bulk}}$$

The electrolyte's contribution for concentration over-potential follows from the analysis of concentrated-solution transport equations (Doyle et al. (1993) [9]; Ecker et al. (2015) [16] [17]). Considering simplified boundary conditions (uniform salt perturbation in the electrolyte), the electrolyte's over-potential due to concentration takes the following representative lumped form:

$$\eta_{el} = \frac{2 \cdot R \cdot T}{F} \cdot (1 - t_0^+) \cdot ln \left(\frac{c_0 + \Delta c}{c_0 - \Delta c} \right)$$

where: t_0^+ is the cationic transference number, c_0 is the rest salt concentration and Δc is its perturbation under load (applied current).

Governed by the solid-phase and liquid-phase diffusion coefficients, this contribution is the slowest of the three for concentration polarization: it builds up over the diffusion time-scale (seconds to minutes) and relaxes only gradually once the current is interrupted. Indeed, this behavior is studied through the Galvanostatic Intermittent Titration Technique (GITT) and in other relaxation measurements (when current is abruptly brought to zero). This phenomenon grows with the magnitude of the current previously applied and it accumulates toward the end of discharge, where surface depletion of the limiting electrode drives the terminal-voltage steeply toward cut-off and ultimately fixes the deliverable capacity at a given rate (so-called limiting-current behavior).

Terminal-voltage equation

The three over-potentials are distinguished not only by their physical origin but also by their characteristic time-scales: (i) instantaneous - ohmic; (ii) fast - activation; (iii) slow - concentration.

Integrating these over-potential terms, in cases of cell's charge or discharge, a complete equation, suitable for describing every physical aspect, for the cell's terminal-voltage can be obtained. The relation is derived by the following non-linear function ([31]):

$$
\begin{aligned}
V(t) = & \left(U^{+}\left(\frac{c_{ss}^{+}(t)}{c_{s,max}^{+}}\right) - U^{-}\left(\frac{c_{ss}^{-}(t)}{c_{s,max}^{-}}\right)\right) \\
& + \left(\varphi_e^{+}(0^{+},t) - \varphi_e^{-}(0^{-},t)\right) + \left(\eta^{+}(t) - \eta^{-}(t)\right) \\
& + \eta_{shell}^{+}(t) - R_{\Omega}(t)\cdot I(t)
\end{aligned}
$$

where: $U^{\pm}(.)$ represents the Open-circuit potential (OCP) of electrodes, $c_{ss}^{\pm}$ are the solid-state concentrations, $\varphi_e^{\pm}(.)$ is related to the electrolyte potential difference, $\eta^{\pm}$ are the over-potential terms tied to activation and concentration polarizations, η_{shell}^{+} introduces a voltage drop due to battery aging, R_{Ω} is the lumped resistance of the cell.

Finally, the polarization mechanisms affecting the terminal-voltage equation can be effectively described in Figure 4.1.

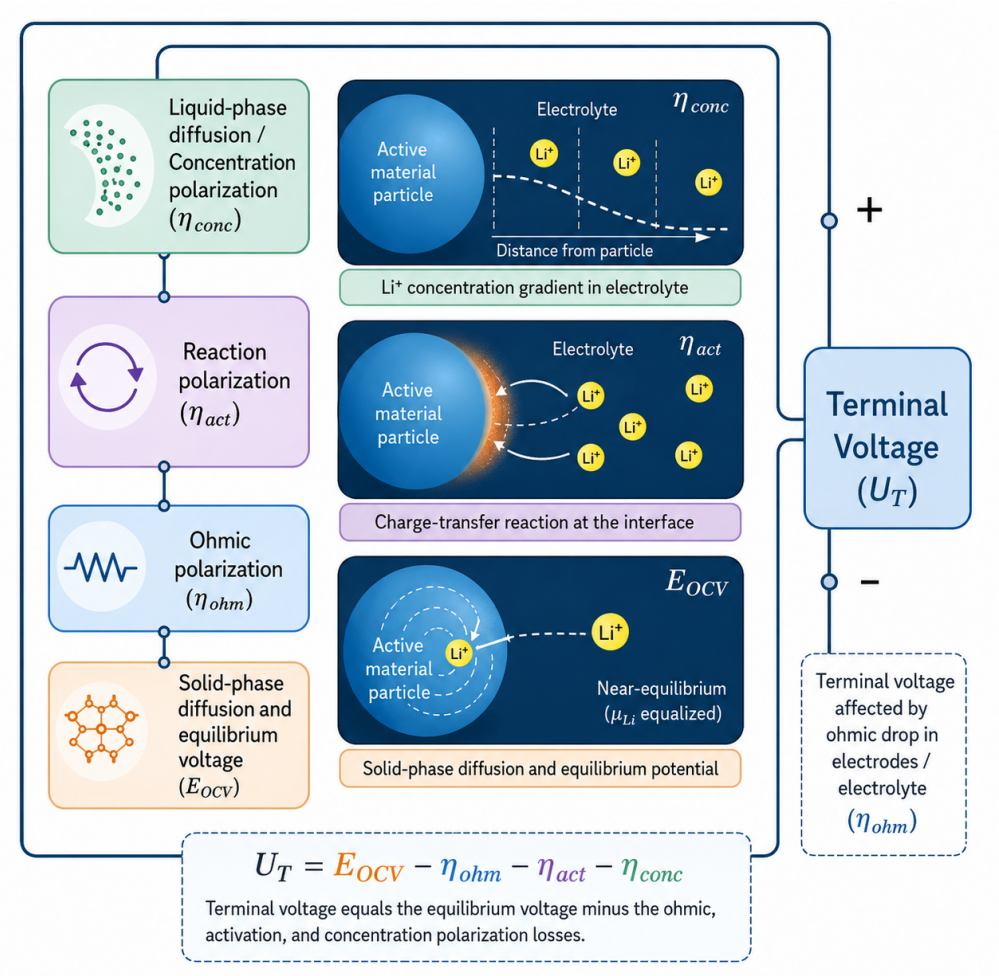


Figure 4.1: Polarization-mechanisms of a common Li-ion battery

4.2 SPMe: Governing Principles and Set of Equations

The SPMe is described by a set of algebraic and partial-differential equations, derived from simplifications applied to DFN/P2D models.

This section provides a general analysis made for basic equations of electrochemical models, associated to the main physical internal mechanisms, analyzed deeply in section 4.1. Therefore, the main laws are then considered as the starting point to develop the equation-framework for Single-Particle Model with electrolyte (SPMe).

4.2.1 Electrochemical modeling principles

The partial-differential equations, involved in a generic electrochemical model (e.g., P2D or SPMe), are based on the physical laws developed in the 1800s and 1900s.

More specifically, the basic modeling principles are presented for a typical Li-ion battery discharge case, showing a clear structure of internal physical mechanisms electrode-by-electrode, through the electrolyte, thereby mapping each process with its governing law.

The fundamental principles of electrochemical models are:

- **Current Collectors**: Electron Transport $\rightarrow$ Ohm's law
- **Negative Electrode**:
  1. Solid-phase Diffusion of lithium $\rightarrow$ Second Fick's Law
  2. Lithium Oxidation (loss of electrons) $\rightarrow$ Butler-Volmer Equation
- **Negative Electrode / Electrolyte interface**: Li^+ Solvation (Not represented by a specific equation; lumped into the interfacial Butler-Volmer kinetics)
- **Electrolyte**: Li^+ Transport $\rightarrow$ Concentrated Solution Theory - Stefan-Maxwell Equation
- **Electrolyte / Positive Electrode interface**: Li^+ De-Solvation (Not represented by a specific equation; lumped into the interfacial Butler-Volmer kinetics)
- **Positive Electrode**:
  1. Lithium Reduction (acquisition of electrons) $\rightarrow$ Butler-Volmer Equation
  2. Solid-phase Diffusion of lithium $\rightarrow$ Second Fick's Law

This set of equations is summarized considering the battery cell's components during a common discharge: external circuit, negative or positive electrode's particles, electrode-electrolyte interface, electrolyte. The basic principles are represented by: Ohm's law, second Fick's law, Stefan-Maxwell equation and Butler-Volmer equation.

It is worth noticing that the previous equations can depend on several variables in classical electrochemical models; they will be illustrated in detail for an SPMe in the following sub-section.

4.2.2 SPMe: Set of equations

The SPMe framework is based on the work made by Marquis et al.(2019) [11], and summarized by Brosa-Planella et al. (2022) [8].

Marquis et al. (2019) started from the knowledge of P2D models. They basically use the P2D equations to obtain, through asymptotic derivation methods, a corrected form of SPM, i.e. SPMe, that accounts for integration of the electrolyte behavior inside the basic equation-set. The main

purpose of this work was to develop a more accurate extension of SPM models, gaining additional accuracy and range of applicability over other existing models, whereas maintaining a similar degree of computational complexity. This reduction is realized in terms of memory requirements and computational time, with several application in the fields of BMS, simplified parameter estimations and optimizations. More specifically, by adding a single partial-differential equation (PDE) and by applying an algebraic correction to the terminal-voltage equation, due to non-uniform effects in the electrolyte, the accuracy of predictions for an SPMe greatly improves with respect to simple SPM.

Richardson et al. (2020) [12] presented a reliable alternative in the definition of the SPMe framework. More precisely, they focused on the systematic derivation and validation of a Single Particle Model, starting from DFN model, considering, as basic assumption, the electrodes composed of uniformly sized spherical particles. The adopted procedure was anchored on a specific asymptotic method, based on the disparity between the thermodynamic voltage and the one resulting from the characteristic change in overpotential during the lithiation or de-lithiation. After the comparison between SPM and DFN model, the researchers implemented some correction term, tied to the spatial non-uniformities inside the electrolyte, motivated by the clear discrepancies between the two model categories. The obtained cSPM (corrected Single Particle Model), or equivalently SPMe, shows a model accuracy which is significantly improved over that of SPM. Finally, they provided different validations of the obtained model, using mainly NMC or LFP cathode chemistries of some Li-ion batteries, as real case-studies. They outlined that ease of SPMe simulations, in terms of computational times and global effort, is a good feature for applications such as the Battery-Management-Systems (BMS), optimal cell design, and for parameter estimation studies.

Therefore, the following set of equations is considered the basis of SPMe modeling theory. SPMe, as expressed in section 2.1.3, is a one-dimensional model in space.

Overall, the SPMe consists of two independent linear PDE problems that describe the concentration of lithium in the negative and positive particles, and an independent linear PDE problem which describes the concentration of lithium-ions in the three regions of the electrolyte. The Butler-Volmer and terminal-voltage equations are simple algebraic expressions. Since all the three PDE problems are independent, the SPMe framework has naturally a parallel structure; the linearity of the PDEs is also an advantage for the application of numerical methods or determination of simpler analytic solutions (as stated by Marquis et al. (2019) [11]).

Electrode's Particles equations The basic physical principles of this equation-set essentially are: mass and charge conservation in solid-phase materials.

In SPMe modeling, it is assumed that the particles lithiate and de-lithiate uniformly, thereby considering to have a single representative particle for each electrode. The electrode's particles equations (or solid-state related equations) are based on Fick's laws, accompanied from specific boundary conditions.

$$\frac{\partial c_k}{\partial t} = \frac{1}{r^2} \cdot \frac{\partial}{\partial r} \left(r^2 \cdot D_k(c_k) \cdot \frac{\partial c_k}{\partial r} \right) \quad , \quad in\ 0 < r < R_k$$

$$\frac{\partial c_k}{\partial r} = 0 \quad , \quad at\ r = 0$$

$$-D_k(c_k) \cdot \frac{\partial c_k}{\partial r} = \frac{j_k}{F \cdot a_k} \quad , \quad at\ r = R_k$$

$$c_k = c_{k,0} \quad , \quad at\ t = 0$$

$$j_n = \frac{i_{app}(t)}{L_n} \quad , \quad j_p = -\frac{i_{app}(t)}{L_p}$$

(with subscript $k \in (n, p)$ indicating negative (n) and positive (p) electrodes);

where: c_k is the solid-state lithium concentration, D_k is the particle diffusivity coefficient, R_k is the electrode's particle radius ($R_{p,p}$ and $R_{p,n}$ for positive and negative electrode, respectively), j_k is the interfacial (electrode-electrolyte) current density, a_k is the interfacial (electrode-electrolyte) surface-area per unit of volume, $i_{app}(t)$ is the applied external current, L_n and L_p are electrode's thicknesses.

These equations are typically solved in a numerical way, although in the cases for which the diffusivity D_k is constant, it is possible to solve them analytically.

Electrolyte equations The physical laws adopted as a basis for the electrolyte equations are: mass and charge conservation inside the electrolyte.

The SPMe accounts for electrolyte dynamic effects, thereby it includes the equation to govern the lithium-ions transport inside the electrolyte. It is based on Nernst-Planck equation, with specific boundary conditions. It is worth noticing that only this equation is developed through space, not using the radial coordinate, rather the thickness coordinate (x).

$$\varepsilon(x) \cdot \frac{\partial c_e}{\partial t} = \frac{\partial}{\partial x}\left(D_e(c_e) \cdot B(x) \cdot \frac{\partial c_e}{\partial x} - \frac{t_0^+}{F} \cdot i_e\right) + \frac{a(x) \cdot j(x,t)}{F} \quad , \quad in\ 0 < x < L$$

$$\frac{\partial c_e}{\partial x} = 0 \quad , \quad at\ x = 0, L$$

$$c_e = c_{e,o} \quad , \quad at\ t = 0$$

with:

$$\varepsilon(x) = \begin{cases} \varepsilon_n, & in\ 0 \le x \le L_n \\ \varepsilon_s, & in\ L_n < x < L - L_p \\ \varepsilon_p, & in\ L - L_p \le x \le L \end{cases}$$

$$a(x) = \begin{cases} a_n, & in\ 0 \le x \le L_n \\ a_s, & in\ L_n < x < L - L_p \\ a_p, & in\ L - L_p \le x \le L \end{cases}$$

$$i_e(x,t) = \begin{cases} (i_{app}(t)/L_n) \cdot x, & in\ 0 \le x \le L_n \\ i_{app}(t), & in\ L_n < x < L - L_p \\ (i_{app}(t)/L_p) \cdot (L - x), & in\ L - L_p \le x \le L \end{cases}$$

$$B(x) = \begin{cases} B_n, & in\ 0 \le x \le L_n \\ B_s, & in\ L_n < x < L - L_p \\ B_p, & in\ L - L_p \le x \le L \end{cases}$$

$$j(x,t) = \begin{cases} j_n(t), & in\ 0 \le x \le L_n \\ 0, & in\ L_n < x < L - L_p \\ j_p(t), & in\ L - L_p \le x \le L \end{cases}$$

where: $\varepsilon(x)$ is the electrode porosity, c_e is the lithium-ions concentration in electrolyte, D_e is the electrolyte diffusivity coefficient, $B(x)$ is the Bruggeman transport efficiency, t_0^+ is the transference number, i_e is the average current density, a_x is the interfacial (electrode-electrolyte) surface-area per unit of volume , $j(x,t)$ is the exchange-current density, and L is the total cell's thickness.

The solution for $c_e(x,t)$ can be used to calculate the electrolyte potential φ_e, through the integration of the following expression, which represents the second electrolyte equation:

$$i_e(x,t) = \sigma_e(c_e) \cdot B(x) \cdot \left(-\frac{\partial \varphi_e}{\partial x} + \frac{2(R \cdot T)}{F} \cdot (1 - t_0^+) \cdot \frac{1}{c_e} \cdot \frac{\partial c_e}{\partial x} \right) \quad , \quad in\ 0 < x < L$$

where: $\sigma_e(c_e)$ (or equivalently $\kappa(c_e)$) is the electrolyte conductivity.

Electrode's kinetics The SPMe uses a simplified version of Butler-Volmer equation to express the electrode's kinetics.

$$j_{k0}(x,t) = F \cdot k_k \cdot \sqrt{\frac{c_e(x,t)}{c_{e,0}} \cdot \frac{c_k(r,t)}{c_k^{max}} \cdot \left(1 - \frac{c_k(r,t)}{c_k^{max}}\right)}\Bigg|_{r=R_k}$$

where: $j_{k,0}(x,t)$ is the exchange-current density of electrodes, $k_{0,k}$ is the electrode's reaction-rate constant ($k_{0,p}$ for positive electrode and $k_{0,n}$ for negative electrode), $c_e(x,t)$ is Li-ions concentration in electrolyte, whereas $c_k(r,t)$ is the lithium concentration in electrodes.

Terminal-voltage equation The terminal-voltage equation is expressed using an algebraic equation, as already seen in sub-section 4.1.6.

$$V(t) = U_{eq} - \eta_r - \eta_c - \Delta\varphi_s - \Delta\varphi_e$$

where: U_{eq} is the open-circuit voltage (OCV) of the cell, η_r is the potential drop due to activation overpotential, η_c is the potential drop due to concentration overpotential, $\Delta\varphi_s$ is the voltage drop due to ohmic losses in the two electrodes, and $\Delta\varphi_e$ is the voltage drop due to ohmic losses inside electrolyte.

During the cell discharge (with $i_{app} > 0$), considering a flow of Li-ions from the negative electrode to the positive one, the physical quantities η_r, η_c, $\Delta\varphi_s$, $\Delta\varphi_e$ are all positive, obtaining a reduction in the cell's OCV, which results from these different loss mechanisms. During the cell charge (with $i_{app} < 0$), having an inverse flow of Li-ions from the positive electrode to the negative one, the same physical quantities (η_r, η_c, $\Delta\varphi_s$, and $\Delta\varphi_e$) have the opposite sign, resulting in an extra-potential, added to cell's OCV, in order to overcome the internal resistances of cell.

4.3 SPMe Parametrization and Comparison with alternative models

This section introduces the model's parametrization, properly developed in the chapter 5. The experimental tests, described in section 3.3, produce data about: voltage, current and temperature. The tests also indicates the values of capacity (integral of current in the time), energy and power. However, a physics-based model requires a complex set of parameters, regarding geometric, thermodynamic, transport and kinetic aspects. The purpose pf this section is to illustrate a high-level physics-grounded Parametrization for SPMe.

In general, three modeling types can be adopted to simulate, in an increasing level of accuracy, the battery behavior; in order, they are:

- ECM models;
- SPM/SPMe models (Thesis case);
- DFN models.

In the following sub-sections (based on the IonWorks article [32]), only the Thesis case-study (SPMe) is analyzed, considering its main features for proper parametrization, and exposing a brief comparison with suitable alternatives (ECM and DFN model) for battery modeling. The treatment of SPMe parameterization, compared to simpler alternatives (e.g. ECM), or more complex one (e.g. DFN model) highlights the robustness of a reliable modeling, realized for the battery Kokam cell, while retaining a good trade-off between complexity and accuracy.

4.3.1 SPMe: Lumped physics-based model

Lumped physics-based models can capture some physical aspects of the cell, such as solid-state diffusion (transport properties) and intercalation kinetics (kinetic properties) in each electrode. However, they simplify the electrolyte dynamics (SPM does not consider it at all) and assume uniformity through electrodes thickness (no spatial variation, with single representative particles for each electrode).

The main advantage of the lumped physics-based models is related to a more approximated Parametrization procedure: they sit between ECMs and full-physics models. They can simulate battery behavior, regarding electrode-specific SoC, over-potentials, and internal heat generation, without the need of full teardown data of the battery. That does not mean they are not reliable: they work very well under defined conditions or limitations. Anyway, it is important to consider the limitations: they are based on fitted full-cell OCV curves, they may not resolve electrolyte gradients or electrode heterogeneity (only one particle for each electrode), and they can miss local specific effects, such as lithium plating or electrolyte depletion.

Although P2D models offer potentially greater accuracy, they can describe similar physical insights of a simpler lumped-physics model, at a higher computational costs and with the common requirement of a more detailed parametrization.

It is important to underline that lumped physics-models fits almost the same quantity of individual parameters with respect to other models, but adopting a different approach.

According to F. Brosa-Planella et al. (2022) [8], SPM complexity is similar to that of ECM, in terms of computational cost, although SPM requires 17 parameters, 8 for each electrode plus the battery temperature.

The SPMe, adopted in the Thesis, that completes the SPM framework, describing the electrolyte dynamics, improved the electrochemical model accuracy and performance. Considering always the study of Brosa-Planella et al. (2022), SPMe complexity is slightly higher than the one of SPM, including in its framework (seen in detail in section 4.2), two PDEs for electrode's particles, one additional PDE for the electrolyte, and two algebraic equations (simplified Butler-Volmer equation and terminal-voltage equation). However, the three PDEs are spatially one-dimensional, thereby they are decoupled and can be solved very efficiently. Overall, SPMe requires 30 parameters (apart from physical constants R and F, and the input parameters, such as the current $i(t)$): 9 for each electrode, 11 for electrolyte and separator, and the battery temperature.

SPMe model shows a good agreement with results from DFN model, for a wide range of operating conditions, thereby it can be used for many practical applications. Among the main limitations, SPMe does not capture the spatial distribution of lithium concentration across each electrode, due to its physical interpretation. Another important weakness of SPMe is tied to higher

current-rates, for which there is the risk of electrolyte depletion (usually around 2C). In these scenarios, the agreement between SPMe and DFN model breaks down.

SPMe lumped parameters

As explained before, SPMe is very convenient for different scenarios, but taking into account its known limitations.

In terms of parametrization, the real difference between P2D model and SPMe lies in the fact that the parameters cannot be identified as spatially-resolved (x-thickness dependent) quantities; rather, they are obtained as lumped quantities. Indeed, full-cell voltage and current data cannot distinguish the particle radii or the solid-phase diffusivity coefficients independently for each electrode. In addition, these quantities are strictly correlated through the diffusion phenomena (shown mainly in GITT tests); at full-cell level, the diffusion response time-scale depends on the ratio (as seen in sub-section 3.2.1):

$$\tau_D = \frac{R_p^2}{D_s} \ [s] \tag{4.4}$$

(this further complicates their individual estimation).

In the same way, electrode area A, coating thickness L, active-material volume fraction ε_s, and maximum lithium concentration $c_{s,max}$, for each electrode are not identifiable separately as well as in the previous case.

The only certain quantity to be evaluated is the lumped electrode capacity from slow-rates tests; the total capacity is calculated as:

$$Q = \frac{A \cdot L \cdot \varepsilon_s \cdot c_{s,max} \cdot F}{3600} \ [Ah] \tag{4.5}$$

In general, an SPMe does not necessarily require the cell teardown. Indeed, SPM and SPMe parametrization procedures typically need full-cell OCV data, multi-rate capability tests, GITT tests and/or HPPC tests to extract the lumped diffusion time-scales and reaction rate groups. As seen before, SPMe is a more complete model, because, it can integrate an analogous lumped treatment of electrolyte transport-related parameters, so it usually requires richer fitting, while remaining feasible exploiting only full-cell experiments.

4.3.2 Effective parametrization of a battery model

The main purpose of parametrization is to build a complete and plausible set of parameters for a chosen model class. The primary source is curve fitting, but also literature references or empirical tuning (based on physics) can be seen as other methods to extract several information for the battery. Further details about SPMe parameterization will be provided in section 5.4.

Therefore, the difficulty of the work includes: (i) selecting of which parameters are suitable for being fitted or fixed, (ii) choosing appropriate test data (Pseudo-OCV or GITT or others), (iii) applying physical constraints, and (iv) validating the resulting set of parameters against independent experiments. Another fundamental aspect to be taken into consideration is the following: different parameter combinations can reproduce a similar output, so severe constraints to parametrization, anchored to documented physics, have to be applied during the parametrization workflow. Generally, P2D models can have the problem of identifiability for this reason, so it is always important to check if the obtained values for certain parameters are physically possible or not. In conclusion, the main objective of battery parametrization is to construct a reliable or plausible physical parameter-set, identifiable from the available data of the tests and validated in other experimental conditions (outside the fitting set of tests).

SPMe Parametrization

The level of Parametrization for SPMe is decidedly a good compromise between optimal fidelity and experimental campaign costs. More specifically, cell's teardown and half-cell data are replaced with a simpler full-cell OCV characterization, while all transport parameters can be fitted as lumped groups or simplified functions. Other parameters are simple scalar values, with no-dependence on spatial position (through the thickness direction x of the cell). In the following Table 4.1, a basic workflow for Parametrization of a typical SPMe is reported.

Parametrization Step	**Estimated parameters for SPMe**
1. Full-cell OCV curve	Electrodes OCP curves; Lumped electrode capacities ($Q = (A \cdot L \cdot \varepsilon_s \cdot c_{s,max} \cdot F)/3600$); Initial concentrations/stoichiometries
2. Full-cell rate capability and pulse test (voltage)	Lumped solid-state diffusion time-scales ($\tau = R_p^2/D_s$ (functions of T & SoC))
3. Full-cell rate capability and pulse test (temperature)	Thermal capacity of the cell; Heat transfer coefficients

Table 4.1: SPMe: general Parametrization workflow

SPMe models require a basic experimental campaign, such as the one described in section 3.3. In more detail, the trade-off is already presented in the Step 1; it is evident that lumped models are based on the knowledge of global full-cell OCV data and lumped capacity, rather than the single measurements of A, L, ε_s, $c_{s,max}$, in an independent way. This procedure is more direct, fast, and it also means that the identifiability of the parameters depends more on the quality of fitting. Then, the ability to recover the values of fundamental parameters, such as solid-state diffusion lumped time-scale τ_D or global lumped capacity of the cell Q_{cell} is excellent adopting this modeling type. The several full-cell experiments, without the need of half-cell or three-electrode configurations is an advantage, with no pretense of obtaining quantities that data cannot constrain.

The thermal sub-model can be activated for temperature dependence of different parameters (common point with DFN model). Dynamic voltage tests are essential to extract some properties of the cell and even for validation of the final model. Finally, additional operations, such as teardown of the cell, electrodes OCP curves, specific tests with half-cell configurations can be useful to resolve some ambiguities inside the parametrization, that data alone cannot fix.

4.3.3 PyBaMM models: comparison among the classes

PyBaMM implements different model classes for lithium-ion cells, and its documentation provides comparison notes and several parametrization workflow for each class.

PyBaMM model	Model class	Level of complexity	Required main Steps
ECM	Equivalent circuit	Low	Pulse fitting, RC time constants
SPM	Lumped physics-based	Moderate	Full-cell OCV, rate capability, pulse data
SPMe	Lumped physics-based	Moderate to High	SPM + electrolyte transport
DFN	Full-physics-based	High	Half-cell configuration, EIS test, teardown of cell

Table 4.2: Available model classes in PyBaMM

Table 4.2 summarizes the four possibilities of model classes exist in PyBaMM. The level of complexity increases remarkably from ECM models to DFN models.

In general, PybaMM provides internal parameter-sets from literature (inside "Parameter-values" objects), extraction files support, final model's plots and parameters sensitivity functions to be called. It does not provide a substantial parameter estimation workflow, so selection of a certain optimizer (global and/or local), identifiability checks, and possible validation loops still remain a work of the user.

It is important to consider battery degradation modeling: parameter-sets evolve over a cell's lifetime, as analyzed in section 3.4. The capacity-fade needs to track how parameters shift with aging, and each aging state needs its own parameter set tied to specific characterization data.

Chapter 5

SPMe: Model Parametrization

This chapter contains the core of the Thesis: it develops the chain for the entire SPMe parameterization.

The first section classifies the suitable parameter-sets as starting point for subsequent parametrization, choosing "Mohtat2020" over other two valid alternatives integrated in PyBaMM. The second section introduces the required PyBaMM model's parameters, distinguishing them into two categories: scalar and function parameters. The third extensive section describes the Sensitivity-analysis from two points of view. Indeed, a first general introduction with the major literature works is made, illustrating results and procedures; at the same time, a personal DoE-based sensitivity analysis, carried out as a premise of parameterization, is illustrated for each parameter-group.

The fourth section introduces the effective Parametrization procedure used to build a complete SPMe, summarizing the different steps and relative sub-steps, aimed at calibrating the model's parameters, through several methods for estimation/identification. The fifth section shows all the results achieved, step-by-step, following the order established by the parametrization workflow. Finally, the sixth section collects the tuned parameters into the canonical set, and the seventh section adds some details about the addition of further thermal modeling.

More specifically, the adopted approach, made for the calibration/tuning of the entire parameter-set, is termed general parametrization strategy: it refers to a classic procedure in which only literature and full-cell experimental data were used to extract meaningful parameters for the model.

5.1 Suitable PyBaMM parameter-sets for Kokam cell

Even if it is a simplified Physics-based model, more specifically belonging to lumped-physics category, Single-Particle Model with electrolyte (SPMe) requires anyway a large set of geometric, thermodynamic, transport and kinetic parameters, the majority of which cannot be obtained from a manufacturer data-sheet or simple full-cell measurements. Because these parameters encode the specific microstructure and chemistry of the cell under study, they are not freely transferable between cells of different design: the open-circuit potential (OCP) functions, the solid-phase diffusivities, the electrode stoichiometric windows and the reaction-rate constants vary markedly with the electrode chemistry and even with the manufacturing route.

For this reason, the parametrization of a new cell is most robustly approached not by fitting all the parameters from scratch, which is an ill-posed problem, given their number and mutual correlation, but by adopting consistent literature parameter-set as baseline. Such a parameter-set supplies physically plausible initial values and, equally important, the functional forms of the material properties; then, they are progressively re-identified against the cell's own experimental data. The choice of the reference set is consequential: a set drawn from a cell of similar chemistry

and architecture minimizes the magnitude of corrections that the subsequent parameter calibration procedure must apply, and it reduces the risk of converging onto a physically inconsistent combination of parameters, that nevertheless can reproduce a reasonable terminal-voltage. It is a well-documented common error, since shifting strongly correlated parameters against one another can yield the same external response, while substantially altering the inferred internal state of the cell (from Ecker et al. (2015) [16] [17]).

Three candidates parameter-sets, all distributed as default parameter-sets within the PyBaMM frame-work, were assessed during the Thesis development, before the final selection was made:

1. "Chen2020";
2. "Ecker2015";
3. "Mohtat2020".

Chen2020 set originates from the teardown-based parametrization of a commercial LG-M50 21700 cylindrical cell, reported by Chen et al. (2020) [4]. The cell has a High-Energy design, containing a nickel-rich NMC811 positive electrode and a bi-component negative electrode composed of approximately $90\ wt\%$ graphite and $10\ wt\%$ silicon oxide (SiO_x). The 35 parameters-set was obtained through an extensive experimental campaign. More precisely, different tests were performed, such as FIB-SEM tomography, ICP-OES, EDS, GITT and EIS with "half-cell" configurations. Then, the parameter-set was validated against constant-current discharge (at C/2, 1C, and 1.5C) within a Pseudo-two-dimensional (P2D) model. Although comprehensive, the parameter-set presents two important features, that limit its suitability as a baseline for the cell studied here: the cylindrical format, and, more importantly, the silicon-bearing negative electrode, whose pronounced volumetric expansion and dual (graphite/SiO_x) transport behavior, that the authors themselves were unable to represent with single effective parameters; indeed, the graphite diffusivity was ultimately being tuned independently at each C-rate. Furthermore, as the exact electrolyte of the commercial-cell was unknown, standard electrolyte properties were adopted from literature, introducing a further source of uncertainty.

Ecker2015 set parametrization is reported across a two-part publication: Part I (Ecker et al. (2015a) [16]) details the experimental determination of the parameters, while Part II (Ecker et al. (2015b) [17]) presents their integration into a physical-chemical model and its validation. The study characterizes a commercial $7.5\ Ah$ high-energy pouch cell, manufactured by Kokam (SLPB75106100). The entire parametrization was performed through some characterization tests, such as: cell teardown, mercury porosimetry, and electrochemical measurements on laboratory-made coin-cells. At first sight, its parameter-set seems the most natural candidate of the three, since cell shares both the pouch format and the manufacturer of the cell investigated in this Thesis. However, ICP analysis of the positive electrode revealed a manganese-free, cobalt-rich oxide ($Li(Ni_{0.4}Co_{0.6})O_2$) cathode, rather than a typical NMC composition. Therefore, positive electrode thermodynamics and kinetics encoded by the set are not representative of a typical NMC chemistry. In addition, the model validation reported in the article (Part II) of that work required several non-negligible adjustments to the as-measured parameters, including the negative-electrode particle radius, the anode exchange-current density, the activation energy of solid-state diffusion, and the SEI-related capacity loss. All that indicates that the directly measured set was not self-consistent for predictive simulations without empirical corrections.

Mohtat2020 set, reported by Mohtat et al. (2020) [13], describes a $5.0\ Ah$ graphite/NMC pouch cell, fabricated at University of Michigan Battery-Laboratory, with operating voltage range of $(3.0 - 4.2)\ V$. The cell pairs a conventional NMC positive electrode with a pure graphite negative electrode, and the parameter-set was generated specifically in the context of reduced-order modeling.

Indeed, the work develops a multi-particle extension of the SPMe (i.e., electrochemical-mechanical(-thermal) coupling model, or MPMe), that extends the SPMe frame-work, and it is derived using a particular methodology (the single-particle asymptotic method, developed by Marquis et al. (2019) [11]). Accordingly, the parameter-set provides analytic half-cell OCP functions for both electrodes, explicitly identified electrode stoichiometric windows, single effective solid-phase diffusivities and per-electrode reaction-rate constants; that is precisely the basic parameter identification structure, required by an SPMe. The cell was additionally characterized and validated across a various range of practical charging rates up to 2C.

The main features of the three candidate parameter-sets for the Thesis parametrization are summarized in Table 5.1.

Feature	**Chen2020**	**Ecker2015**	**Mohtat2020**
Source cell	LG-M50 (commercial)	Kokam SLPB75106100 (commercial)	UMBL graphite/NMC (laboratory)
Format	21700 cylindrical	Pouch	Pouch
Rated capacity	$5\ Ah$	$7.5\ Ah$	$5\ Ah$
Positive-electrode chemistry	NMC811 (Ni-rich)	$Li(Ni_{0.4}Co_{0.6})O_2$ (Mn-free)	NMC532
Negative-electrode chemistry	Graphite + SiO_x ($90/10\ wt\%$)	Graphite	Graphite
Voltage window	$(2.5 - 4.2)\ V$	$(2.7 - 4.2)\ V$	$(3.0 - 4.2)\ V$
Cell Design	High-Energy	High-Energy	NMC/graphite practical/fast charging
Target model	P2D	P2D or SPMe	SPMe (with MPMe extension)
Electrolyte composition	$1M\ LiPF_6$, $EC : EMC = 3 : 7$	$1M\ LiPF_6$, $EC : EMC = 1 : 1$	$1M\ LiPF_6$, $EC : EMC = 3 : 7$

Table 5.1: Summary of the three most suitable parameter-sets for parametrization

An important note: the common electrolytes selected for the three cases are composed of the salt $LiPF_6$, and the solvent (in different ratios) Ethylene-carbonate (EC) / Ethyl-methyl-carbonate (EMC).

5.1.1 Final parameter-set selection

Mohtat2020 parameter-set was ultimately selected as the reference for this Thesis, due to several converging reasons.

First, the chemistry is the most important factor to be matched: the target cell is an NMC/graphite cell, and "Mohtat2020" is the only candidate whose positive electrode is a genuine NMC, and

whose negative electrode is pure graphite, as the Kokam case-study. Ecker's parameter-set differs in the cathode (manganese-free, cobalt-rich oxide), while Chen's parameter-set differs in the anode composition (silicon-bearing). Since the parameters that most strongly influence the simulated voltage response (i.e., the OCP curves, the stoichiometric windows and the solid-phase diffusivities) are governed by the electrode chemistry (a fact reflected in the sensitivity-driven tuning choices of both Chen et al. (2020) [4], and Ecker et al. (2015) [16] [17], who identified the solid-phase diffusivity as among the most influential parameters), chemical proximity is the dominant selection criterion.

Second, even the cell architecture must be considered: "Mohtat2020", exactly like the cell under study, is a pouch cell, so that the geometric parameters can be scaled from the total capacity of $5\ Ah$ baseline towards $11\ Ah$ of the target cell, whereas the cylindrical geometry of "Chen2020" would require a less direct transformation. However, from this point of view, Ecker's cell is a Kokam pouch cell, so that was its most favorable point for its possible selection as baseline.

Third, the model compatibility is also crucial: Mohtat's parameters-set was curated for an SPMe-class model, and it maps onto its state-variables. Meanwhile, "Chen2020" and "Ecker2015" sets target the full P2D models and, as both source publications acknowledge, they required appreciable empirical tuning, even to reproduce constant-current discharge experiments.

Fourth, the pure-graphite negative electrode composition of "Mohtat2020" is described by a well-resolved OCP, exhibiting the characteristic staging plateaus, and by a graphite-specific diffusivity, thereby avoiding the additional, poorly constrained parameters that a silicon-containing anode would introduce (e.g. Chen's cell).

Finally, Mohtat's cell was characterized in a rate-regime that is consistent with the high-power applications, targeted for the Thesis cell, rather than in the low-rate regime, which is typical of the two other high-energy reference cells.

For these detailed reasons, "Mohtat2020" is adopted as the baseline parameter-set, and it is a basic assumption of the entire model's parametrization. However, it is emphasized that this set is not employed as unchanged: it provides the functional forms and the physically consistent initial-values, from which the cell-specific parametrization departs, as it will be described in the following chapter; so, some individual parameters are going to be progressively re-identified against experimental data, measured on the Kokam $11\ Ah$ cell.

In terms of modeling, the key point is that the cathode / anode pair fixes the open-circuit voltage functions, the usable stoichiometric windows and the theoretical capacity balance.

Moreover, regarding the battery analyzed in this Master Thesis, the Kokam High-Power pouch cell, with code SLPB55205130H, is an NMC/graphite system, which is consistent with a general automotive trend toward layered-oxide cathodes combined with graphite-based anodes. Probably the chemistry type could be NMC111 or NMC532, considering that the cell is manufactured in 2009, and officially reported in Kokam documents since 2012. This information is very important to be considered in the parametrization of the following electrochemical modeling activity, underling that chemistry is the most influential factor for the cell's properties.

5.2 SPMe model Parameters in PyBaMM

In this Master Thesis, as specified before, PyBaMM tool was exploited to build an SPMe model. Therefore, it is important to classify the parameters, that represent the basis of the model itself. Indeed, they are used inside the model equations (already implemented in PyBaMM), to obtain a

valid output.

Considering the official reference of PyBaMM ([15]), a complete list of parameters is split inside two tables: Table 5.2 and Table 5.3. In more detail, the first one is related only to purely scalar parameters, while the second one is related to function-parameters that depend on one or more free variables. In each Table, all the SPMe model parameters in PyBaMM are listed, the parameter category (according to Ecker's studies) is specified, and for scalar parameters and some function-parameter (assumed to be constant) their corresponding values from Mohtat's parameter-set are reported, while only for function-parameters their free-variables dependence is explicitly described.

Scalar Parameter name	**Parameter category**	**"Mohtat2020" parameter-set value**
Nominal cell capacity [A·h]	Geometrical	5.0
Upper cut-off voltage [V]	Electrical	4.2
Lower cut-off voltage [V]	Electrical	2.8
Electrode height [m]	Geometrical	1.0
Electrode width [m]	Geometrical	0.205
Number of electrodes connected in parallel to make a cell [-]	Geometrical	1.0
Number of cells connected in series to make a battery	Geometrical	1.0
Positive electrode thickness [m]	Geometrical	$6.7 \cdot 10^{-5}$
Negative electrode thickness [m]	Geometrical	$6.2 \cdot 10^{-5}$
Separator thickness	Geometrical	$1.2 \cdot 10^{-5}$
Maximum concentration in positive electrode [mol/m^3]	Material properties	35380
Maximum concentration in negative electrode [mol/m^3]	Material properties	28746
Initial concentration in electrolyte [mol/m^3]	Material properties	1000
Positive electrode Bruggeman coefficient (electrode) [-]	Material properties	1.5
Positive electrode Bruggeman coefficient (electrolyte) [-]	Material properties	1.5
Negative electrode Bruggeman coefficient (electrode) [-]	Material properties	1.5
Negative electrode Bruggeman coefficient (electrolyte) [-]	Material properties	1.5
Separator Bruggeman coefficient (electrolyte) [-]	Material properties	1.5
Faraday constant [C/mol]	Constant	96485.3
Ideal gas constant [$J/(K \cdot mol)$]	Constant	8.314
Reference temperature [K]	Thermal	298.15
Initial temperature [K]	Thermal	298.15

Table 5.2: Scalar Parameters of SPMe model in PyBaMM

Function-Parameter name	**Parameter category**	**Free-variables dependence**	**Possible Mohtat's value (assumed scalar case)**
Current function [A]	Electrical	Time [s]	
Initial concentration in positive electrode $[mol/m^3]$	Material properties	Radial distance (r) [m], Through-cell distance (x) [m]	31513
Initial concentration in negative electrode $[mol/m^3]$	Material properties	Radial distance (r) [m], Through-cell distance (x) [m]	$\sim$48.87
Positive electrode OCP [V]	Electrical	Positive particle stoichiometry [-]	
Negative electrode OCP [V]	Electrical	Negative particle stoichiometry [-]	
Positive particle radius [m]	Material properties	Through-cell distance (x) [m]	$3.5 \cdot 10^{-6}$
Negative particle radius [m]	Material properties	Through-cell distance (x) [m]	$2.5 \cdot 10^{-6}$
Positive electrode active material volume fraction [-]	Material properties	Through-cell distance (x) [m]	0.445
Negative electrode active material volume fraction [-]	Material properties	Through-cell distance (x) [m]	0.610
Separator porosity [-]	Material properties	Through-cell distance (x) [m]	0.400
Positive electrode porosity [-]	Material properties	Through-cell distance (x) [m]	0.300
Negative electrode porosity [-]	Material properties	Through-cell distance (x) [m]	0.300
Electrolyte diffusivity $[m^2/s]$	Transport properties	Electrolyte concentration $[mol/m^3]$, Temperature [K]	
Positive particle diffusivity $[m^2/s]$	Transport properties	Positive particle stoichiometry [-], Temperature [K]	
Negative particle diffusivity $[m^2/s]$	Transport properties	Negative particle stoichiometry [-], Temperature [K]	
Electrolyte conductivity $[S/m]$	Electrical	Electrolyte concentration $[mol/m^3]$, Temperature [K]	
Positive electrode conductivity $[S/m]$	Electrical	Temperature [K]	100.0
Negative electrode conductivity $[S/m]$	Electrical	Temperature [K]	100.0
Cation transference number [-]	Transport properties	Electrolyte concentration $[mol/m^3]$, Temperature [K]	0.38
Positive electrode exchange-current density $[A/m^2]$	Kinetics	Electrolyte concentration $[mol/m^3]$, Positive particle surface concentration $[mol/m^3]$, Maximum positive particle surface concentration $[mol/m^3]$, Temperature [K]	
Negative electrode exchange-current density $[A/m^2]$	Kinetics	Electrolyte concentration $[mol/m^3]$, Negative particle surface concentration $[mol/m^3]$, Maximum negative particle surface concentration $[mol/m^3]$, Temperature [K]	
Thermodynamic factor [-]		Electrolyte concentration $[mol/m^3]$, Temperature [K]	1.34
Positive electrode OCP entropic change $[V/K]$	Thermal	Positive particle stoichiometry [-]	
Negative electrode OCP entropic change $[V/K]$	Thermal	Negative particle stoichiometry [-]	
Ambient temperature [K]	Thermal	Distance across electrode width [m], Distance across electrode height [m], Time [s]	298.15

Table 5.3: Function-Parameters of SPMe model in PyBaMM

5.2.1 Some notes about SPMe model parameters

The "Number of electrodes connected in parallel to make a cell" is an explicit parameter of the PyBaMM parameter-set. It would reflect the number of layers inside the battery cell. However, to respect the convention adopted by all the parameter-sets already implemented from literature, it is considered equal to one. It is explained by the fact that the parameter-set requires (not explicitly) total electrodes area. Therefore, considering in this sense to have a single equivalent couple of electrodes, the total electrodes area can be calculated by operating a simple product:

$$A_{electrode,total} = N_{layers} \cdot H_{electrode} \cdot W_{electrode}$$

Exploiting this relation, it was set to consider a single equivalent couple of electrodes (so, for this reason the number of layers is well-motivated to be equal to one); then, the dimensions (height $H_{electrode}$ and width $W_{electrode}$) of the equivalent electrodes were evaluated to obtain the total area of electrodes.

The "Current-function" is not an actual model parameter, rather it represents an input in case of need for an externally imposed time-based current profile.

In the Thesis, it was preferred, in order to reduce the time of simulation, to use directly the C-rate setting in the simulated experiments, rather than following the measured current from real tests. The parameter of nominal-cell capacity was exploited properly for this scope.

Two fundamental parameters for the workflow were: "Initial-concentration in positive electrode" and "Initial-concentration in negative electrode" (both expressed in mol/m^3). They are strictly correlated with stoichiometries at the initial SoC. During the entire Parameterization procedure, the initial concentrations for anode and cathode were estimated to obtain the stoichiometry windows. However, in PyBaMM their values can be completely overwritten if the experiment receives the input "initial-SoC" (equal to something between 0 and 1.0). This was avoided during the entire parametrization, allowing a correct estimation of stoichiometries.

From Mohtat et al. studies (2019) [33], the following relations are valid between stoichiometries and state-of-charge (SoC):

$$x(SoC) = x_0 + (x_{100} - x_0) \cdot SoC$$

$$y(SoC) = y_0 + (y_{100} - y_0) \cdot SoC$$

where: x is the stoichiometry of negative electrode (graphite), while y is the stoichiometry of positive electrode (NMC).

Stoichiometries and Li-concentrations for each electrode are correlated by a clear relation:

$$x(SoC) = \frac{c_{s,n}(SoC)}{c_{s,n,max}}$$

$$y(SoC) = \frac{c_{s,p}(SoC)}{c_{s,p,max}}$$

where: $c_{s,n}(SoC)$ and $c_{s,n,max}$ are respectively the local and the maximum concentrations of lithium for anode, while $c_{s,p}(SoC)$ and $c_{s,p,max}$ are respectively the local and the maximum concentrations of lithium inside cathode.

Considering some function-parameters from last Table 5.3, some of them are assumed as scalar-parameters. In particular, the large complexity of DFN models could require a more precise spatial dependence for some parameters, such as particle radii, porosities and active volume fractions. For simplicity, as explained in section 4.3, they are considered as constant values across the SPMe modeling.

In contrast with some scalar assumptions, it is fundamental to assume a vector-form (dependence on SoC and/or temperature) for the following parameters:

- Electrodes Open-circuit-potentials (OCPs)
- Particles-Diffusivity coefficients (D_s)

Actually, Mohtat's parameter-set adopts particles-diffusivity coefficients as constant across all SoC range, although variable with temperature. However, different literature studies (e.g., Chen et al. (2020) [4]) suggest that a strict dependence of these coefficients on stoichiometries is really important to catch some real physical aspects of the battery. In Thesis Parametrization, electrodes OCPs and particles-diffusivity coefficients are considered functions of stoichiometries. Indeed, half-cell or three-electrodes configurations would be useful to track the real slope of these functions.

Finally, the Bruggeman-related parameters are represented by five coefficients. Some of them are relative to solid-phase structure of electrodes, others are referred to electrolyte inside the cell. More precisely, Bruggeman coefficients are dimensionless parameters used in PyBaMM to represent the reduction of transport properties caused by the porous microstructure of the electrodes and separator. Indeed, the electrolyte and solid-phases are not treated as straight or ideal pathways; instead ion and electron transport are hindered by porosity, tortuosity, particle packing, and pore connectivity. These are the reasons for which PyBaMM introduces so many Bruggeman coefficients, that substantially add to the model a transport-efficiency correction. This efficiency is commonly expressed as: $B = \varepsilon_s^b$, where ε_s is the relevant phase volume fraction and b is the Bruggeman coefficient. This correction converts bulk transport properties into effective properties inside the porous medium, such as effective electrolyte diffusivity, effective ionic conductivity, or effective electronic conductivity. A last consideration: higher Bruggeman coefficients indicate stronger micro-structural obstruction, and therefore lower effective transport capability, increasing concentration gradients and ohmic losses, especially at high C-rates. In the absence of real analysis of internal cell structure, values close to 1.50 are used as a classical approximation (this is Thesis case) for packed spherical particles, although real electrodes may deviate from this idealized morphology.

5.3 Sensitivity Analysis of SPMe Parameters

This wide section represents the basis of Parametrization procedure.

Basically, Sensitivity Analysis identifies the parameters that have the major impact on the model outputs (e.g. cell's terminal-voltage), in order to build a solid parameters calibration. Indeed, the purpose is to focus on the estimation of the parameters having medium-to-high weight on the model response, leaving those with low sensitivity to be assumed from literature. This is necessary for complex models, that require 30 or more parameters, such as electrochemical ones, in which it is not possible to reach a complete characterization of the battery, even performing cell's teardown or specific characterization tests.

From the perspective of electrochemical model parameter identification, usually obtaining physical parameters based on experiments is time-consuming and very laborious, even with experimental errors in the process which cannot be avoided. Therefore, Sensitivity-Analysis is the premise of every parametrization-strategy, making possible to avoid the waste of time and resources on the calibration or tuning of low-impact parameters; this procedure ensures in any case the model accuracy.

Considering a practical classification of model's parameters, a generic study of sensitivity can distinguish various levels of importance: low, moderate, high, very-high.

This section is divided into two main parts. First, some reliable theoretical studies are

summarized with their application fields, methodologies and results, to explain the practical meaning of Sensitivity-Analysis of parameters for an Electrochemical model, in different conditions. Second, a personal DoE-based analysis of SPMe parameters is illustrated, with some mathematical coefficients; the purpose is to view, through different kinds of plots, the immediate impacts of certain groups of parameters on the voltage response of battery cell.

5.3.1 Sensitivity of Electrochemical Model Parameters: Reference Studies

In general, Electrochemical models are increasingly used to accurately describe the internal dynamics of lithium-ion batteries, involving a large amount of parameters; this make the parameters optimization computationally very expensive. Indeed, the identification of all the model's parameters is very time-consuming and often with poor accuracy.

Therefore, the identifiability of the parameters for an electrochemical model can be examined through a general sensitivity-analysis, i.e. an analysis for the variation of the model output due to the variation of a one parameter or of a certain group of parameters. Sensitivity analysis is typically exploited to reduce the workload in the subsequent parametrization process. This approach is largely used in various lithium-ion battery electrochemical models to facilitate the identifiability of the model's parameters.

Zhang et al. (2014) [34] carry out a local sensitivity analysis for 30 parameters of their electrochemical model for an LFP battery, using simulation-based methods. More precisely, they used the technique "One-factor-at-a-time" (OFAT, or equivalently OAT), in order to analyze the model's sensitivity, assuming cell's terminal-voltage and cell's surface temperature as targeted model outputs. Moreover, their work implement a step-by-step parameter identification experiments, with a design based on the sensitivity analysis results.

Li et al. (2020) [35] analyze the parameter sensitivity for an electrochemical model under both the charging process and real-world driving cycles. In more detail, this study focuses on the analysis of 26 physical parameters, using a specific method, referred to a lithium Nickel-Manganese-Cobalt-Oxide(NMC) / graphite cell. They analyzed the impact of the parameters not only on terminal-voltage, but also for essential states in an electrochemical model-based BMS, such as cathode-bulk SoC, cathode-surface SoC and anode-side reaction over-potential. Furthermore, the article highlights the influence of C-rates and Depth-of-discharge (DoD) on capacity-related parameters and other parameters.

Li et al. (2020) consider 26 parameters (ignoring complex functions of cathode/anode OCPs and of electrolyte conductivity), divided into four categories: geometric, transport, kinetic, and concentration parameters. Then, they introduce fundamental ranges for parameter evaluations taken from 25 other different literature studies for NMC/graphite cells; they are of critical importance for a correct parameter sensitivity-analysis and identification.

The effective sensitivity-analysis is based on a specific methodology, with the purpose of investigating the variability of the BMS states against the individual variations of a certain model's parameter. More specifically, "One-at-a-Time" procedure (OAT) was applied to analyze the output variability against the variations of an input parameter within its typical range. It is executed with 7 different rate cycles in CC-CV charge, with high dependence from two variables: State-of-Charge and Current-rate.

Using a probabilistic approach, a Sensitivity-Index (SI), with values between 0 and 1, was used

for a numerical-scaled evaluation of each parameter on the model outputs:

$$SI(SoC, C) = \sqrt{\frac{1}{N_s} \cdot \sum_{j=1}^{N_s} (x_{ij} - \bar{x_i})^2}$$

where: N_s is the number of value points in each parameter range, and $\bar{x_i}$ is the average value of state-variables x_{ij}.

In order to complete the study, the Average-Sensitivity-Index (ASI) of the parameters at 5 Depth-of-discharge (DoD) regions (used to investigate the relationship between the variance of the parameter sensitivity and variance of SoC) was calculated as follows (generic case):

$$ASI(DoD_i, C) = \frac{1}{N_{DoD,x}} \cdot \sum_{j=1}^{N_{DoD,x}} SI(SoC, C)$$

where: $N_{DoD,x}$ is the number of data points in a x-DoD region, before reaching the cut-off voltage.

The methods of computation for SI and ASI slightly change, considering the parameter analysis in the case of real-world driving cycles.

Li et al. (2020) exploited 3640 CC-CV charging experiments and 260 WLTP cycling experiments that were simulated with a reduced-order electrochemical model in MATLAB.

The main results of the study can be summarized as follows:

All 7 capacity-related parameters (L^+, L^-, ε_s^+, ε_s^-, $c_{s,max}^+$, $c_{s,max}^-$, A) show a significant sensitivity variance for the terminal-voltage in different DoD regions; it is due to the horizontal shift of the end-of-charge point with capacity-change. Indeed, electrode's capacities are evaluated as follows:

$$Q = \frac{A \cdot \varepsilon_s^+ \cdot L^+ \cdot c_{s,max}^+ \cdot F \cdot |\theta_{100}^+ - \theta_0^+|}{3600} = \frac{A \cdot \varepsilon_s^- \cdot L^- \cdot c_{s,max}^- \cdot F \cdot |\theta_{100}^- - \theta_0^-|}{3600}$$

In contrast, the variance of the remaining 19 parameters only results in a vertical shift of the entire terminal-voltage curve, where the variance inside the different DoD regions is small.

The sensitivity of the 19 parameters, not tied to capacity, can be increased significantly with C-rate. This means there is a possibility to rise up the identifiability of these parameters with higher C-rates in experiments. Instead, this effect of C-rates is not noticed for the 7 capacity-related parameters.

The main outcomes were obtained with the combined use of CC-CV charging experiments and WLTP cycles to investigate the multiple BMS-states. According to the sensitivity rankings of the parameters, 14 parameters are sensitive for terminal-voltage, and they were identified with acceptable accuracy based on terminal-voltage measurement data. Moreover, the 7 capacity-related parameters have a relatively wide impact on the sensitivity-level for the terminal-voltage. The identification of these parameters could be crucial for model's parameterization, adding reach information on electrode capacity-level degradation mechanisms.

Finally, the sensitivity of all 26 physical parameters is analyzed not only for terminal-voltage, but also for cathode-bulk SoC, cathode-surface SoC and anode-side reactions over-potential. The previous 12 over 26 parameters are insensitive not only for cell's terminal-voltage, but also for the other BMS states, both for anode or cathode. Finally, the study demonstrates the actual insensitivity, for all the cases, of separator and electrolyte parameters for the analyzed cell.

The main result of the study shows the analysis of sensitivity of the entire set of 26 parameters, based on terminal-voltage measurement data, obtained through MATLAB simulations. This identification was achieved using terminal-voltage data under WLTP profile with global optimization algorithms (e.g., genetic algorithm).

The work shows in Figure 5.1 the ranking of normalized Sensitivity-Index (SI) of all the 26 parameters related to terminal-voltage; it was assumed that only parameters with SI greater than 0.01 are defined as sensitive parameters for terminal-voltage.

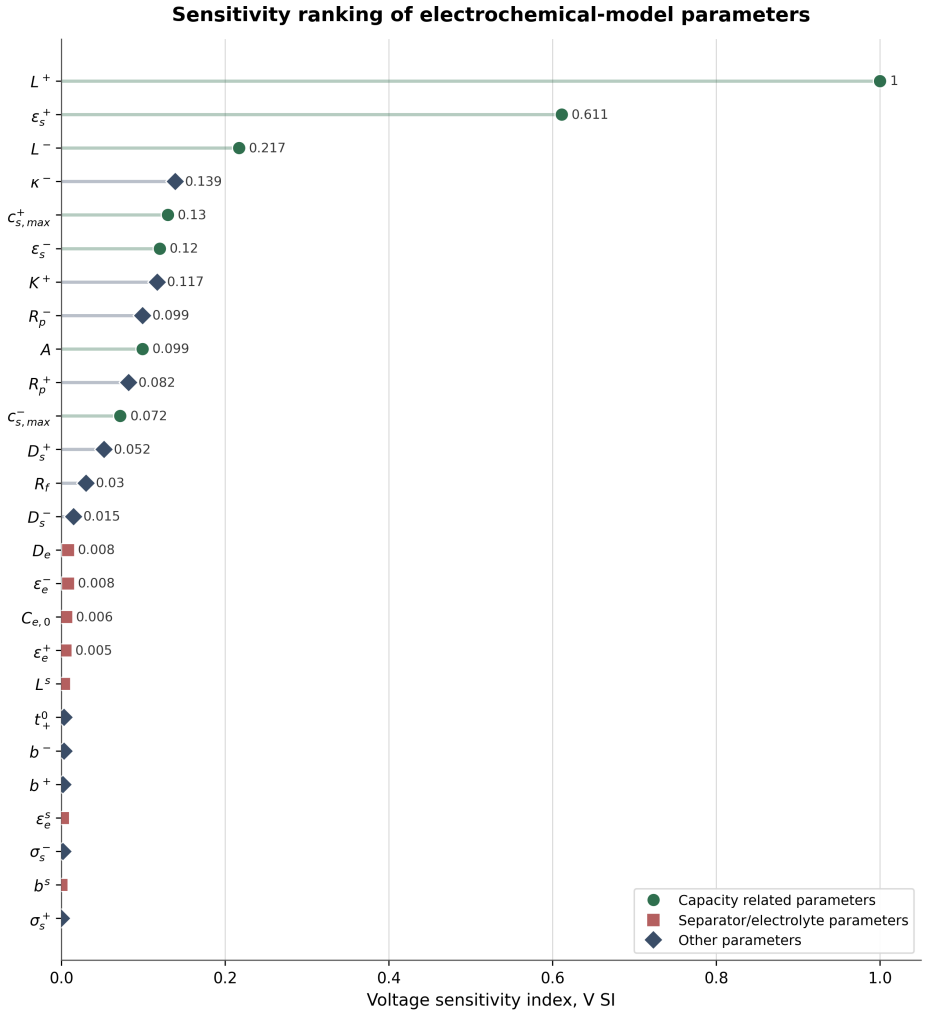


Figure 5.1: Normalized SI for Terminal-voltage of 26 parameters (from Li et al. (2020))

Overall, the plot shows that out of 26 investigated parameters, 14 parameters present a SI greater than 0.01, so they can be considered as the most sensitive properties for an electrochemical model of NMC/graphite cells. All the 7 capacity-related parameters are extremely influential for terminal-voltage, while electrolyte and separator properties have lower impact on the model. Furthermore, some kinetic, diffusion and specific electrode properties have great importance for the electrochemical model's parametrization.

J. Chen et al. (2025) [36] focused on the analysis of an electrochemical-thermal modeling of a Li-ion battery cell. In particular, the researchers developed a framework based on a Sensitivity Analysis to investigate the impact of model parameters on voltage and temperature outputs and the influence of key operating variables, such as C-rate and ambient temperature. The subsequent parameterization was carried out adopting non-invasive characterization techniques for the Li-ion battery cell, which is a Kokam pouch cell with $7.5\ Ah$ of nominal capacity.

The core of their activity is exactly the same as that of this Thesis: they avoided the application of invasive methods of cell's characterization, which obtain the internal cell parameters through expensive and time-consuming procedures, focusing instead on non-invasive approaches, that

provided easily data about current, voltage and surface temperature. Therefore, the application of a sensitivity analysis was crucial to understand how a group of model's parameters can affect the model's behavior, with a deep study of the mechanisms behind it.

This paper proposed two approaches for the sensitivity-analysis: (i) the common OAT (One-At-a-Time), where only a parameter is varied within its boundaries, while the others remain fixed at their nominal values; (ii) the more extensive GSA (Global Sensitivity Analysis), which involves simultaneously the variation of several or all the model parameters, obtaining a comprehensive exploration of the parameter values and assessing a sensitivity in a "global sense" (J. Chen et al. (2025)).

The primary index to comprehensively analyze the sensitivity of the parameters and their interaction, within a given parameter value space, is the Sobol index, which can assess the total variance of the model output in terms of individual contributions and their interactions.

J. Chen et al. (2025) study aimed to analyze the identifiability of 39 parameters of an electrochemical-thermal model, using terminal-voltage and temperature outputs as the two sensitivity targets, varying the model parameters across the entire value space, applying the Sobol evaluation.

The work started with a development of electrochemical-thermal coupled model, using literature and non-invasive testing to estimate the model's parameter values. The Global Sensitivity Analysis was then carried out using: (i) full-order and first-order Sobol indices, which were computed to rank the impact of model's parameters on the two selected outputs, i.e. terminal-voltage and surface temperature of cell; (ii) second-order Sobol indices were applied to reveal the interactions among specific model's parameters. The sampling method associated to the GSA is the Quasi Monte-Carlo (QMC) method, which utilizes quasi-random, low-discrepancy sequences, ensuring a uniform distribution of input parameter values. Moreover, in order to explore the influence of some operating factors on parameter identifiability, the Sobol indices were evaluated under nine different operating conditions, characterized by changes in ambient temperature and discharge C-rates. Coherent parameter boundaries were chosen to realize the entire analysis, considering that they deeply influence the sensitivity results. Finally, a general ranking method was applied to rank and group the parameters according to their sensitivity and impact on the model.

Practically, the GSA relies on the analysis of the sensitivity of 39 model's parameters, applying the Sobol's approach, in order to investigate the output variance of the model against the variance of one, two, or all input parameters at the same time. The effects of operating variables on the model's output were studied, selecting: $25\ ^{\circ}C$, $0\ ^{\circ}C$ and $35\ ^{\circ}C$ for the temperatures, C/5, 1C, 2C for the discharge C-rates.

J. Chen et al. (2025) computed three Sobol indices, each one with a certain meaning, using the concepts of variance (V) and mean value (E).

The first-order sensitivity analyzes the effect of a parameter X_i on the output Y, without the interaction with other inputs, thereby the model's total variance normalizes the partial contribution to the variance of a single parameter; it is assessed through first-order Sobol index:

$$S_i = \frac{V_i}{V(Y)} = \frac{V_{X_i}(E_{X_{\sim i}}(Y|X_i))}{V(Y)}$$

where: X_i as a generic model parameter, Y as the selected model output, and $X_{\sim i}$ represents all the parameters different from X_i.

The second-order sensitivity is evaluated normalizing the variance of the output caused by inputs X_i and X_j with respect to total variance of the model; it is expressed through second-order Sobol index:

$$S_{ij} = \frac{V_{ij}}{V(Y)}$$

The total-order sensitivity is computed as the sum of all the Sobol orders, with many contributions attributed to same parameter X_i, thereby assessing the global effect of this parameter on the chosen

model's output; it is given by:

$$S_{T_i} = S_i + S_{ij} + ... + S_{ik} = 1 - \frac{V_{X_{\sim i}}(E_{X_i}(Y|X_{\sim i}))}{V(Y)}$$

In this study, the researchers adopted the Root-Mean-Square-Error (RMSE) as the model output Y, considering the difference between the simulated terminal-voltage (or temperature) and the corresponding nominal values assumed as references; in the case of terminal-voltage (and similarly for the temperature), it is calculated as follows:

$$RMSE = \sqrt{\frac{1}{N_t} \cdot \sum_{i=1}^{N_t} (V_i - V_{ref,i})^2}$$

where: N_t is the number of data-points, V_i is the simulated voltage value in the i^{th} data-point, and $V_{ref,i}$ is the voltage value of the reference in the i^{th} data-point.

Once obtained the Sobol indices, the results are influenced by sampling errors of QMC method, thereby to quantify their uncertainty, the so-called Bootstrap Confidence Intervals (BCIs) were employed by the researchers.

The last approach adopted in this complete work to categorize the model's parameters relied on the identification of the most critical parameters, considering the two model's outputs, using a specific ranking, based on the method of Pareto dominance. So, the parameters that maximize the Sobol indices for terminal-voltage and temperature are more influential and dominant that the others.

Regarding the results, the total-order Sobol indices were used to make a global assessment of model's parameter influence for the outputs.

Considering the terminal-voltage, J. Chen et al. (2025) verified that the most influential parameters is the cathode thickness, followed by other six capacity-related parameters and specific impedance-related parameters (among them solid-phase diffusivity and reaction-rates). Indeed, the variations of these kinds of parameters affect deeply the battery internal properties, changing the time to reach the lower cut-off voltage, so the overall deliverable capacity. Moreover, several interactions, through second-order sensitivity were found, and among them, the most significant one is between the cathode thickness and anode thickness, followed by relation between cathode thickness and the corresponding active volume fraction.

In general, the parameters, that show a Sobol Index greater than 0.1, are considered highly sensitive to the model's outputs.

In addition, the total-order Sobol indices for terminal-voltage of 23 electrochemical-thermal parameters, under different ambient temperatures and C-rates, are computed and reported in the work, leading to different considerations about the strong influence of these operating conditions on model's output.

The results of the entire work, related to cell's terminal-voltage, in specific conditions, i.e. at $25\ ^{\circ}C$ and 1C discharge, are visualized in Figure 5.2, substantially confirming the previous sensitivity-analysis outcomes, shown by Li et al. (2020).

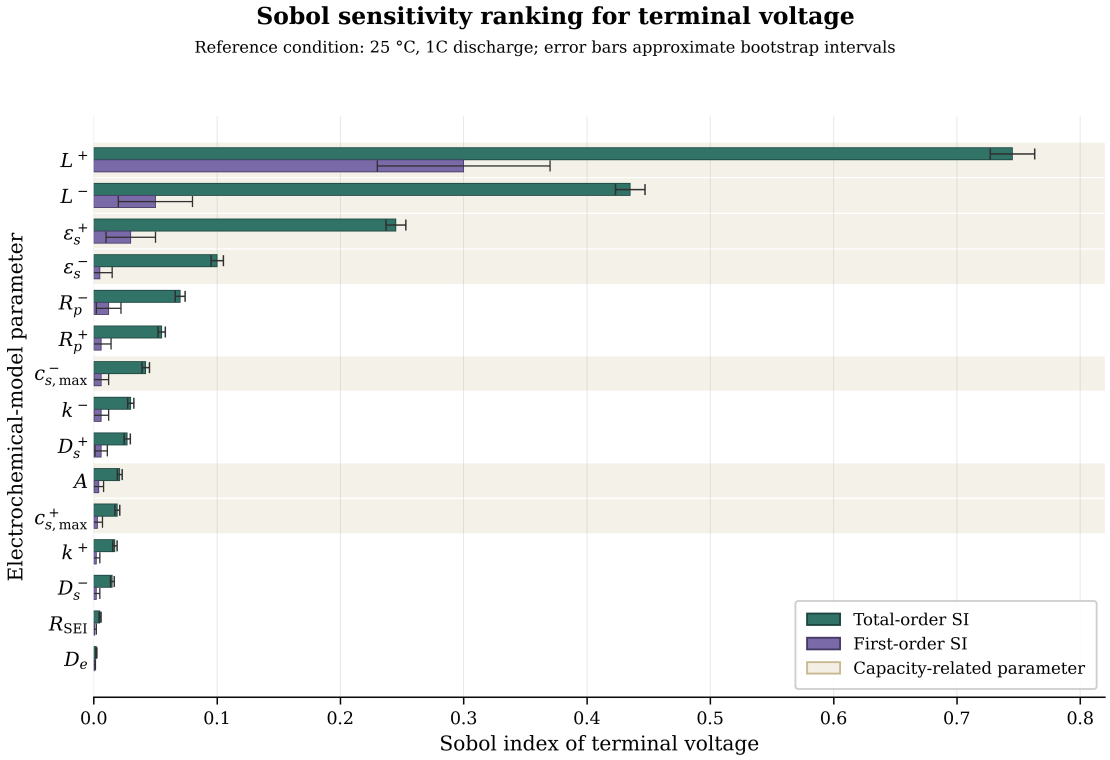


Figure 5.2: Sobol Indices from sensitivity-analysis on terminal-voltage for the 15 most impactful model's parameters

The authors made further considerations on the effect of the model's parameters, at different ambient temperatures and C-rates, even for cell surface temperature, obtaining similar outcomes as the ones for terminal-voltage.

To summarize, the main conclusions of this work can be considered the pillar of the personal sensitivity-analysis:

- The selection of a certain ambient temperature and C-rate can increase the sensitivity of a certain group of parameters up to two orders of magnitude;
- The lowering of ambient temperature and the increasing of C-rate make easier the identifiability of impedance-related parameters, but reduce the identifiability of capacity-related parameters;
- The ambient temperature data can be exploited to identify some specific parameters which have slight effects on terminal-voltage, but are more sensitive to surface cell temperature.

Overall, the results of this work can be considered the basis of the present Thesis for the part related to sensitivity-analysis, because they lead to the foundation of a solid framework for non-invasive SPMe model's parametrization, mainly relying on electrical measured data, i.e. cell's terminal-voltage.

Liu et al. (2025) [37] proposed a new method for sensitivity-analysis of electrochemical model's parameters; their study is referred to identification and effective parameter estimation for a simplified model of lithium-ion batteries. The approach is based on an effective parameter sensitivity-analysis to determine the identifiability of parameters, by classifying and ranking their sensitivity-values through their influence on model accuracy. The purpose is to focus on the estimation of parameter with the higher sensitivity rankings, leaving those with low sensitivity indices at assigned fixed values.

The obtained results, after high-sensitivity parameter calibration, optimization and calibration, show that the hybrid procedure for a simplified electrochemical modeling can effectively and

accurately identify main model's parameters.

More specifically, this study operates an electrochemical modeling for a Li-ion battery cell, integrating SPMe parameters sensitivity-analysis, parameter decoupling based on sensitivity and PSO-based parameter optimization only for high-sensitivity parameters. Regarding the first part of the work, key high-sensitivity parameters are first identified based on experimental data and general electrochemical analysis. Then, the sensitivity studies are exploited to classify the parameters into low and high-sensitivity categories. Low-sensitivity parameters are fixed in the model's parameter-set, while high-sensitivity parameters are decoupled and optimize to improve the model efficiency and accuracy. This results in a good estimation of model outputs, without affecting the model's fidelity. Furthermore, since optimization focuses only on decoupled high-sensitivity parameters, the model's computational cost is remarkably reduced.

The analysis of this work were performed on a LCO/graphite lithium-ion battery cell; thereby, it is specifically used for method development and experimental validation. The analysis is made on 11 parameters that characterize the main aspects of a simplified SPMe model; they belong to various categories: geometric, material properties, diffusion and kinetics.

The methodology to reveal the sensitivity levels of each one of 11 parameters consists of the following strategy: for a certain parameter, a $\pm 10\%$ value change is applied to that parameter, while keeping all the other parameters at their initial values. The effect of this change on the output terminal-voltage, after model's simulation, can be used to quantify the sensitivity of a certain parameter, useful for model's fidelity. Thus, a large variation in terminal-voltage indicates a high-sensitivity, whereas a small variation in terminal-voltage indicates low-sensitivity.

This evaluation of sensitivity-level for a generic parameter is given by the following formula:

$$S_{param} = \left| \frac{U_{T,\phi \pm 10\%} - U_{T,\phi_{iniz}}}{U_{T,\phi_{iniz}}} \right|$$

where: $U_{T,\phi_{iniz}}$ is the initial terminal-voltage with initial parameter ϕ_{iniz}, and $U_{T,\phi \pm 10\%}$ is the change in terminal-voltage due to a variation of $\pm 10\%$ of one parameter starting from ϕ_{iniz} during the whole SoC operating range.

The experiments used for the simulation of the simplified model are discharge cycles, repeated several times, to highlight the dependence of the parameters on aging. The results show that geometric (e.g., electrode thicknesses) and some material properties (e.g., stoichiometries, maximum concentrations), diffusivity coefficients and some kinetic terms (e.g., lumped resistance) are the most impacting on the terminal-voltage. Meanwhile, various parameters, related to electrolyte, or other cell's properties (tied to transport or specific kinetic aspects) have a low influence on the model. The research specifies that a parameter is considered with high-sensitivity value if it causes at least $5\ mV$ of voltage variation in terminal-voltage with respect to the initial case.

Finally, the work of Liu et al. has fixed low-sensitivity parameters (grouped as ϕ_{LS}), while high-sensitivity parameters (grouped as ϕ_{HS}) has been prioritized and optimized in the model parameter-set. They also noticed that for battery at different aging stages, although the sensitivity values of each individual parameter generally change, the sensitivity rankings remains the same one.

Further experimental results confirm the goodness of the adopted methodology, demonstrating, through validation phase, that sensitivity analysis can greatly improve the model accuracy and, at the same time, reduce the computational costs of electrochemical modeling.

Ma et al. (2023) [38] studied a complex modeling implementing the phenomenon of lithium plating inside the data-base of electrochemical models. In order to improve the simulation accuracy of the electrochemical model for the lithium plating reaction, they carry out a practical sensitivity-analysis of model's parameters, using the cell terminal-voltage as the main target, associated with the anode-potential and the anode-surface lithium-ion concentration as additional sensitivity objectives.

This enabled the comprehensive evaluation of crucial characterizing variables for lithium-plating. This work analyzed the sensitivity values of parameters at 25 °C, adding even 5 °C and 40 °C as other ambient-temperatures.

This work carried out a full sensitivity-analysis on 20 model parameters using the data-base of equations typical of a P2D model. They even analyzed the temperature effects on the parameters, and the correlations between sensitivity parameters and anode potential (investigating primarily the charging methods of the LIB). In this case, the authors declared the use of COMSOL Multiphysics software to build a full-order P2D model, using the finite-element method to solve its typical equations. The object of study is a Li-ion NMC622/graphite battery cell.

In this study, only scalar parameters were analyzed (e.g., excluding OCP functions or similar complex parameters), covering a comprehensive range of cathode, anode and electrolyte-related parameters.

They are divided into four groups:

- Geometric: cathode thickness, anode thickness, separator thickness, solid-phase volume fractions, electrode's porosities, electrode's particle radii;
- Concentration: electrode's maximum Li-ion concentrations;
- Transport: electrode's conductivities, solid-phase Li-ion diffusion coefficients, Bruggeman coefficients;
- Kinetic: reaction-rate constants, electrode's film resistance.

The paper investigates the sensitivity of model's parameters using different CC-charging rates. Moreover, the three external temperatures are exploited to study the relationship between temperature and parameter sensitivity levels.

The effective parameter sensitivity-analysis was carried out using the method "OFAT" (One-Factor-at-a-Time"), meaning that the value of each parameter is varied individually, maintaining constant the other parameters (same Li et al.(2020) [35] method). Globally, Ma et al. (2023) analyzed 1200 simulation cases, in order to investigate the effect of electrochemical parameters on model outputs, that are: terminal-voltage, anode-potential and anode surface Li-ion concentration.

The approach was identical even in terms of numerical evaluation of the sensitivity indices of Li et al. (2020) work, using the same assumption (uniform probabilistic distribution of points for the parameters inside their bounds). Indeed, in order to quantify the specific effect of the input parameters on the uncertainty of the model outputs, the population standard deviation (SD) is used to evaluate he sensitivity values of the parameters on chosen model outputs. In this case, SD depends not only on C-rates and SoC, but also on temperature; so, the equation is:

$$SD(T, C, SoC) = \sqrt{\frac{1}{N} \cdot \sum_{i=1}^{N} (x_i - \bar{x})^2}$$

where: N denotes the number of parameter states, x_i is the value of model-output, and $\bar{x}$ is the average value of x_i

Then, in order to clearly describe the relationship between parameter sensitivity and SoC intervals, the average standard deviation (ASD) was calculated within a certain SoC interval as an indicator of parameter sensitivity; the generic formula is given by:

$$ASD(T, C, SoC_{min} - SoC_{max}) = \frac{1}{N_{SoC_i}} \cdot \sum_{j=1}^{N_{SoC_i}} SD(T, C, SoC_j)$$

where: N_{SoC_i} indicates the number of data-points in the i_{th} SoC interval, and the sub-script j is the j_{th} SoC-point in a certain SoC interval.

The results of the study clearly show the difference in the block of 20 initial model's parameters. Essentially, 13 parameters are sensitive to terminal-voltage, and most of them are cathode-related parameters. Meanwhile, nine parameters have high-sensitivity levels to anode-potential and anode-surface Li-ion concentration, and all of them are anode-related. Globally, seven parameters are sensitive to the three targeted model outputs, all related to anode quantities: thickness, solid-phase volume fraction, particle radius, maximum lithium-ion concentration, reaction-rate constant, film resistance, Bruggeman coefficient.

The effects of the selected C-rates and/or SoC intervals strongly influenced the impact on the cell's terminal-voltage, confirming the high complexity of electrochemical models in the exact parameter identification. The influence of a certain C-rate on the 20 model's parameters analyzed in this study is show in Figure 5.3.

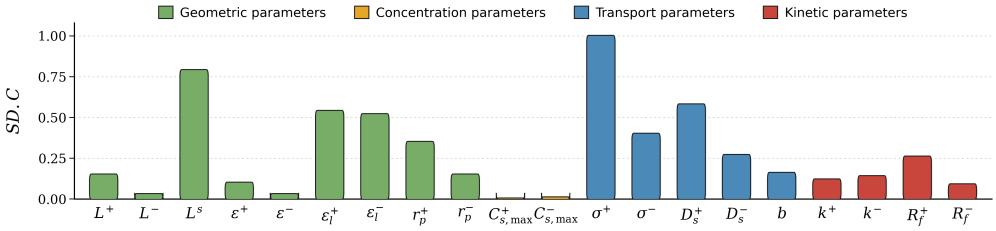


Figure 5.3: Normalized SD about influence of C-rates on parameters (from Ma et al.)

Considering terminal-voltage as the main target for the analysis, only six parameters are sensitive to it and less sensitive to the variables selected for lithium plating criterion, all referred to cathode quantities; they are: solid-phase diffusion coefficient, particle radius, maximum Li-ion concentration, thickness, solid-phase volume fraction and reaction-rate constant.

Furthermore, the results show that temperature has a differential effect on the parameter sensitivity levels. Indeed, the terminal-voltage sensitivity of electrochemical parameters generally increases at low temperatures with respect to high temperatures. This indicates that the identifiability of most impacting parameters can be enhanced by lowering the temperature in the identification process.

The authors further analyzed the effects of some specific parameters correlated with the anode potential, in order to consider the perspectives of the charging safety and the avoiding of accelerated battery aging (due to lithium plating) for Li-ion batteries.

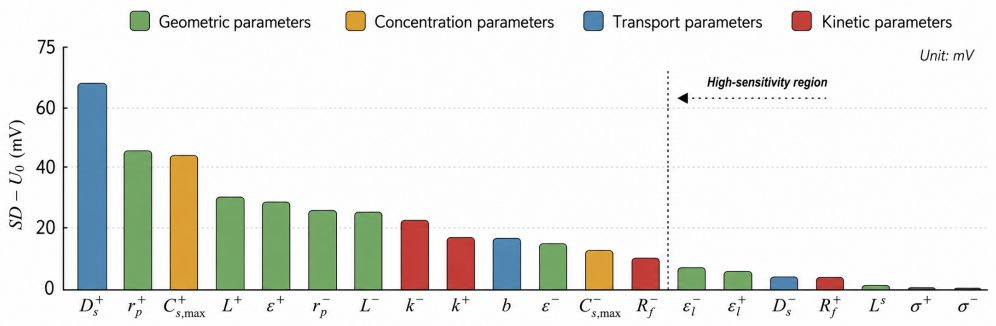


Figure 5.4: Sensitivity rankings on terminal-voltage for 20 parameters (from Ma et al.)

In Figure 5.4, the authors classified the high-sensitivity parameters to terminal-voltage as the ones exceeding average of at least 10 mV of impact, and in total they are 13 of the original 20 parameters. In conclusion, considering the results of this work, it is clear that the most sensitive parameters for battery's terminal-voltage are the cathode-related ones, rather than anode parameters, which are, instead, more influential for lithium-plating phenomenon.

Schmidt et al. (2010) [39] performed a parameter sensitivity-analysis and estimated the identifiability of different parameters using the Fisher-information Matrix (FIM) method, in which the terminal-voltage was chosen as the main target of model outputs. Although FIM methodology offers a minimum variance bound and confidence interval of the parameters, its calculation process is very complex for high-order electrochemical models.

5.3.2 DoE-based Sensitivity Analysis

This study is focused on terminal-voltage impact of certain groups of electrochemical-model's parameters. The parameter-groups are five:

1. Cell-level geometry;
2. Thermodynamic aspects (OCP functions & stoichiometries);
3. Electrolyte and Separator properties;
4. Electrode's micro-structure properties;
5. Transport and Kinetics properties of electrodes.

Inside each group, different sensitivity analysis were carried out separately for sub-group of parameters, depending on the level of sensitivity which those specific parameters have from the literature's sensitivity studies. For example, Bruggeman coefficients and active-volume material fractions belonging to group-4 cannot be studied together, because they have theoretical very different levels of sensitivity in the model; the same discussion is for particle-diffusivities and electrode's conductivities.

The sensitivity-analysis strategy is the following: similar to OAT approach, it consists of keeping all the parameters of SPMe fixed at "Mohtat2020" default values/functions, and varying only the parameters which have been chosen in a specific group. In this way, the impact on the cell's terminal-voltage is related only to a specific sub-group and immediate visual/numerical evaluations can be performed. The process is repeated with the purpose of completely covering the entire parameter-set of the model.

This personal sensitivity analysis is based on the use of Design-of-Experiments (DoEs); the method employed for DoE is Latin-Hypercube-Sampling (LHS). Furthermore, two different coefficients were exploited to evaluate mathematically the sensitivity levels of parameters: (i) first-order Sobol index, (ii) Spearman's rank-correlation index. Further details about these choices will be given in the next subsections.

Moreover, all the parameters are varied inside plausible ranges for typical High-Power cells, considering all the previous literature studies as starting point. This step is fundamental to see the corresponding terminal-voltage changes as a function of time or discharged-capacity.

In all the cases, the varied parameters inside the PyBaMM's parameter-set produce less or more visible changes on the terminal-voltage curve, considering always as reference the Mohtat's baseline cell's voltage curve, as default-case for comparisons. The experiments employed for the entire analysis are multi-rate discharges, in particular at three common rates (for real applications): 0.5C, 1C, 2C. Only for group 2 of parameters, in order to evidence the thermodynamic effects of the parameters, lower rates were adopted: C/20, C/2, 1C.

Sensitivity-Analysis via Design-of-Experiment with LHS method

In general, design of experiments, also known as experimental design, refer to the construction of procedures that attempt to explain how changes in one aspect of a system can lead to changes to

other aspects of that system (usually they analyze input/output relations).

Therefore, applied to sensitivity of SPMe parameters, a Design-of-Experiment (DoE) is a structured methodology for planning a set of model evaluations in such a way as to extract the maximum amount of information on the influence of the input parameters upon a chosen output, while keeping the number of simulations to a minimum (Montgomery, 2017 [40]). In contrast to the elementary One-Factor-At-a-Time (OFAT) approach, in which a single parameter is perturbed while all the others are held fixed at their reference values, a DoE varies several parameters simultaneously. This allows the parameter space to be explored globally rather than along isolated coordinate directions, and, in principle, enables the interactions between parameters to be detected, in contrast to OFAT screening that is, by construction, unable to reveal them.

In the present analysis, the sampling of the parameter space is carried out by means of Latin-Hypercube-Sampling (LHS) technique (McKay et al. (1979) [41]). For a generic problem, involving k uncertain parameters and a budget of $Nsamples$, the procedure sub-divides the range of each parameter into N equiprobable intervals and draws exactly one value from each interval; then, the values are combined across the k-dimensions, so that the projection of the sample, set onto any individual parameter-axis, covers the whole range uniformly, with no interval left empty and none sampled twice. Compared with purely random sampling (e.g., Monte-Carlo), this exact stratification of LHS method guarantees a more uniform and space-filling coverage of the multi-dimensional domain for an equal number of samples; thereby, this avoids the clustering and the gaps that random strategies typically generate (Helton and Davis, 2003 [42]).

In practice, each SPMe parameter, or more often each sub-group of parameters, belonging to the same physical block of PyBaMM's parameter-set, is assigned to a variation range, taken from literature references. The LHS algorithm generates N parameter-combinations within these ranges, and every combination is simulated with the SPMe model at three discharge rates, yielding a corresponding terminal-voltage curve. The ensemble of all such curves constitutes the so-called "voltage-fan" plot, in which the spread of the simulated responses about the Mohtat's default baseline provides an immediate, qualitative visualization of how strongly the parameters, under estimation, affect the cell voltage. Analyzing the parameters in coherent groups, rather than all at one, keeps each fan interpretable and it prevents the effect of a dominant block from masking the subtler contributions of the others.

RMSE and Qualitative Sensitivity Indices

For the current Sensitivity-Analysis, a quantitative ranking of the SPMe parameters is required, combined with the qualitative picture offered by the voltage-fan plots.

In general, the deviation of each simulated curve from Mohtat's baseline is condensed into a single-scalar figure of merit, namely the "Root-Mean-Square Error" (RMSE), related to terminal-voltage; it is expressed by:

$$RMSE = \sqrt{\frac{1}{N} \cdot \sum_{j=1}^{N} (V_{sim}(t_j) - V_{base}(t_j))^2} \tag{5.1}$$

where: N is the number of evaluation points along the curve, V_{sim} is the simulated voltage, and V_{base} is the baseline voltage. This quantity is the primary evaluation term for the assessment of quality of the model's parametrization, related to the voltage difference between simulation and experiment baselines. It will be used for the following Sensitivity-Analysis and the subsequent SPMe parametrization strategy.

Then, the two complementary indices are computed to rank the parameters, according to their influence on this RMSE.

The Spearman's rank correlation coefficient ρ_s (Spearman,1904) quantifies the strength and the direction of the monotonic relationship between a given parameter and the output. It is defined as a Pearson correlation coefficient evaluated on the ranks of the data, and, in the absence of ties, it reduces to:

$$\rho_s = 1 - \frac{6 \sum_{i=1}^{N} d_i^2}{N \cdot (N^2 - 1)}$$

where: d_i is the difference between the rank of the i_{th} parameter-value and the rank of the corresponding output, while N is the number of data observations.

Basically, Spearman coefficient ρ_s indicates quantitatively how strongly two sets of ranks are correlated (through difference d_i). The coefficient takes values in $[-1, +1]$; a magnitude close to unity denotes a strong monotonic dependence, while a value near zero indicates a weak one. Its principal merits are its simplicity and the fact that it requires no model-evaluations beyond those already performed for the DoEs. Instead, its main limitation is that, by construction, it can detect only monotonic trends.

The first-order (approximated) Sobol index S_1 (Sobol, 2001) belongs to the family of variance-based methods. It decomposes the total variance of the output into contributions attributable to each parameter individually and to their mutual interactions; so, it measures the fraction of the output variance that is explained by a single-parameter acting alone:

$$S_{1,i} = \frac{\mathrm{Var_{X_i}[E(Y \mid X_i)]}}{\mathrm{Var(Y)}}$$

where: Y denotes the output (in this case, RMSE), and X_i is the i_{th} parameter.

Essentially, Sobol index is used to represent the proportion of variance, explained by an input or group of inputs (i.e. X_i). The index lies in $[0, 1]$, the sum of the first-order indices over all parameters being at most unity; the residual fraction represents the higher-order interaction effects. In this Thesis, S_1 is evaluated as an approximated form, in the sense that it is estimated directly from the available LHS ensemble, rather than from the dedicated sampling scheme ordinarily prescribed for an exact Sobol estimation. The choice keeps the computational cost contained, while preserving the variance-based interpretation of the index.

As described, the two sensitivity indices are conceptually distinct and, accordingly, behave differently. Spearman's coefficient is a rank-based measure, that presupposes a monotonic input-output relationship, whereas Sobol index is a variance-based measure, that makes no assumption regarding the shape of that relationship, thereby it is capable of capturing non-monotonic and non-linear behaviors, as well as (through its higher-order terms) the interactions between the parameters.

This distinction is particularly relevant for the present analysis, because the chosen output (the RMSE with respect to the baseline) is, by definition, non-negative and exhibits a characteristic V-shaped dependence on each parameter: both a decrease and an increase of a parameter relative to its reference value can enlarge the deviation from the baseline, and hence the RMSE. For such a symmetric response, the increasing and the decreasing branches tend to compensate among themselves within a rank correlation, so that Spearman's coefficient may severely underestimate the importance of a parameter (RMSE), that is actually dominant. Meanwhile, the Sobol index, being insensitive to the direction of the trend and concerned solely with the amount of explained variance, is unaffected by this drawback and correctly identifies the most influential parameters.

For this reason, in the present sensitivity-analysis, the first-order Sobol index S_1 is regarded as the most reliable indicator for the RMSE-based sensitivity ranking, whereas Spearman's coefficient is retained as a complementary and computationally inexpensive cross-check.

Overall, the indices values of Spearman and first-order Sobol depend strongly on the adopted bounds for the parameters, so they are numerically range-dependent. This means that tables with rankings of sensitivity levels are essentially influenced by per-group chosen parameter's bounds.

Parameter-sensitivity: Group-1

The first group is composed of parameters related to cell-level geometry, i.e. total electrode's area, cathode & anode thicknesses, separator & current-collectors thicknesses.

First sub-group The first sub-group isolates the dominant capacity-scaling effect of the total electrode-area on the terminal-voltage ($A_{tot} = H \cdot W \cdot N_{layers}$).

The electrode-area directly controls: (i) the cell-capacity ($Q \ \alpha \ A_{tot}$); (ii) the effective current-density ($j \ \alpha \ I/A_{tot}$); (iii) the discharge-duration at a given C-rate. Indeed, it is expected that electrode-area has a large impact on the terminal-voltage shape, causing horizontal shifts through the variation of this parameter.

The ranges of variation of the three parameters affecting the total electrode-area calculation are shown in Table 5.4.

Parameter Name	**Range's Bounds**
Electrode height (H_{elc})	(0.060, 0.130) m
Electrode width (W_{elc})	(0.080, 0.200) m
Number of layers (N_{layers})	(10, 30)

Table 5.4: First sub-group: parameter ranges

Therefore, Figures 5.5 and 5.6 show the sensitivity-rankings per C-rate with first-order Sobol and Spearman, while Figures 5.7, 5.8, and 5.9 are related to terminal-voltage variations due to electrode-area changes.

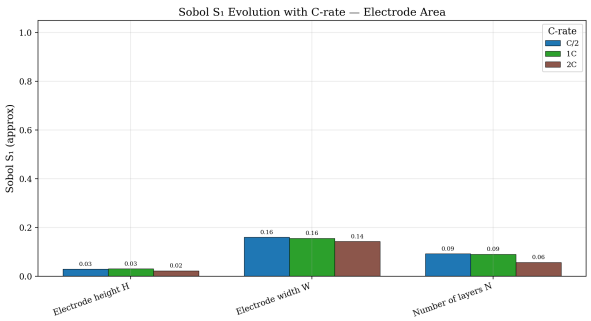


Figure 5.5: First order Sobol-Index

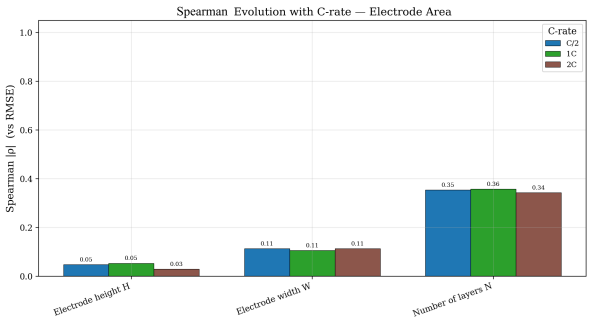


Figure 5.6: Spearman-Index

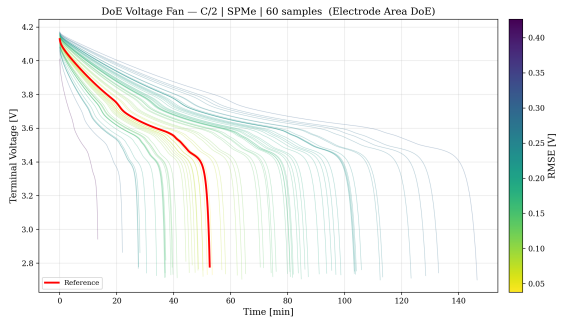


Figure 5.7: Voltage curves at C/2

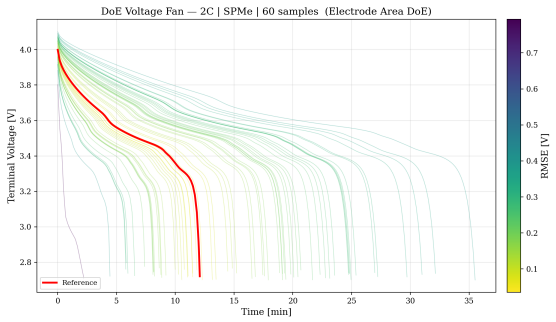


Figure 5.8: Voltage curves at 2C

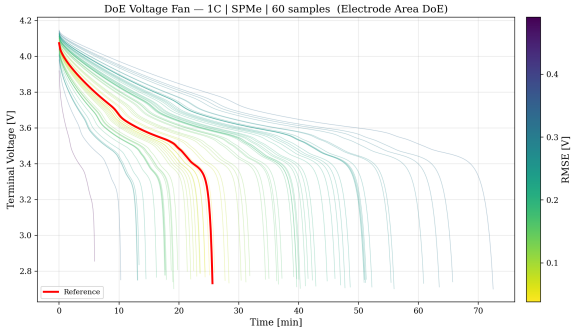


Figure 5.9: Voltage curves at 1C

The two plots regarding the adopted indices give different levels of sensitivity on the three parameters to evaluate electrode-area: first-order Sobol index attributes more weight to one of the two electrode's dimensions rather than the other parameters, while Spearman index attributes more weight to number-of-layers rather than electrode's dimensions.

Overall, the plots on DoE voltage fan show the wide impact of electrode area-related parameters on the terminal-voltage, at every C-rate.

A final note: after the end of this first analysis, a simple electrode-area scaling (through the product of the factor $11/5$) was applied for all the subsequent steps, in order to use the capacity of real Kokam cell.

Second sub-group The second sub-group focuses on the two high-sensitivity geometric parameters, mainly affecting the electrode's transport and overall cell-capacity. Indeed, fixing the electrode-area, in this case, isolates the subtler transport-related effects of the coating thicknesses, which would otherwise be masked by the dominant capacity-scaling effect of the electrode-area.

The bounds used for the two parameters, analyzed in this sub-group, are presented in Table 5.5.

Parameter Name	**Range's Bounds**
Cathode thickness (L_p)	(35, 75) μm
Anode thickness (L_n)	(40, 85) μm

Table 5.5: Second sub-group: parameter ranges

Thus, Figures 5.10 and 5.11 report the two sensitivity rankings (Sobol and Spearman), while Figures 5.12, 5.13, and 5.14 show the voltage discharge curves at three C-rates.

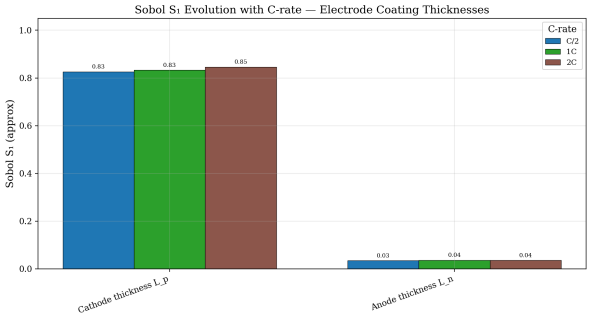


Figure 5.10: First-order Sobol-Index

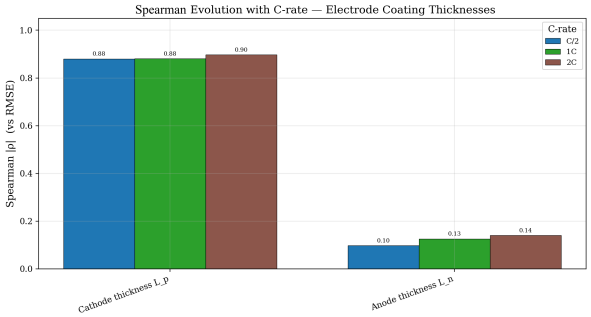


Figure 5.11: Spearman-Index

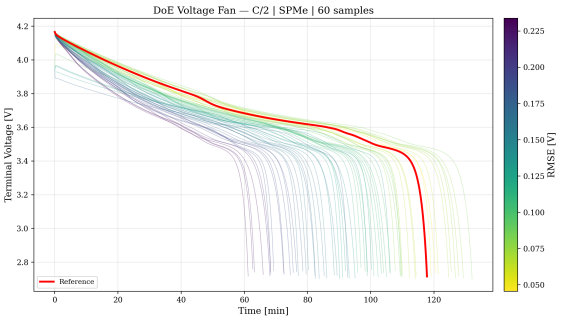


Figure 5.12: Voltage curves at C/2

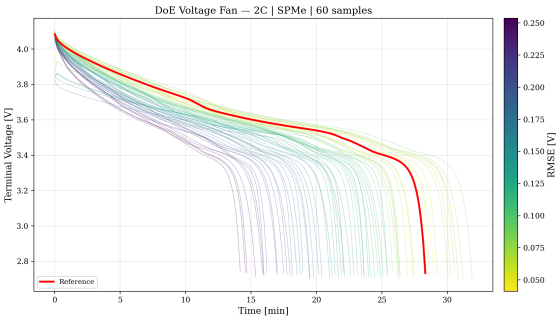


Figure 5.13: Voltage curves at 2C

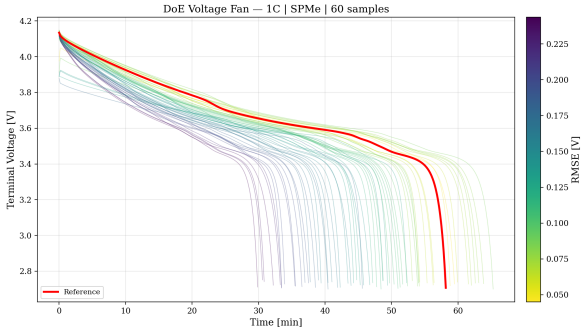


Figure 5.14: Voltage curves at 1C

The two plots regarding sensitivity indices show a typical feature seen and analyzed in different Li-ion battery sensitivity-studies: the positive electrode thickness is more dominant with respect to negative electrode thickness, in terms of impact on terminal-voltage. Furthermore, Sobol and Spearman indices have similar ranking-values, confirming the validity of the current analysis with respect to literature.

Even in this case, the DoE voltage-fan plots highlight the importance of anode and cathode thicknesses, at every C-rate, clearly influencing the discharge-time.

Third sub-group The third sub-group completes the cell-level geometry block by isolating the remaining internal-layer parameters: separator and current-collectors. They are expected to have low sensitivity on $V(t)$, thereby the analysis is included for completeness and to confirm that their contribution for model's accuracy is absolutely negligible.

The typical ranges adopted for the three parameters analyzed in this case are reported in Table 5.6.

Parameter Name	Range's Bounds
Separator thickness (L_s)	(10, 30) μm
Positive current-collector (Al) thickness ($L_{cc,p}$)	(10, 25) μm
Negative current-collector (Cu) thickness ($L_{cc,n}$)	(8, 20) μm

Table 5.6: Third sub-group: parameter ranges

The sensitivity-levels are shown in Figures 5.15 and 5.16, whereas the voltage-fan plots at different C-rates are presented in Figures 5.17, 5.18, and 5.19.

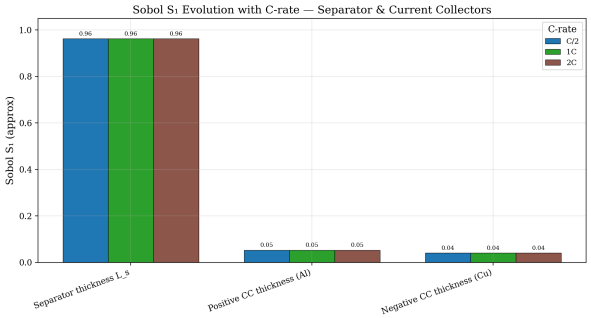


Figure 5.15: First-order Sobol-Index

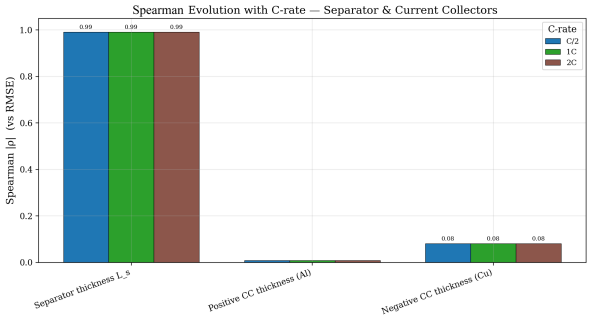


Figure 5.16: Spearman-Index

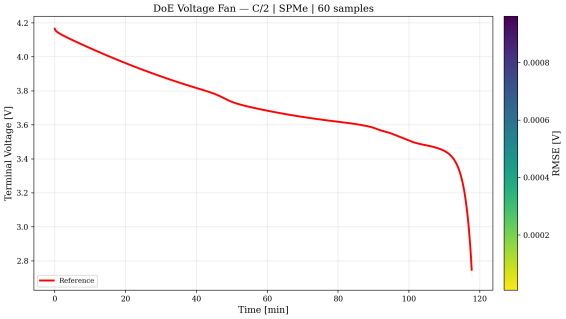


Figure 5.17: Voltage curves at C/2

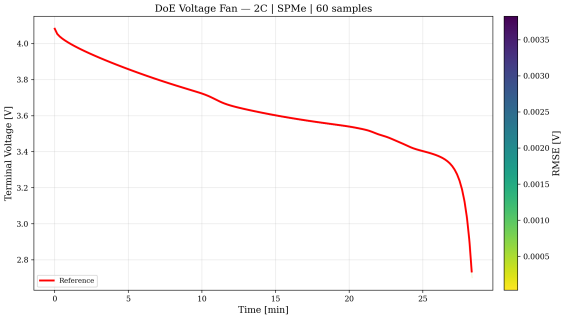


Figure 5.18: Voltage curves at 2C

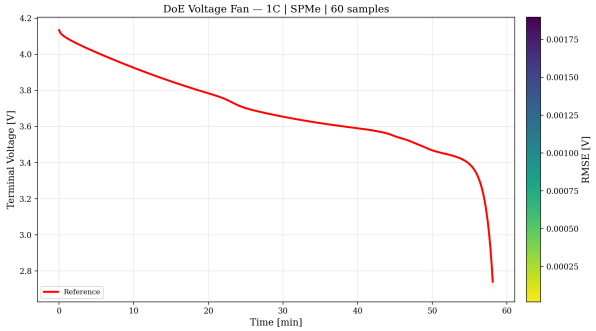


Figure 5.19: Voltage curves at 1C

From the sensitivity-ranking plots, only the separator thickness has clearly a certain weight in the modeling, considering it affects the electrolyte transport path of Li-ions between the two

electrodes; however, its Sobol index is high only relatively to the other low-sensitivity parameters, whereas globally its calibration is negligible.

The voltage-fan plots confirm the practical null-impact of these parameters on the terminal-voltage curves at each C-rate, confirming that these are low-sensitivity geometric properties.

Parameter-sensitivity: Group-2

The second group is composed of parameters related to thermodynamic aspects of the cell, i.e. electrode's OCP functions and stoichiometries.

First sub-group The first sub-group focuses on OCP electrode functions, that are among the most influential parameters in any electrochemical model, dominating the equilibrium voltage. Being functions of stoichiometries, OCP curves sensitivity is analyzed through the application of multiplicative coefficients of perturbation, called: (i) α_{U_p} - cathode OCP multiplier; (ii) α_{U_n} - anode OCP multiplier; thereby, they are expressed as:

$$U_{p,modified}(y) = \alpha_{U_p} \cdot U_{p,original}(y)$$
$$U_{n,modified}(x) = \alpha_{U_n} \cdot U_{n,original}(x)$$

These terms capture global gain or uncertainty on OCP functions, while preserving the qualitative shape of the s curves.

In practice, OCP uncertainty can arise from: material batch variability, measurement hysteresis, temperature effects (not captured by relative entropic terms), and fitting residuals from analytical expressions.

Table 5.7 summarizes the bounds employed for the two multiplicative OCP factors.

Parameter Name	**Range's Bounds**
Cathode OCP multiplier (α_{U_p})	(0.970, 1.030)
Anode OCP multiplier (α_{U_n})	(0.970, 1.030)

Table 5.7: First sub-group: parameter ranges

The multiplicative coefficients are sampled in a narrow range around 1.0 (in this case, with $\pm 3\%$ of variation), to explore how small shape/magnitude changes in OCP curves can propagate into terminal-voltage error.

The first Figure 5.20 highlights the scaled ranges of Mohtat's OCP curves. In Figure 5.21 the sensitivity (Spearman and Sobol) indices are shown, while in Figures 5.22, 5.23, and 5.24 the voltage discharge curves, at slow-to-medium rates, are reported.

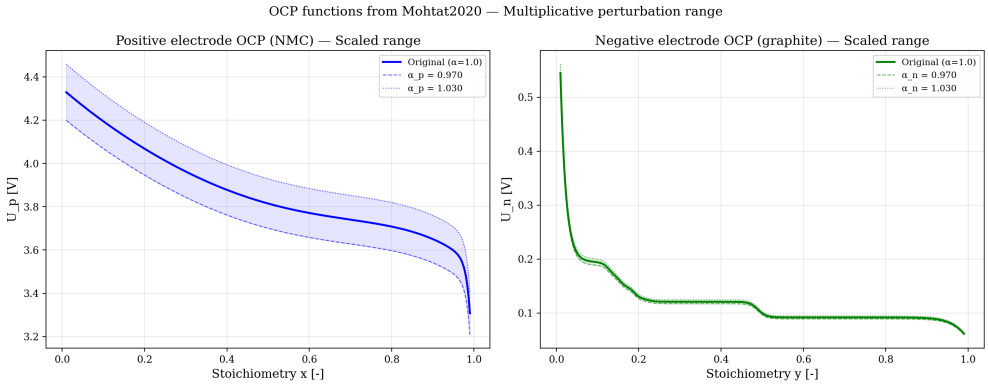


Figure 5.20: Mohtat's OCP perturbed functions

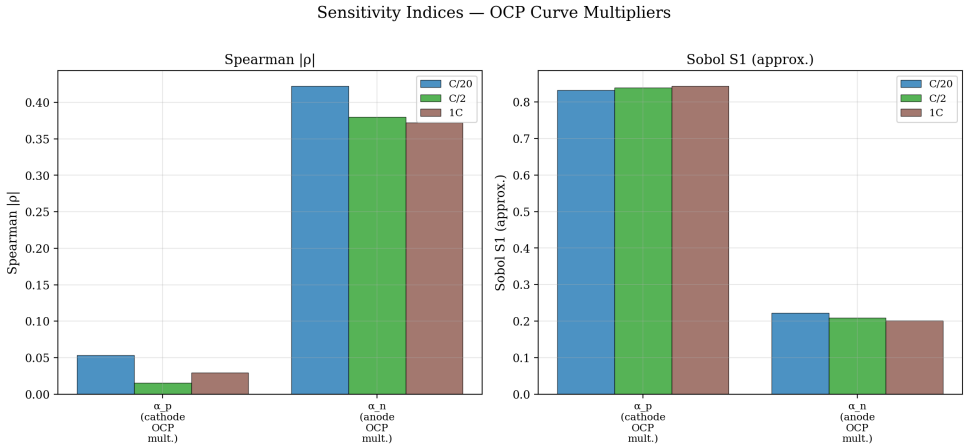


Figure 5.21: OCP multipliers Sensitivity Indices

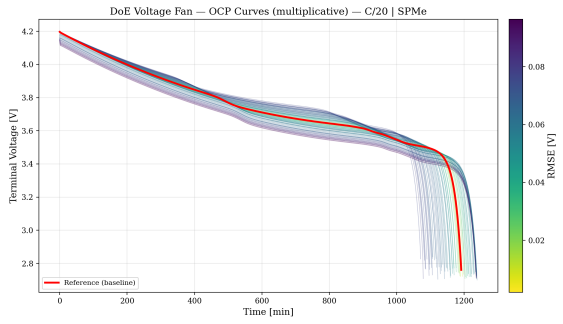


Figure 5.22: Voltage curves at C/20

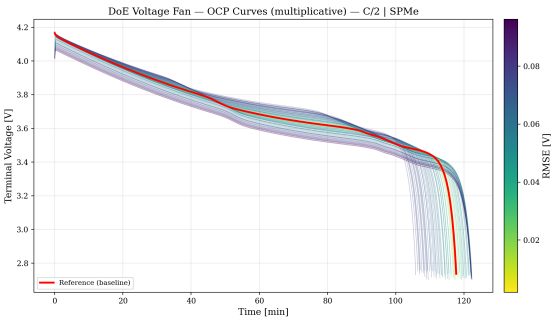


Figure 5.23: Voltage curves at C/2

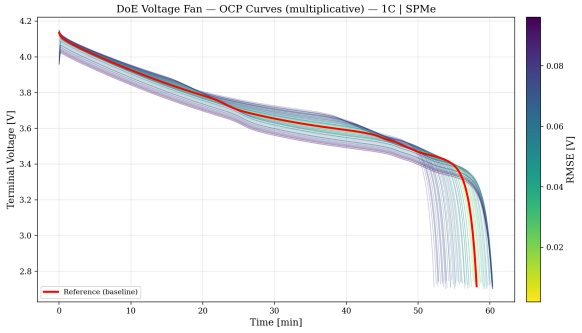


Figure 5.24: Voltage curves at 1C

Overall, α_p coefficient influences more the cathode OCP curve than α_n coefficient for anode OCP curve, due to different potential scales, as seen in the first plot.

In this specific case, Spearman index shows its limits in the estimation of real sensitivity levels, attributing much more weight to anode OCP factor, due to strong non-monotonic RMSE estimation for the perturbed voltage curves. Therefore, only Sobol index is reliable, distributing the impact in a more correct way, with a wide impact of α_p with respect to α_n.

Finally, the voltage-fan plots show a clear voltage-shape dependence (with vertical shifts) at all the rates (C/20, C/2, 1C) from the OCP functions.

Second sub-group The second sub-group analyzes the effect of Li-ions utilization factors inside the electrodes, which are regulated by stoichiometries, on the cell voltage. In particular, in this case, the analysis establishes a free parameter (anode stoichiometry at 100% of SoC, x_{100}), and a computed parameter from a constraint (cathode stoichiometry at 100% of SoC, y_{100}). The constraint is the following:

$$U_p(y_{100}) - U_n(x_{100}) = V_{max} = 4.2\ V$$

where: U_p and U_n are the OCP functions of cathode and anode respectively, stored inside the Mohtat's parameter-set.

Thus, given x_{100}, y_{100} is computed by the equations-system:

$$U_p(y_{100}) = V_{max} + U_n(x_{100})$$

$$y_{100} = U_p^{-1}(V_{max} + U_n(x_{100}))$$

The inversion of U_p is well-conditioned, because NMC OCP function is monotonically decreasing with stoichiometry.

The free-parameter of this sub-group has the following range of variation:

$$\text{Anode} - \text{stoichiometry } (\text{x}_{100}) \rightarrow (0.72, 0.97)$$

The stoichiometry variations are absorbed by initial-concentration parameters, considering that PyBaMM does not provide explicitly the stoichiometries. In addition, in this case, due to the fact that only one parameter is considered in the analysis, and the others are computed through constraints, the sensitivity indices are not evaluated.

In Figure 5.25 the stoichiometries at 100% SoC are viewed using OCP functions, while in Figures 5.26, 5.27, and 5.28 voltage discharge variations, at slow-to-medium rates, are shown as a function of stoichiometries.

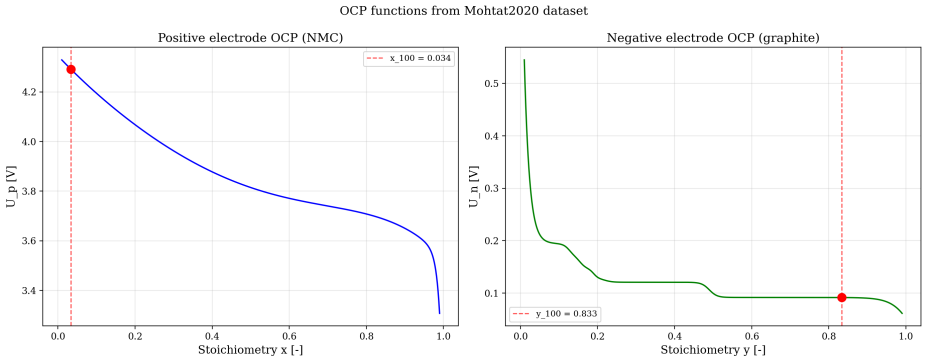


Figure 5.25: Starting Mohtat's stoichiometries at 100 %

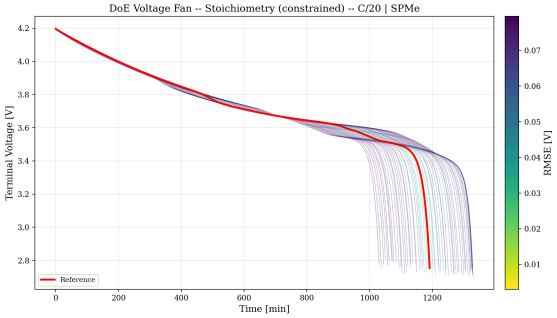


Figure 5.26: Voltage curves at C/20

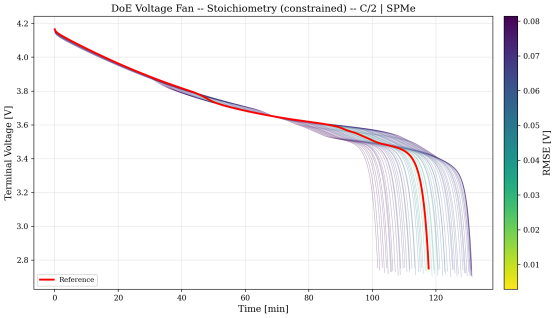


Figure 5.27: Voltage curves at C/2

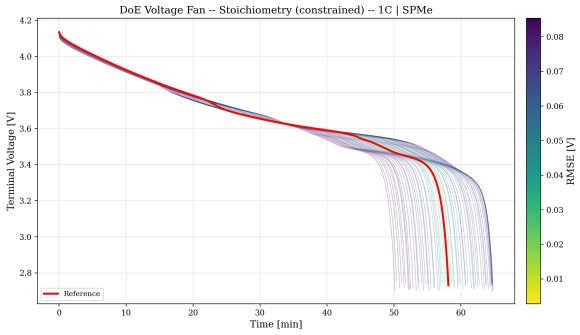


Figure 5.28: Voltage curves at 1C

Essentially, as shown in the voltage-fan plots, stoichiometries fix the termination or initialization of voltage curves, so they affect the discharge duration through their dependencies on capacity of electrodes.

Parameter-sensitivity: Group-3

The third group is composed of parameters related to electrolyte and separator properties, i.e. transport/diffusivity, conductivity and concentration parameters of electrolyte, specific features (porosity and Bruggeman coefficient) of separator.

First sub-group The first sub-group summarizes all the properties related to electrolyte of the battery, with globally five analyzed parameters. Two parameters are concentration-dependent, i.e.

electrolyte-conductivity ($\kappa(c_e)$) and diffusivity ($D_e(c_e)$). Since the full functional forms should be preserved, even for them, a multiplicative scaling factor for both parameters is applied ($\pm 50\%$ around starting 1.0); so the formulas are:

$$\kappa_{new}(c_e) = \alpha_\kappa \cdot \kappa_{original}(c_e)$$

$$D_{e,new}(c_e) = \alpha_{D_e} \cdot D_{e,original}(c_e)$$

The transference number (t_0^+), initial-electrolyte concentration ($c_{e,0}$), and thermodynamic factor (k_T) are scalar parameters which are varied directly. In general, the electrolyte parameters are considered as low-sensitivity parameters for NMC/graphite cell's terminal-voltage.

Table 5.8 shows the bounds of variation assumed for all the electrolyte-related scalar and function parameters.

Parameter Name	**Range's Bounds**
Electrolyte conductivity scaling (α_κ)	(0.5, 1.5)
Electrolyte diffusivity scaling (α_{D_e})	(0.5, 1.5)
Transference number (t_0^+)	(0.20, 0.40)
Initial electrolyte concentration ($c_{e,0}$)	(800, 1200) mol/m^3
Thermodynamic factor (k_T)	(0.5, 3.0)

Table 5.8: First sub-group: parameter ranges

Thus, Figures 5.29 and 5.30 show the sensitivity indices at various rates, whereas Figures 5.31, 5.32, and 5.33 represent the voltage-fan plots at the corresponding rates.

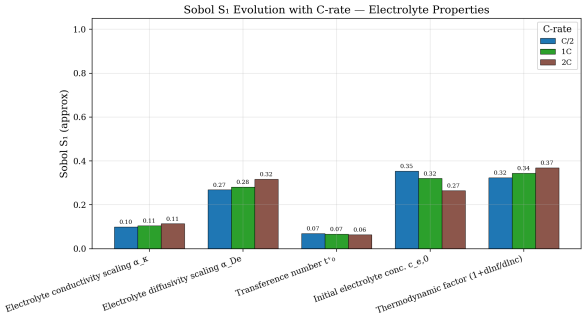


Figure 5.29: First-order Sobol-Index

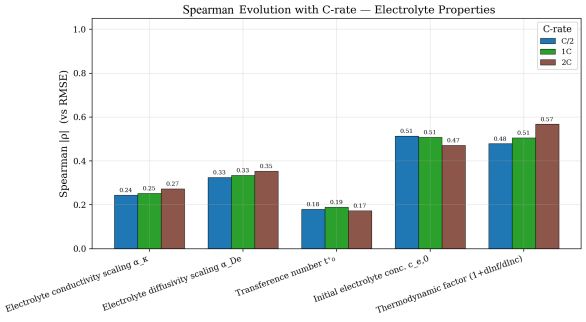


Figure 5.30: Spearman-Index

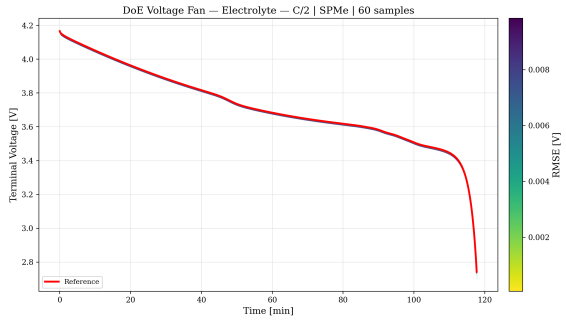


Figure 5.31: Voltage curves at C/2

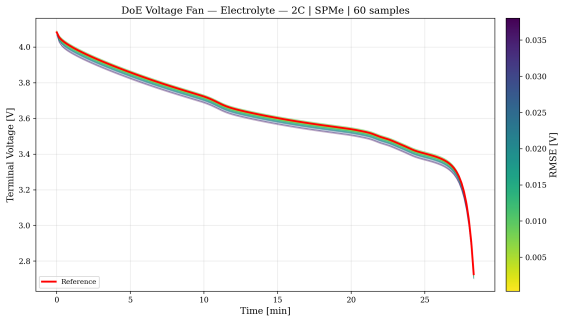


Figure 5.32: Voltage curves at 2C

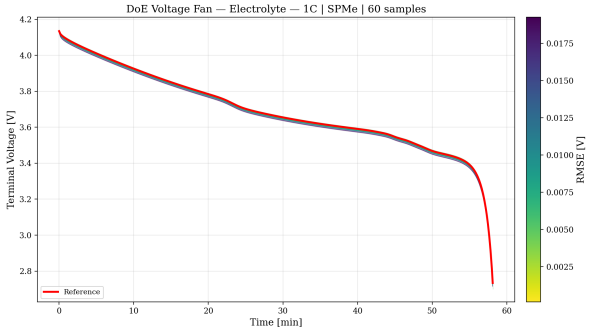


Figure 5.33: Voltage curves at 1C

In this case, the sensitivity indices are similar in the split of contributions, considering that electrolyte diffusivity, initial-electrolyte concentration and thermodynamic factor assume the largest weight for the model output.

The voltage-discharge curves highlight a clear effect of C-rate on the importance of the electrolyte transport parameters: higher rates mean more relevant role assumed by electrolyte-related parameters (due to higher limitations in Li-ions transport).

Second sub-group The second sub-group focuses on the two remaining separator-specific transport properties: porosity and Bruggeman coefficient. The separator porosity (ε_s) controls the effective electrolyte volume available for ionic transport through the separator. Together with the Bruggeman exponent (b_s), it determines the effective ionic conductivity and diffusivity via Bruggeman relation:

$$\kappa_{eff} = \kappa \cdot \varepsilon_s^{b_s}$$

$$D_{e,eff} = D_e \cdot \varepsilon_s^{b_s}$$

Both parameters are expected to have low-sensitivity for NMC/graphite terminal-voltage.
Table 5.9 reports the used bounds, for ranges of variation, regarding two separator properties.

Parameter Name	**Range's Bounds**
Separator porosity (ε_s)	(0.30, 0.60)
Separator Bruggeman coefficient (b_s)	(1.0, 2.5)

Table 5.9: Second sub-group: parameter ranges

Then, in Figures 5.34 and 5.35 the two sensitivity indices are reported, whereas Figures 5.36, 5.37, and 5.38 show the plots for voltage discharges at the three common C-rates.

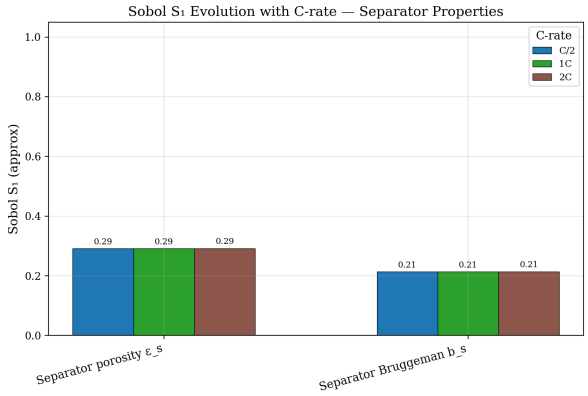


Figure 5.34: First-order Sobol-Index

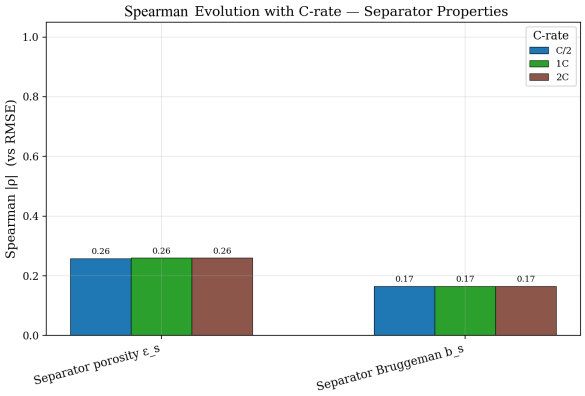


Figure 5.35: Spearman-Index

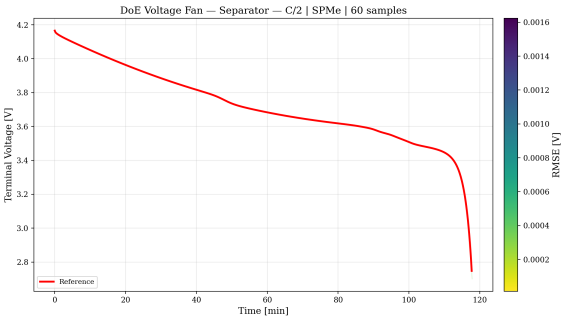


Figure 5.36: Voltage curves at C/2

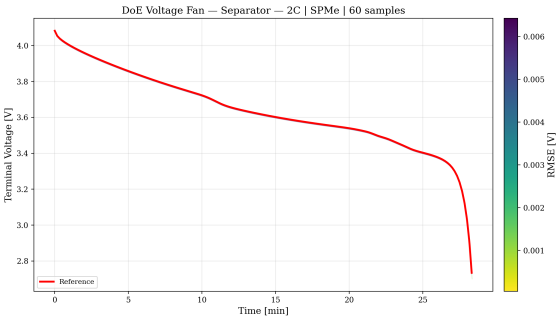


Figure 5.37: Voltage curves at 2C

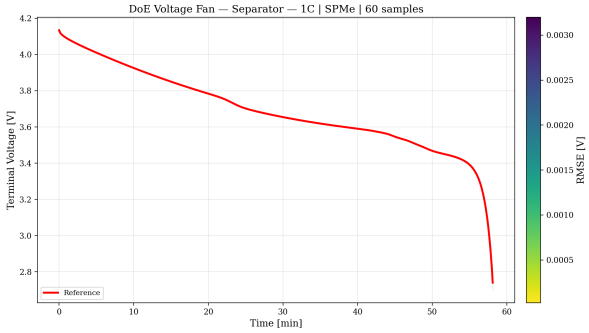


Figure 5.38: Voltage curves at 1C

Both Sobol and Spearman indices evaluate similar sensitivity values for separator-related properties, almost the same ones for the two parameters.

The voltage-fan plots clearly describe the null-impact of these parameters on cell's terminal-voltage, so they are basically negligible in the parameter calibration.

Parameter-sensitivity: Group-4

The fourth group includes various parameters related to electrode's micro-structure properties, i.e. porosities, active-material (AM) volume fractions, particle radii, Bruggeman coefficients, maximum Li-ion concentrations.

First sub-group The first sub-group explores the electrolyte-phase transport effectiveness toward electrodes; the related parameters are electrode porosities and Bruggeman coefficients. Both parameter types govern the effective ionic conductivity and diffusivity inside the porous electrode via the Bruggeman relation:

$$D_{e,eff} = D_e \cdot \varepsilon_e^b$$

$$\kappa_{eff} = \kappa \cdot \varepsilon_e^b$$

Overall, from literature studies, these parameters are consistently considered as moderate-to-low sensitivity parameters for terminal-voltage. An important note: the Kokam cell has a HP design that affects some properties of the electrodes, such as the porosities, which are typically higher with respect to a HE cell, in order to facilitate the ionic transport at high current-densities.

Table 5.10 summarizes the physical ranges used to evaluate the sensitivity of the four parameters.

Parameter Name	**Range's Bounds**
Cathode porosity ($\varepsilon_{e,p}$)	(0.20, 0.45)
Anode porosity ($\varepsilon_{e,n}$)	(0.20, 0.50)
Cathode Bruggeman coefficient (b_p)	(1.3, 2.5)
Anode Bruggeman coefficient (b_n)	(1.3, 2.5)

Table 5.10: First sub-group: parameter ranges

Finally, Figures 5.39 and 5.40 show the sensitivity values of the two used indices, whereas Figures 5.41, 5.42, and 5.43 represent the voltage-fan plots at various C-rates.

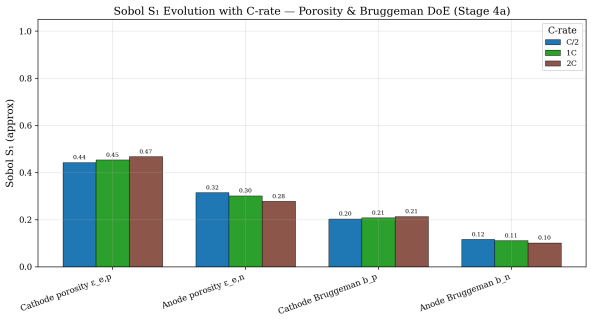


Figure 5.39: First-order Sobol-Index

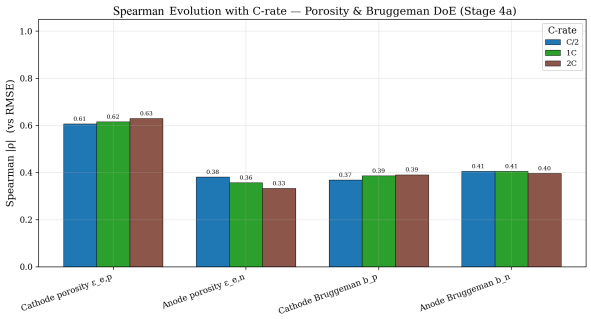


Figure 5.40: Spearman-Index

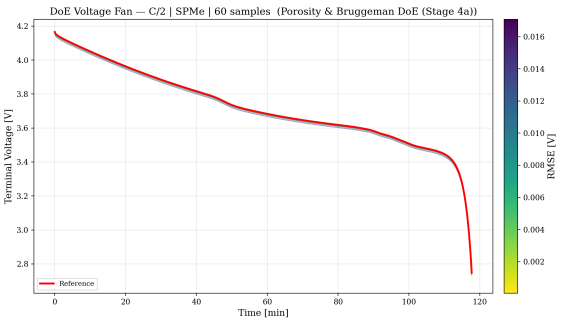


Figure 5.41: Voltage curves at C/2

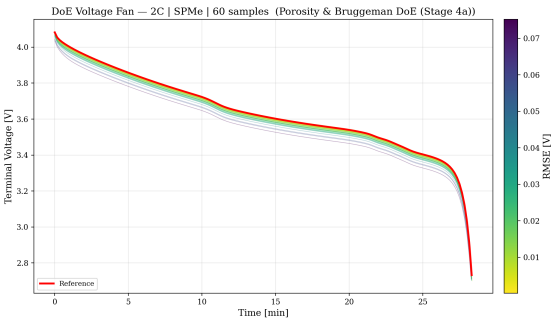


Figure 5.42: Voltage curves at 2C

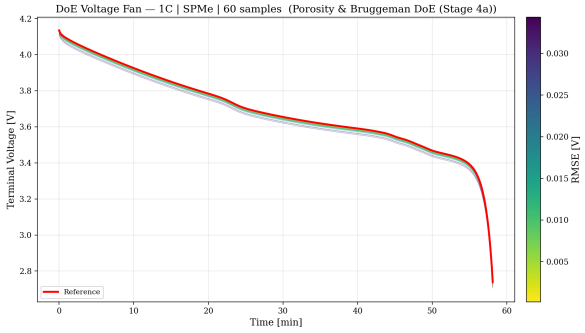


Figure 5.43: Voltage curves at 1C

The sensitivity plots show similar rankings for the parameters, although the most reliable results are always from first-order Sobol index: cathode quantities are predominant in the model output, with porosities showing a moderate sensitivity, while Bruggeman coefficients showing low sensitivity.

The voltage discharge curves underline the increasing impact of the four analyzed parameters with higher C-rates, shifting the curves in vertical direction.

Second sub-group The second sub-group focuses on two electrode parameters: anode and cathode active-material volume fractions ($\varepsilon_{s,p}$ and $\varepsilon_{s,n}$).

In general, the active-material volume fractions control: (i) the specific interfacial area ($a_k = 3 \cdot \varepsilon_{s,k}/R_{p,k}$); (ii) the effective capacity per unit of electrode volume; (iii) the volumetric solid-phase reaction rate (via a_k).

Literature works consistently rank them as high-sensitivity parameters for terminal-voltage, and among the most impactful micro-structural quantities.

Furthermore, from High-Power design considerations, HP electrodes typically have lower active material fractions than HE designs; this means more porosity traded for Li-ions transport (as seen in sub-section 1.3.2).

Table 5.11 summarizes the applied ranges for the active-volume fractions analyzed in this sub-group.

Parameter Name	**Range's Bounds**
Cathode active-material volume fraction ($\varepsilon_{s,p}$)	(0.30, 0.65)
Anode active-material volume fraction ($\varepsilon_{s,n}$)	(0.35, 0.70)

Table 5.11: Second sub-group: parameter ranges

Thus, in Figures 5.44 and 5.45 the sensitivity levels of the two coefficients are shown, whereas Figures 5.46, 5.47, and 5.48 report the voltages-fan plots at the three common rates.

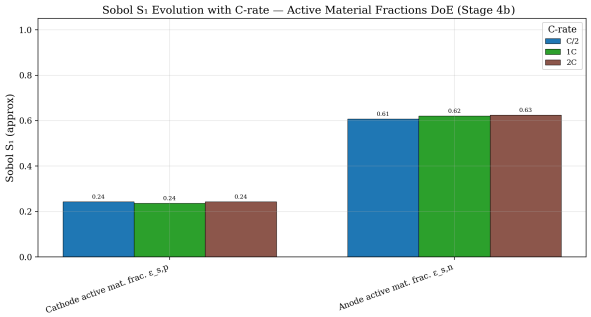


Figure 5.44: First-order Sobol-Index

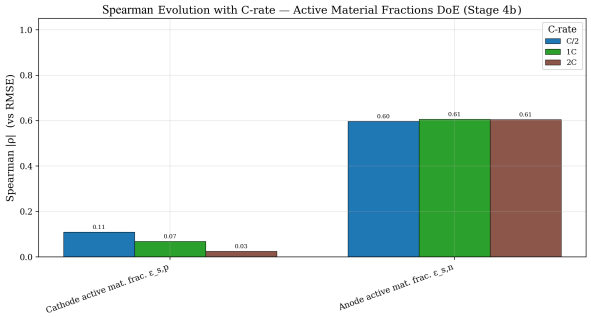


Figure 5.45: Spearman-Index

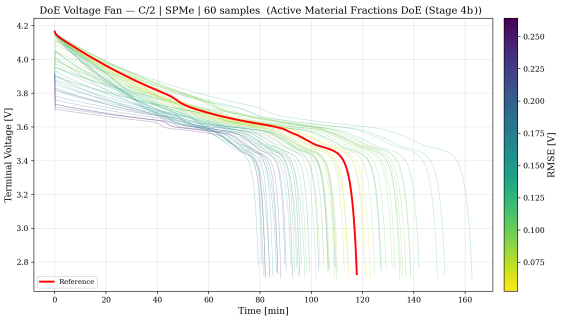


Figure 5.46: Voltage curves at C/2

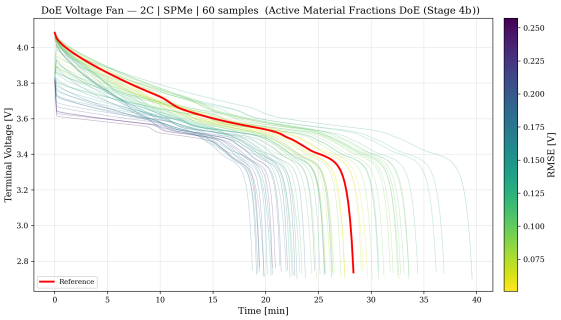


Figure 5.47: Voltage curves at 2C

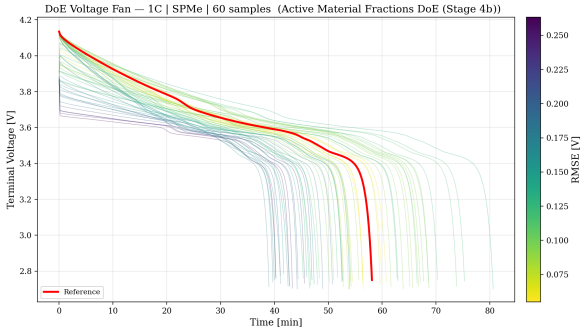


Figure 5.48: Voltage curves at 1C

Both sensitivity indices describe a slightly different situation from literature: in this case, anode active-material volume fraction has more impact on the terminal-voltage, with respect to their cathode counter-part; this mainly depends on the ranges adopted for DoE-based analysis.

Meanwhile, the voltage discharge curves at every rate highlight the great importance of these parameters for the capacity-side, manifested through horizontal shifts. It is worth noting the same impact of these properties on the terminal-voltage, independently of the adopted C-rate.

Third sub-group The third sub-group analyzes the impact of electrode's particle radii ($R_{p,p}$ and $R_{p,n}$) on cell's voltage.

The particle radii control: (i) the solid-phase diffusion time-scale ($\tau_D = R_p^2/D_s$), making them dominate the concentration-gradient overpotential inside the particles; (ii) the specific interfacial (electrode-electrolyte) area ($a_k = 3 \cdot \varepsilon_{s,k}/R_{p,k}$).

Both effects sharpen as current increases, so the particle radii are expected to gain sensitivity from C/2 to 2C. Literature generally ranks them as high-sensitivity parameters for terminal-voltage.

Finally, considering High-Power cell designs, typically they may use smaller particles to reduce solid-phase diffusion limitations at high C-rates (as seen in sub-section 1.3.2).

Table 5.12 summarizes the used ranges for the electrode's particle radii analyzed in this sub-group.

Parameter Name	**Range's Bounds**
Cathode particle radius ($R_{p,p}$)	(1.0, 11.0) μm
Anode particle radius ($R_{p,n}$)	(1.5, 12.0) μm

Table 5.12: Third sub-group: parameter ranges

In Figures 5.49 and 5.50 the two sensitivity indices are illustrated for these parameters, whereas Figures 5.51, 5.52, and 5.53 report the voltages-fan plots at the three different C-rates.

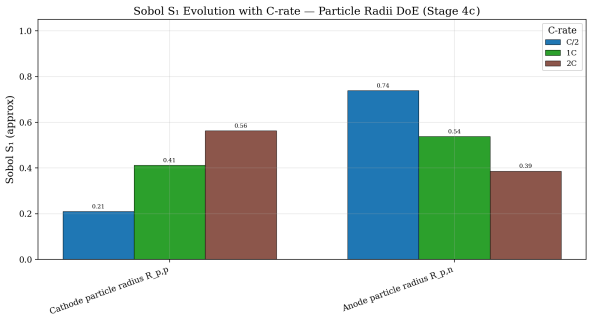


Figure 5.49: First-order Sobol-Index

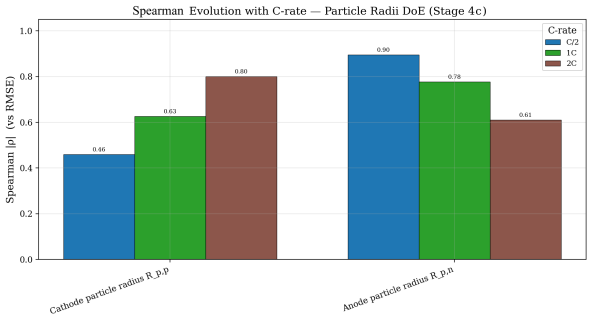


Figure 5.50: Spearman-Index

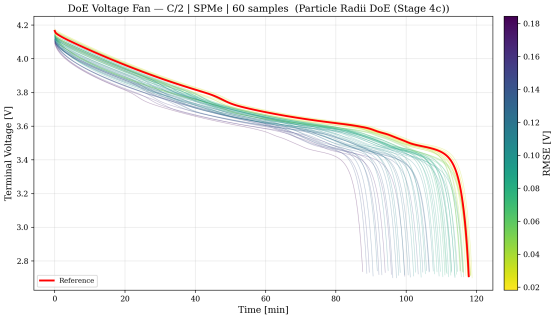


Figure 5.51: Voltage curves at C/2

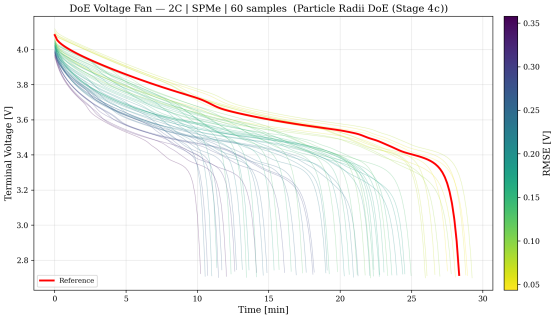


Figure 5.52: Voltage curves at 2C

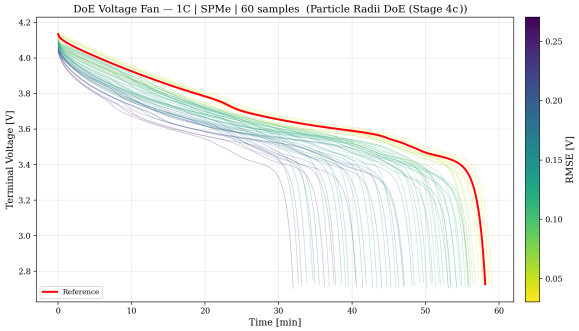


Figure 5.53: Voltage curves at 1C

The two sensitivity indices indicate a similar impact of the electrode's particle radii on terminal-voltage. In particular, their weight vary clearly across the various C-rates, with cathode particle radius becoming more important at higher C-rates, while the exact opposite case occurs for anode particle radius.

Meanwhile, the voltage-fan plots show a similar situation: the discharge curves, at every rate, highlight the influence of these two parameters for the mass-transport phenomenon, through mainly vertical shifts. The influence of particle-radii typically increases with C-rate, as seen in the three plots, passing from C/2 to 2C.

Fourth sub-group The fourth sub-group analyzes two fundamental electrode parameters, i.e. the maximum lithium concentrations in the solid-electrode particles. They are: (i) $c_{s,max,p}$ - NMC cathode crystallographic limit; (ii) $c_{s,max,n}$ - Graphite anode crystallographic limit.

These parameters are chemistry-locked, determined by the crystal structure of the active materials. They are among the very highest sensitivity parameters for terminal-voltage, because they directly control: (i) the theoretical electrode capacity $Q \quad \alpha \quad c_{s,max}$; (ii) the stoichiometric range $\theta = c_s/c_{s,max}$; (iii) the OCP curves mapping from concentration to voltage.

In general, the effective $c_{s,max}$ values in a porous composite electrode can differ from the ideal single-crystal value, due to inactive material, incomplete lithiation pathways and particle-size distributions.

In Table 5.13, the bounds of variation for the two analyzed parameters are shown.

Parameter Name	**Range's Bounds**
Cathode maximum Li concentration ($c_{s,max,p}$)	(45000, 53000) mol/m^3
Anode maximum Li concentration ($c_{s,max,n}$)	(26000, 33500) mol/m^3

Table 5.13: Fourth sub-group: parameter ranges

Then, in Figures 5.55 and 5.54 sensitivity levels are reported using the two indices, whereas in Figures 5.56, 5.57, and 5.58 the voltage-fan plots are presented at every C-rate.

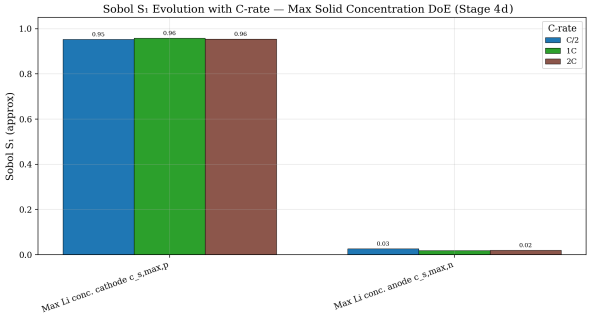


Figure 5.54: First-order Sobol-Index

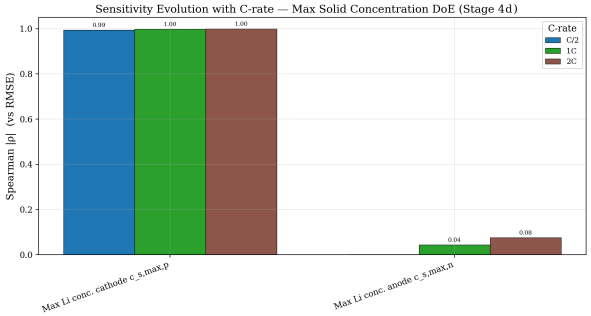


Figure 5.55: Spearman-Index

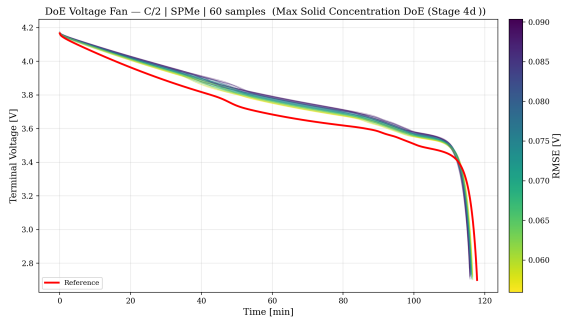


Figure 5.56: Voltage curves at C/2

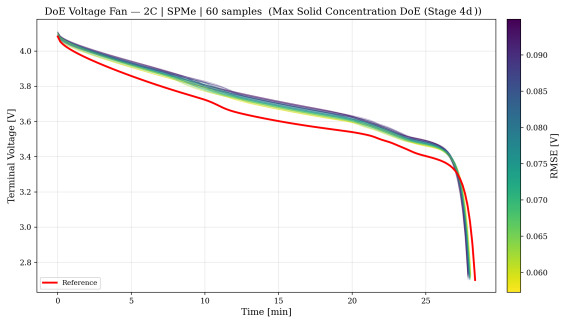


Figure 5.57: Voltage curves at 2C

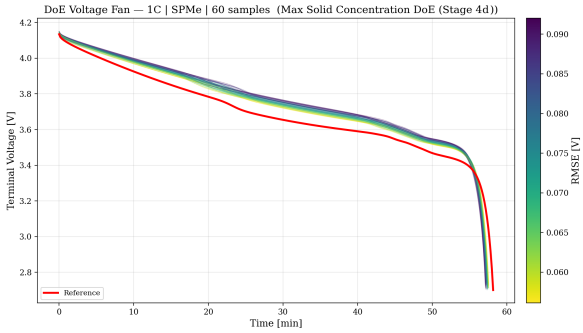


Figure 5.58: Voltage curves at 1C

Both graphs for sensitivity indices are very clear: there is an absolute predominance of cathode's maximum Li-concentration with respect to anode's one.

The voltage discharge curves vary relatively to the quantities that these parameters can affect, causing a more evident vertical shift, due to their influence for some thermodynamic aspects, rather than a severe change of electrode's capacity.

Parameter-sensitivity: Group-5

The fifth group of parameters includes different characteristic features regarding transport and kinetics of electrodes, i.e. solid-state diffusivity, reaction-rate constants, electrode's conductivities, charge-transfer coefficients, and film-resistances.

First sub-group The first sub-group focuses on solid-phase diffusivities, using the classical function-parameter approach, i.e. multiplicative scaling. Therefore, the perturbed model is evaluated through two factors; the new diffusivities become:

$$D_{s,p,modified}(y,T) = \alpha_{D_{s,p}} \cdot D_{s,p,original}(y,T)$$

$$D_{s,n,modified}(x,T) = \alpha_{D_{s,n}} \cdot D_{s,n,original}(x,T)$$

where: $\alpha_{D_{s,p}}$ is the cathode diffusivity multiplier, and $\alpha_{D_{s,n}}$ is the anode diffusivity multiplier.

In PyBaMM's parameter-sets, the solid-phase diffusivities are stored as functions of stoichiometry and temperature, not as scalar constants.

Solid-phase coefficients are among the most sensitive transport parameters in an NMC/graphite cell. Basically, they control lithium-ion transport within the active material particles, affecting concentration gradients and over-potentials. In the SPMe, D_s enters the solid-phase diffusion equation, directly controlling the particle-level concentration dynamics.

Table 5.14 reports the range's bounds chosen for the particle-diffusivities, considering that log-scale sampling of the multiplicative factors is essential to explore the full physically reasonable range.

Parameter Name	**Range's Bounds**
Positive-particle diffusivity multiplier ($\alpha_{D_{s,p}}$)	(0.01, 100)
Negative-particle diffusivity multiplier ($\alpha_{D_{s,n}}$)	(0.01, 100)

Table 5.14: First sub-group: parameter ranges

Figures 5.59 and 5.60 represent the plots for the sensitivity rankings related to the two indices, whereas Figures 5.61, 5.62, and 5.63 show the voltage-fan plots at the three C-rates.

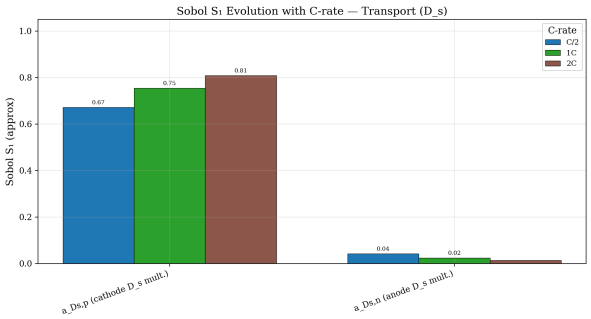


Figure 5.59: First-order Sobol-Index

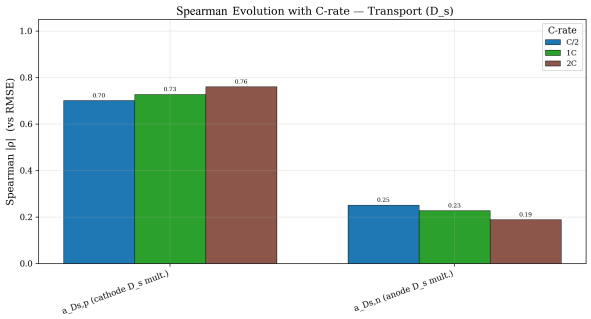


Figure 5.60: Spearman-Index

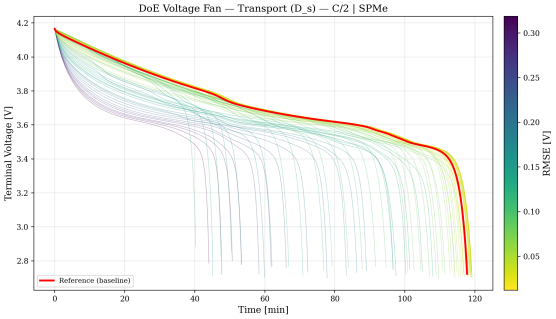


Figure 5.61: Voltage curves at C/2

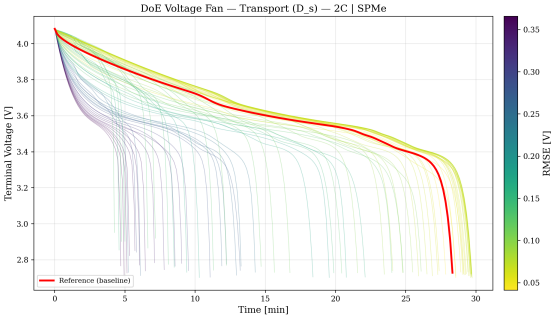


Figure 5.62: Voltage curves at 2C

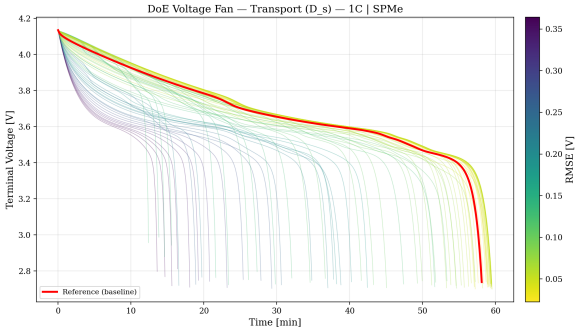


Figure 5.63: Voltage curves at 1C

The two plots on sensitivity levels report a similar assessment: the impact of positive-particles diffusivity is wider than the one of negative-particle one (this is confirmed also by literature studies, e.g. Li et al. (2020) [35] and Ma et al. (2023) [38]).

Meanwhile, the voltages curves at the three rates tell a clear story: the voltage shape is heavily affected by diffusivity functions, and the effect is more evident at high C-rates, according to electrochemical phenomena inside the battery.

Second sub-group The second sub-group analyzes the sensitivity of parameters related to Butler-Volmer kinetics. They are four parameters: reaction-rate constants ($k_{0,p}$, $k_{0,n}$) applied to "Exchange-current density" functions, and charge-transfer coefficients (α_c, α_a).

The interfacial reaction-rate at each electrode obeys the Butler-Volmer equation, with $\alpha_a + \alpha_c = 1$ as single-electron transfer constraint. Therefore, reaction-rate constants are scaled to set the magnitudes of the kinetic response. Meanwhile, charge-transfer coefficients are applied to set the asymmetry of the response between the anodic and the cathodic branches. The quantities are not independent physical mechanisms, rather two coefficients of the same equation.

An important note: actually, PyBaMM's default intercalation-kinetics option is "symmetric Butler-Volmer", which uses the following simplified form to express the interfacial (reaction) current density:

$$j = 2 \cdot j_0 \cdot sinh\left(\frac{F \cdot \eta_{act}}{2 \cdot R \cdot T}\right)$$

where: j_0 is the scalar exchange-current density, tied to k_0 coefficient.

Table 5.15 expresses the bounds applied in this sub-group for the typical Butler-Volmer parameters.

Parameter Name	**Range's Bounds**
Cathode reaction-rate constant multiplier ($k_{0,p,scale}$)	(0.1, 10)
Anode reaction-rate constant multiplier ($k_{0,n,scale}$)	(0.1, 10)
Cathode charge-transfer coefficient (α_c)	(0.45, 0.55)
Anode charge-transfer coefficient (α_a)	(0.45, 0.55)

Table 5.15: Second sub-group: parameter ranges

In Figures 5.64 and 5.65 the two used sensitivity indices are reported, whereas in Figures 5.66, 5.67, and 5.68 the voltage-fan plots at three rates are shown.

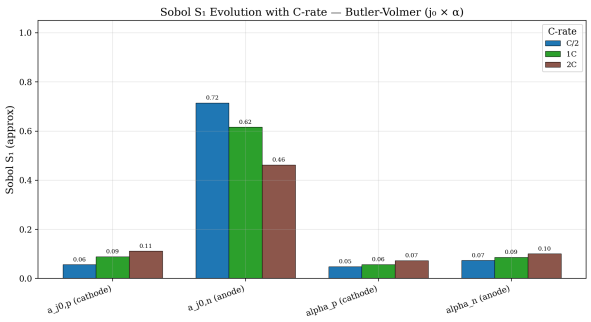


Figure 5.64: First-order Sobol-Index

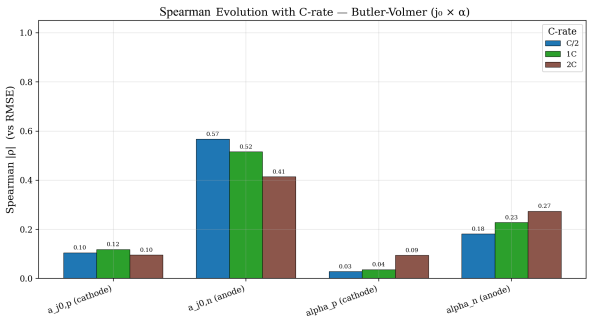


Figure 5.65: Spearman-Index

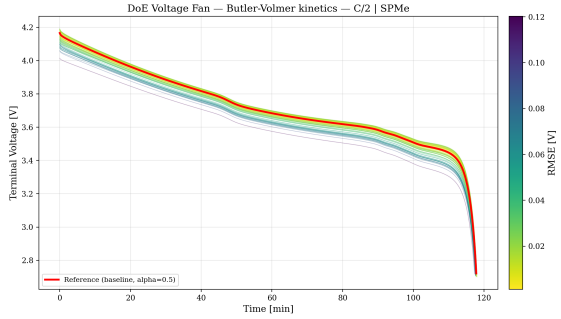


Figure 5.66: Voltage curves at C/2

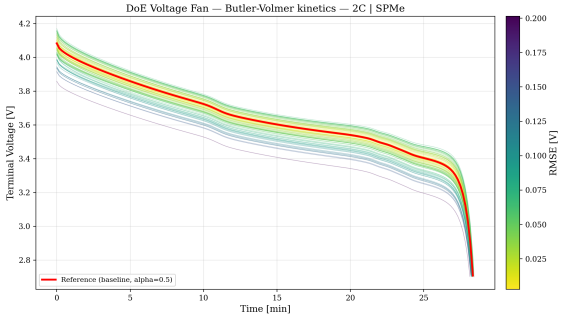


Figure 5.67: Voltage curves at 2C

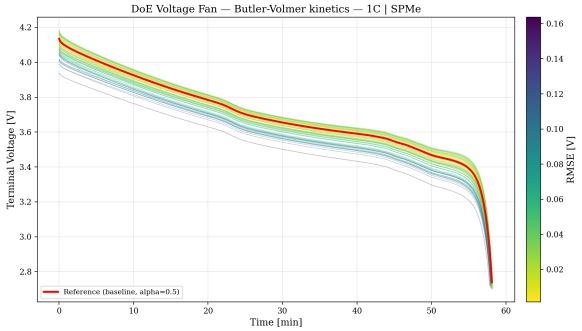


Figure 5.68: Voltage curves at 1C

From the plots on sensitivity indices, the assessment is similar, but slightly different from literature: $k_{0,p}$ scaling is less impactful than its counter-part $k_{0,n}$ one. As said before, typically charge-transfer coefficients are symmetric (both equal to 0.5), so they will have low impact on the terminal-voltage.

The voltage-fan plots are evidently coherent with the expected behavior: higher C-rates increases the kinetic aspects importance on the model output, shifting the voltage curves in vertical direction.

Third sub-group The third sub-group is related to electrode conductivities of electrons. The two corresponding parameters are: positive-electrode conductivity $\sigma_{s,p}$, and negative-electrode conductivity $\sigma_{s,n}$.

In general, the electronic conductivities of the solid-electrode matrix determine the electronic current distribution in the porous electrodes. From sensitivity articles, it is clear that $\sigma_{s,p}$ and $\sigma_{s,n}$ are ranked among the least sensitive parameters for terminal-voltage in NMC/graphite cells. This is due to the fact that electronic conductivity of the composite electrodes is typically several orders of magnitude higher than the ionic conductivity of the electrolyte, so in comparison their effect is negligible.

In Table 5.16, the ranges of variation used for electrode conductivities are presented.

Parameter Name	**Range's Bounds**
Cathode conductivity ($\sigma_{s,p}$)	(3, 316) S/m
Anode conductivity ($\sigma_{s,n}$)	(10, 3162) S/m

Table 5.16: Third sub-group: parameter ranges

Then, Figures 5.69 and 5.70 show the sensitivity levels using the two indices, whereas Figures 5.71, 5.72, and 5.73 report the voltage-fan plots at various C-rates.

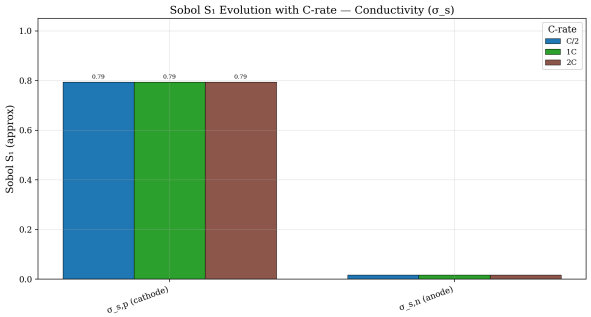


Figure 5.69: First-order Sobol-Index

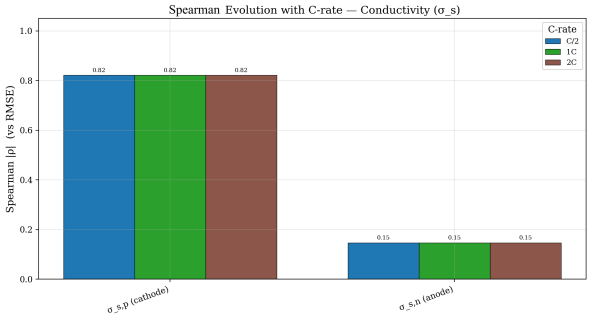


Figure 5.70: Spearman-Index

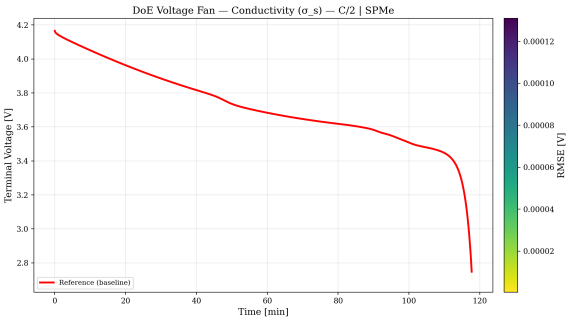


Figure 5.71: Voltage curves at C/2

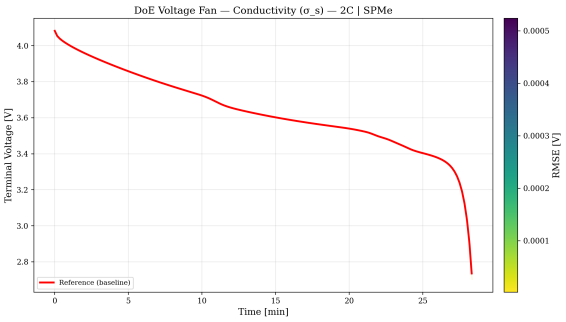


Figure 5.72: Voltage curves at 2C

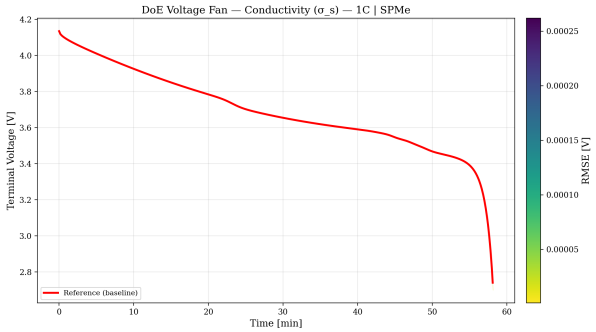


Figure 5.73: Voltage curves at 1C

The Sobol and Spearman indices evaluate a similar ranking for cathode and anode conductivities; also here, the cathode quantity is more relevant than anode one for the model output.

The voltage discharge curves are practically unchanged, confirming the null-impact of these parameters on cell's response.

Fourth sub-group The fourth sub-group completes the analysis perturbing the two per-electrode interfacial film-resistances of SPMe: anode/graphite film-resistance $R_{f,n}$, and cathode/NMC film-resistance $R_{f,p}$.

In general, a film-resistance is a thin, electronically/ionically resistive layer at the electrode-electrolyte interface (SEI-layer on graphite, CEI/contact and passivation films on NMC, plus any cell-built contact lumped resistance). Its signature in the cell-voltage is purely ohmic:

$$\Delta V_{film} = R_f \cdot j$$

where: R_f is the film resistance expressed in Ωm^2, and j is the interfacial current-density expressed in A/m^2. The voltage-drop is instantaneous, linear in current, and with no-time constant.

In the PyBaMM implementation, the two film-resistances are not explicit parameters. For this reason, the two quantities are injected through two different independent ohmic-resistance levers, which the tool provides for a full-cell.

Thereby, they are included among the other parameters in this way: (A) $R_{f,n}$ is implemented through negative-electrode SEI film-resistance; (B) $R_{f,p}$ is implemented through cell-level contact resistance. The two quantities are computed as:

$$R_{f,n} = \rho_{SEI} \cdot L_{SEI} \quad [\Omega \cdot m^2]$$

$$R_{f,p} = R_{contact} \cdot A_p \quad [\Omega \cdot m^2]$$

where: ρ_{SEI} is the SEI-layer resistivity, L_{SEI} is the SEI-layer thickness, $R_{contact}$ is the lumped contact resistance, and A_p is contact area.

Table 5.17 reports the bounds used for the ranges of variation applied for the film-resistances.

Parameter Name	**Range's Bounds**
Cathode film-resistance ($R_{f,p}$)	(1, 100) $\Omega \cdot cm^2$
Anode film-resistance ($R_{f,n}$)	(1, 100) $\Omega \cdot cm^2$

Table 5.17: Fourth sub-group: parameter ranges

Thus, Figures 5.74 and 5.75 show the levels of sensitivity indices, while Figures 5.76, 5.77, and 5.78 represent the voltage-fan plots at the three rates.

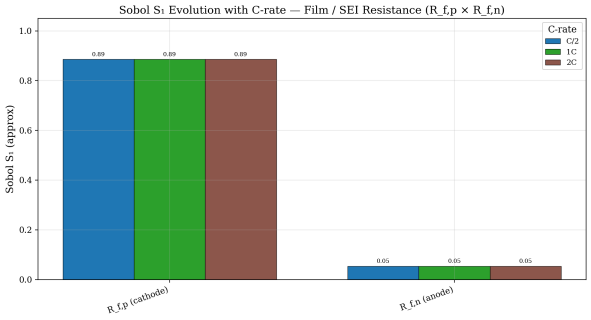


Figure 5.74: First-order Sobol-Index

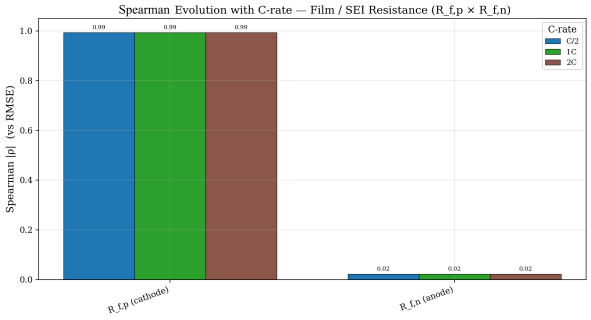


Figure 5.75: Spearman-Index

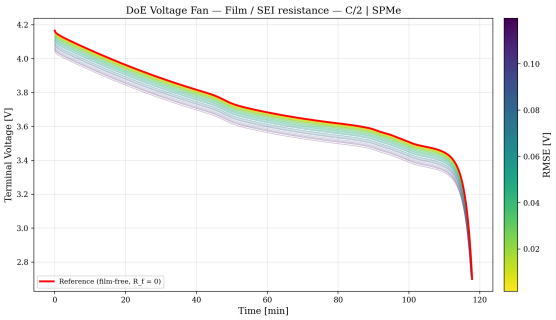


Figure 5.76: Voltage curves at C/2

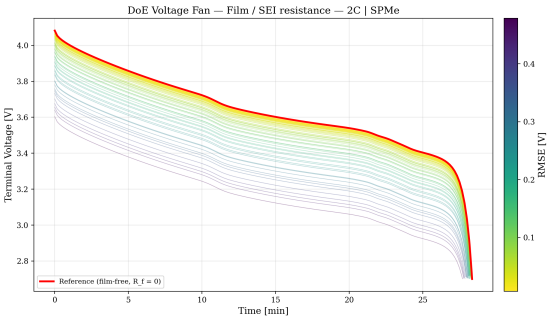


Figure 5.77: Voltage curves at 2C

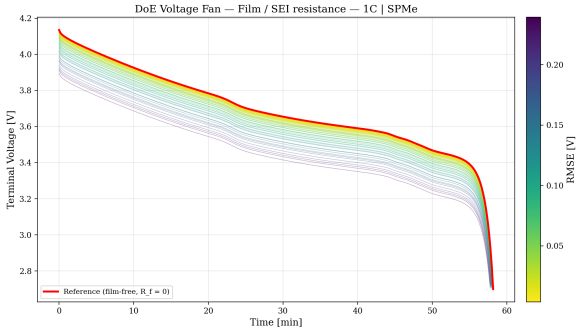


Figure 5.78: Voltage curves at 1C

The impact of film-resistance is split between anode and cathode in a different way: cathode contribution is more decisive on the model response with respect to anode one. However, for convention, in the future parametrization, only $R_{f,n}$ will be initialized to a certain value.

The voltage discharge curves highlight the weight of these ohmic parameters for the model output, causing an instantaneous decrease of voltage at every time, and the effect is remarked at higher rates.

5.3.3 Summary of Sensitivity-Analysis

After the end of deep study of electrochemical model's parameters, it is important to summarize the results obtained, before proceeding with the effective parameterization workflow.

According to literature studies (Li et al. (2020) [35], J. Chen et al. (2025) [36], Ma et al. (2023) [38], Liu et al.(2025) [37]), and personal DoE-based Sensitivity-Analysis, different qualitative levels of sensitivity, on a common scale, were attributed to the PyBaMM parameter-set, as shown in the following Table 5.18.

SPMe Parameter	Sensitivity-level
Nominal cell capacity (Q_{nom})	High
Voltage window ($V_{min},\ V_{max}$)	High
Number of internal layers (N_{layers})	High
Electrode height (H_{elc})	High
Electrode width (W_{elc})	High
Cathode thickness (L_p)	Very High
Anode thickness (L_n)	Very high
Separator thickness (L_s)	Low
Current-collectors (Al, Cu) thicknesses (L_{cc})	Low
Cathode OCP ($U_p(y)$)	Very High
Anode OCP ($U_n(x)$)	Very high
Cathode stoichiometries (y_0, y_{100})	Very High
Anode stoichiometries (x_0, x_{100})	Very High
Electrolyte conductivity ($\kappa(c_e)$)	Low
Electrolyte diffusivity ($D_e(c_e)$)	Low
Transference number (t_0^+)	Low
Initial electrolyte concentration ($c_{e,0}$)	Low
Thermodynamic factor (f_T)	Low
Separator porosity (ε_s)	Low
Separator Bruggeman (b_s)	Low
Cathode porosity ($\varepsilon_{e,p}$)	Moderate
Anode porosity ($\varepsilon_{e,n}$)	Moderate
Cathode active-material fraction ($\varepsilon_{s,p}$)	High
Anode active-material fractions ($\varepsilon_{s,n}$)	High
Positive particle radius ($R_{p,p}$)	High
Negative particle radius ($R_{p,n}$)	High
Cathode Bruggeman (b_p)	Low
Anode Bruggeman (b_n)	Low
Maximum cathode Li-concentration ($c_{s,max,p}$)	Very High
Maximum Anode Li-concentration ($c_{s,max,n}$)	Very High
Positive particle diffusivity ($D_{s,p}(y)$)	Very High
Negative particle diffusivity ($D_{s,n}(x)$)	Very high
Cathode Reaction-rate constant ($k_{0,p}$)	High
Anode Reaction-rate constant ($k_{0,n}$)	High
Charge-transfer coefficients (α_c, α_a)	Low
Cathode film-resistance ($R_{f,p}$)	Low
Anode SEI-resistivity (ρ_{SEI})	Moderate
Cathode conductivity ($\sigma_{s,p}$)	Low
Anode conductivity ($\sigma_{s,n}$)	Low

Table 5.18: Parameter-groups sensitivity-levels for the Parametrization procedure

A general summary of the entire Sensitivity-Analysis can be shown in the following pictures.

In Figure 5.79, the scheme of the entire Workflow for the personal DoE-based (with LHS method) Sensitivity-Analysis is shown, with a description of the main steps.

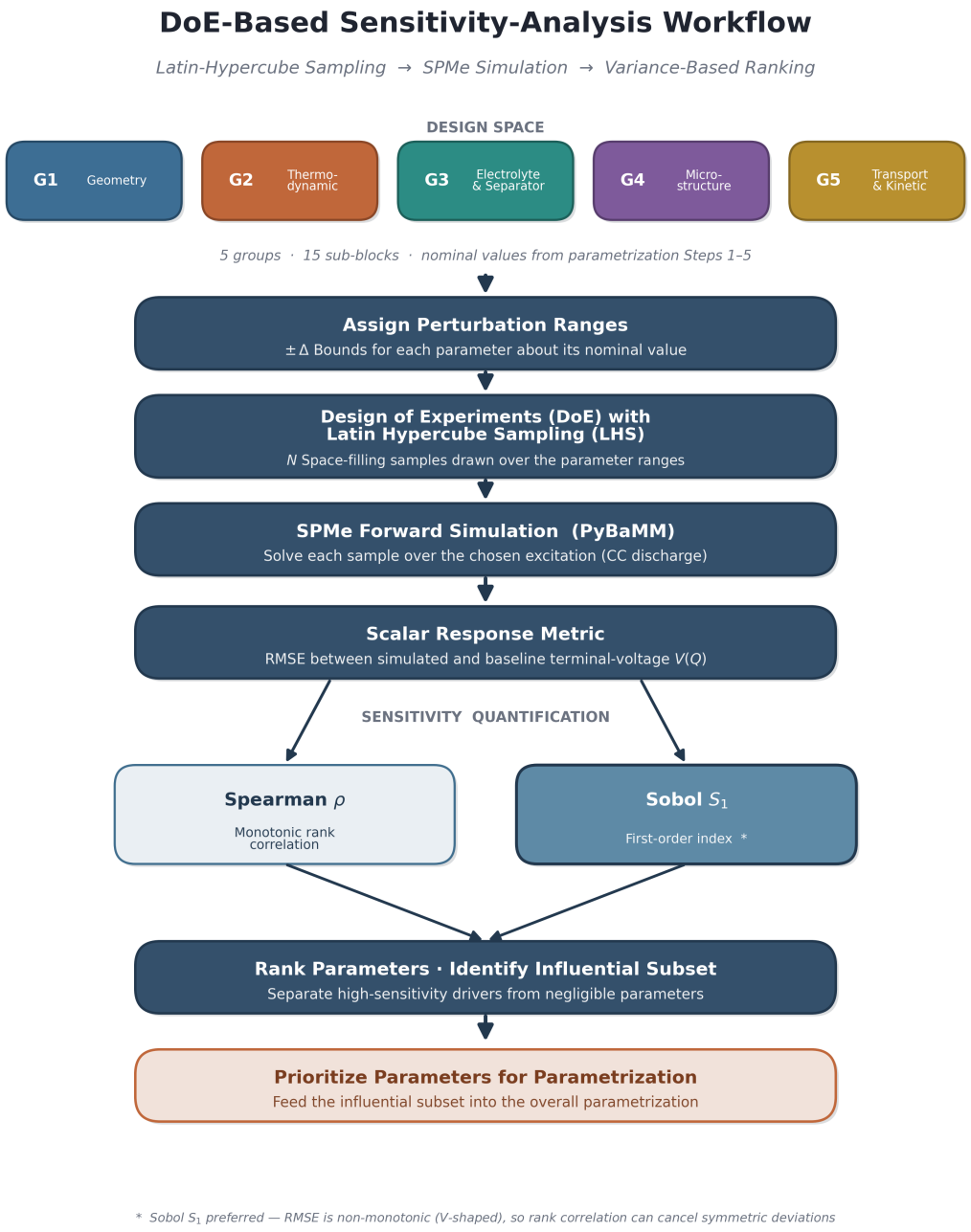


Figure 5.79: DoE-based Sensitivity Analysis: Adopted Workflow

Meanwhile, the diagram of the 5 analyzed parameter groups, for the sensitivity-analysis, and the subsequent SPMe parametrization, is illustrated in Figure 5.80.

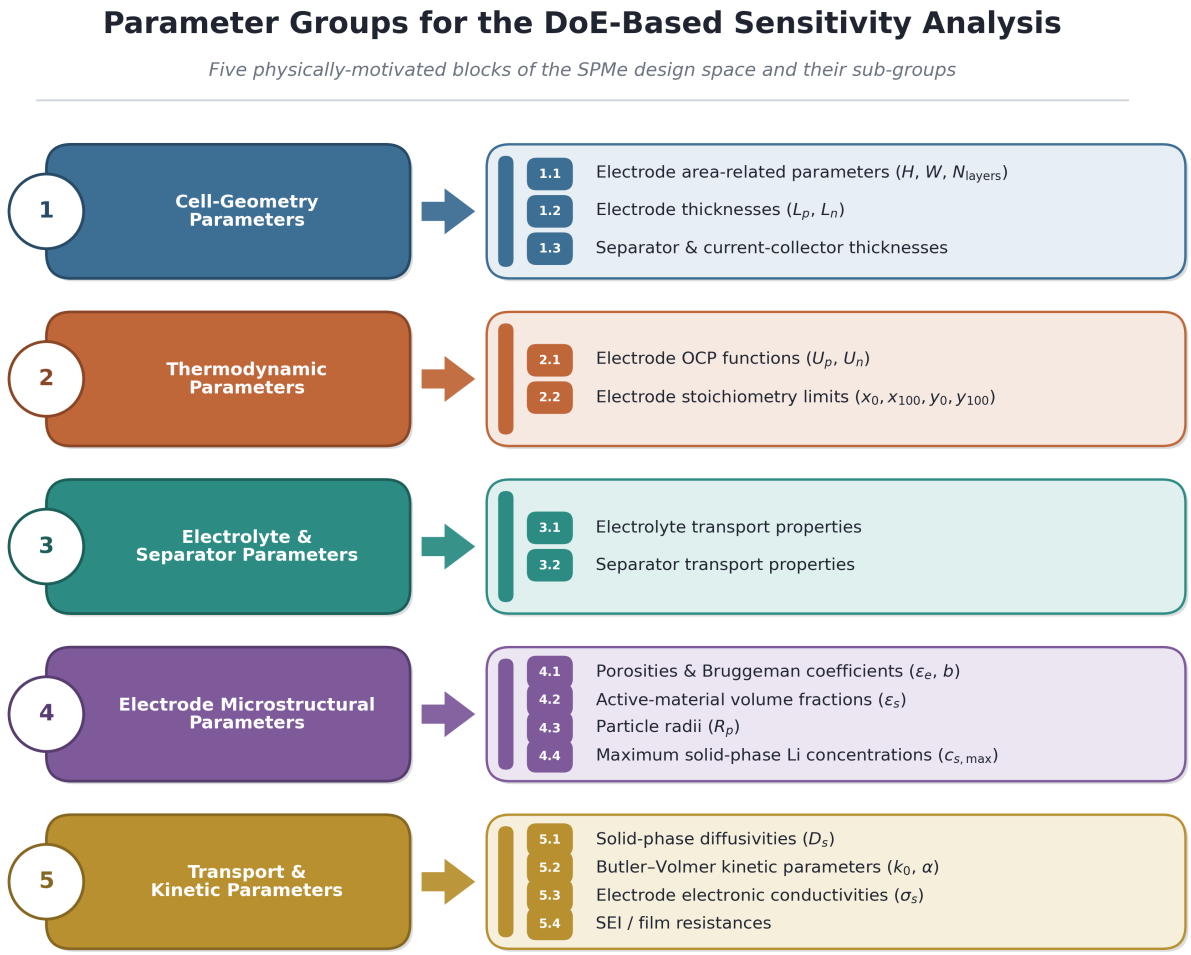


Figure 5.80: Parameter groups for SPMe Modeling

5.4 SPMe General Parametrization Strategy

The parametrization of a physics-based lithium-ion battery model is a decisive stage in the construction of a reliable simulation framework, because the predictive capability of the model depends directly on the physical consistency and identifiability of its input parameters.

The Parametrization of the adopted electrochemical model, i.e. SPMe, for the Kokam SLPB55205130H cell proceeds along a structured, seven-step workflow, that progressively transforms a generic NMC/graphite reference parameter-set into a cell-specific calibrated model. The procedure is designed for a full-cell experimental characterization, as described in section 3.3, in which neither electrode teardown nor ex-situ chemical testing is available; therefore, every parameter must be obtained from the manufacturer datasheet, from the published literature, or from the suite of full-cell electrochemical tests performed on the cell.

Following F. Brosa Planella et al. (2022) [8], the SPMe is characterized by thirty parameters, in addition to the physical constants and the applied current, as anticipated in sub-section 4.3, and the workflow assigns each of these parameters an explicit estimation route. Three estimation methods recur throughout the description of strategy below: (i) Method A (literature or datasheet values), (ii) Method B (physics-informed pre-estimation, or direct extraction from tests data), and (iii) Method C (fitting or optimization against experimental measurements).

Rationale of Parametrization Strategy

The ordering of these steps is deliberate. It is based on the previous Sensitivity-Analysis, with the main results summarized in sub-section 5.3.3. Parameters that are insensitive for the terminal-voltage response are fixed from the literature, whereas the high-sensitivity parameters are reserved for the central fitting step and determined on the firmest possible empirical footing (considering the High-Power design features, as exposed in sub-section 1.3.2).

This prioritization follows the reviewed sensitivity-analysis works for Li-ion battery cells: Li et al. (2020) [35], J. Chen et al. (2025) [36], and Ma et al. (2023) [38], which ranked the physical parameters of an electrochemical model by their normalized sensitivity index and showed that only a subset materially influences the predicted voltage, while Liu et al. (2025) [37] formalized the complementary strategy of optimizing the high-sensitivity parameters and assigning fixed values to the rest. The "Mohtat2020" parameter-set (Mohtat et al. (2020) [13]) supplies the reference functional forms and the starting parameter values, as exposed in sections 5.1 and 5.2, whereas the overall framework draws on the teardown based parametrization methodology of Chen et al. (2020) [4].

Furthermore, a central consideration for the whole strategy is the structural distinction between the High-Power (HP) Kokam cell, studied here, and the High-Energy (HE) Kokam cell, characterized by Ecker et al. (2015) [16] [17]. As explained in sub-section 1.3.2, HP cells employ thinner electrode coatings and higher porosities to support fast charge and discharge, so the HE literature values are treated as upper bounds, rather than direct starting points.

5.4.1 Step 1 - Cell-level Geometry

The first Step establishes the macroscopic geometry and the capacity-scaling of the model from the manufacturer datasheet and general literature (Method A). The external dimensions, nominal capacity, mass and operating voltage window are read directly from the Kokam catalogue, and the electrode area is estimated from the pouch footprint and number of stacked layers. The equivalent single-layer geometry is mapped to the full-cell capacity through the framework's electrode-height scaling, which is physically equivalent to stacking additional identical layers. Moreover, this step fixes the geometric basis on which every subsequent micro-structural and transport parameter is defined.

5.4.2 Step 2 - Open-circuit Potentials and Electrode's Stoichiometries

The second Step anchors the thermodynamic behavior of the model, by determining the electrode's operating windows. The half-cell open-circuit potential (OCP) functions for the positive and negative electrodes are retained from the Mohtat's parameter-set, while the four stoichiometry limits, which delimit the lithiation range of each electrode are obtained by fitting (Method C). Because the measurable full-cell open-circuit voltage (OCV) is the difference of the two half-cell potentials, i.e.:

$$V_{cell}(SoC) = U_p(y) - U_n(x)$$

the stoichiometry limits are identified by minimizing the discrepancy between this model expression and the experimental near-equilibrium OCV, taken from the slow Pseudo-OCV test at C/50 (with alternative provided by GITT relaxation end-points). The optimization is a well-conditioned four-parameter problem, solved through a global differential-evolution search, followed by a local Nelder-Mead refinement, under an electrode state-of-health (SoH) voltage constraint (imposed at V_{max}). The resulting stoichiometry state-of-charge (SoC) mapping is foundational:

it fixes the correspondence between cell SoC and electrode's stoichiometries, on which every downstream step relies.

5.4.3 Step 3 - Electrolyte and Separator Properties

The third Step assigns the electrolyte transport properties and the separator parameters from literature (Method A). The exposed sensitivity studies and personal DoE-based sensitivity-analysis consistently rank these quantities as having a low influence on the terminal-voltage of NMC/graphite cells, justifying the choice to fix rather fit them. The concentration-dependent functional forms for the ionic conductivity and the salt diffusivity are basically reduced to scalar values, as adopted in the "Mohtat2020" parameter-set ([13]), and they are appropriate for the standard $LiPF_6$-based electrolyte of the cell. The electrolyte thermodynamic factor is initialized to a unit-value, considering an ideal electrolyte, whereas the remaining separator properties are frozen at their reference Mohtat's values. Treating this block as fixed reduces the dimensionality of the later optimization, without compromising the terminal-voltage accuracy.

5.4.4 Step 4 - Electrode's Microstructure Properties

The fourth Step initializes the electrode's microstructure, i.e., porosities, active-material volume fractions, particle radii, Bruggeman coefficients, and maximum solid lithium-concentrations, from the literature, with adjustments reflecting High-Power design (Method A). The maximum solid concentrations are chemistry-locked from crystallographic data of electrodes, thereby they remain fixed throughout, whereas the active-material fractions and particle radii are high-sensitivity quantities, that are deliberately left as provisional values, to be refined during the central fitting/optimization Step. Therefore, the Step 4 supplies physically reasonable starting points for the micro-structural parameters of electrodes, and identifies explicitly which of them will be subsequently optimized. The assumption of very-high sensitivity properties, i.e. maximum solid Li-concentrations, at literature values, is a crucial choice, because it will affect the final results, in terms deliverable capacity.

5.4.5 Step 5 - Transport, Kinetics, and Global Voltage Fitting

The fifth Step is the core of the entire workflow, and the point at which the experimental campaign is really exploited. It determines the kinetic and transport parameters that dominate the voltage response and that cannot be obtained reliably from literature alone. Moreover, it realizes a global optimization for 12 parameters, of which some are from Step 1 and others from Step 4. Rather than launching a single high-dimensional optimization, the Step is decomposed into a sequence of several sub-steps, which first reduce the search space through physics-informed pre-estimation (method B) and a data-driven OCP correction, and only then they perform a constrained global optimization (Method C). The pre-estimation sub-steps extract independent, physically interpretable starting values from dedicated experiments (e.g., GITT, HPPC, and constant-voltage (CV) holds), so that the optimizer is launched from a well-informed and tightly bounded region. This structure operationalizes the sensitivity-ranking-then-optimization philosophy shown by Li et al. (2020) [35], J. Chen et al. (2025) [36], Ma et al. (2023) [38], and Liu et al. (2025) [37]. The sub-steps are described in turn below.

Step 5a - Solid diffusivity of positive electrode from GITT

The apparent solid-phase diffusion coefficient of the cathode is pre-estimated from exploiting the GITT transients. During each current-pulse, the voltage evolves with the square-root of time, as

explained in sub-section 3.2.1, and the classical analysis for spherical particles is related to the slope of this transient (considering Weppner-Huggins approach [21]), together with the local slope of the equilibrium OCV; thereby, it is possible to extract the diffusion coefficient at the corresponding stoichiometry. Because the cathode dominates the overpotential over much of the operating range, the extracted values furnish a meaningful estimation of the cathode diffusivity, as a function of positive-electrode stoichiometry. These discrete estimates are condensed into a robust polynomial expressed in the native stoichiometry variable y, which serves as the cell-specific shape of the diffusivity; the optimization step later adjusts only its overall magnitude. The spherical-particle convention adopted for the diffusion coefficient, which matters when comparing values across studies, follows the high-power cell characterization of Schmalstieg et al. (2018) [18] [19].

Step 5b - Film and SEI resistance from HPPC

The lumped ohmic and film resistance is pre-estimated from the instantaneous voltage drop at the onset of each HPPC pulse, evaluated across several current levels and state-of-charge (SoC), through Method B. Following the "Mohtat2020" convention and the physical understanding that solid-electrolyte interface forms predominantly on the graphite electrode, this resistance is assigned to the negative electrode, and it is represented as a thin interface layer of fixed thickness, characterized by a bulk resistivity. The extracted profile provides the starting estimation for this resistance in the optimization.

Step 5c - Electrode's conductivities and charge-transfer coefficients

The solid-phase electronic conductivities, which are transport parameters for both electrodes, have typically low sensitivity terminal-voltage; therefore they are assigned their reference values at this stage. Meanwhile, the anodic and cathodic charge-transfer coefficients of the Butler-Volmer kinetics are taken to be symmetric, retaining the Mohtat's assumption of equal coefficients on both electrodes (Method A). This choice is supported by near-symmetric values reported for the related Kokam cell, by Ecker et al. (2015) ([16] [17]).

Step 5d - Reaction-rate constants from constant-voltage (CV) holds

The magnitude of the exchange-current density on each electrode, i.e. the reaction-rate constant, is pre-estimated from the current-decay envelope recorded during a constant-voltage hold (in a 1C complete cycle), at the upper cut-off of $4.2\ V$ (Method B). The decay is described by a double-exponential model, whose fast time-constant reflects the interfacial kinetics of cathode, whereas the slow time-constant is tied to some kinetic aspects and diffusion phenomena of anode. Matching both the simulated fast and slow time-constants to the measured ones yields multiplicative corrections to the reference reaction-rate constants. These scale-factors are passed as tightly constrained inputs to the subsequent optimization.

Step 5e - Cathode OCP correction from averaged C/50 data

Once the transport and kinetic parameters have been bounded, a small but systematic residual remains between the model and the measured voltage that cannot be removed within the physical bounds of an SPMe, carrying the default half-cell potentials. This residual is consistent with a mismatch between the reference cathode OCP and the true NMC potential of the cell; the present sub-step extracts a corrected, cell-specific cathode OCP directly from the experimental data. The correction is governed by an identifiability argument: since only the difference between the two OCP functions ($U_p(y)$ and $U_n(x)$) is observable from full-cell voltage, the entire correction is attributed

to the cathode by convention, with the better-characterized graphite potential held fixed at the one of "Mohtat2020" parameter-set. The corrected NMC potential is obtained by averaging the slow C/50 charge and discharge curves (Pseudo-OCV), to cancel hysteresis (as explained in section 3.4), and obtaining the resulting equilibrium estimation through the graphite OCP and the Step 2 stoichiometry mapping. A local regression of the residual, restricted to a trusted SoC window and projected onto a monotonic profile to preserve physical validity, yields a corrected cathode OCP, which is exported as a model-compatible function for use in the optimization (Method B $\rightarrow$ C).

Step 5f - Global Optimization

Considering the pre-estimations of the diffusivity-shape, the film resistance, the reaction-rate scales and the corrected cathode OCP, all established in the previous five sub-steps, 12 high-sensitivity parameters are refined jointly against the multi-rate constant-current discharge measurements (6 rates), through Method C. The optimization combines a global population-based search, Differential-Evolution, with local simplex refinement, Nelder-Mead already used in Step 2. The entire process is organized into three successive stages, that balance broad exploration against local polishing, while preserving the physical pre-estimates. A per-rate cost normalization ensures that each discharge rate contributes comparably to the objective, preventing the fast rates from dominating the fitting; furthermore, a volume-fraction closure couples the electrode's porosities to the corresponding active-material volume fractions, thereby the converged electrodes remain internally consistent.

More specifically, the three-tier architecture comprises: (1) the first stage with 9 parameters, from Step 1 (geometry), Step 4 (material properties) and Step 5a (diffusion/transport); (2) the second stage with 3 parameters, from steps 5b and 5d (kinetics); (3) the third stage with all 12 parameters for global-polish. Finally, the Step 5f delivers the effective parameter-set, that reproduces the cell behavior across the tested rates.

Step 5g - Diagnostic verification

Once the parameter-set is frozen, an independent diagnostic block verifies its physical consistency, without modifying any value. It compares the OCV anchors, used for fitting against the closest available estimation of true equilibrium, by overlaying the slow Pseudo-OCV curve with the GITT end-of-rest voltages; it checks that the model diffusion time-constants, τ_D (seen in 3.2.1 and 4.3), are consistent with the empirical relaxation times observed in each GITT rest; it documents the change from the literature-default functions to the fitted ones. Therefore, this Step provides an internal validation of the fitting outcomes and is purely diagnostic (no additional information inside the parametrization chain).

5.4.6 Step 6 - Thermal Parameters (optional)

The current SPMe is isothermal, although a lumped thermal model could be set, having proper data from testing. The sixth step can equip the optional lumped thermal model. The cell density, the specific heat capacity, the heat-transfer coefficient and the thermal conductivity are assigned from datasheet and literature, and the entropy coefficients are taken as functions of stoichiometry from the "Mohtat2020" parameter-set (Method A). Usually, the multi-temperature data may enable the activation energies governing the temperature dependence of some functions, through the Arrhenius fitting (as seen in sub-section 3.2.1 for solid-phase diffusivities).

5.4.7 Step 7 - Validation of the Canonical Parameter-Set

The final Step quantifies how faithfully the frozen parameter-set reproduces every available experimental test. The tests are classified according to their role in the parametrization, i.e. those used directly as optimization (training tests), those that contribute only to the pre-estimation of a single parameter (adjustment tests), and those that were never used at any stage (pure validation tests). Each of them is re-simulated with the same pre-conditioning protocol of the one used for real experiments. Reporting the agreement "simulation-experiment" separately for each class establishes the generalization behavior of the model, and delineates its domain of validity, distinguishing the regime in which the SPMe is faithful from the conditions under which its simplified assumptions begin to limit accuracy.

5.4.8 Conclusions of SPMe Parametrization

The seven Steps forms a coherent progression: from the macroscopic, datasheet-level description of the cell, through the thermodynamic anchoring of the electrode windows, the literature-based assignment of the low-sensitivity electrolyte and separator parameters, and the crucial electrode's micro-structural properties, to the physics-informed pre-estimation and global optimization of the high-sensitivity parameters; finally, the workflow is completed with diagnostic verification and general validation. Each parameter is traceable to one of the three estimation methods, and the sequence is constructed, so that the most consequential, and least directly measurable parameters are determined at the end, on the firmest empirical footing that the available full-cell campaign can provide.

5.4.9 Summary of the adopted Parametrization Procedure

A general summary of the SPMe Parametrization procedure could be useful to fix some basic concepts applied before, and to highlight the fundamental methods for parameters calibration, considering their sub-division in well-ordered steps and relative levels of sensitivity.

Estimation methods for model's parameters

In this Parametrization procedure, three methods of estimation are identified for the parameters of the electrochemical model. These methods are described in Table 5.19.

Method type	Estimation Method	Description
Method A	Literature / Data-sheet	Use of published references, manufacturer data, or "Mohtat2020" parameter-set
Method B	Empirical Tuning / Pre-estimation	Physics-informed adjustment or direct extraction from tests (GITT, HPPC, CV-hold in cycling)
Method C	Fitting / Optimization	Cost-function minimization (Differential-Evolution + Nelder-Mead methods) against experimental data

Table 5.19: Estimation methods for the Parametrization-Plan

During the Parametrization procedure, the following passages were typically adopted:

- Method A $\rightarrow$ Method C: Start from Literature (A), Refine via Optimization (C) in the core fitting step.
- Method B $\rightarrow$ Method C: Pre-estimate from test data (GITT/HPPC), then Refine in the global Optimization.

Step-by-step model's parametrization

Overall, this part contains a step-by-step summary of the entire parametrization strategy, with a brief insertion of optimization techniques applied during the workflow.

Table 5.20 synthesizes the seven-step workflow defined for the adopted parameterization-plan, together with the associated parameter groups, experiments, and the recommended estimation sources.

Step and Main Objective	Analyzed Parameters Group	Main calibration-sources
1. Define cell-level geometry	Nominal capacity, number of internal layers, voltage window, effective area/scaling, first bounds for electrode thicknesses L_n and L_p, separator thickness, current collector thicknesses	Sources: Kokam datasheet and literature
2. Identify equilibrium voltage behavior and stoichiometric windows	OCP functions $U_p(y)$ and $U_n(x)$, and stoichiometries x_{100}, x_0, y_{100}, y_0	Experimental data: C/50 Pseudo-OCV, GITT relaxation OCV
3. Fix low-sensitivity electrolyte and separator properties	Electrolyte quantities $D_e(c_e)$, $\kappa(c_e)$, t_0^+, $c_{e,0}$, thermodynamic factor, separator porosity and its Bruggeman coefficient	Sources: literature / baseline datasheet
4. Initialize electrode microstructure consistently with High-Power design	Electrode porosities, Active material volume fractions, representative particle radii, maximum solid concentrations (lithium), Bruggeman coefficients	Sources: literature / parameter-set "Mohtat2020" (baseline), High-Power vs High-Energy design reasoning
5. Fit dynamic transport and kinetics from transient and rate data + Staged voltage Optimization fitting	Diffusion functions $D_{s,p}$, $D_{s,n}$, kinetic constant-rates $k_{0,p}$, $k_{0,n}$, resistive terms $R_{f,p}$, $R_{f,n}$, electrode conductivities; optimization of electrodes quantities (L_p, L_n, $\varepsilon_{s,p}$, $\varepsilon_{s,n}$, $A_{electrode}$, $R_{p,p}$, $R_{p,n}$) and particle diffusivity functions; refinement of kinetic constant-rates and SEI-layer resistivity	Experimental data: GITT, HPPC, multi-rate CC discharge, cycling tests
6. Introduce thermal and temperature-dependent terms	Density, heat capacity, heat transfer coefficients, entropy coefficients, selected activation energies	Sources: literature + multi-temperature GITT support (optional)
7. Validate predictive capability of model	No new fitted parameters; only performance metrics	Training + Adjustment + Validation Tests (with optional dynamic profile from WLTP / UDDS)

Table 5.20: SPMe Parametrization: 7 well-structured Steps

In general, some stages of parametrization are solved through inverse estimation, in which parameter values are obtained by minimizing the discrepancy between the simulated and the measured terminal-voltage, rather than being measured directly. The corresponding objective function (in the present work, it is the root-mean-square voltage error (RMSE), evaluated over one or more discharge curve) is computed by running the full RMSE forward solver, and so it is a black-box quantity.

The general formulation of RMSE is already provided in Eq. 5.1, and it is valid across the entire parametrization workflow.

This feature makes classical gradient-based minimization methods unsuitable and motivates the use of derivative-free optimizers.

More specifically, the Step 2 and Step 5 (encountered before) of the parametrization adopted two different but complementary optimization techniques, in order to carry out the fitting against experimental data: (i) Differential-Evolution (used as alternative of Particle-Swarm Optimization, or PSO), and (ii) Nelder-Mead.

These two methods were employed in a complementary "global-then-local" configuration: Differential-Evolution for the broad exploration of the parameter space, and the Nelder-Mead method for the subsequent local refinement.

Differential-Evolution (by Storn and Price, 1997 [43]) is a population-based, stochastic global optimizer. It maintains a population of candidate parameter vectors distributed across the bounded search domain and improves them over successive generations by means of three basic operations. In the "mutation"-step, a trial vector is generated by adding the scaled difference between two randomly chosen population members to a third member; in the "recombination"-step (crossover), the trial vector inherits a mixture of coordinates from this mutant step and from an existing parent-vector; and in the "selection"-step, the trial vector replaces the parent only if it yields a lower objective value. Because every new candidate is built from differences between members of the current population, the search adapts automatically to the local scale and orientation of the cost landscape, while the use of an entire population (rather than a single iterate) makes the method robust against premature convergence to local minima. Differential-Evolution requires no derivative information and is well-suited to the high-dimensional, non convex fitting problems encountered in this case; so, in this study, it was configured with a population of fifty individuals and with Sobol-sequence initialization.

Nelder-Mead method (by Nelder and Mead, 1965 [44]) is, by contrast, a deterministic local optimizer, belonging to the family of direct-search methods. It operates on a "simplex" (i.e., a geometric figure defined by $n + 1$ vertices in a n-dimensional parameter space), in which each vertex represents a candidate solution with an associated cost. At every iteration, the objective is evaluated at all vertices, and the simplex is re-shaped through a sequence of elementary geometric operations (e.g., reflection, expansion, contraction, and shrinkage), that displace it away from its worst-performing vertex and toward regions of lower cost. Thereby, the simplex migrates downhill and progressively contracts around a minimum. The method converges efficiently to local optimum at a modest computational cost, but it offers no guarantee of reaching the global optimum and may stagnate if started far from the real solution. Nelder-Mead is consequently more effective as a refinement (or so-called "polishing") stage, applied once a promising region of the parameter space has already been located.

As explained before, the main objective of all the optimization techniques set in the Parametrization-Plan is to minimize the Root-Mean-Square-Error (RMSE minimization), referred to the difference between baseline simulations and experiments, in terms of terminal-voltage.

Basically, the two algorithms were combined in order to exploit their complementary properties. In the estimation of electrode-stoichiometry boundaries (Step 2) and in the principal geometric and transport fit (Step 5f, stage 1), Differential-Evolution was executed first to locate the basin of the global optimum from a broad initialization, and its result was then refined by Nelder-Mead to converge on a sharper local-minimum. In the subsequent narrow-bound stages, i.e., the kinetic refinement (Step 5f, stage 2) and the final simultaneous polish of the full parameter-set (Step 5f, stage 3), a high-quality starting point was already available from the preceding stages, thereby Nelder-Mead

was applied on its own. Both optimizers are derivative-free, and standard implementations of each one are available in "SciPy" optimization-library, used for this work.

In conclusion, this hybrid strategy balances the global robustness of the population-based search against the local precision and efficiency of the simplex-based method, so this is the perfect combination required for an objective function that is simultaneously multi-dimensional, non-smooth, and computationally expensive to be evaluated.

Overall, it is important to make two considerations about some parameters:

- The anode's SEI-resistivity can impact on the voltage response only if the SEI-layer degradation sub-model is activated for SPMe.
- The group of thermal parameters can affect the terminal-voltage of cell, at different temperatures, only if thermal lumped sub-model is activated for SPMe.

In conclusion, the following brief Flow-chart well synthesizes the purpose of each Step; thereby, parametrization follows this sequence:

1. Fixes the cell-level geometric frame;
2. Identifies the equilibrium thermodynamics;
3. Freezes the weakly sensitive electrolyte/separator block
4. Defines the effective electrode architecture;
5. Calibrates the response through transport and kinetic fitting;
6. Identifies main thermal properties;
7. Provides the model validation.

In this case, it is important to remember the absolute absence of teardown or half-cell measurements / specific physico-chemical tests for the single electrodes. Therefore, under such conditions, the most robust strategy is not to fit everything simultaneously, but to proceed with certain criteria: assign low-sensitivity and structure-defining parameters from literature and design reasoning, extract whatever can be pre-estimated from targeted full-cell tests, and reserve numerical optimization only for the reduced set of dominant dynamic quantities and/or for the refinement of previous quantities.

This sequence is intentionally rigorous and hierarchical, because it separates geometric, structural, thermodynamic, transport, kinetic and thermal aspects as much as possible, before the global fitting stage, thereby improving identifiability of the parameters and reducing the overfitting risk.

5.5 Results from SPMe Parametrization Workflow

This section shows the step-by-step results obtained from the general Parametrization Strategy for SPMe.

More precisely, the various plots from Step 1 to Step 7 are reported, in order to highlight the enhancement of the starting Mohtat's parameter-set to the last best validated parameter-set for the analyzed Kokam pouch cell (SLPB55205130H).

Usually, each Step contains a verification of the current baseline, through three multi-rate discharge curves (at 0.5C, 1C, 2C). The final Step for validation will operate on all the available experimental tests for model's generalization.

Only the Step 6 is developed outside the main parameterization procedure, considering that the entire workflow was carried out for the ambient-temperature of 25 °C.

The following sub-sections contain the updated (or retained from "Mohtat2020") parameters, shown in the final tables, respecting the designed strategy. Clearly, the function-parameters are reported, whether possible, as analytical-functions outside the several tables.

5.5.1 Step 1: Cell-level geometry and capacity-scaling

The Step 1 implements the systematic assignment of all cell-level geometry parameters for the SPMe model, following the methods prescribed in the Parametrization strategy.

The capacity-scaling was adopted to modify the capacity of the cell from $5\ Ah$ from Mohtat's set to the actual $11\ Ah$ of Kokam-cell. This procedure was applied to one of the two electrode dimensions, in this case electrode-height.

Some of the parameters in this Step are assigned in this step (e.g., L_p, L_n, $A_{electrode}$), but they will be refined in the Step 5.

In Figure 5.81, the Mohtat's baseline was represented with voltage as a function of time or discharge-capacity, after the capacity-scaling procedure, and directly compared with experimental discharges at three different C-rates (0.5C, 1C, 2C).

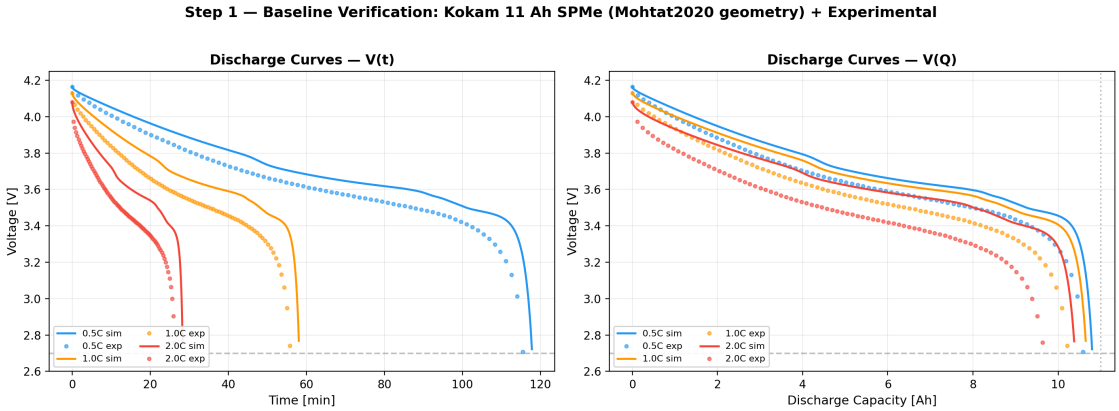


Figure 5.81: Step 1 - Updated Baseline: Voltage discharge curves at 3 C-rates

In Figure 5.82, a comparison among available approaches for electrode-area scaling is proposed, considering that the final choice was the approach 1, establishing an estimated area of $4510\ cm^2$.

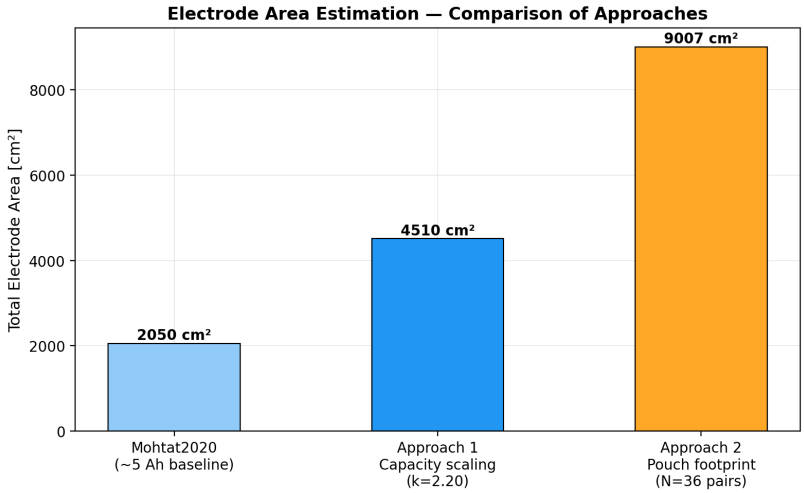


Figure 5.82: Electrode-are scaling approaches

In Figure 5.83, a final comparison among typical electrode's coating thicknesses from compatible literature's parameter-sets was reported.

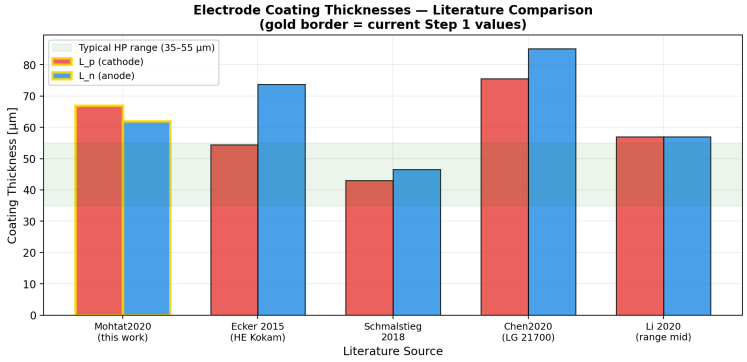


Figure 5.83: Electrode coating thicknesses from literature

In Figure 5.84, a first error assessment between simulated SPMe voltage curves and corresponding experimental discharges was made, using the RMSE computation and local-error plots, considering, even in this case, the three classical discharge rates.

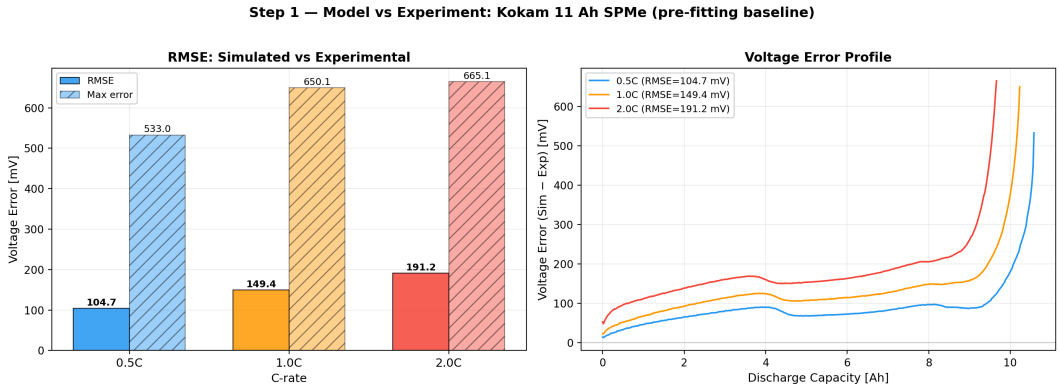


Figure 5.84: Difference between SPMe simulations and experiments

Finally, Table 5.21 summarizes all the parameters involved in the Step 1.

Parameter	**Symbol**	**Value and Unit**
Nominal cell capacity	Q_{nom}	11 Ah
Lower cut-off voltage	V_{min}	2.7 V
Upper cut-off voltage	V_{max}	4.2 V
Number of internal layers	N_{layers}	1
Electrode-height (scaled)	H_{elc}	2.20 m
Electrode-width	W_{elc}	0.205 m
Total electrode Area	$A_{electrode}$	0.451 m^2
Cathode thickness	L_p	67 μm
Anode thickness	L_n	62 μm
Separator thickness	L_s	12μm
Positive current-collector thickness	$L_{cc,p}$	25 μm
Negative current-collector thickness	$L_{cc,n}$	10 μm

Table 5.21: Step 1: List of updated or retained Parameters

The number-of-layers is left equal to 1, as explained in 5.2, so it is not used to compute the total electrode-area.

5.5.2 Step 2: OCP functions and stoichiometric window identification

The Step 2 operates the fitting of the four stoichiometry boundary values (x_{100}, x_0, y_{100}, y_0), by minimizing the error between the model full-cell OCV and the experimental Pseudo-OCV curve obtained from average C/50 charge-discharge data, as seen in the Parametrization strategy.

The reference equation is the following:

$$OCV_{model}(SoC) = U_p(y(SoC)) - U_n(x(SoC))$$

where: $x(SoC)$ is the anode stoichiometry and $y(SoC)$ is the cathode stoichiometry.

The half-cell OCP functional forms, $U_p(y)$ and $U_n(x)$, are initially kept from the Mohtat's parameter-set.

The eSOH voltage constraint at the upper cut-off is enforced via Brent's method, which reduces the number of free parameters from 4 to 3; the constraint is the following:

$$U_p(y_{100}) - U_n(x_{100}) = V_{max} = 4.2\ V$$

The applied optimization methods are in order: (i) Differential-Evolution; (ii) Nelder-Mead.

The optimization methods employed for Step 2 were: (1) Differential-Evolution (iterations - 500 x 90); (2) Nelder-Mead (iterations - 2500).

The following Table 5.22 illustrates the bounds used for optimization-problem with three free-variables (x_0, y_0, y_{100}), and one constrained variable (x_{100}).

Free-parameters	**Adopted bounds**
NMC stoichiometry at 100% SoC	$(0.01, 0.15)$
Graphite stoichiometry at 0% SoC	$(0.001, 0.05)$
Graphite stoichiometry at 100% SoC	$(0.70, 0.98)$

Table 5.22: Stoichiometry bounds before optimization

In Figure 5.85, the Mohtat's half-cell OCP functions are shown for anode and cathode, considering the curves inside their respective default stoichiometric windows.

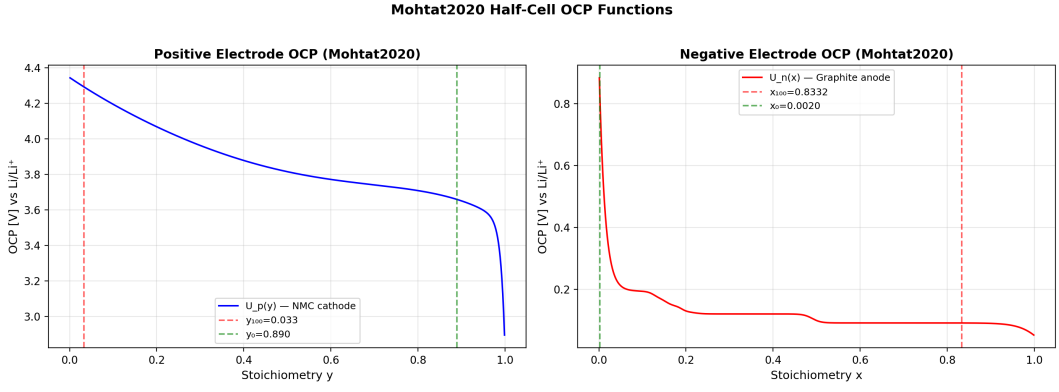


Figure 5.85: Default Mohtat's OCP functions

In Figure 5.86, the experimental C/50 average curve extracted from Pseudo-OCV is represented, together with the plot of hysteresis, which is the result of difference between charge data and discharge at the corresponding SoC points. More specifically, the mean value of hysteresis is $41.8\ mV$, compatible with HP cells (this topic was deeply exposed in section 3.4).

Moreover, the measured capacity, after the end of C/50 charge, is $11.27\ Ah$, slightly higher than the measured capacity from the end of C/50 discharge, equal to $11.18\ Ah$.

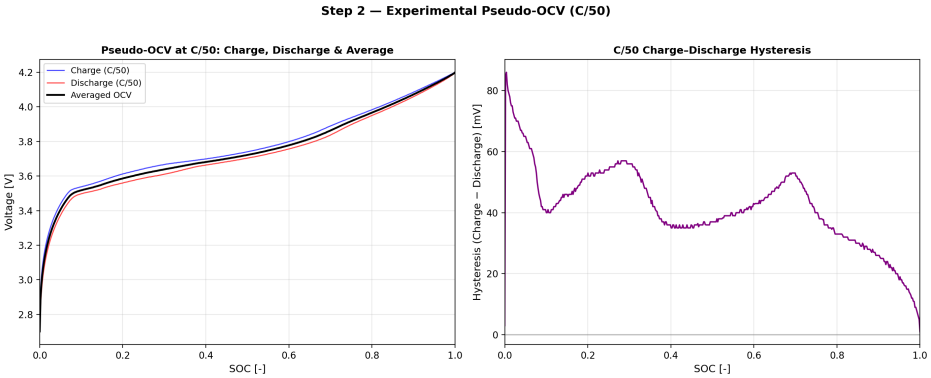


Figure 5.86: Experimental average Pseudo-OCV and corresponding hysteresis

In Figure 5.87, the effective fitting procedure of simulated curves with respect to experiment is shown, in order to calculate the stoichiometries. The voltage residual plot is essentially the difference between the SPMe simulation voltage (before and after the fitting) and the experimental voltage. In particular, the RMSE, after optimization, is equal to approximately $\sim 13\ mV$, improved by previous $\sim 19\ mV$ from Mohtat's set. The maximum error reached after the fitting is around $\sim 85\ mV$ (residual amount).

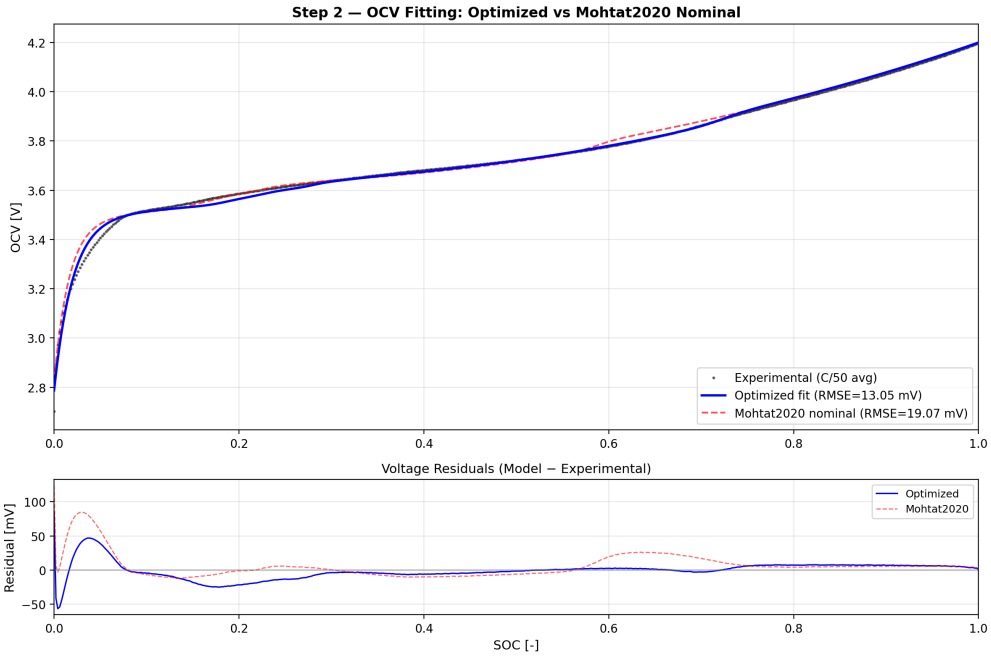


Figure 5.87: OCV fitting for stoichiometries extraction

In Figure 5.88, two plots regarding the "Differential-Voltage-Analysis" (i.e. DVA) are shown. In more detail, DVA is a diagnostic post-processing technique applied to low-current voltage-capacity

data, such as the Pseudo-OCV tests, in order to enhance the electrochemical features embedded in the OCV profile of a lithium-ion cell.

The main results of DVA are:

- the first plot with $d(OCV)/d(SoC)$ curve as a function of SoC, that highlights the voltage regions where the cell potential changes rapidly, which are associated with variations in the lithiation states of the active materials;
- the second plot with the inverse representation dQ/dV as a function of OCV, which is generally referred to as incremental capacity or differential capacity analysis, and it emphasizes voltage plateaus as characteristic peaks.

In this case, the DVA provides a good assessment of the consistency of the obtained stoichiometric windows, and this validates the reconstructed full-cell OCV. As a reminder, the proper full-cell OCV is refined in the next Step 5e.

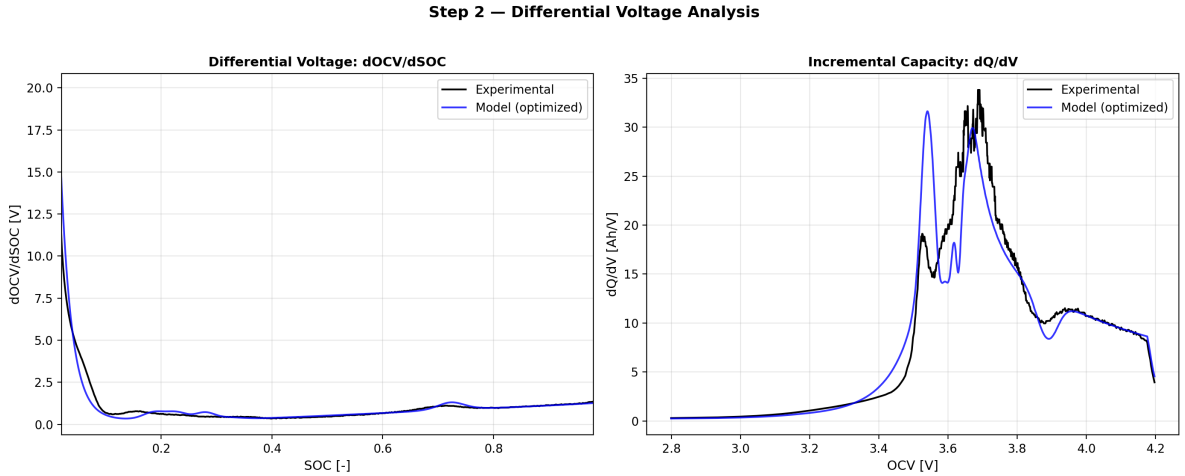


Figure 5.88: Differential Voltage Analysis (DVA)

In Figure 5.89, the fitted electrode stoichiometric values are compared with the Mohtat's ones in the first plot; the two other graphs illustrate the new stoichiometric windows applied for positive electrode OCP and negative electrode OCP.

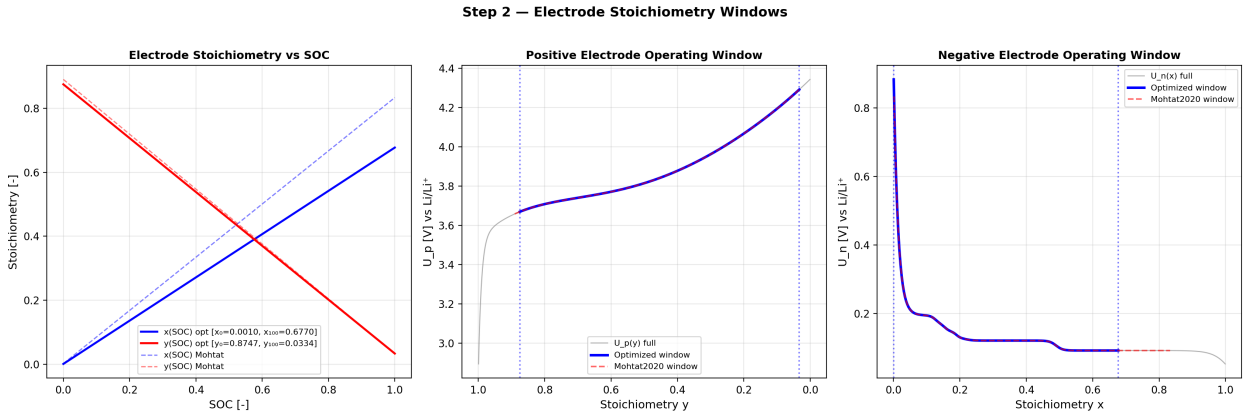


Figure 5.89: Fitted stoichiometry windows

Finally, in Figure 5.90, the plot for a simple verification discharge at 0.5C and 1C is reported, highlighting the dependence of effective capacity on stoichiometric windows: it decreases from 11 Ah to approximately 8.70 Ah.

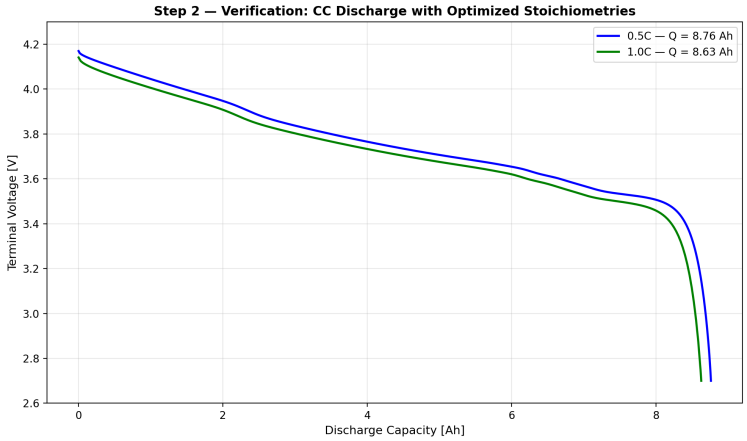


Figure 5.90: Discharge verification plot

Table 5.23 reports the parameters extracted from Step 2.

Parameter	**Symbol**	**Value and Unit**
Positive electrode OCP	$U_p(y)$	Function* $[V]$
Negative electrode OCP	$U_n(x)$	Function* $[V]$
Anode stoichiometry at 100% SoC	x_{100}	~ 0.677
Anode stoichiometry at 0% SoC	x_0	~ 0.001
Cathode stoichiometry at 100% SoC	y_{100}	~ 0.033
Cathode stoichiometry at 0% SoC	y_0	~ 0.875

Table 5.23: Step 2: List of updated or retained Parameters

Considering fixed maximum Li-ion concentrations for the two electrodes, from computed stoichiometries two explicit PyBaMM parameters are derived:

$$c_{s,p,init} = y_{100} \cdot c_{s,p,max} \simeq 1183.22\ mol/m^3$$

$$c_{s,n,init} = x_{100} \cdot c_{s,n,max} \simeq 19462.27\ mol/m^3$$

Step 2b: Capacity-recalibration

The Step 2b is necessary to re-calibrate the capacity of the cell, after the update of the stoichiometric window.

Indeed, the Step 1 established a new electrode-height through scaling it by $k = Q_{target}/Q_{Mohtat}$, assuming the default Mohtat's stoichiometry utilization window. After the Step 2 fitting procedure, the parameter-set has acquired a different stoichiometry window for the HP cell. Because the delivered capacity depends on the product of electrode area and stoichiometry window width:

$$Q \quad \alpha \quad \Delta\theta \cdot A_{electrode}$$

the change of $\Delta\theta$, while keeping fixed area $A_{electrode} = H_{electrode} \cdot W_{electrode}$ (with $N_{layers} = 1$), causes a capacity mismatch.

The correction of capacity, applied to electrode-height, preserves the OCV shape because the stoichiometry window remains unchanged.

In Figure 5.91, the plots related to practical capacity re-calibration through electrode-height modification are shown. The C-rates used for verification are: C/20 (to highlight thermodynamics), C/2, 1C.

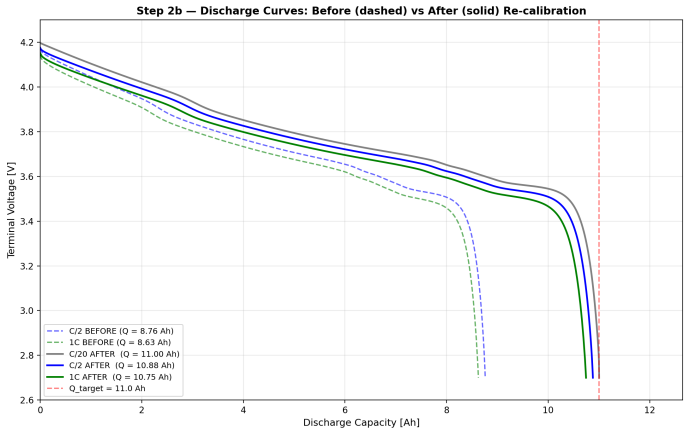


Figure 5.91: Capacity recalibration: before vs. after

In Figure 5.92, the final baseline verification is represented with two plots: voltage versus time; voltage versus discharged-capacity. The differences between SPMe simulation and corresponding experiments are still quite larger.

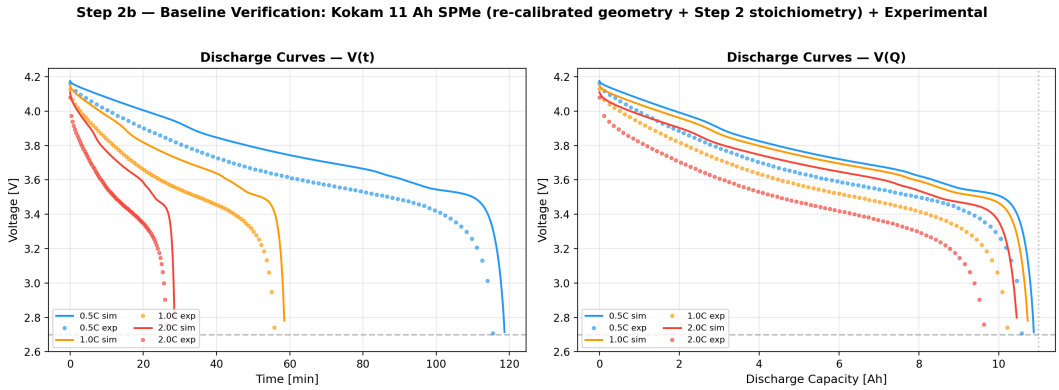


Figure 5.92: Step 2/2b - Updated Baseline: Voltage discharge curves at 3 C-rates

Table 5.24 highlights the corrected parameters for the updated parameter-set.

Parameter	**Symbol**	**Value and Unit**
Electrode-height (corrected)	H_{elec}	$2.728\ m$
Total electrode Area (corrected)	$A_{electrode}$	$0.558\ m^2$

Table 5.24: Step 2b: List of updated or retained Parameters

5.5.3 Step 3: Electrolyte and Separator parameters

The Step 3 implements the systematic assignment of all electrolyte and separator parameters, as described in the general strategy for SPMe model. All the parameters are assigned using the Method A and frozen, based on the confirmed low-sensitivity levels from the DoE-based and literature sensitivity analyses, as seen in section 5.3.

Therefore, this Step does not modify any parameter, rather it simply documents the "Mohtat2020" electrolyte/separator properties (except for the thermodynamic factor), provides also literature checks, and confirms the simulation is consistent after applying Step 1 and Step 2 outputs.

In Figure 5.93, the baseline verifications with model against experiments are shown, at three C-rates (always: 0.5C, 1C, 2C). As said before, they are essentially unchanged from the Step 2b results.

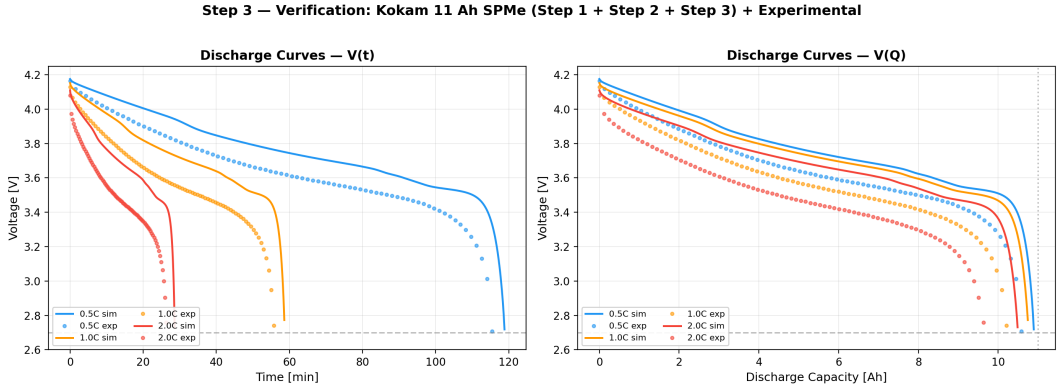


Figure 5.93: Step 3 - Updated Baseline: Voltage discharge curves at 3 C-rates

In Figure 5.94, three plots describe the electrolyte transport properties as functional forms of electrolyte concentration. With SPMe modeling assumption, the electrolyte's conductivity and diffusivity are basically constant, whatever is the value of its concentration (expressed, in this case, in mol/L).

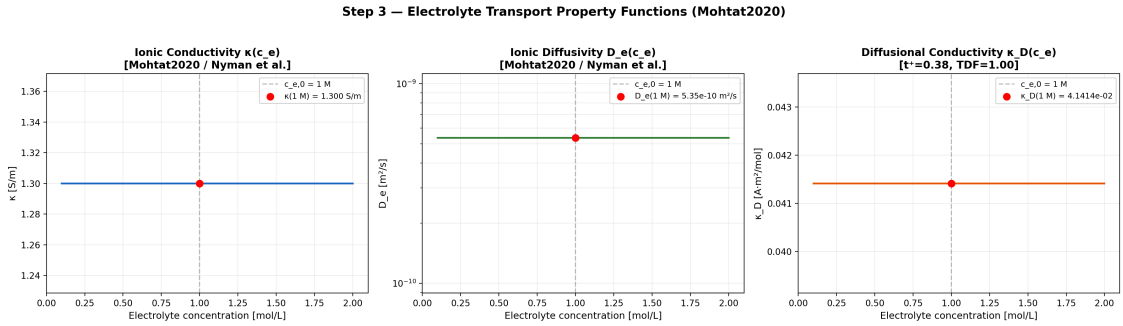


Figure 5.94: Electrolyte functions: Transport properties

In Figure 5.95, the effective electrolyte concentration as a function of time or capacity is essentially constant at the same C-rate. There is a clear phase of electrolyte depletion at the highest C-rates (e.g. 2C), where the concentration becomes negative. This is a known behavior of SPMe formulation with respect to more thorough models, such as DFN (Brosa-Planella et al. (2022) [8]).

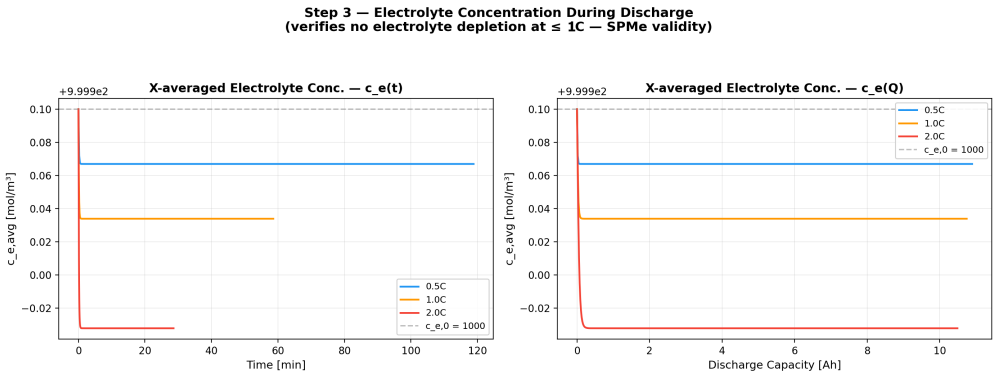


Figure 5.95: Electrolyte concentration at 3 C-rates

In Figure 5.96, the comparisons between model's simulation and corresponding experiments are expressed in terms of RMSE error and local-error.

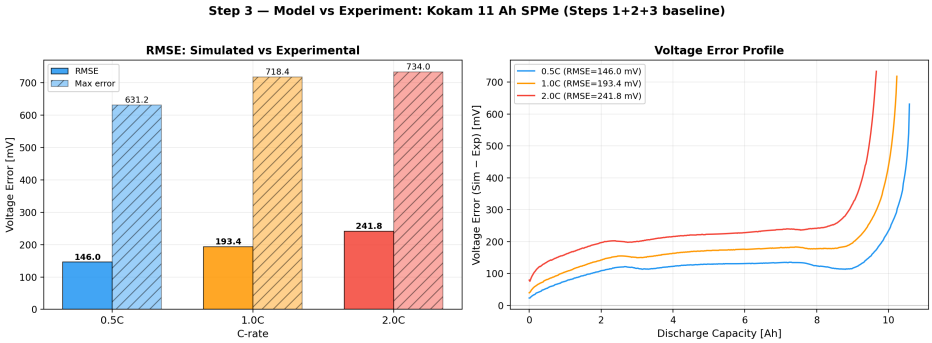


Figure 5.96: Step 3: Residual RMSE for 3 discharge curves

Finally, Figure 5.97 carries out a large literature comparison among different references, related to two scalar properties of electrolyte and separator: transference number (t_0^+) and separator porosity (ε_s), respectively.

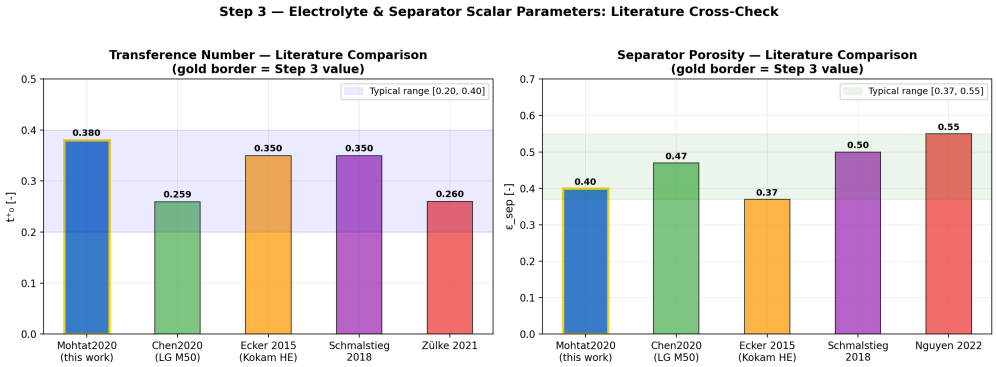


Figure 5.97: Electrolyte and separator properties: literature comparison

The following Table 5.25 summarizes the adopted values/functions from literature.

Parameter	Symbol	Value and Unit
Electrolyte conductivity	$\kappa_e(c_e)$	$1.3\ S/m$
Electrolyte diffusivity	$D_e(c_e)$	$(5.2 \cdot 10^{-10})\ m^2/s$
Transference number	t_0^+	0.38
Initial electrolyte concentration	$c_{e,0}$	$1000\ mol/m^3$
Thermodynamic factor	f_T	1.0
Separator porosity	ε_s	0.40
Separator Bruggeman coefficient	b_s	1.50

Table 5.25: Step 3: List of updated or retained Parameters

5.5.4 Step 4: Micro-structural properties of Electrodes

The Step 4 applies a systematic assignment of all electrode-related microstructure parameters for the SPMe model.

As prescribed in the Parametrization strategy, ten parameters are set (five per electrode), using a combination of:

- Method A $\rightarrow$ low-sensitivity parameters;
- High-Power design-adjusted literature $\rightarrow$ parameters needing High-Power design correction relative to "Mohtat2020" baseline.

There are some exceptions: (i) particle radii do not strictly depend on cell's design type; (ii) maximum Li-ion concentrations can be determined only by specific crystallographic analysis (chemistry-locked).

The following HP design reasons (after comparisons with Ecker's HE Kokam cell of $7.5\ Ah$) were useful to set the basic microstructure parameters of electrodes of Kokam SLPB55205130H cell:

1. Higher electrode porosities $\rightarrow$ faster ionic transport;
2. Slightly lower active material fractions $\rightarrow$ volume trade-off;
3. Comparable particle radii (set by material supplier);
4. Identical maximum Li-ion concentrations (chemistry-dependent);
5. Similar Bruggeman exponents (pore structure geometry).

In Figure 5.98, the classical baseline verification at three C-rates against corresponding experiments is shown in two plots: voltage versus time; voltage versus discharge-capacity. The more evident improvement, after Step 4, is the more correct voltage termination, that implies another capacity calibration of SPMe's parameter-set.

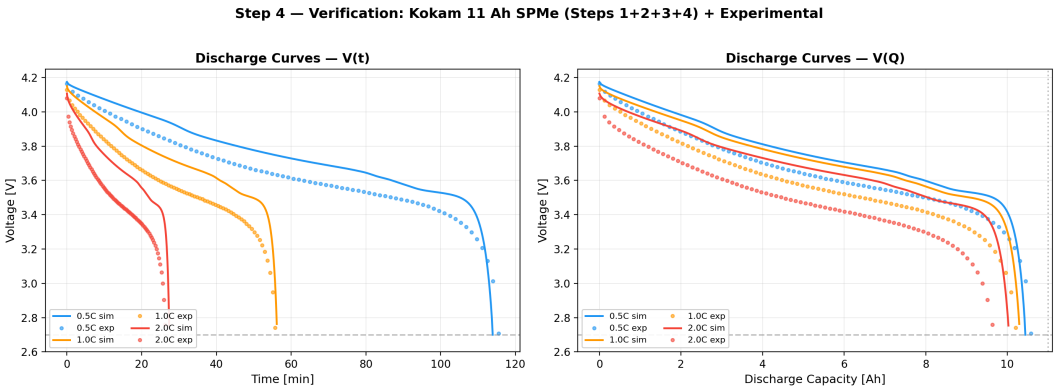


Figure 5.98: Step 4 - Updated Baseline: Voltage discharge curves at 3 C-rates

In Figure 5.99, there is the illustration of the basic principles of Li-ion batteries during discharge: the particle-surface concentration of anode and cathode and the respective stoichiometry trends. More precisely, during discharge, the anode is losing Li-ions, in favor of cathode. Thereby, the surface concentration and stoichiometry of graphite decrease linearly, whereas the surface concentration and the stoichiometry of NMC increase linearly. This respects the law of lithium/mass conservation of SPMe modeling.

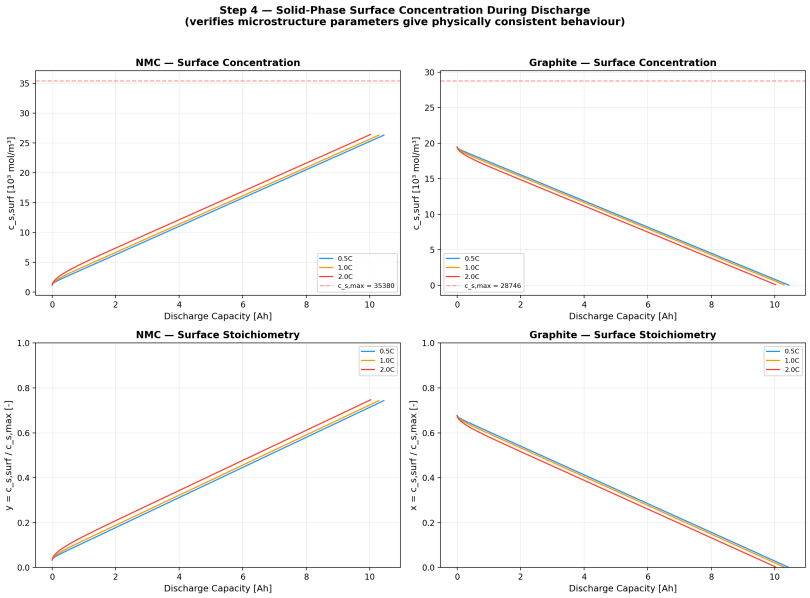


Figure 5.99: Lithium concentration and relative stoichiometries

In Figure 5.100, the two plots regarding the differences between model simulations and experiments (RMSE and local error), at the three C-rate, are reported, with slight decrease with respect to the ones of Step 2 or Step 3.

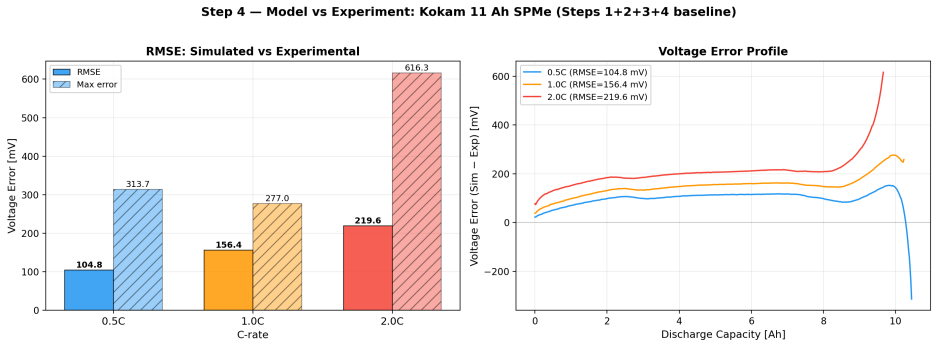


Figure 5.100: Residual RMSE after Step 4

In Figure 5.101, an interesting comparison, among different literature sources, of the moderate-to-high sensitivity properties of electrodes are shown, with the indications of the final Step 4 choices.

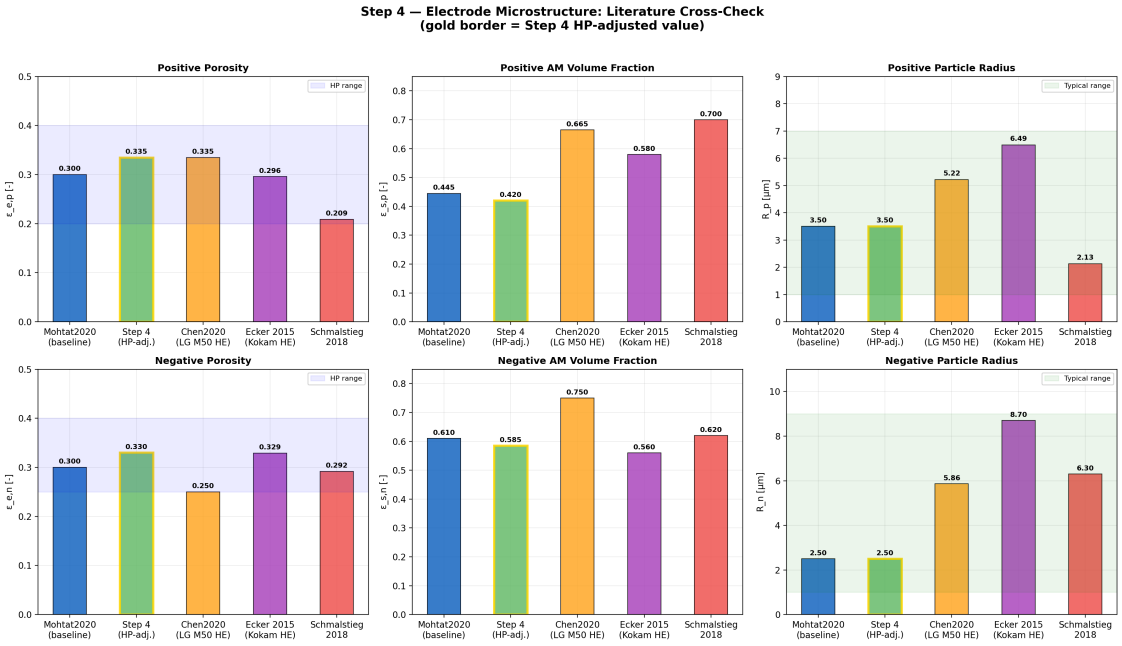


Figure 5.101: Step 4: Literature comparison among different quantities

Finally, in Figure 5.102, the most important characteristic parameters, the maximum solid concentration, are compared across the most important literature studies.

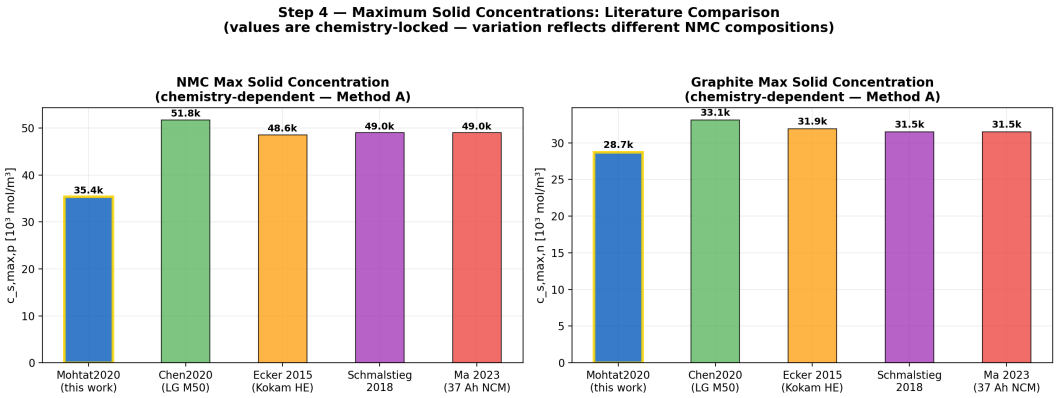


Figure 5.102: Maximum Li-concentration: literature comparison

Table 5.26 summarizes all the properties related to the positive and negative electrodes, seen in this Step.

Parameter	**Symbol**	**Value and Unit**
Cathode Porosity	$\varepsilon_{e,p}$	0.335
Cathode active-material volume fraction	$\varepsilon_{s,p}$	0.420
Positive particle-radius	$R_{p,p}$	$3.5\ \mu m$
Cathode maximum Li-ion concentration	$c_{s,max,p}$	$35380\ mol/m^3$
Cathode Bruggeman coefficient	b_p	1.50
Anode Porosity	$\varepsilon_{e,n}$	0.330
Anode active-material volume fraction	$\varepsilon_{s,n}$	0.585
Negative particle-radius	$R_{p,n}$	$2.5\ \mu m$
Anode maximum Li-ion concentration	$c_{s,max,n}$	$28746\ mol/m^3$
Anode Bruggeman coefficient	b_n	1.50

Table 5.26: Step 4: List of updated or retained Parameters

In addition, different electrochemical quantities are derived from the previous assumed parameters (however, they are not present in PyBaMM parameter-sets).

The cathode and anode filler (binder and conductive carbon) quantities are derived from active-volume fractions and porosities:

$$\varepsilon_{filler,p} = 1.0 \ - \ \varepsilon_{s,p} \ - \ \varepsilon_{e,p} \ = \ 0.245$$

$$\varepsilon_{filler,n} = 1.0 \ - \ \varepsilon_{s,n} \ - \ \varepsilon_{e,n} \ = \ 0.085$$

The specific areas related to anode and cathode, for the electrode-electrolyte interface, are calculated as follows:

$$a_{s,p} = 3 \cdot \frac{\varepsilon_{s,p}}{R_{p,p}} = 0.360\ m^2/cm^3$$

$$a_{s,n} = 3 \cdot \frac{\varepsilon_{s,n}}{R_{p,n}} = 0.702\ m^2/cm^3$$

The effective transport-factors through electrolyte-filled pores of electrodes are obtained exploiting Bruggeman coefficients in this way:

$$f_{transport,p} = \varepsilon_{e,p}^{b_p} \simeq 0.194$$

$$f_{transport,n} = \varepsilon_{e,n}^{b_n} \simeq 0.190$$

5.5.5 Step 5: Transport, Kinetics, and global (experimental-based) optimization

The Step 5 is the largest step of the entire Parametrization framework, as already seen in the general strategy section. It is divided into seven stages or sub-steps; their results will be analyzed one by one, to see the model's development.

The crucial sub-step is basically sub-step 5f, that performs a global (experimental-based) optimization, changing/scaling the values of many scalar/function parameters. The objective is to adapt the SPMe model to experimental reliable tests, i.e. multi-rate CC discharge at different C-rates.

An important note: in some steps with data fitting, it is useful to use the coefficient of determination, commonly denoted as R^2, in order to assess the agreement between experimental data and the corresponding values predicted by the fitted model. Thereby, it can provide a quantitative measurement of how well the simulations reproduce the observed experimental trends, such as in Step 5a or in Step 5d.

Sub-step 5a: GITT pre-estimation of positive-particle diffusivity

The sub-step 5a extracts the apparent solid-phase diffusion coefficient $D_s(SoC)$, from GITT data, using the Weppner-Huggins equation (with Sand-type equation contribution, as seen in 3.2.1).

As a reminder of Weppner-Huggins formula, expressed in Eq. 3.1, the applied equation to extract solid-phase diffusivity, at different SoC points, is:

$$D_s = \frac{4}{\pi \cdot \tau} \cdot \left(\frac{R_p}{3}\right)^2 \cdot \left(\frac{\Delta E_s}{\Delta E_\tau}\right)^2$$

where: τ is the current-pulse duration, R_p is the particle radius (in this case, the positive one), ΔE_s is the change in equilibrium voltage after a SoC step, and ΔE_τ is the voltage change during the pulse due to diffusion.

Two important notes about this formula:

- ΔE_s is measured at the end of each rest-period, with respect to the previous one;
- ΔE_τ is measured in the time-range between 10% and 80% of the current pulse.

In this case of full-cell data, the extracted D_s is a lumped effective value dominated by the rate-limiting electrode. The simplification makes sense, considering that for NMC/graphite cells, the NMC cathode typically dominates the over-potential in the mid-SoC range, while graphite-OCV is relatively flat. Therefore, the extracted values are a meaningful initial estimation for $D_{s,p}$.

Finally, the points extracted for D_s at each SoC (from 75 GITT-pulses) was condensed into a polynomial via robust least-squares regression in log_{10}-space, being a SoC-dependent function; the polynomial was evaluated numerically via Horner's algorithm.

In Figure 5.103, two plots obtained from GITT-discharge data are shown.

The first plot represents the trends of $D_{s,p}(SoC)$ function, exploiting the 75 GITT-pulses, to obtain the values of lumped diffusivity at each point; then, this function is attributed to cathode. It is interesting to notice the reference positive-particle diffusivity from Mohtat's parameter-set, that is actually constant across the entire SoC range; its value is: $8.0 \cdot 10^{-15}\ m^2/s$.

The second plot is the trend of equilibrium-OCV as a function of SoC, and it is extracted using the last rest points of GITT test, where the cell typically reaches the thermodynamic-equilibrium.

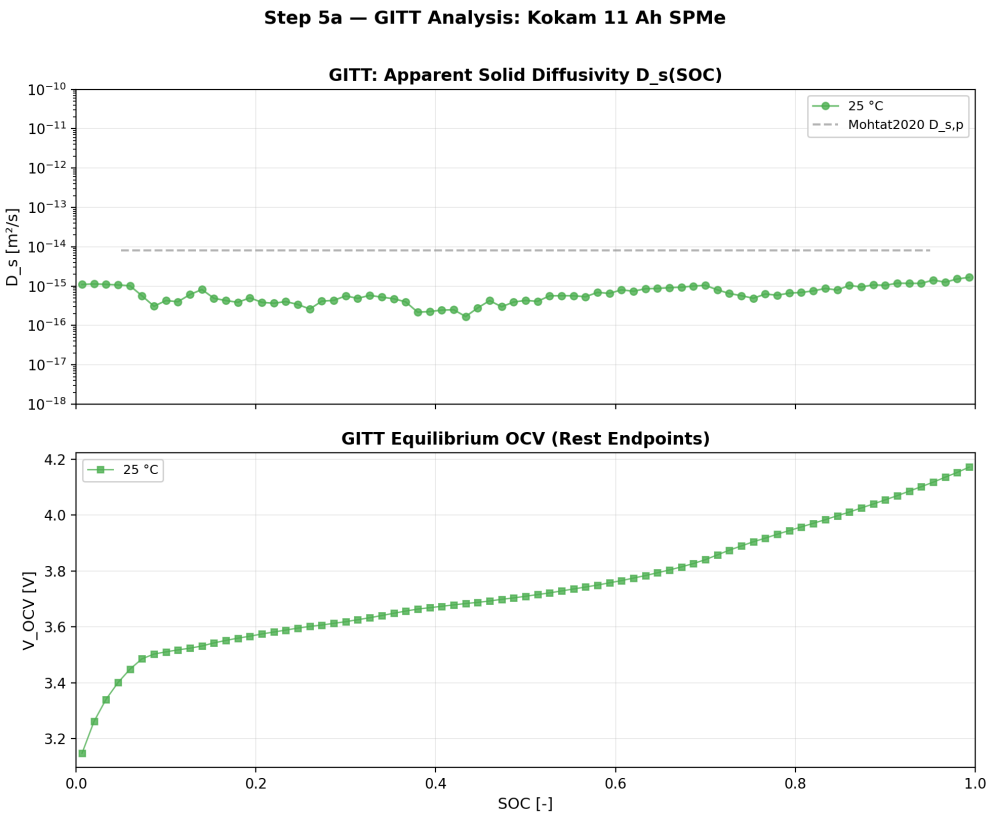


Figure 5.103: Extraction of diffusivity-function and equilibrium-OCV

Figure 5.104 illustrates the good quality of the fitted functions against experimental data. More specifically, in the three plots, the voltage is always linear with $\sqrt{t}$, as stated from Sand-type equation. The coefficient of determination (R^2) is greater than 0.95, and this means there is a high degree of correlation between fitted and experimental data (at the SoCs: 99%, 50%, 1%).

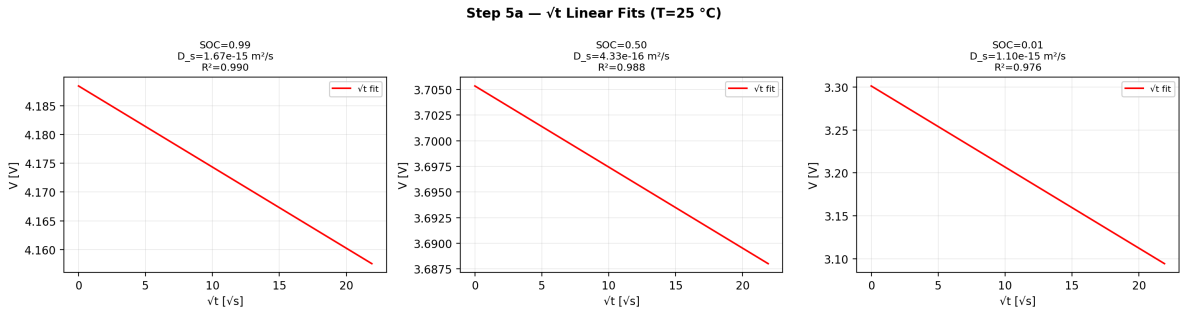


Figure 5.104: Fitting quality: V vs. $\sqrt{(t)}$

Table 5.27 reports the two diffusivity coefficients of this sub-step.

Parameter	**Symbol**	**Value and Unit**
Positive-particle diffusivity (GITT-extracted)	$D_{s,p}(y,T)$	Function* $[m^2/s]$
Negative-particle diffusivity	$D_{s,n}(x,T)$	Function* $[m^2/s]$

Table 5.27: Step 5a: List of updated or retained Parameters

After the GITT-points extraction for the positive-particle diffusivity function ($D_{s,p}(y)$), three

methods of interpolation, evaluated numerically via Horner's scheme, were compared (all in log_{10}-space):

1. 6^{th}-order polynomial, with Savitzky-Golay smoothing and least-square fit;
2. 3^{rd}-order polynomial, with robust Huber-loss structure;
3. 2^{nd}-order polynomial, with a simpler Huber fit.

.

In Figure 5.105, the three interpolation methods are shown, each one with a different fitted curve. The first plot compares the three fitted functions against the GITT-extracted points for diffusivity, as a function of its stoichiometry (y), considering only reliable data (between 99.5% and 5% of SoC). The second plot reports the quality of fitting, using the residuals between fitted curves and the GITT-extracted points, highlighting the required trade-off in the selection of one technique rather than others.

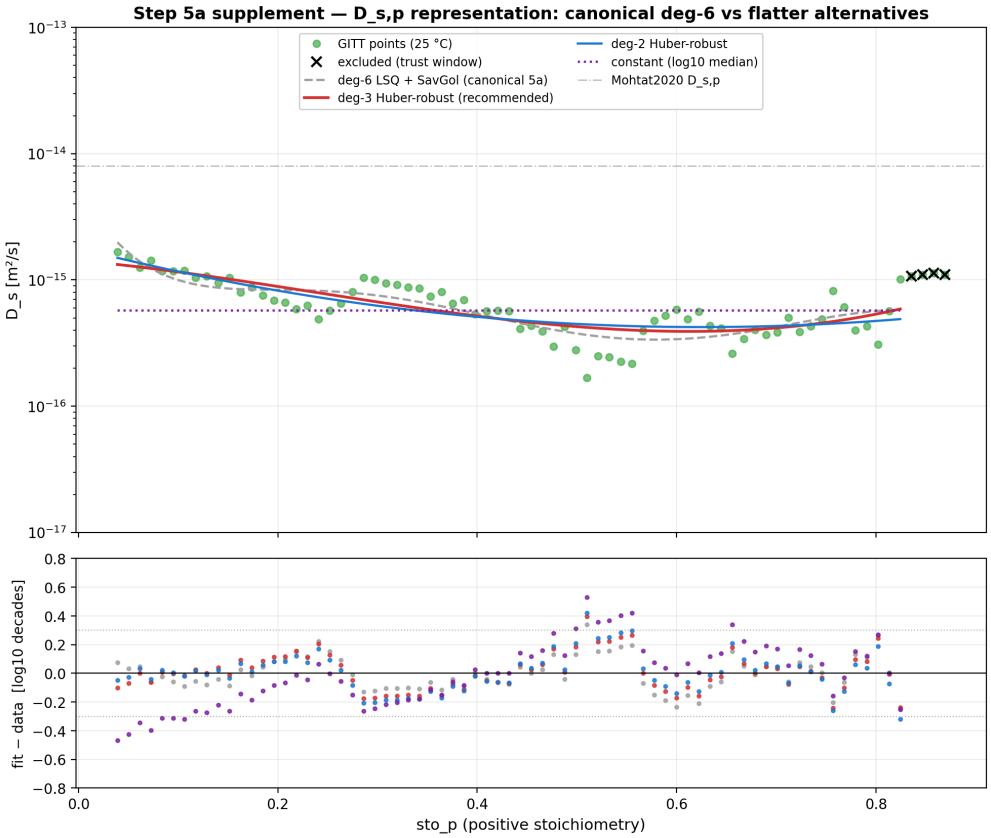


Figure 5.105: Interpolation methods for $D_{s,p}$ fitting

The final choice was the 3^{rd}-order Huber polynomial, with the aim of constructing a flatter diffusivity-function, more similar to the constant Mohtat's default value for $D_{s,p}$. The mechanism that regulates this type of interpolation is based on the regression features: lower degree and robust loss, obtaining a flat function.

Therefore, the GITT-extracted $D_{s,p}(y)$ function is expressed by this equation:

$$log_{10}(D_{s,p}(y)) = 2.98 \cdot y^3 - 2.15 \cdot y^2 - 0.72 \cdot y - 14.85$$

Meanwhile, the retained $D_{s,n}(x)$ from Mohtat's parameter-set is essentially independent of anode's stoichiometry (rather it depends on temperature, as explained in previous section 5.2); its value is: $5.0 \cdot 10^{-15}\ m^2/s$.

Sub-step 5b: HPPC pre-estimation of SEI resistivity

The sub-step 5b extracts the ohmic/film resistance $R_0(SoC)$ from HPPC experimental data. The instantaneous voltage drop, at the start of each HPPC pulse, divided by the pulse current, gives:

$$R_0 = \frac{|\Delta V|}{|I|}, \quad at\ each\ SoC$$

Considering to have multiple current-levels, from C/5 to 2C, it is possible to check for linearity (Ohm's law) in contrast with non-linear kinetic effects.

The HPPC-extracted R_0 is a total cell-level lumped resistance, however in the SPMe, film/SEI resistance is assigned per electrode. Following the Mohtat's convention (SEI-layer predominantly grows on graphite), R_f, as anticipated, is assigned only to negative electrode; instead, positive film-resistance ($R_{f,p}$) is set to zero.

As seen in section 5.3.2, the film-resistance R_f is exploited to calculate the corresponding SEI-resistivity, following these equations:

$$R_f = R_0 \cdot A_{cell}$$

$$\rho_{SEI} = \frac{R_f}{L_{SEI}}$$

where: R_f is film resistance expressed in $\Omega \cdot m^2$, and ρ_{SEI} is the SEI-resistivity expressed in $\Omega \cdot m$, A_{cell} is the electrode area, and L_{SEI} is the SEI-layer thickness.

In Figure 5.106, the plot shows the extracted value of ohmic R_0 resistance referred to whole cell, considering 5 pulses of charge and discharge (at C/5, C/3, C/2, 1C, 2C), at each variation of 10% of SoC. All the values of R_0 are inside the range between $7.5\ m\Omega$ and $10\ m\Omega$.

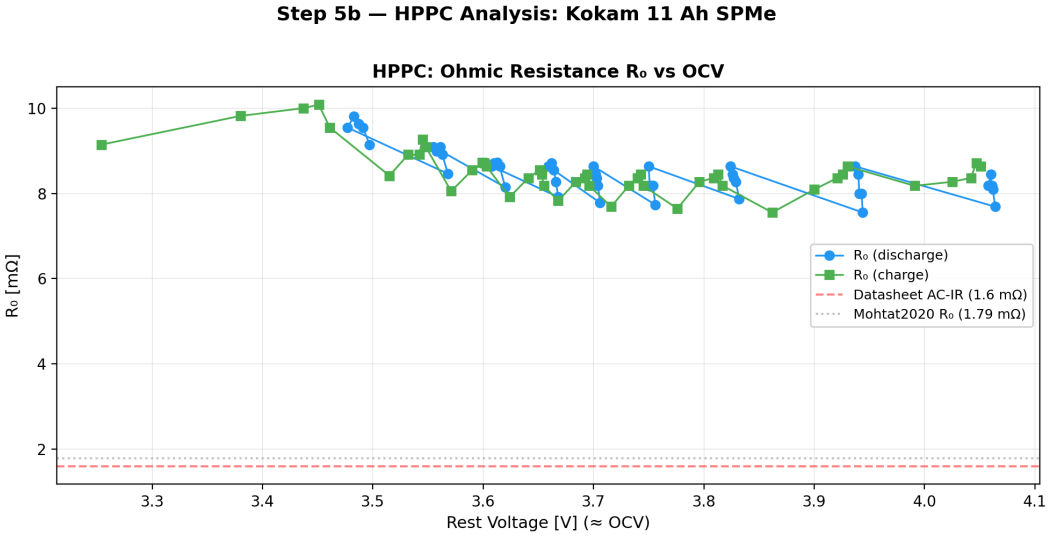


Figure 5.106: R_0 extraction from HPPC test

In Figure 5.107, a graph about the calculated ohmic-resistance values against the various current-levels is shown. The R_0 values are not constant with different current-pulses, and this implies the presence of high non-linearity effects, explained by Butler-Volmer kinetics.

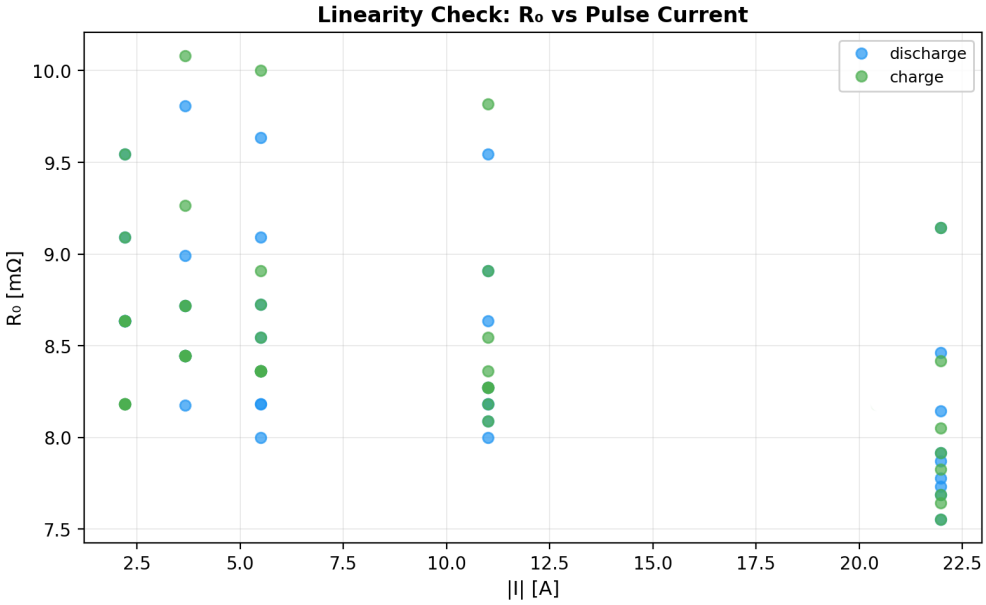


Figure 5.107: Resistance vs. current-rates: linearity check

Table 5.28 reports the two assumptions regarding the two film-resistances.

Parameter	**Symbol**	**Value and Unit**
Positive film-resistance (assumed)	$R_{f,p}$	$0\ \Omega$
SEI film-resistance (extracted)	$R_{f,n}$	$\sim 4.724\ m\Omega \cdot m^2$

Table 5.28: Step 5b: List of updated or retained Parameters

The R_0 median-value, between charge and discharge pulses, of the whole cell (from which is obtained R_f, n) is: $8.447\ m\Omega$.

This value is decidedly higher than internal AC resistance declared into the data-sheet of the cell: $1.6\ m\Omega$.

The SEI-resistivity used inside the parameter-set is calculated as follows:

$$\rho_{SEI} = \frac{R_{f,n}}{L_{SEI}} \simeq 944765\ \Omega \cdot m$$

A note: L_{SEI} is the standard SEI thickness taken from Mohtat's parameter-set.

Sub-step 5c: Electrode's conductivities and charge-transfer coefficients

The sub-step 5c is the simplest stage of the entire Step 5 framework. Basically, it documents and verifies the assignment of:

1. Electrode electronic conductivities ($\sigma_{s,p}$, $\sigma_{s,n}$);
2. Charge-transfer coefficients (α_a, α_c) for both electrodes;

Both categories of parameters have low-sensitivity, thereby they are frozen to Mohtat's values (Method A).

In Figures 5.108 and 5.109, the analysis of charge-transfer aspects was proposed.

The first plot shows the difference for the voltage discharge curve at 1C, as a function of discharge-capacity, assuming Mohtat's case (symmetric charge-transfer) or Ecker's case (asymmetric

charge-transfer); the overall impact of the two coefficients on the model response is minimal, with peak of variation around $2.5\ mV$.

The second plot represents the normalized exchange-current density, obtained from Butler-Volmer equation, highlighting again the differences between symmetric charge-transfer and asymmetric charge-transfer.

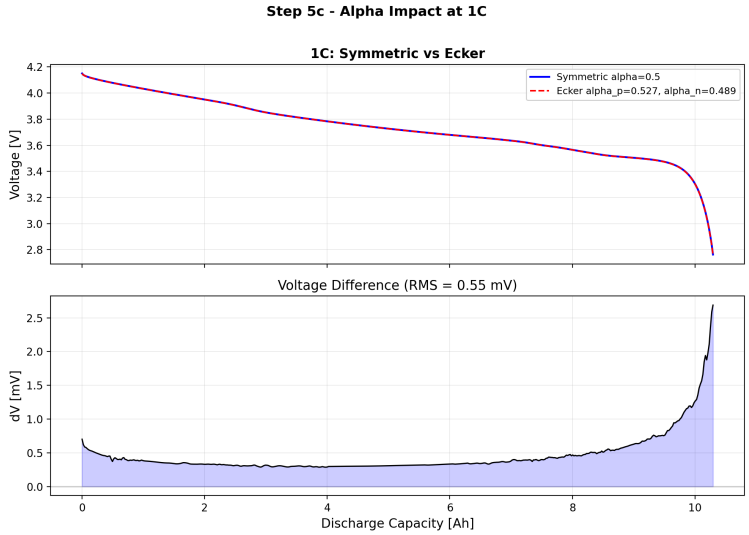


Figure 5.108: Voltage discharge impact of charge-transfer (at 1C)

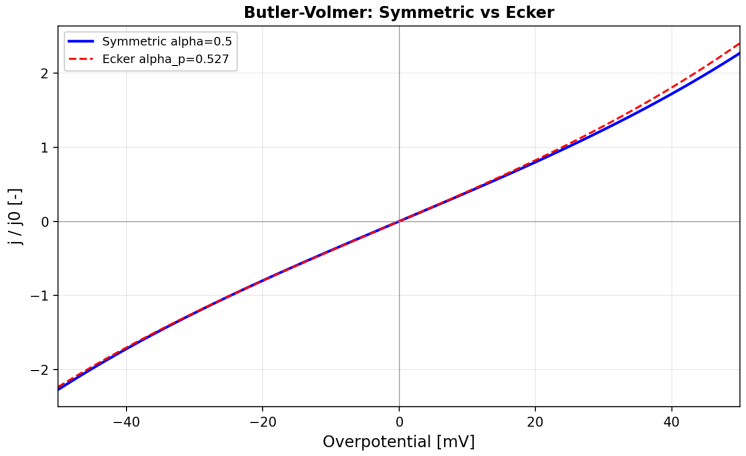


Figure 5.109: Butler-Volmer: exchange current-density with charge-transfer

Table 5.29 summarizes the assignment of the four parameters for this sub-step.

Parameter	**Symbol**	**Value and Unit**
Cathode conductivity	$\sigma_{s,p}$	$100\ S/m$
Anode conductivity	$\sigma_{s,n}$	$100\ S/m$
Cathodic charge-transfer coefficient	α_c	0.5
Anodic charge-transfer coefficient	α_a	0.5

Table 5.29: Step 5c: List of updated or retained Parameters

Sub-step 5d: Pre-estimation of reaction-rate coefficients

The sub-step 5d pre-estimates the reaction-rate coefficients $k_{0,p}$ and $k_{0,n}$, as scaling factors of respective exchange-current densities. As already explained, this stage exploits the CV-hold phase of a cycling test, using the Method B, with a double-exponential fitting. In particular, a cycle test at 1C is exploited for this case of pre-estimation of the two coefficients.

As a reminder, the applied equation to study the kinetic effects is expressed by current-decay with two different time-constants:

$$I(t) = I_1 \cdot e^{-t/\tau_1} + I_2 \cdot e^{-t/\tau_2} + I_\infty$$

where: τ_{fast}, in the range $(50 - 200)\ s$, is dominated by cathode charge-transfer, whereas τ_{slow}, in the range $\sim (500 - 2000)\ s$, reflects a mixed anode-kinetics / solid-diffusion envelope (with some contribution even of SEI-layer resistance).

Finally, scale-factors are computed by running the baseline SPMe simulation with the same CC-CV charge protocol of cycling, fitting the double exponential behavior, and taking the following ratios:

$$k_{0,p,scale} = \frac{\tau_{1,sim}}{\tau_{1,exp}}$$

$$k_{0,n,scale} = \frac{\tau_{2,sim}}{\tau_{2,exp}}$$

In Figure 5.110, the plot shows essentially the current-decay, with double-exponential behavior, as a function of time, in CV-hold phase.

The first exponential term is tied to $k_{0,p}$, with experimental $\tau_{fast} \simeq 185\ s$. The second exponential term is tied to $k_{0,n}$, with experimental $\tau_{slow} \simeq 1292\ s$.

The quality of fitting is really high, almost perfect, with the coefficient of determination: $R^2 = 0.9991$.

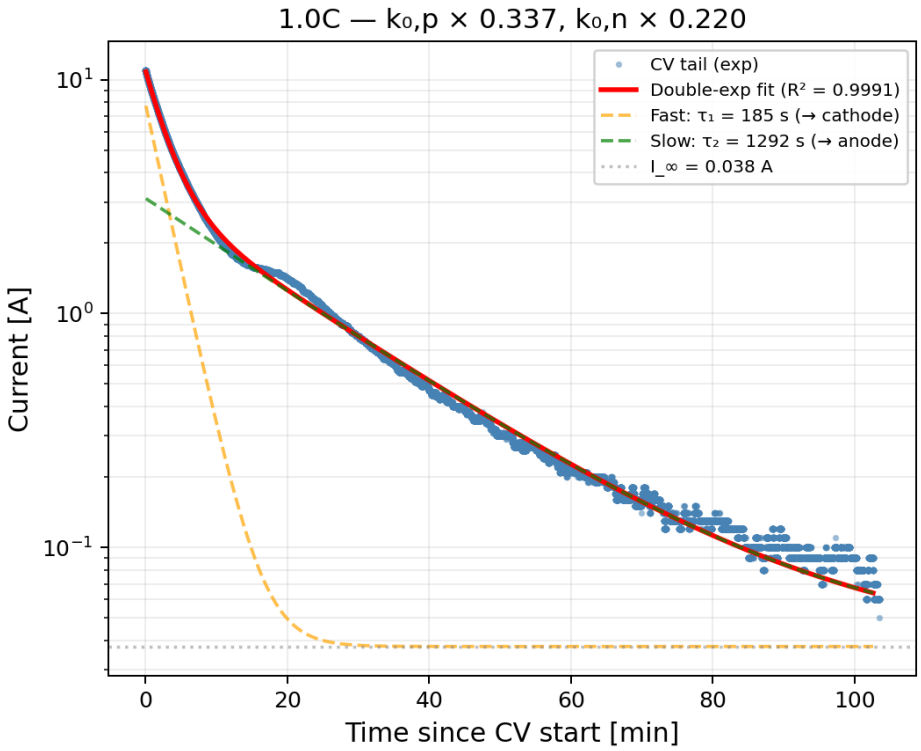


Figure 5.110: Double-exponential cycling-fitting using CV-phase after charge at 1C

In Figure 5.111, a cross-validation plot, focusing on the CV-hold phase of cycling tests, at 11 different C-rates, between experiments and simulations, is shown. This graph is purely a fast validation of the obtained results against experiments, after the end of this sub-step (5d): the kinetic coefficients, and the other parameters tied to CV-hold phase of cycling tests (SEI-resistivity and diffusion coefficients at 100% SoC) will be refined in next sub-steps.

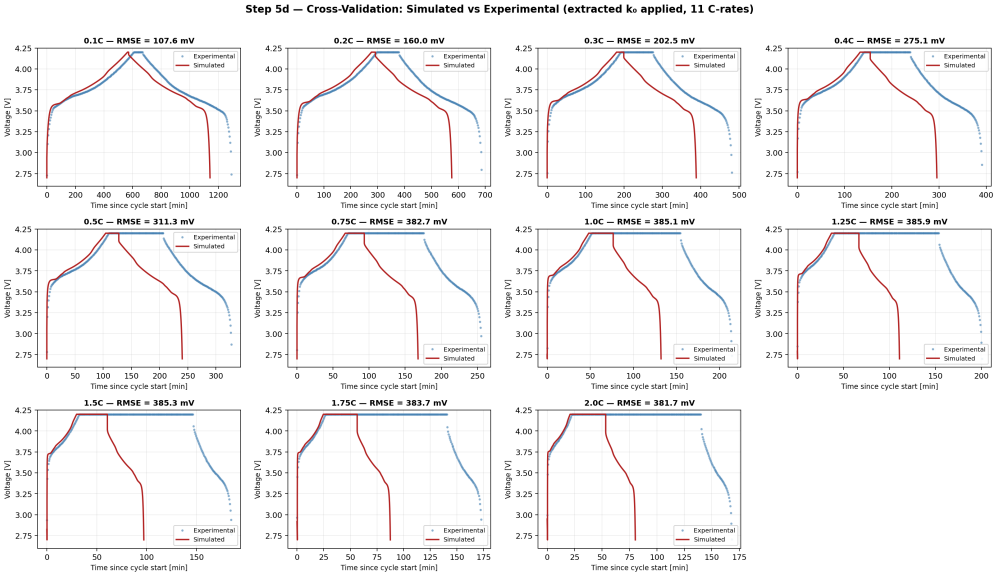


Figure 5.111: Step 5d: Cycling validation at different C-rates

In Figure 5.112, a final assessment of RMSE values, regarding the previous cross-validation, is reported per C-rate.

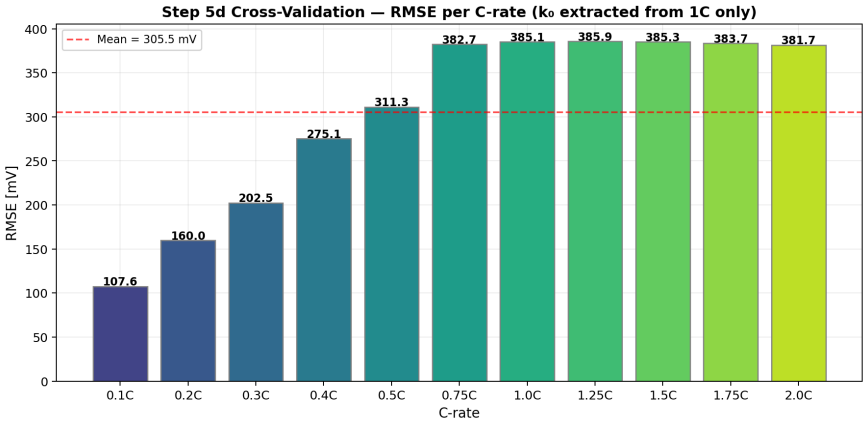


Figure 5.112: RMSE assessment for cycling experiments after sub-step 5d

Table 5.30 reports the scaled reaction-rate constants applied to Mohtat's baseline.

Parameter	**Symbol**	**Value and Unit**
Cathode reaction-rate constant	$k_{0,p}$	$0.3372 \cdot k_{0,p,Mohtat}$
Anode reaction-rate constant	$k_{0,n}$	$0.2199 \cdot k_{0,n,Mohtat}$

Table 5.30: Step 5d: List of updated or retained Parameters

The scaling factors of the two default Mohtat's coefficients are calculated in this way:

$$\tau_{fast,sim} = 62.23\ s\ \ ;\ \ \tau_{slow,sim} = 284.04\ s$$

$$\tau_{fast,exp} = 184.56\ s\ \ ;\ \ \tau_{slow,exp} = 1291.61\ s$$

$$k_{0,p,scale} = \frac{\tau_{fast,sim}}{\tau_{fast,exp}} = 0.3372$$

$$k_{0,n,scale} = \frac{\tau_{slow,sim}}{\tau_{slow,exp}} = 0.2199$$

Sub-step 5e: Cathode OCP function correction with Pseudo-OCV

The sub-step 5e adjusts the positive electrode OCP function, starting from Mohtat's NMC OCP one. It extracts a local polynomial correction of cathode's OCP, minimizing residual error against the C/50 averaged Pseudo-OCV, with the graphite OCP held fixed at Mohtat's reference.

The attribution of the whole correction to the positive electrode OCP is a standard choice: graphite OCP is well-characterized shared chemistry (Ecker et al. (2015) [16] [17], Mohtat et al. (2020) [13]), whereas NMC is the most variable electrode.

As a reminder, the basic equation used in this stage is given by:

$$U_{p,exp}(y(SoC)) = V_{avg}(SoC) + U_{n,Mohtat}(x(SoC))$$

where: $V_{avg}(SoC)$ is the average function of SoC from Pseudo-OCV data.

The basic method, to perform the OCP fixing, is a local/residual regression, based on "PCHIP" approach. Basically, the sub-step models the small OCP correction directly through:

$$r(y) = U_{p,exp}(y) - U_{p,Mohtat}(y)$$

where: $r(y)$ is the residual, dependent on cathode stoichiometry (y).

This approach carries out a shape-preserving monotone interpolation, through robust (median) residual bins, and without any over-shoot.

Two essential features of cathode's OCP correction are: (i) use of trust-window for experimental Pseudo-OCV data in the range $(8 - 100)\%$ of SoC, reverting to Mohtat's reference outside it; (ii) application of isotonic-guard, guaranteeing a monotonically decreasing (and physically valid) NMC OCP.

In Figure 5.113, the extracted voltage curve from average Pseudo-OCV data as a function of SoC (%) is shown, considering it as reference to reconstruct the NMC OCP function.

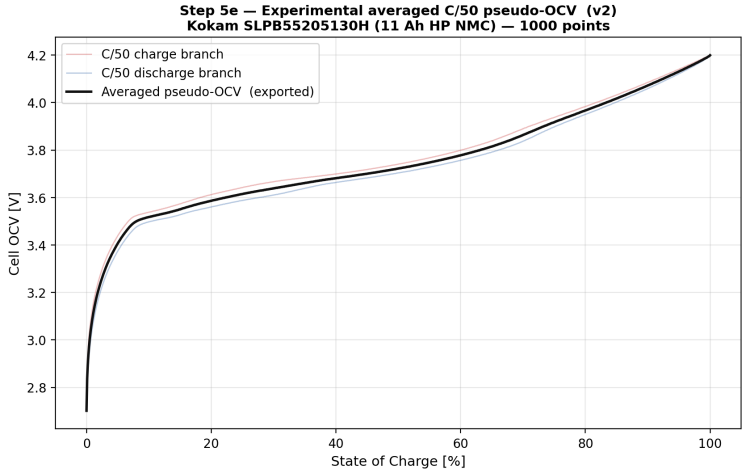


Figure 5.113: Experimental average C/50 Pseudo-OCV curve

Figure 5.114 represents the practical procedure implemented in this sub-step, i.e. the default Mohtat's OCP curve, function of its stoichiometry, corrected through the use of experimental data. The trust window is limited, from 100 % SoC down to 8% SoC, where an artifact of the curve is excluded from correction, due to its non-physical shape. The second plot shows the local correction performed for the cathode's OCP, with residuals reaching peak values of $25\ mV$.

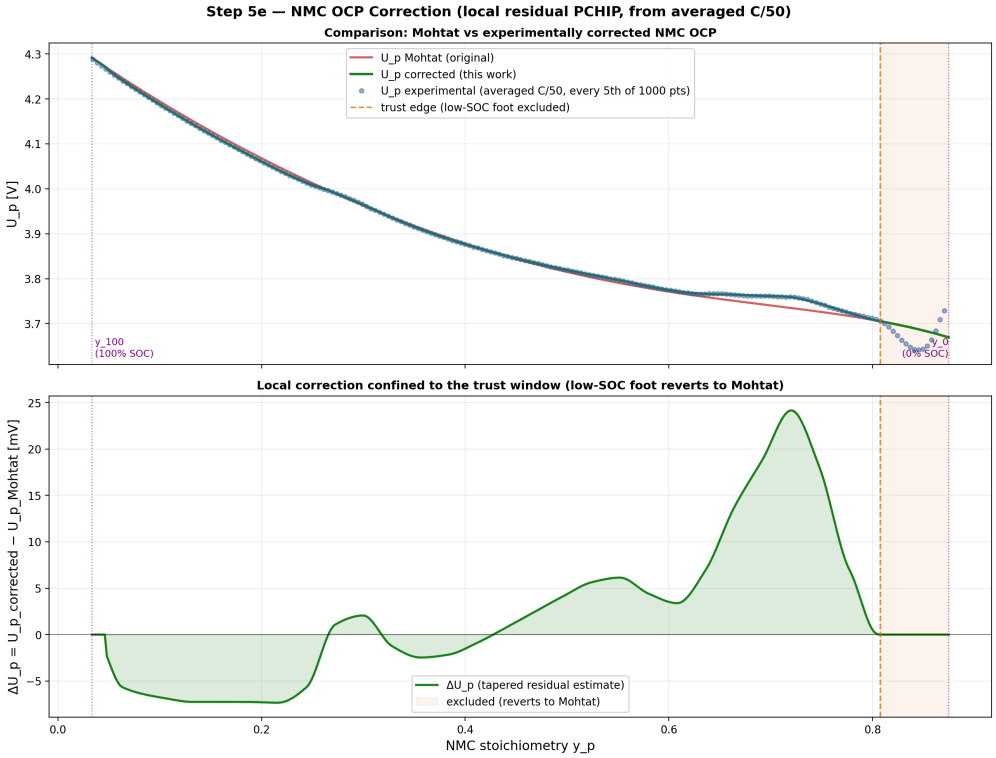


Figure 5.114: Cathode's OCP correction plots

In Figure 5.115, the quality of averaged C/50 Pseudo-OCV fitting is shown with two sub-plots. The first plot reports the full-cell OCV curve against State-of-Charge, before and after the correction. The RMSE value widely decreases from $13.1\ mV$ of previous case until $9.4\ mV$ of actual one, with a clear enhancement of the model response. The second plot is a graph of local error between the simulation and experimental data, highlighting the decisive improvement of the OCV shape in the SoC range $(8 - 100)\%$.

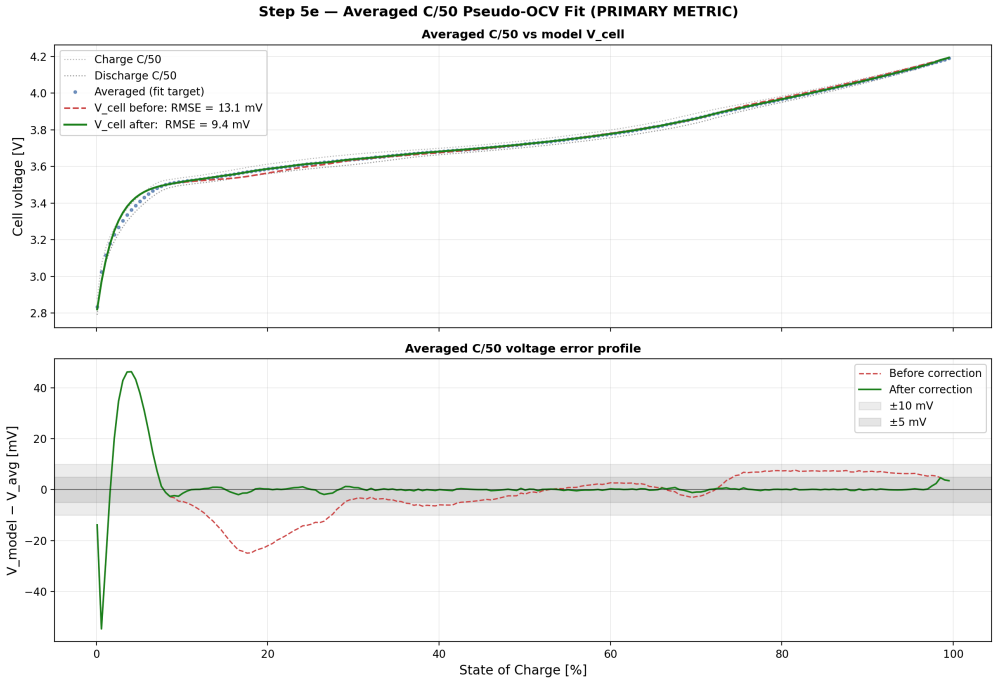


Figure 5.115: Full-OCV curve validation plots

In Figure 5.116, an updated Differential-Voltage-Analysis is described with two new sub-plots. The first plot is relative to incremental capacity dQ/dV against SoC; it essentially shows the evident improvement of its shape, better following the experimental curve, with respect to previous case. The second plot represents the incremental slope of $d(OCV)/d(SoC)$ versus SoC; even in this case, the model's enhancement is verified, although not as clear as the one of first plot.

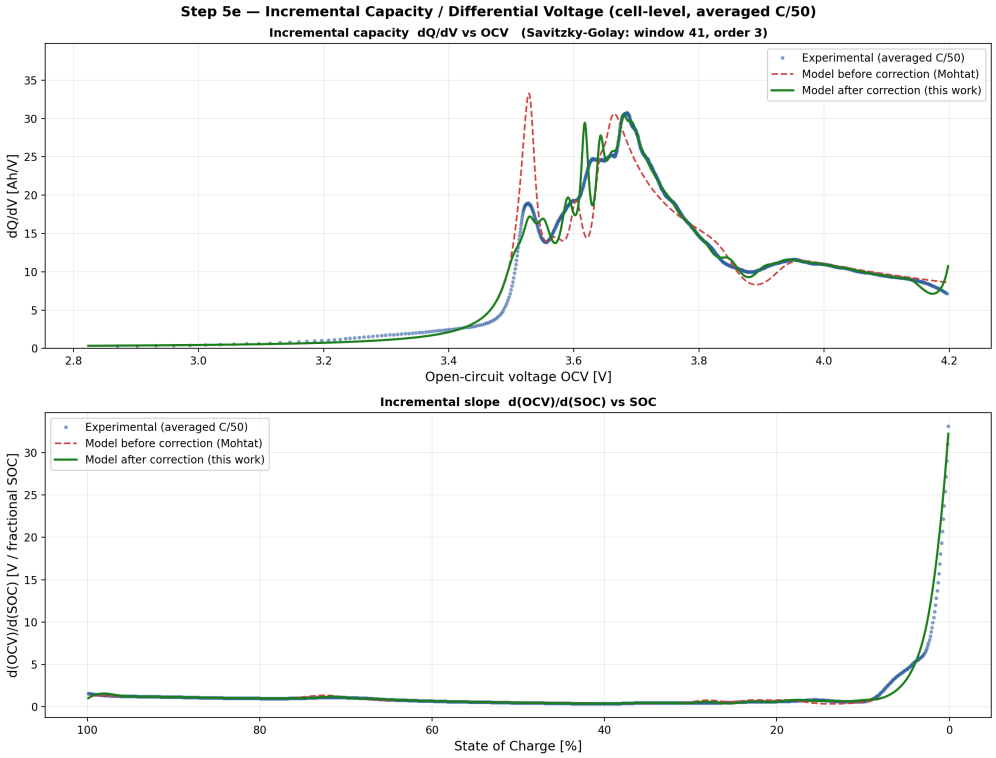


Figure 5.116: Differential Voltage Analysis (at cell-level)

In Figure 5.117, a practical comparison between the OCV function from Pseudo-OCV data and

the one from the GITT-extracted OCV data is made. The first plot shows the obtained equilibrium voltage points from GITT tests in charge or discharge, with slight differences due to hysteresis; their shape is very similar to the trend of averaged Pseudo-OCV data for full-cell OCV. The second plot analyzes the differences between refined cell's OCV curve and the corresponding voltage rest-points from GITT tests.

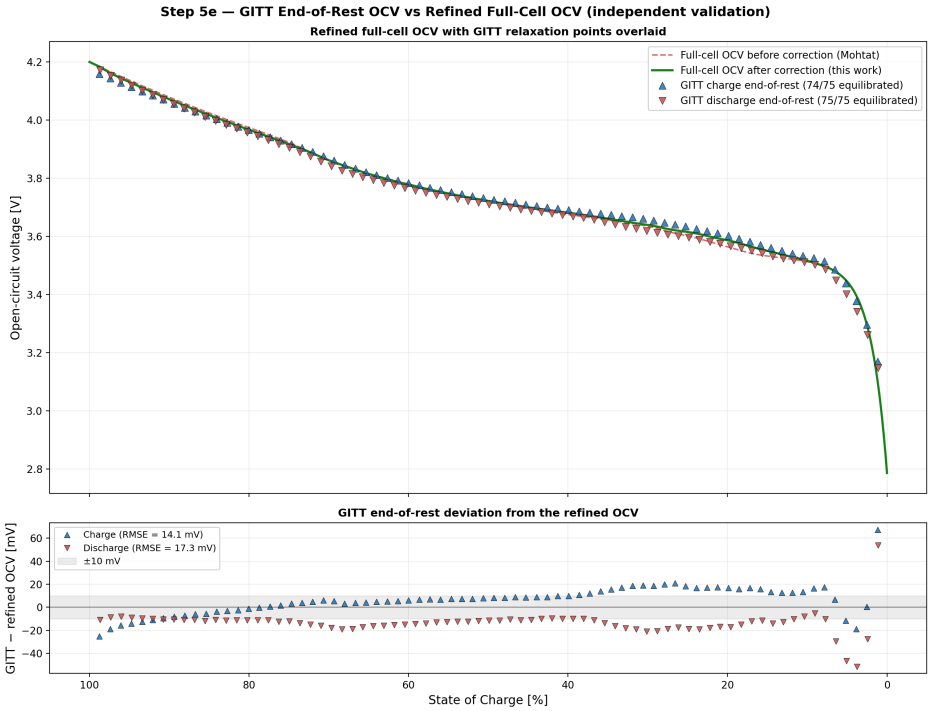


Figure 5.117: Cell's OCV function: average Pseudo-OCV versus GITT tests

In Figure 5.118, a GITT cross-validation for charge and discharge tests is shown. It considers two sub-plots: the first one focuses on GITT charge end-of-rest residuals, before and after the OCP correction, reporting a RMSE of $14.1\ mV$; the second one analyzes the GITT discharge end-of-rest residuals, in the same two conditions, with a final RMSE of $17.3\ mV$.

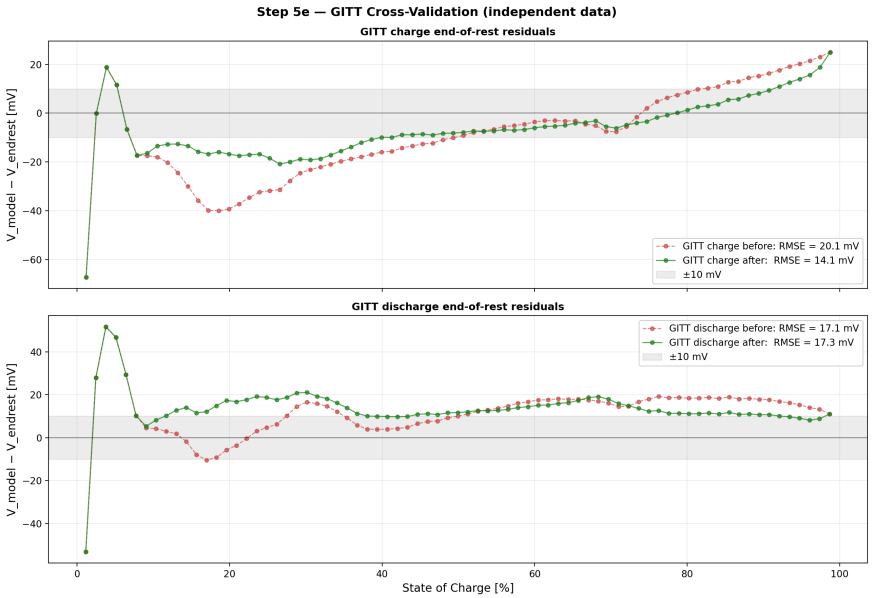


Figure 5.118: GITT cross-validation plots

Table 5.31 summarizes the modified or retained function-parameters of this sub-step.

Parameter	Symbol	Value and Unit
Positive electrode OCP (corrected)	$U_p(y(SoC))$	Function* [V]
Negative electrode OCP (retained)	$U_{n,Mohtat}(x(SoC))$	Function* [V]

Table 5.31: Step 5e: List of updated or retained Parameters

In conclusion, the improvement of cell's OCV curve is quantified in percentage terms: RMSE lowered from $13.1\ mV$ to $9.4\ mV$, thereby with an improvement of approximately 28.2%.

Sub-step 5f: Global Optimization with three-stage architecture

The sub-step 5f is the most crucial step of the entire Parametrization, considering that it optimizes 12 parameters of the model, within tight bounds, in order to make the entire strategy more reliable for the final model's parameters.

This step is composed of three stages, in which high-sensitivity parameters are optimized: the first stage deals with 9 parameters, tied to geometry and electrode micro-structural together with transport/diffusion properties, using the Differential-Evolution and Nelder-Mead approaches; the second-stage contains 3 parameters, more anchored to physical extraction steps (5b, 5d), using only Nelder-Mead; the third and final stage operates on all 12 parameters of the two initial stages, in order to perform a global-polish.

The Stage 1 cover all the 9 impactful parameters for previous steps, using 6 multi-rate discharge tests simultaneously, with inverse-RMSE weighting. The Stage 2 focuses on kinetic refinement, within $\pm 15\%$ range. The Stage 3 operates a global-polish, with allowed variations of $\pm 10\%$ for scalar parameters and ± 0.10 decade for function-parameters.

The following Table 5.32 indicates the number of iterations for each stage, using DE as Differential-Evolution and NM as Nelder-Mead.

Stage	Iterations
Stage 1	DE: 100 x 50 x 9 (45000) & NM: 800
Stage 2	NM: 1000
Stage 3	NM: 1000

Table 5.32: Number of iterations per Stage

Table 5.33 indicates the bounds selected for the optimization of each parameter, sub-divided per stage; they were chosen to respect the type of Kokam cell design. Indeed, some parameters are forced away from Mohtat's starting values, with the aim of making a High-Power design re-anchoring for the final parameter-set.

Stage	Parameter	Bounds
Stage 1	Cathode thickness (L_p)	$(30, 42)\ \mu m$
	Anode thickness (L_n)	$(56, 68)\ \mu m$
	Positive active material volume-fraction ($\varepsilon_{s,p}$)	$(0.300, 0.445)$
	Negative active material volume-fraction ($\varepsilon_{s,n}$)	$(0.420, 0.610)$
	Electrode-width (W)	$(0.268, 0.310)\ m$
	Positive particle radius ($R_{p,p}$)	$(1, 11)\ \mu m$
	Negative particle radius ($R_{p,n}$)	$(1, 15)\ \mu m$
	Cathode diffusivity scaling-factor ($D_{s,p,scale}$)	$(0.1, 10)$
	Anode diffusivity scaling-factor ($D_{s,n,scale}$)	$(0.1, 10)$
Stage 2	SEI-layer resistivity (ρ_{SEI})	$\pm 15\%$
	Cathode reaction-rate coefficient ($k_{0,p}$)	$\pm 15\%$
	Anode reaction-rate coefficient ($k_{0,n}$)	$\pm 15\%$
Stage 3	Global-polish on all 12 parameters	$\pm 10\%$ or $\pm 0.10 - decade$

Table 5.33: Parameter bounds per Stage

The selected range for areal-capacity, through these bounds, in particular through tuning the total electrode-area, was in the following reasonable range:

Areal-capacity $\rightarrow (13.0 - 15.0)\ Ah/m^2$.

Figure 5.119 represents the optimization convergence history. The entire process lasted for 24 hours, working on the minimization of RMSE between simulations and experiments. The starting RMSE value, averaged among the 6 discharge experiments, was around $(100 - 110)\ mV$, and finally decreased to approximately $18\ mV$.

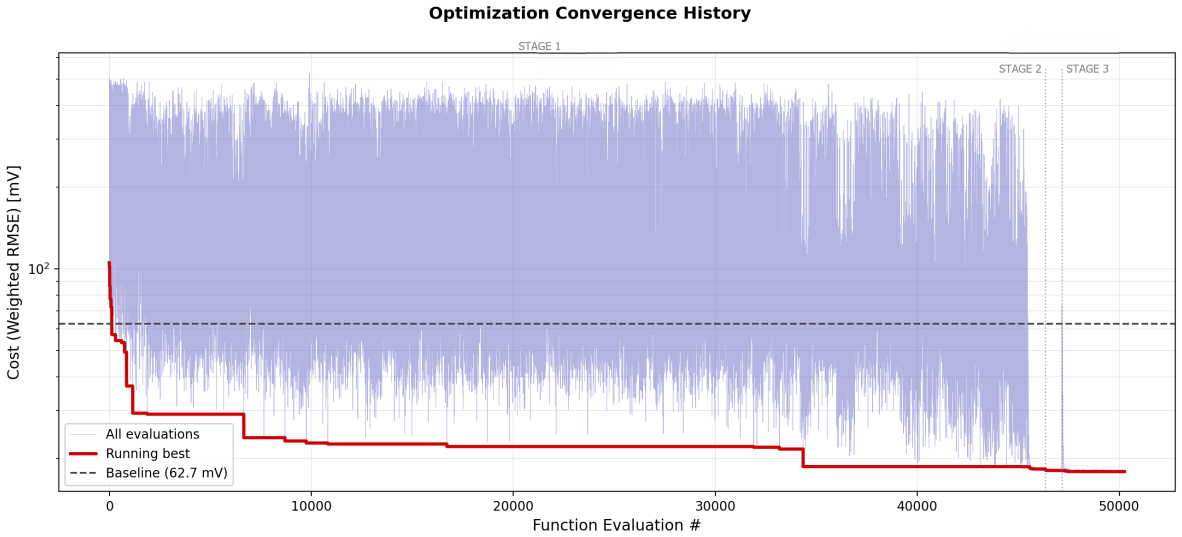


Figure 5.119: Step 5f: optimization convergence history

In Figure 5.120, two plots "voltage versus time" are shown: the first one represents the results before the optimization, the second one after the optimization; the improvement of terminal-voltage curves, at every C-rate, after the optimization Step, is evident.

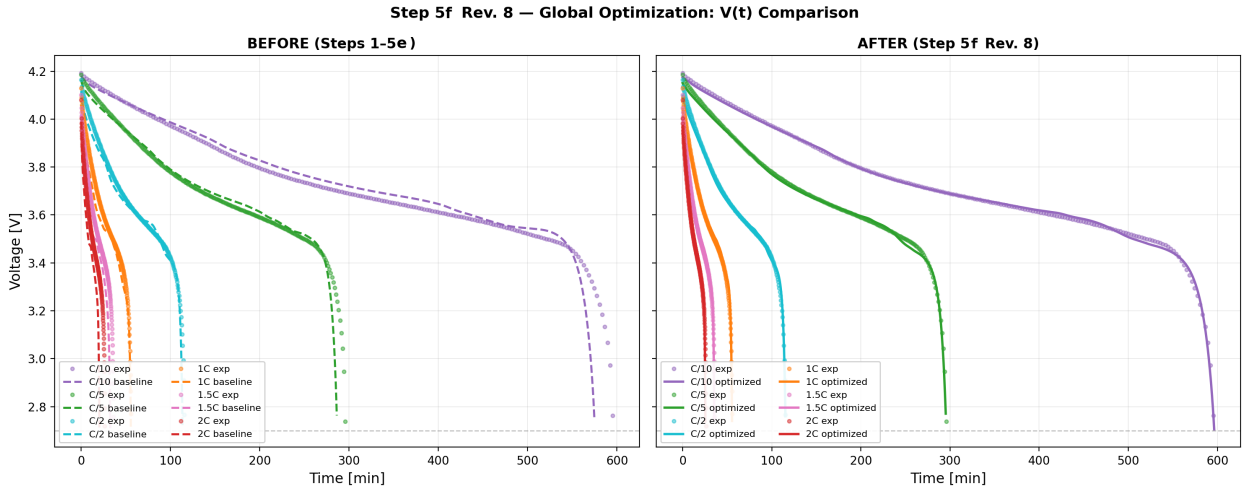


Figure 5.120: Voltage vs time plots: before and after Step 5f

In Figure 5.121, a general assessment of voltage curves against the discharge-capacity is made. More precisely, the picture shows a comparison "before versus after", underlining the enhancement of the SPMe simulations with respect to experiments, after the optimization conclusion. The evolution of the 6-rates voltage curves is evident, with a sharp improvement of their shapes around the plateau-region and even near the knee-region.

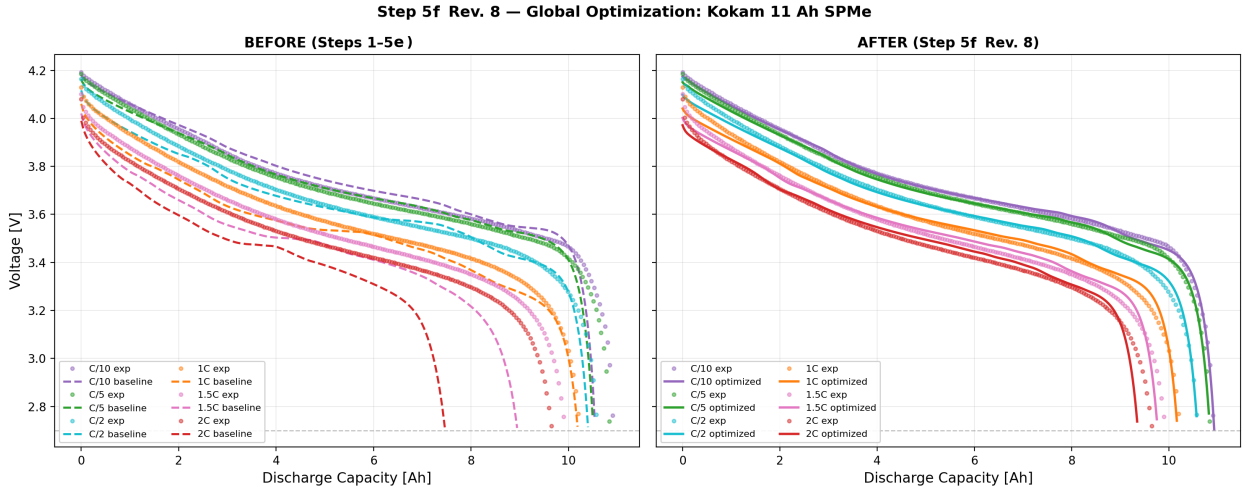


Figure 5.121: Voltage vs. discharge-capacity: before and after Step 5f

In Figure 5.122, the local error is evaluated between simulations and experiments, at the 6 used C-rates, before and after optimization. The plots highlight the great enhancement of terminal-voltage curves at lower rates, whereas the results are slightly worse at higher rates, as usual feature of SPMe modeling.

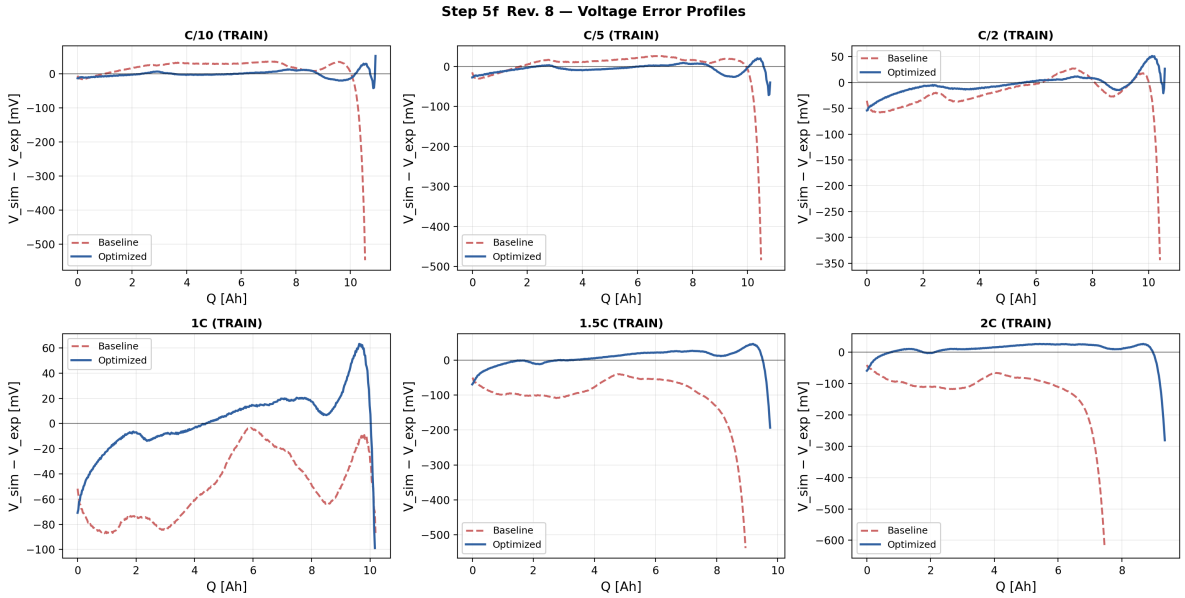


Figure 5.122: Step 5f: voltage error profiles

Figures 5.123 and 5.124 show the final results obtained at the end of Stage 3, reporting CC-discharge verifications. The 6 voltage curves show a progressive increase of RMSE from the lowest rate to the highest one, confirming the limitations of the model in the reproduction of real experiments at elevated C-rates. Overall, the results are a trade-off between tests at very different rates, therefore the achieved outcome is optimal for the final parameter calibration.

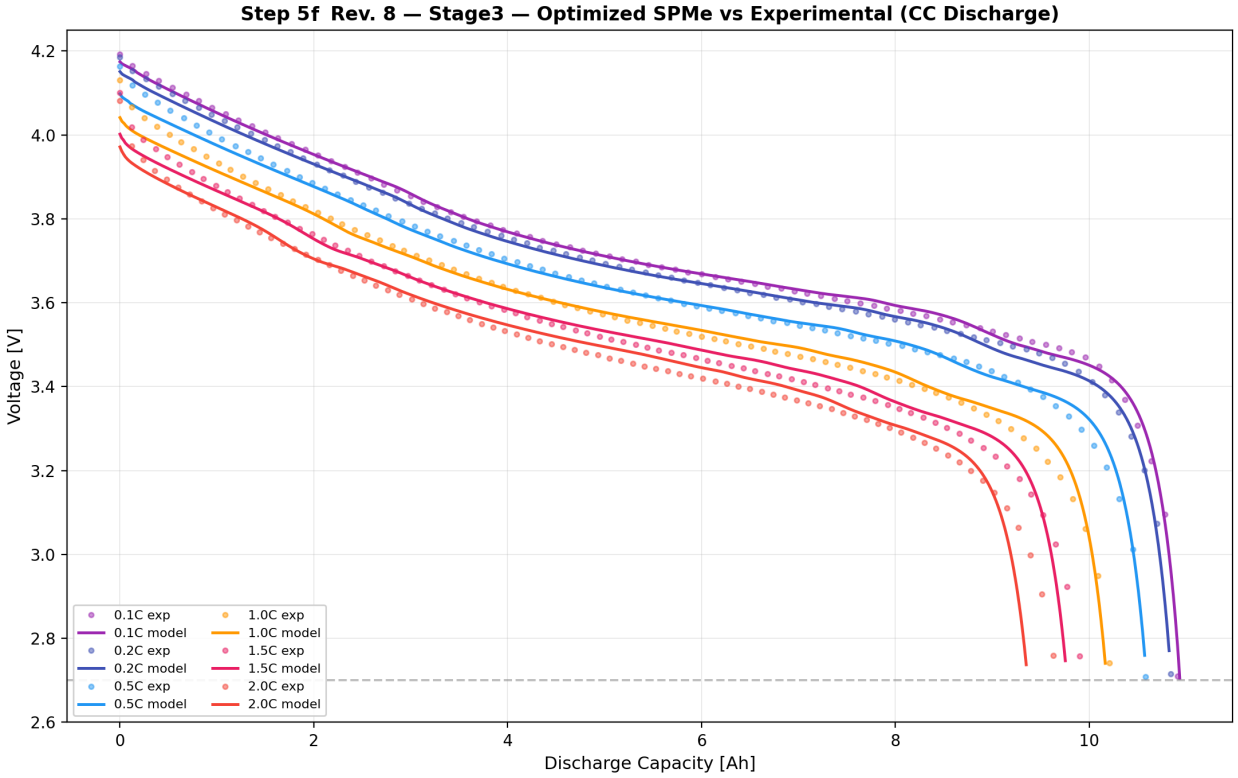


Figure 5.123: Step 5f: Optimized SPMe 6 rates CC discharges

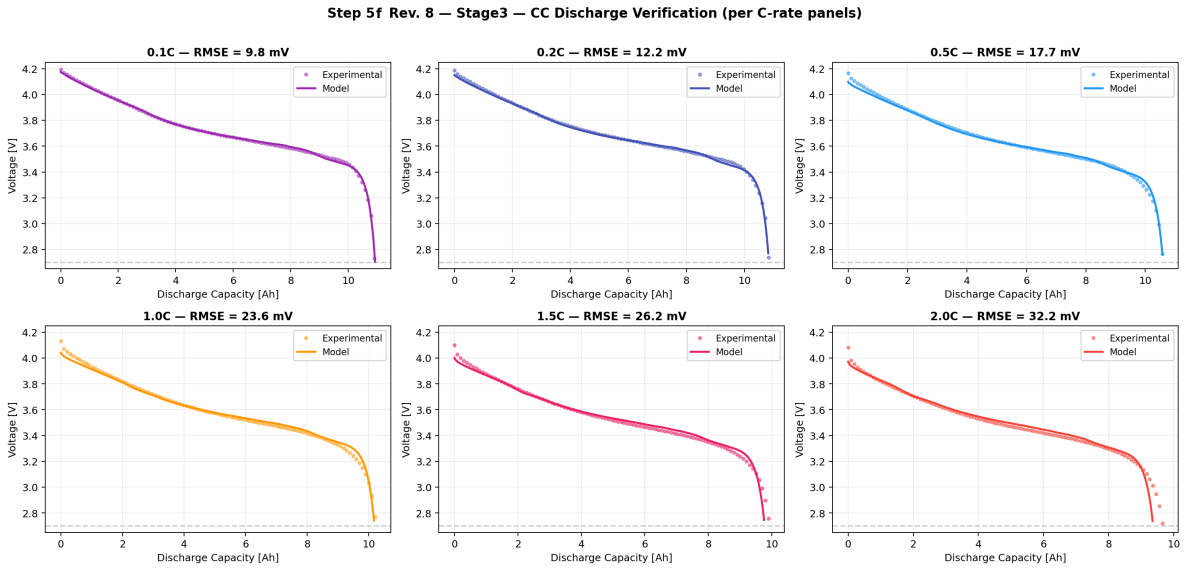


Figure 5.124: Step 5f: CC discharge verification per C-rate

In Figures 5.125 and 5.126, two verification plots are shown: the first plot is related to GITT-charge validation, whereas the second plot is related to the GITT-discharge verification. Both graphs confirm the validity of the optimized parameter-set against complex pulsed experiments.

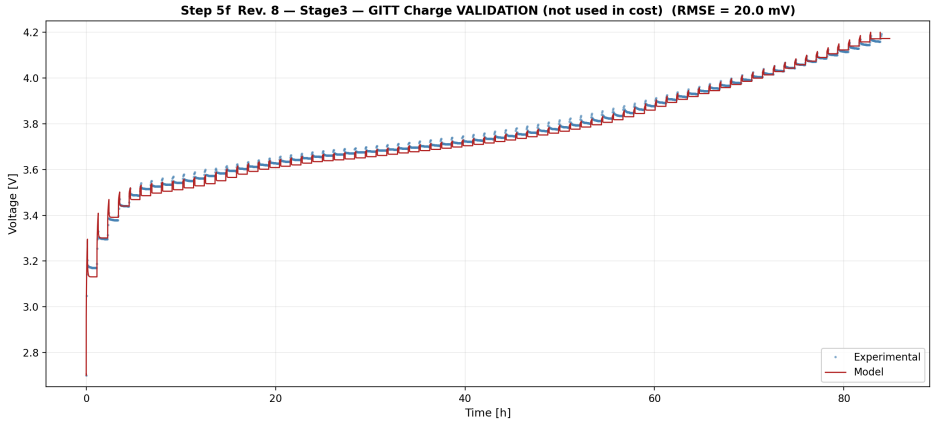


Figure 5.125: Step 5f: validation plot for GITT charge

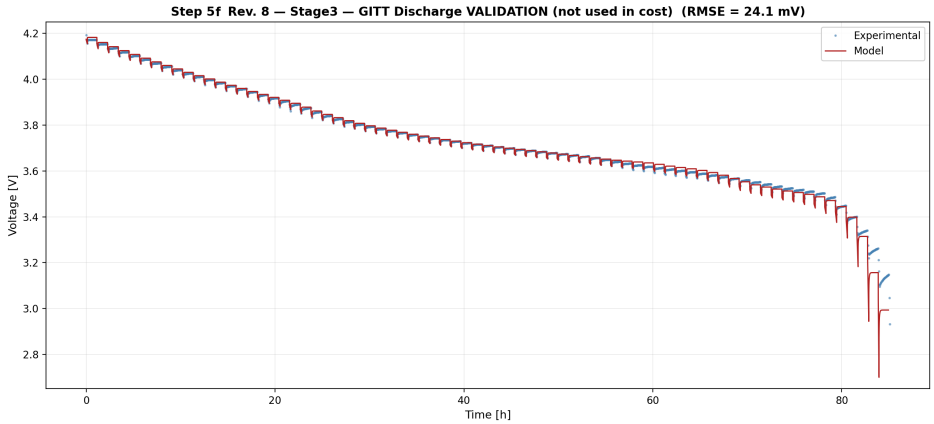


Figure 5.126: Step 5f: validation plot for GITT discharge

In Figure 5.127, an assessment of RMSE on training tests from 0.1C discharge to 2C discharge is shown, through a bar-diagram. It confirms the theory explained before about the limitations at high C-rate (near to 1.5C / 2C) of SPMe model. Overall, optimal results have been reached at the lower rates (C/10, C/5, C/2).

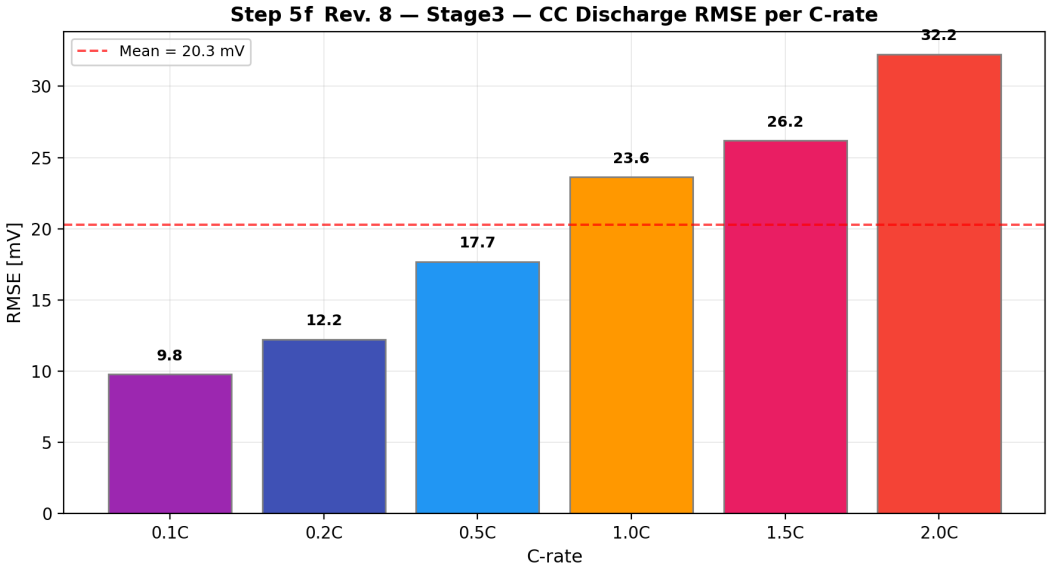


Figure 5.127: Step 5f: CC discharge RMSE per C-rate

The final Figure 5.128 shows the evident improvement, in terms of RMSE, of the model simulations, at least for multi-rate CC discharges, after the optimization. The red bars indicate the RMSE evaluated for the 6 multi-rate discharges before the current optimization Step. Instead, the blue bars represent the practical improvement of the model response, after the optimization; in all the cases, the average error was decreased of at least 55%, demonstrating the goodness of the applied procedure.

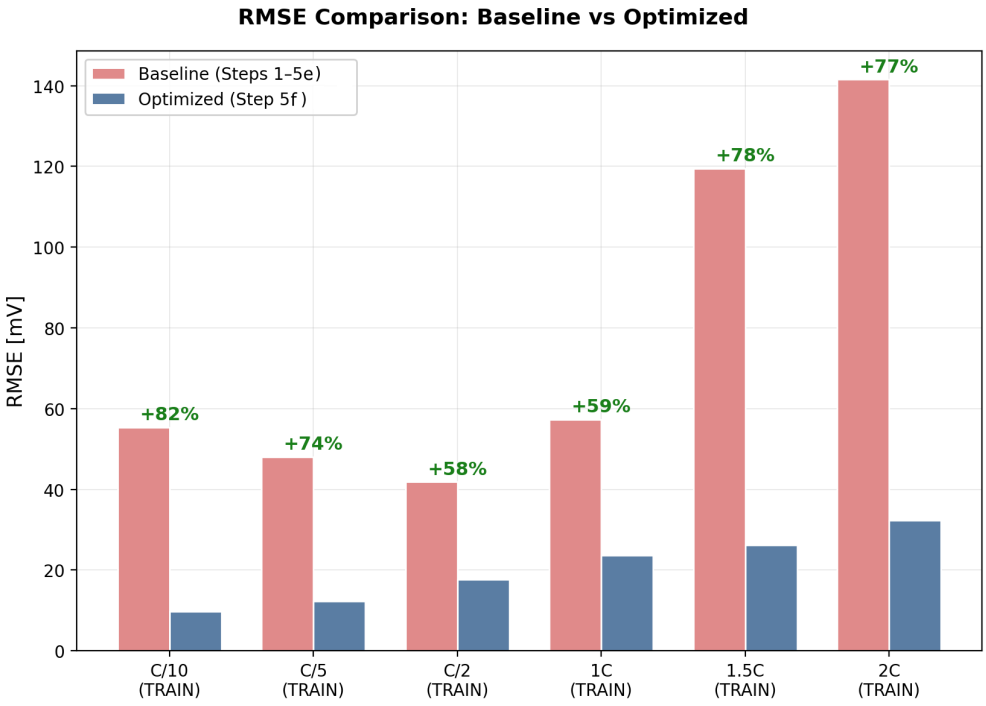


Figure 5.128: RMSE comparison per C-rate: Before vs. After

Finally, the results of the 12 optimized parameters, at the end of Stage 3, are summarized in Table 5.34.

Parameter	**Pre- and post-optimization values**
Cathode thickness (L_p)	$67.0\ \mu m \rightarrow 39.76\ \mu m$
Anode thickness (L_n)	$62.0\ \mu m \rightarrow 66.55\ \mu m$
Positive active material volume-fraction ($\varepsilon_{s,p}$)	$0.420 \rightarrow 0.443$
Negative active material volume-fraction ($\varepsilon_{s,n}$)	$0.585 \rightarrow 0.422$
Electrode-width (W)	$0.205\ m \rightarrow \sim 0.277\ m$
Positive particle radius ($R_{p,p}$)	$3.50\ \mu m \rightarrow 1.99\ \mu m$
Negative particle radius ($R_{p,n}$)	$2.50\ \mu m \rightarrow 5.07\ \mu m$
Cathode diffusivity scaling-factor ($D_{s,p,scale}$)	$1.0 \rightarrow \sim 2.795$
Anode diffusivity scaling-factor ($D_{s,n,scale}$)	$1.0 \rightarrow \sim 1.314$
SEI-layer resistivity (ρ_{SEI})	$944.8\ k\Omega \cdot m \rightarrow 967.47\ k\Omega \cdot m$
Cathode reaction-rate coefficient ($k_{0,p}$)	$0.337 \cdot k_{0,p,Mohtat} \rightarrow 0.289 \cdot k_{0,p,Mohtat}$
Anode reaction-rate coefficient ($k_{0,n}$)	$0.220 \cdot k_{0,n,Mohtat} \rightarrow 0.240 \cdot k_{0,n,Mohtat}$

Table 5.34: Stage 3 final results (end of optimization)

The values of total electrode-area and corresponding specific/areal capacity are expressed as follows:

$$A_{electrode} = H_{elc} \cdot W_{elc} \simeq 0.7548\ m^2$$

$$C_{specific} = \frac{Q_{nom}}{A_{electrode}} \simeq 14.57\ Ah/m^2$$

The value of areal capacity is perfectly suitable for an old HP cell, such as the Kokam one analyzed in this Thesis.

From Mohtat et al. (2020) [13], the two kinetic coefficients are included in exchange-current density functions; they are:

$$k_{0,p,Mohtat} = (5.0 \cdot 10^{-11})\ m^{2.5} \cdot mol^{-0.5} \cdot s^{-1} \quad , \quad k_{0,n,Mohtat} = (1.1 \cdot 10^{-11})\ m^{2.5} \cdot mol^{-0.5} \cdot s^{-1}$$

The two diffusivity functions, from "Mohtat2020", are only scalar values across stoichiometry windows; considering that $D_{s,p}(y)$, in the new parameter-set, becomes a 3^{rd}-order polynomial function, only $D_{s,n}(x)$ remains a scalar value:

$$D_{s,n}(x) = 5.0 \cdot 10^{-15}\ m^2/s$$

The specific interfacial-areas between each electrode and electrolyte are re-computed as follows:

$$a_{s,p} = 3 \cdot \frac{\varepsilon_{s,p}}{R_{p,p}} \simeq 0.668\ m^2/cm^3$$

$$a_{s,n} = 3 \cdot \frac{\varepsilon_{s,n}}{R_{p,n}} \simeq 0.250\ m^2/cm^3$$

Finally, considering an amount of binder around 10% for anode and 15% for cathode, the recalculated porosities become:

$$\varepsilon_{e,p} = 1.0 - \varepsilon_{s,p} - 0.15 = 0.407$$

$$\varepsilon_{e,n} = 1.0 - \varepsilon_{s,n} - 0.10 = 0.478$$

The porosities are increased from previous estimations in Step 4, resulting more aligned to HP theoretical design.

Sub-step 5g: Diagnostic verification

The sub-step 5g is simply a diagnostic-step, in which no parameter is modified; it offers a complete view of the last updated functions.

More precisely, it produces two complementary visualizations of the full-cell behavior at quasi-equilibrium:

- Full-cell OCV comparison → Pseudo-OCV (at C/50) versus GITT end-of-rest;
- Diffusion time constant $\tau(SoC)$ at each pulse.

In addition, the updated functions of diffusivity and OCP for both electrodes are analyzed with their new shapes, with respect to Mohtat's default ones.

In Figure 5.129, a representation of the updated OCP functions, after the last steps, is shown in two sub-plots. The first one is related to the OCP corrected function against the Mohtat's basis one for positive electrode, whereas the second sub-plot illustrates the fixed graphite OCP function. Both OCP functions are visualized inside their fitted stoichiometric windows.

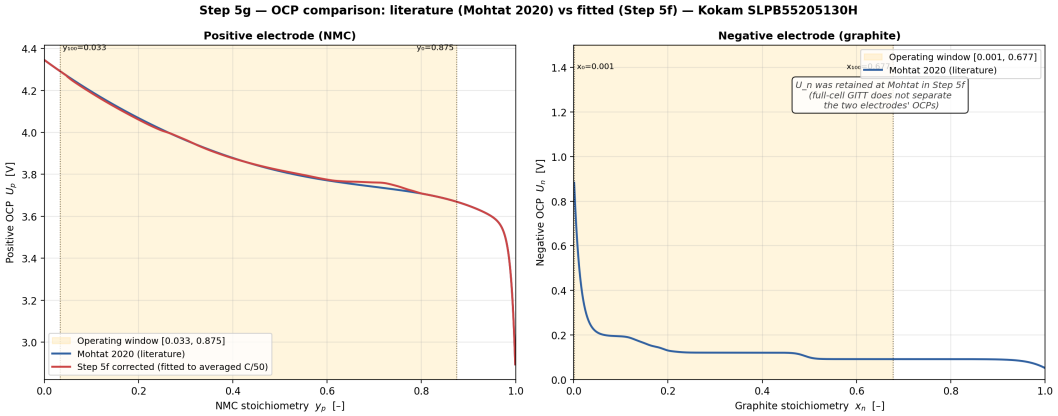


Figure 5.129: Step 5g: OCP comparison for NMC and graphite

In Figure 5.130, the two solid-phase diffusivity functions are shown in two separated sub-plots (at constant temperature of $25°C$). In the first plot, it is presented the scaled diffusivity $D_{s,p}$ for positive electrode, with a characteristic U-shape (as in other literature works); the mean value assumed by this function is well below the Mohtat's default one. A similar situation is viewed in the second graph for graphite's diffusivity, which is given by a constant value, as seen in the previous assumptions.

In both cases, there is a symptom that the simulated diffusion behavior of the cell is much slower than the one provided by Mohtat's parameter-set; this means a lower speed in the ions-transport inside the particles of anode and cathode, with respect to Mohtat's default.

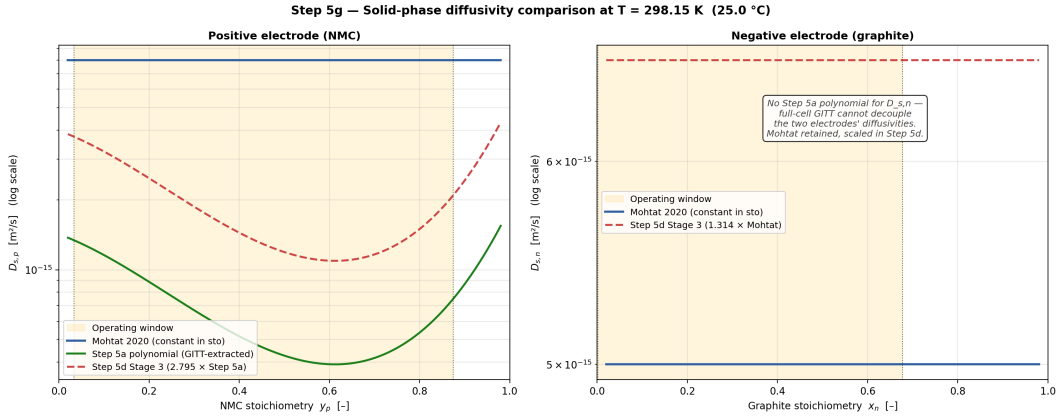


Figure 5.130: Step5g: D_s comparison for cathode and anode

The two Figures 5.131 and 5.132 perform a full-comparison, in terms of equilibrium voltage, between pseudo-OCV tests and GITT tests. The first figure analyzes the two tests, both in the charge case, showing certain differences (GITT extracted points are all below the Pseudo-OCV points). The second figure focuses on the differences between the two tests in the discharge case (GITT extracted points are above with respect to Pseudo-OCV points). These pictures highlight that hysteresis, consequence of residual over-potentials (even at C/50), influences much more the Pseudo-OCV tests than GITT tests.

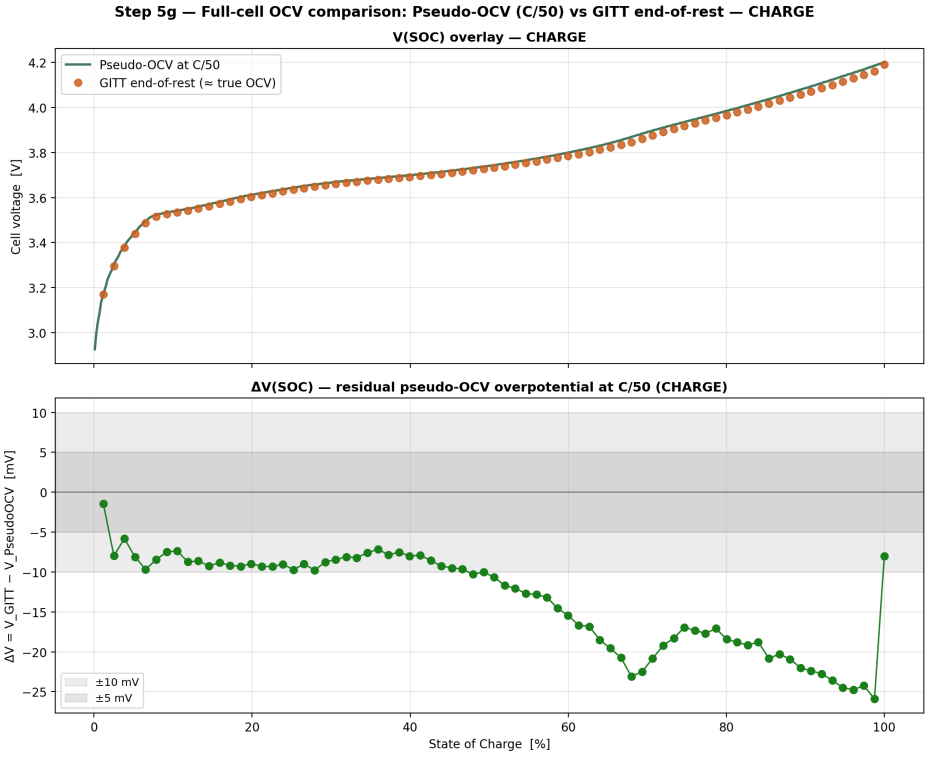


Figure 5.131: Step 5g: OCV charge comparison - Pseudo-OCV vs. GITT

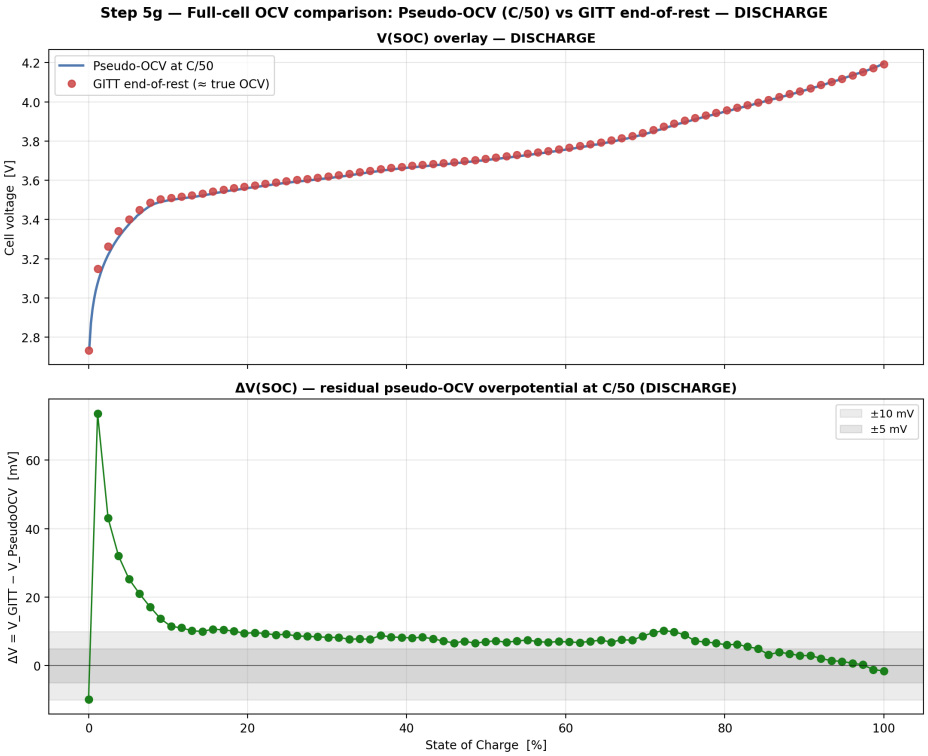


Figure 5.132: Step 5g: OCV discharge comparison - Pseudo-OCV vs. GITT

In the last Figure 5.133, a complex double comparison is made in terms of time-constants, obtained from model's solid-phase diffusivities (through formula $\tau = R_p^2/D_s$) and from experimental GITT-charge and GITT-discharge. All the time-constants are considered as functions of SoC.

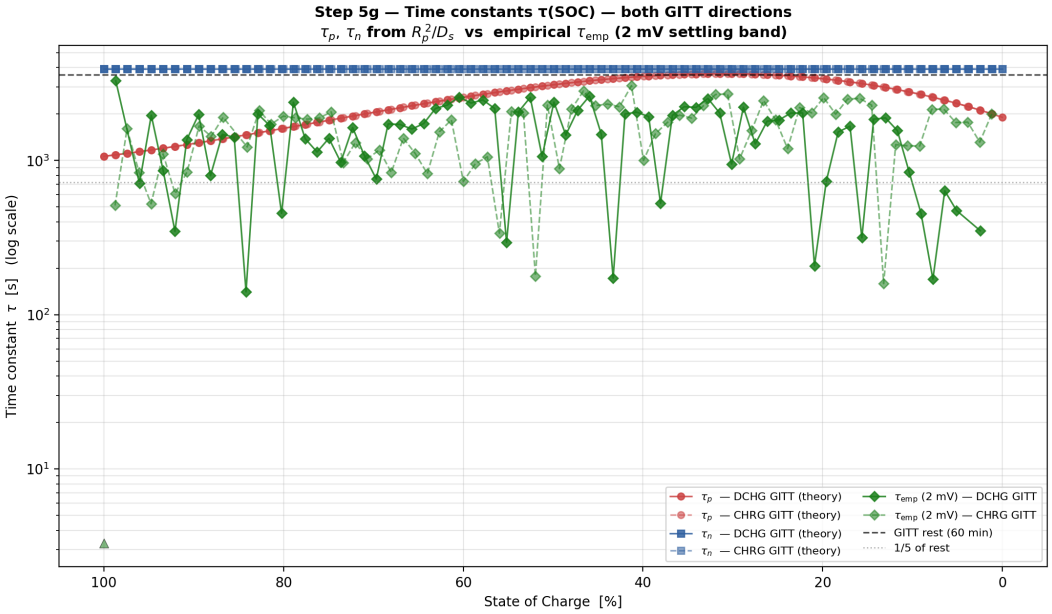


Figure 5.133: Step 5g: GITT time-constants (empirical vs model)

The first aspect to analyze is the GITT-duration rest ($60\ min$), that establishes if this settled rest is sufficient for the experimental equilibrium. Actually, this aspect is satisfied, because the experimental τ_{emp} profile is almost always well below the $60\ min$ time-limit. Essentially, the real cell is experimentally well equilibrated, after each pulse of GITT tests.

Meanwhile, the plot shows also the model's τ_p and τ_n, tied to diffusion phenomena for positive and negative electrodes. In both cases, the time-constants are above the experimental full-cell time-constant τ_{emp}. This means that the cell actually relaxes faster than single-particle diffusion would predict, through the model, although the magnitude orders of τ_{emp} and τ_p/τ_n are comparable; this last feature is positive, because the real and simulated diffusion phenomena have a similar duration.

This is the last step of effective parametrization, concluding the block of Step 5. The next and final stage will validate the model.

5.5.6 Step 7: Final validation of model's parameter-set

The final Step 7 validates the final parameter set produced by the full-parametrization chain (from Step 1 to Step 5g).

As assumed in the parametrization strategy, the validation is made against all the available experimental tests, distinguishing rigorously them into three blocks:

1. Training (optimization) tests;
2. Adjustment (pre-estimation) tests;
3. Pure-validation tests.

In Figure 5.134, the plot shows the validation of SPMe model against the training multi-rate 6 discharge tests. These results are the same ones analyzed in the previous Step 5f.

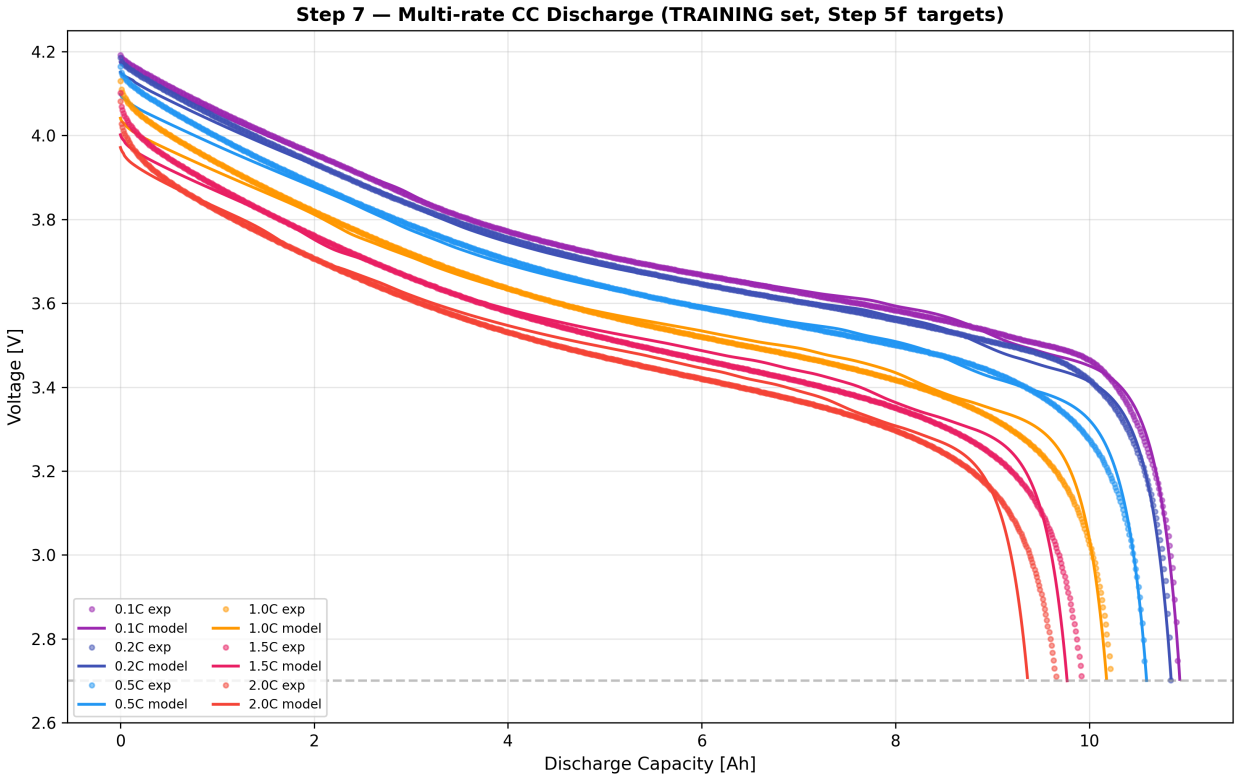


Figure 5.134: Validation plot: 6 multi-rate discharges

In Figure 5.135, the two plots show the validation of the model against the Pseudo-OCV tests, performed at C/50. The difference between simulations and experiments is essentially due to

imperfect OCP curves and assumed maximum Li-ion concentration ($c_{s,max,p}$ & $c_{s,max,n}$) values for anode and cathode. Overall, the results are satisfactory for both C/50 charge and discharge branches.

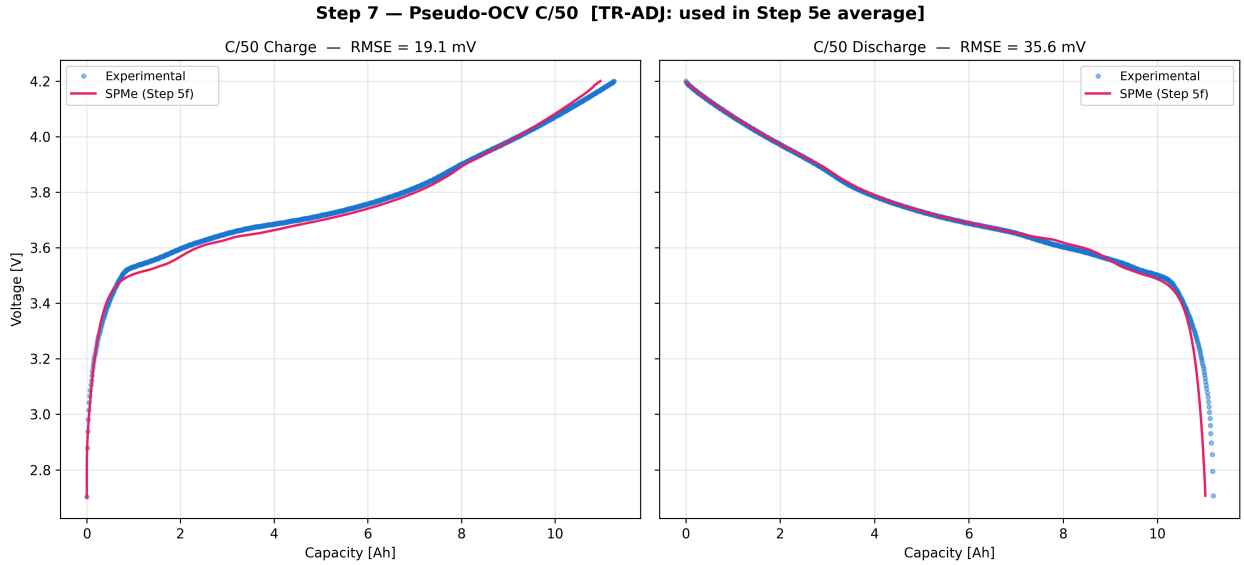


Figure 5.135: Validation plot: Pseudo-OCV (C/50) in charge/discharge

In Figure 5.136, the two GITT tests, charge and discharge, are validated against the real GITT data, showing a good RMSE, considering that they were not used as object of optimization; only the GITT discharge test was exploited to extract the positive electrode diffusivity function, thereby the two GITT can be considered as adjustment tests. The phases of pulse and relaxation are correctly followed by the simulations, with respect to experimental patterns, considering a good compromise in the time-constants for diffusion, as already analyzed in Step 5g.

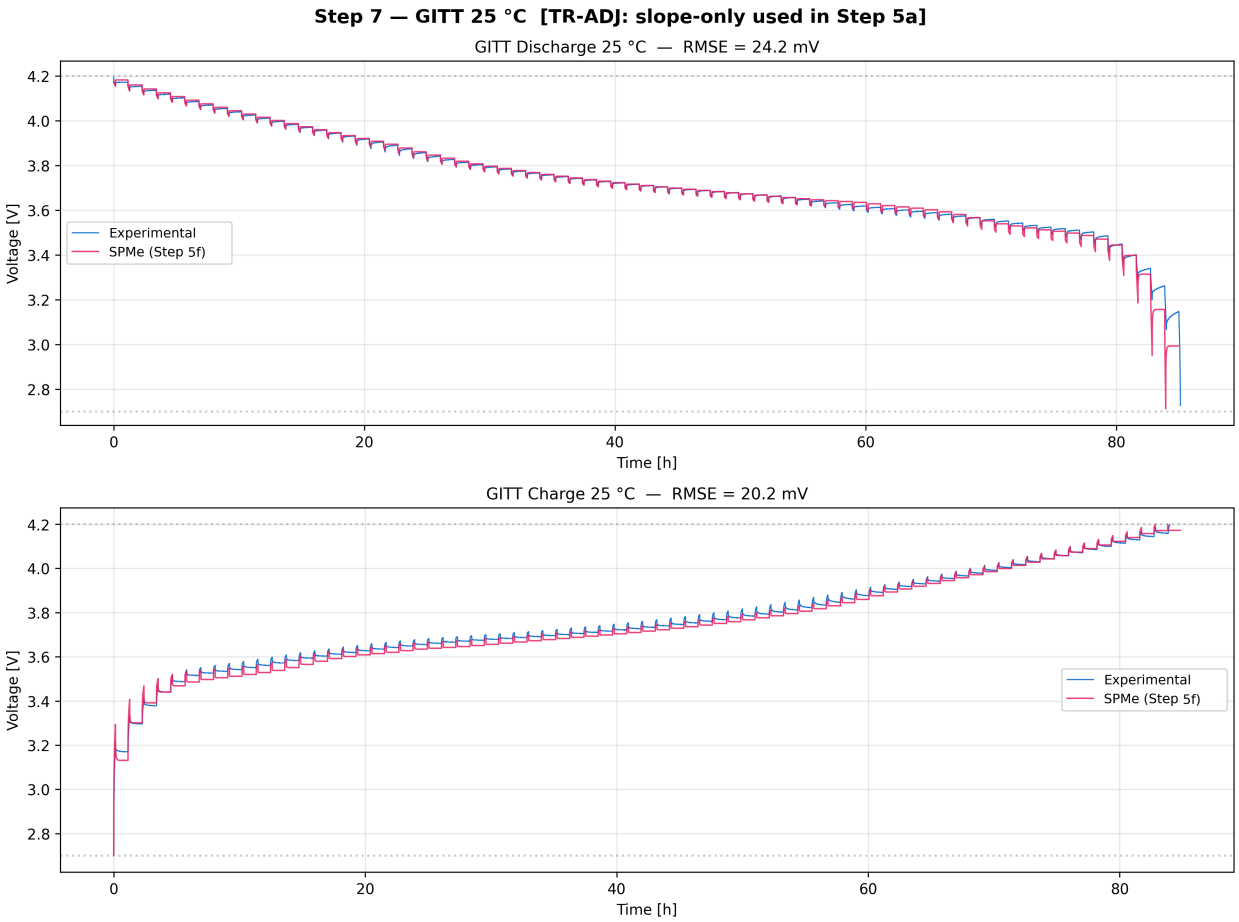


Figure 5.136: Validation plot: GITT charge/discharge at $25°C$

The following three Figures 5.137, 5.138, 5.139 focus on the validation of the three HPPC tests, of which only one was exploited for fitting of SEI-resistivity in Step 5b. These three rapid tests show a good agreement between SPMe simulations and experiments, with very low values of RMSE. HPPC tests can be considered as the most suitable tests for pure model's validation, due to their intrinsic fast dynamics with respect to the other available tests.

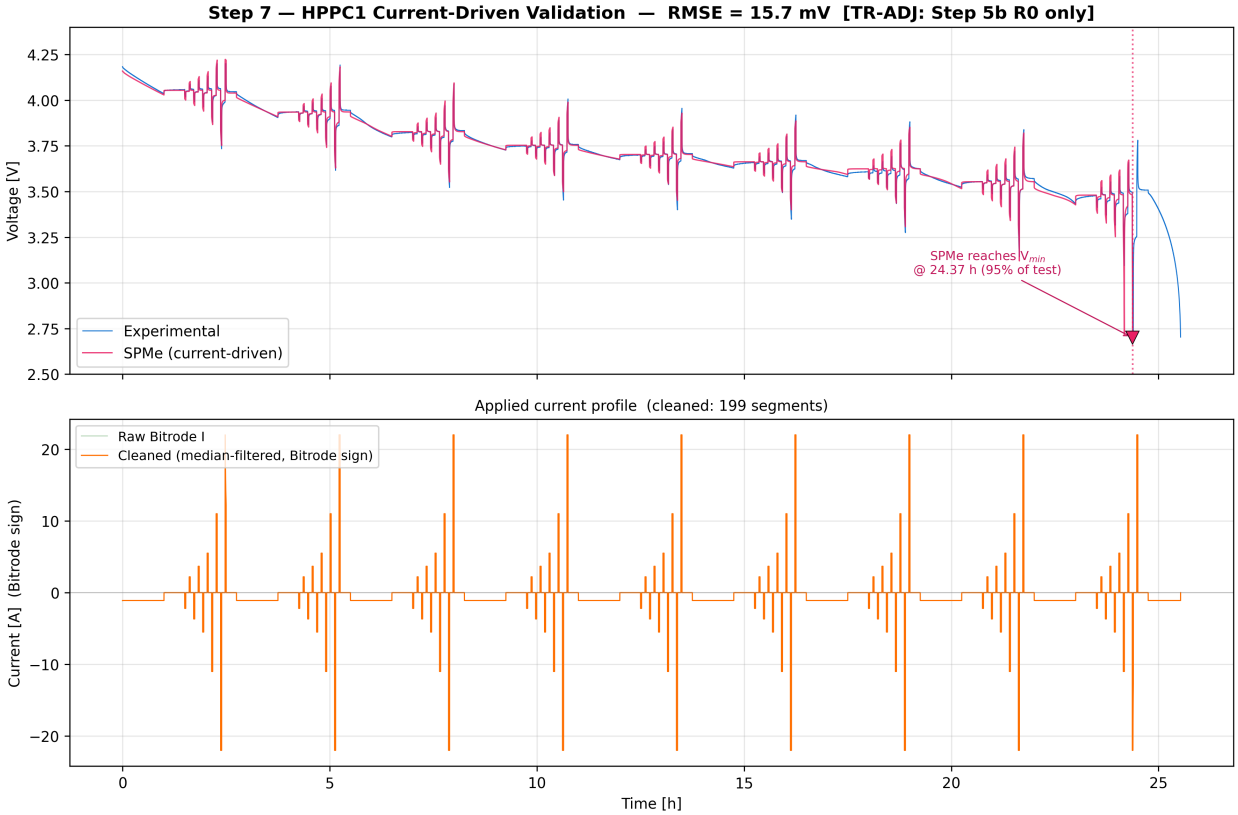


Figure 5.137: Validation plot: HPPC test (1)

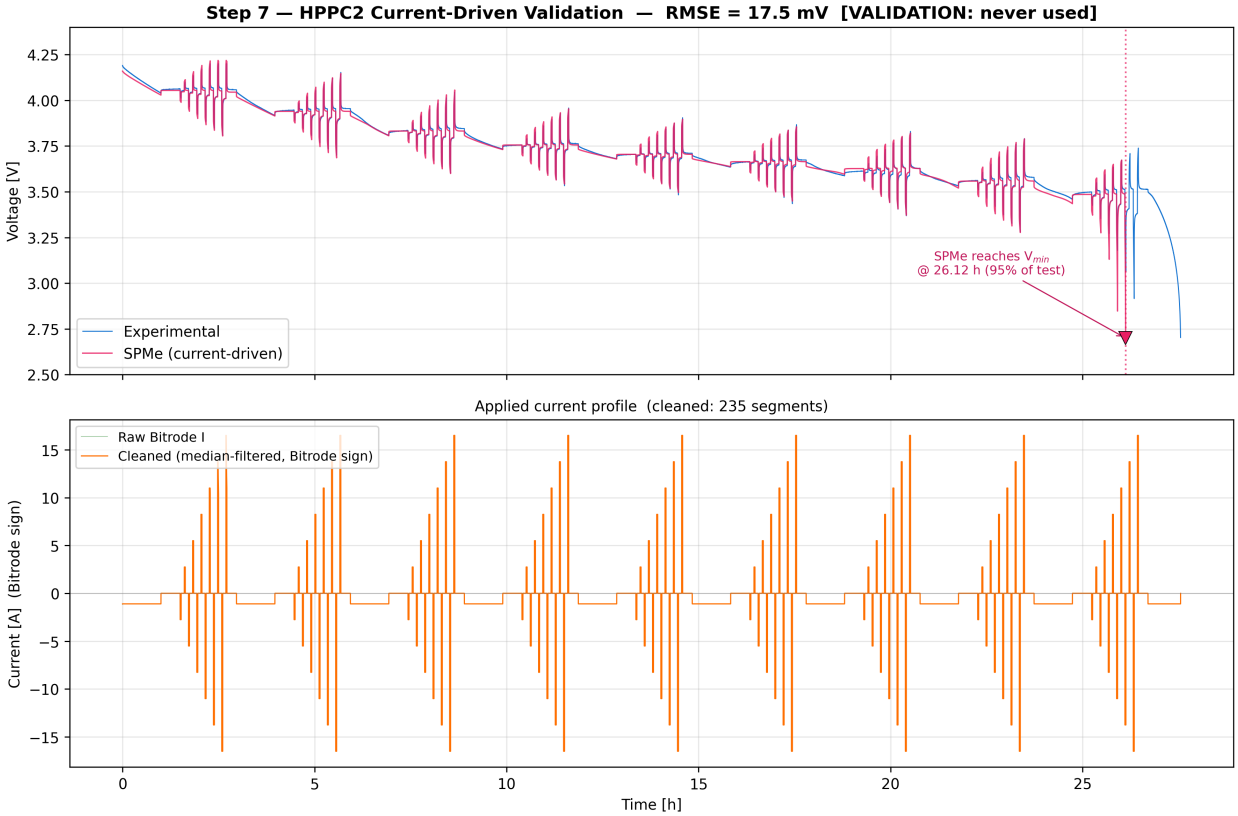


Figure 5.138: Validation plot: HPPC test (2)

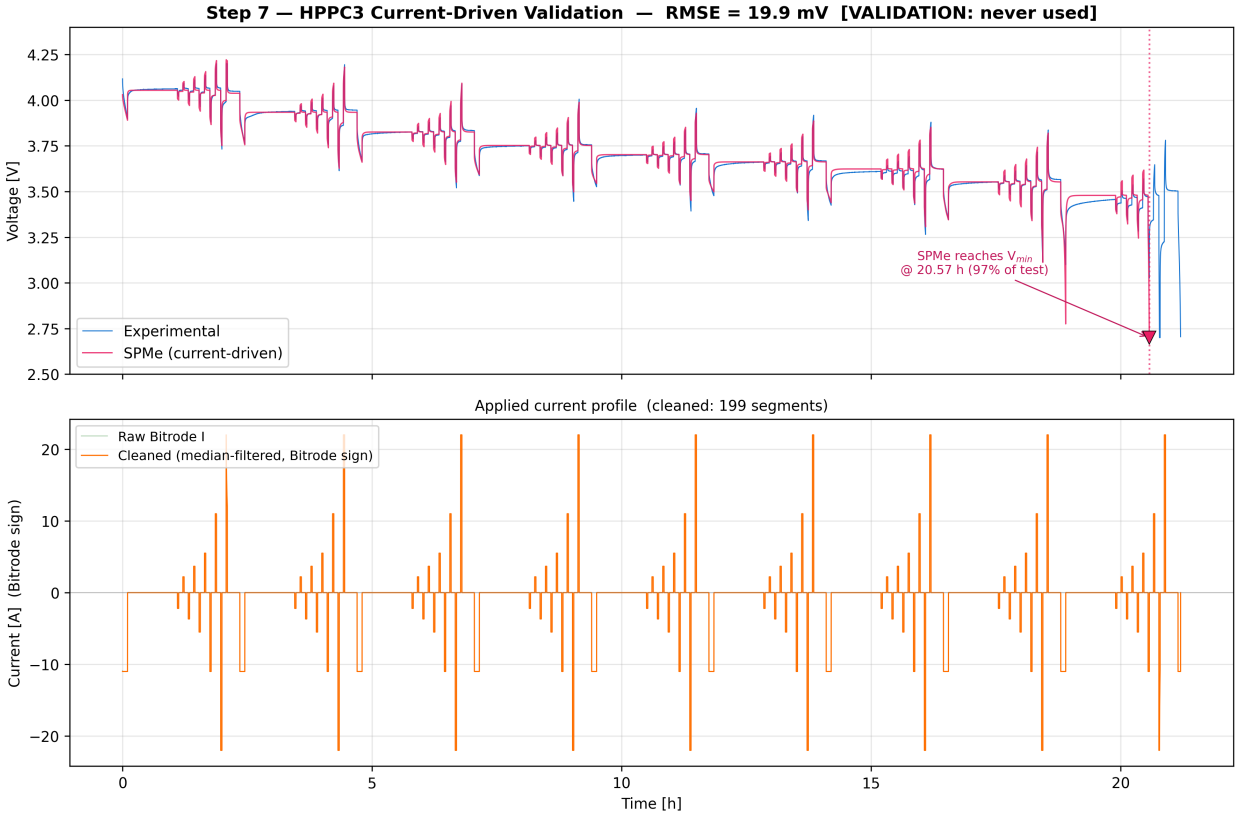


Figure 5.139: Validation plot: HPPC test (3)

In Figure 5.140, the cycling tests are visualized rate-by-rate and validated against corresponding experimental data. They show the best results at lower rates, as also seen in other cases. The CC charge and CC discharge branches of each cycle are perfectly tuned to the experiments; the real remaining differences are remarked during CV phase, due to probable Bitrode-artifacts, derived from its internal control-system.

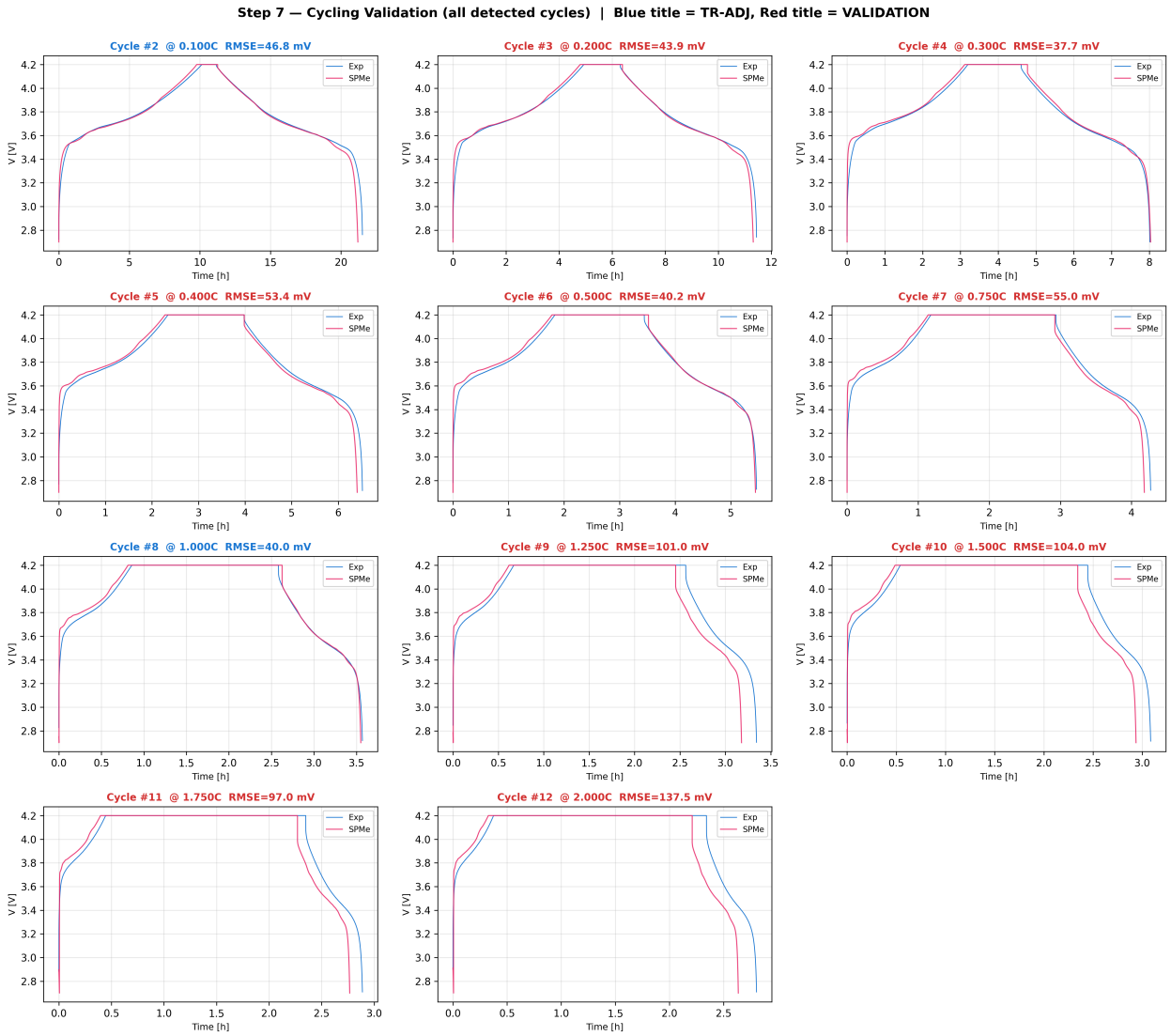


Figure 5.140: Validation plot: CC-CV charge & CC-discharge cycling tests

Figure 5.141 shows the bars of average RMSE related to generalization gaps per test's category. Evidently, the training tests have less RMSE, than the others, because they are exploited for optimization. In general, the category of adjustment tests show a good agreement between SPMe simulations and real experiments, symptom of a good Parametrization, whereas the pure validation tests retain most of the RMSE due to high-rate cycling tests.

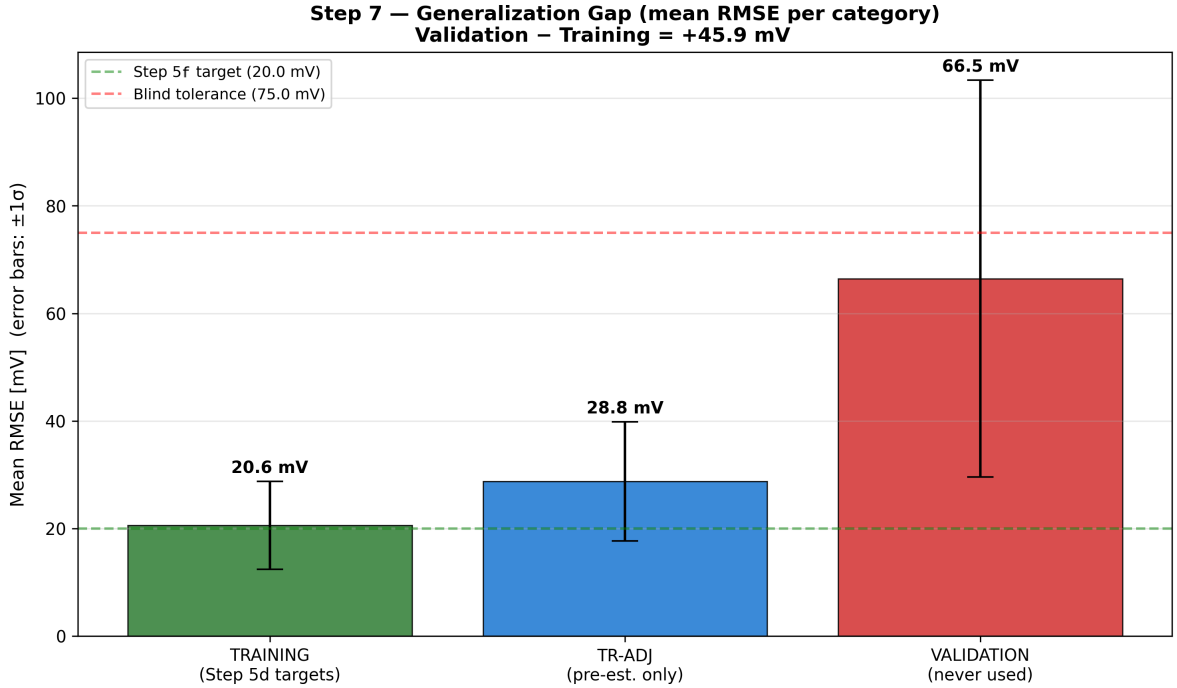


Figure 5.141: Average RMSE per test category

Finally, in Figure 5.142, a general comparison among the RMSE of all the tests is shown through a bar-diagram. This highlights the tests with less RMSE, i.e. HPPC tests and multi-rate discharge tests, in contrast with cycling tests that show higher values of RMSE, as explained before.

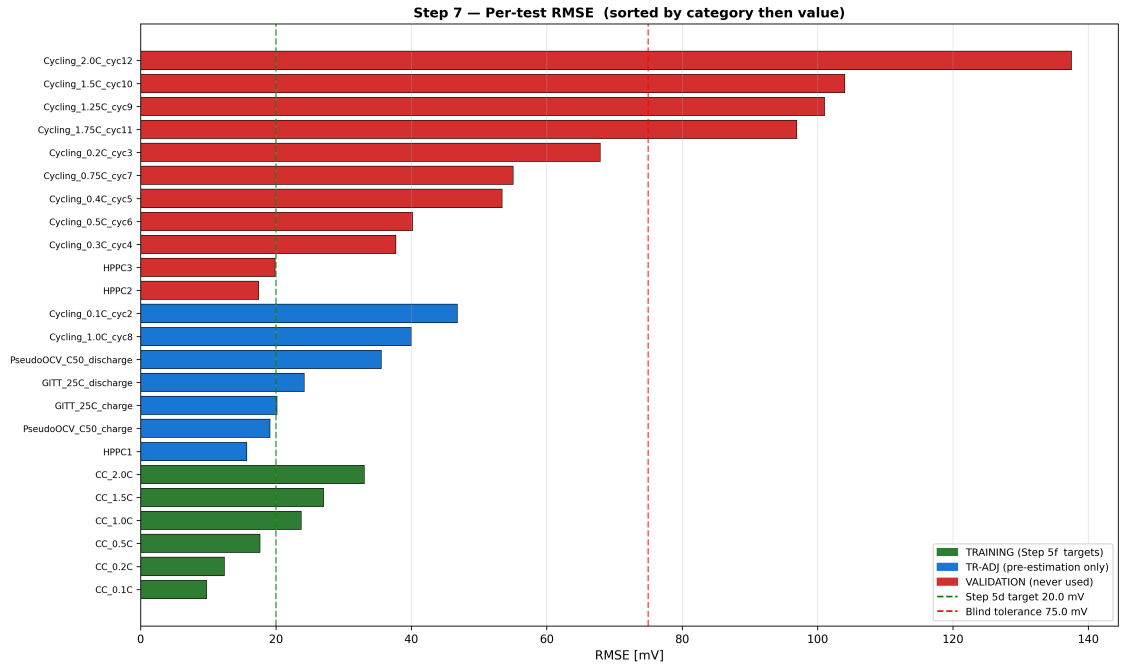


Figure 5.142: Step 7: RMSE values per test

It is worth noting that the entire Parametrization analysis was based on two concepts of voltage-error between SPMe simulations and experiments: (1) average Root-Mean-Square-Error (RMSE), which was considered as the primary mathematical instrument to assess the quality of the workflow results (described by Eq. 5.1, and calculated in every step); (2) local error (mainly exploited in the step 2 and step 5e for the tuning of stoichiometries and OCP curves).

Overall, all the Figures highlight the good results obtained from the Parametrization strategy, with a complex trade-off to generalize the model's parameter-set for all the available tests (at the same temperature of $25\ °C$), from the slowest ones (Pseudo-OCV) to the pulsed ones (GITT, HPPC).

5.6 Summary of SPMe Parametrization: Parameter-set and Workflow

This section focuses on the evolution of parameter-set, starting from Mohtat's default set and arriving to the final validated one.

This parameter-set, definitively obtained after the end of Step 5f, is shown in the following Table 5.35. Below the Table, the function-parameters are expressed, whether possible, in an equation-form.

An important note: different parameters inside the Table are typically functions in several literature works; assuming similar Mohtat's assumptions, many of them are reduced to simple scalar values (e.g., electrolyte's conductivity and diffusivity ($\kappa(c_e)$, $D_e(c_e)$), negative-particle diffusivity ($D_{s,n}(x)$)).

Parameter and Symbol	Value and Unit
Nominal capacity (Q_{nom})	$11\ Ah$
Lower cut-off voltage (V_{min})	$2.7\ V$
Upper cut-off voltage (V_{max})	$4.2\ V$
Number of internal layers (N_{layers})	1
Electrode-Height (H_{elc})	$2.728\ m$
Electrode-Width (W_{elc})	$0.277\ m$
Cathode thickness (L_p)	$39.76\ \mu m$
Anode thickness (L_n)	$66.55\ \mu m$
Separator thickness (L_s)	$12\ \mu m$
Positive current-collector thickness ($L_{cc,p}$)	$25\ \mu m$
Negative current-collector thickness ($L_{cc,n}$)	$10\ \mu m$
Positive electrode OCP ($U_p(y)$)	Function* [V]
Negative electrode OCP ($U_n(x)$)	Function* [V]
Cathode lithium concentration (at 100% SoC) ($c_{s,p,init}$)	$1183.22\ mol/m^3$
Anode lithium concentration (at 100% SoC) ($c_{s,n,init}$)	$19462.27\ mol/m^3$
Cathode porosity ($\varepsilon_{e,p}$)	0.407
Anode porosity ($\varepsilon_{e,n}$)	0.478
Cathode active material volume-fraction ($\varepsilon_{s,p}$)	0.443
Anode active material volume-fraction ($\varepsilon_{s,n}$)	0.422
Positive-particle radius ($R_{p,p}$)	$1.99\ \mu m$
Negative-particle radius ($R_{p,n}$)	$5.07\ \mu m$
Cathode Bruggeman coefficient (b_p)	1.50
Anode Bruggeman coefficient (b_n)	1.50
Maximum cathode lithium-concentration ($c_{s,max,p}$)	$35380\ mol/m^3$
Maximum anode lithium-concentration ($c_{s,max,n}$)	$28746\ mol/m^3$
Electrolyte conductivity ($\kappa(c_e)$)	$1.3\ S/m$
Electrolyte diffusivity ($D_e(c_e)$)	$(5.2 \cdot 10^{-10})\ m^2/s$
Transference number (t_0^+)	0.38
Initial electrolyte concentration ($c_{e,0}$)	$1000\ mol/m^3$
Thermodynamic factor (f_T)	1.0
Separator porosity (ε_s)	0.40
Separator Bruggeman coefficient (b_s)	1.50
Positive-particle diffusivity ($D_{s,p}(y)$)	Function* [m^2/s]
Negative-particle diffusivity ($D_{s,n}(x)$)	$6.57 \cdot 10^{-15}\ m^2/s$
Cathode reaction-rate constant ($k_{0,p}$)	$(1.445 \cdot 10^{-11})\ m^{2.5} \cdot mol^{-0.5} \cdot s^{-1}$
Anode reaction-rate constant ($k_{0,n}$)	$(0.264 \cdot 10^{-11})\ m^{2.5} \cdot mol^{-0.5} \cdot s^{-1}$
Cathodic charge-transfer coefficient (α_c)	0.5
Anodic charge-transfer coefficient (α_a)	0.5
Anode SEI-layer resistivity (ρ_{SEI})	$967.47\ k\Omega \cdot m$
Cathode conductivity ($\sigma_{s,p}$)	$100\ S/m$
Anode conductivity ($\sigma_{s,n}$)	$100\ S/m$

Table 5.35: Final parameter set of Kokam SLPB55205130H

The three equations of the parameter-set are expressed below. Some notes about each function of the last parameter-set are the following: (i) the NMC OCP function is obtained through a

local correction of Mohtat's default one, and in order to have a closed-form documentation-grade representation, it is well-approximated applying the sum of 6 Gaussian terms, computed in Step 5e; the graphite OCP function is retained from Mohtat's parameter-set (assumption of Step 5e); the cathode diffusivity function is a 3^{rd}-order Huber's logarithmic polynomial, obtained from Step 5a.

$$\begin{aligned} U_p(y) = U_p^{Mohtat}(y) + \Delta U_p(y) = \\ = (4.3452 - 1.6518 \cdot y + 1.6225 \cdot y^2 - 2.0843 \cdot y^3 \\ + 3.5146 \cdot y^4 - 2.2166 \cdot y^5 - 0.5623 \cdot 10^{-4} \cdot exp(109.451 \cdot y - 100.006)) \\ + \left(10^{-3} \cdot \sum_{k=1}^{6} A_k \cdot exp\left[-\frac{(y-\mu_k)^2}{2\sigma_k^2} \right] \right) \end{aligned}$$

where: A_k is the amplitude of Gaussian correction, whereas μ_k and σ_k are the extracted coefficients for fitting. These quantities are visualized in the following table 5.36.

k	$A_k\ [mV]$	μ_k	σ_k
1	+5.149	0.02553	0.02087
2	-7.618	0.16471	0.13510
3	+7.435	0.28944	0.02535
4	+6.051	0.53075	0.05254
5	+24.003	0.72334	0.05242
6	-7.834	0.78819	0.03105

Table 5.36: NMC OCP function: Gaussian correction terms

$$\begin{aligned} U_n(x) = 0.063 + 0.8 \cdot exp(-75 \cdot (x + 0.001)) - 0.0120 \cdot tanh((x - 0.127)/0.016) \\ - 0.0118 \cdot tanh((x - 0.155)/0.016) - 0.0035 \cdot tanh((x - 0.220)/0.020) \\ - 0.0095 \cdot tanh((x - 0.190)/0.013) - 0.0145 \cdot tanh((x - 0.490)/0.020) \\ - 0.0800 \cdot tanh((x - 1.030)/0.055) \end{aligned}$$

$$log_{10}(D_{s,p}(y)) = 2.98 \cdot y^3 - 2.15 \cdot y^2 - 0.72 \cdot y - 14.85$$

In Figure 5.143, the schematic of adopted workflow for the entire SPMe Parametrization is shown as summary of physics-based modeling activity.

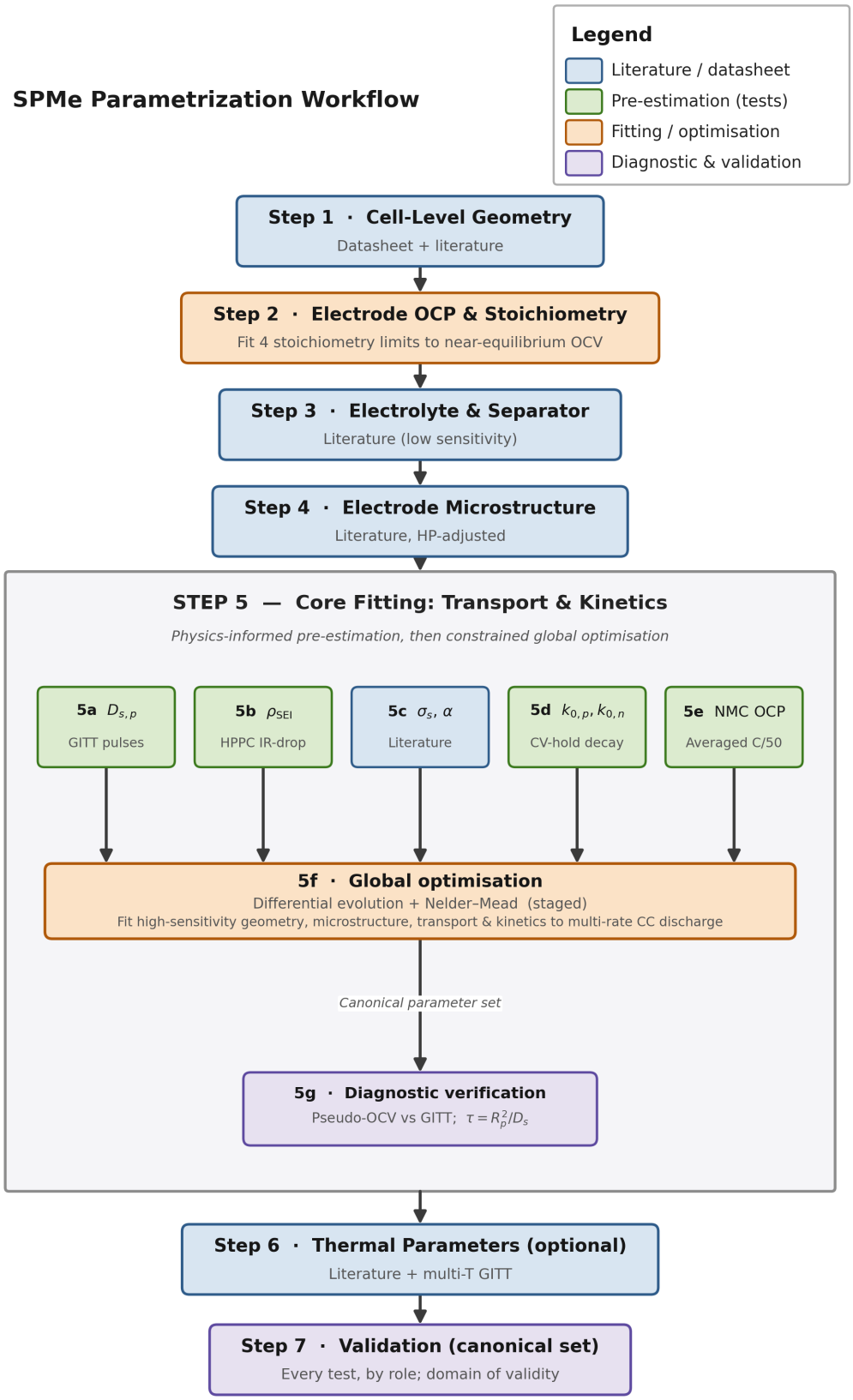


Figure 5.143: SPMe Parametrization Workflow

5.7 Step 6 further development: Thermal models

Once concluded the Parametrization procedure in iso-thermal conditions, i.e. at $25\ ^{\circ}C$, a further model's development could include the introduction of temperature-dependent features, through the use of a thermal model. It is suitable for performing an analysis of cell's parameters at different temperature, as seen with the Step 6 of strategy, requiring new experimental tests, and the implementation of a sub-model inside the software.

In PyBaMM ([15]), the electrochemical sub-models for lithium-ion batteries, such as DFN, SPM and SPMe formulations, can be directly coupled with different thermal sub-models. They provide different levels of spatial resolution for the cell temperature field and allow one to choose a suitable compromise between physical detail and computational costs. In general, PyBaMM offers a wide catalogue of choice:

1. Isothermal model;
2. Lumped-thermal model;
3. One-dimensional (1D) through-cell thermal model;
4. Higher dimensional pouch-cell ("1+1D" and "2+1D") thermal models.

This list shows several possibilities to be selected for a reliable modeling with different levels of details.

Overall, a specific thermal description accounts for the heat generated during battery operation and its exchange with the surrounding environment, while the specific assumptions depend on the selected thermal option.

The Isothermal model is the simplest thermal option, already used in the current parametrization, setting only the "Ambient Temperature [K]"; clearly, it can be used for any cell-geometry. It assumes that the cell temperature remains constant during the simulation and equal to the prescribed ambient temperature. Therefore, no additional thermal dynamics are solved. This approach is useful when temperature variations are negligible, for example under low-current operations, or when the cell is tested in a well-controlled thermal environment. It also represents a convenient baseline, when the main purpose of the simulation is the analysis of electrochemical behavior, rather than thermal effects.

The Lumped-thermal model is a simple model which does not consider the cell dimensions, thereby it is suitable for a global first-level thermal analysis. Basically, the lumped model introduces a dynamic description of the cell temperature, but assumes that the temperature is spatially uniform inside the whole cell. Therefore, the cell is represented by a single average temperature, which evolves according to the balance between internally generated heat and heat dissipated to the external environment. This formulation is computationally efficient and it can be applied to arbitrary or pouch-type geometries. For an SPMe model of a pouch cell, such as the analyzed Kokam SLPB55205130H, the lumped model is often an appropriate first thermal extension, when the objective is to capture the global temperature rise, without resolving internal thermal gradients.

The One-dimensional (1D) through-cell thermal model analyzes the thermal features of the cell, accounting the temperature gradient across the cell-thickness, i.e. the classical x-direction of physics-based models. This one-dimensional thermal model is specifically intended for pouch-cell geometries, resolving the temperature variation across its thickness-direction. Differently from the lumped-model, it can describe temperature gradients between the two external faces of the pouch and the internal layers. This option is more physically detailed than the lumped formulation, and it is useful when through-plane heat conduction or asymmetric cooling conditions are relevant.

However, it also requires additional thermal parameters, such as component thermal conductivities and surface heat-transfer coefficients.

The Higher-dimensional pouch-cell thermal models are suitable for coupling with more complex electrochemical models; they assume a uniform temperature through the thickness of the cell, while accounting for temperature variations in the remaining in-plane directions. Depending on the dimensionality selected for the current-collectors, this formulation can lead to the proper "1+1D" or "2+1D" pouch-cell thermal models. These models are particularly useful, when in-plane temperature gradients, tab-positions, edge cooling, or non-uniform current-collectors effects must be represented. They provide a more detailed spatial description than the lumped model, while avoiding the explicit resolution of the through-thickness temperature profile.

Overall, the choice of thermal sub-model in PyBaMM depends on the required modeling fidelity. The isothermal model is more suitable for purely electrochemical simulations, under constant-temperature conditions (the present work). The lumped model is appropriate for estimating the average temperature evolution, with limited computational costs. The pouch-cell thermal models are preferable when spatial temperature gradients are expected to influence the cell response. In the context of a calibrated SPMe, the lumped thermal model formulation represents a practical compromise for cell-level simulations, whereas the higher-dimensional pouch-cell models become more relevant when the analysis is extended toward thermal management, non-uniform cooling, or module-level integration.

Final notes and Conclusions

This Thesis focuses on two main topics related to automotive Li-ion batteries, i.e. experimental characterization and modeling of a battery cell.

The case-study was a High-Power lithium-ion pouch cell of $11\ Ah$, manufactured by Kokam, and provided by Politecnico di Torino. The Thesis was developed using mixed approaches inspired by literature works.

The activity started with a literature review covering:

- The numerical modeling approaches for Li-ion battery cells;
- The available simulation environments;
- The experimental characterization required for modeling (testing-plan).

The review provided a solid foundation for the subsequent stages of the work.

On the modeling side, the following choices were made:

1. Aligned with the objectives of the activity, a physics-based electrochemical modeling approach was adopted;
2. Among the available alternatives, the Single Particle Model with electrolyte (SPMe) was selected as the modeling type;
3. Different open-source and commercial tools were compared analyzing advantages and drawbacks for the Thesis;
4. PyBaMM, a specific Python-based framework, suitable for battery-modeling, was chosen as the simulation environment.

On the experimental side, an extensive characterization of the cell under-study was performed using two crucial instruments, a battery-cycler and a climatic chamber, at the testing facility of Politecnico di Torino. The testing campaign included non-invasive tests, aimed at characterizing the instantaneous terminal-voltage, through different combinations of charge or discharge currents, often interspersed with relaxation periods. The testing campaign included continuous (e.g., Pseudo-OCV) or pulsed (e.g., GITT or HPPC) tests, in order to explore the different properties of the cell.

The entire cell characterization was performed in isothermal conditions, thereby focusing primarily on cell behavior at ambient temperature. Additional tests at low and high temperatures were also made; however, the corresponding data were not included in the modeling activity.

The obtained experimental data-set was subsequently exploited to parametrize the SPMe model of the cell, starting with the core activity of the whole Thesis.

Indeed, this part aimed at identifying the optimal parameter-set of the SPMe, with the objective of minimizing the discrepancies between simulated and experimental instantaneous terminal-voltages. The parameter-set included five main categories of quantities:

1. Geometrical properties (e.g., electrode and separator thicknesses, electrode area);
2. Thermodynamic properties (e.g., electrode's OCP and stoichiometry windows);

3. Micro-structural properties (e.g., porosities, Li-concentrations, particle radii, active volume fractions);
4. Transport properties (e.g., electrode/electrolyte diffusivities and conductivities)
5. Kinetic properties (e.g., reaction-rate constants, film resistances).

The PyBaMM built-in Mohtat's parameter-set was selected as the starting point of model's parametrization.

The proper parametrization process was organized into two main steps:

1. A sensitivity-step, aimed at increasing confidence in the model and quantifying, through DoEs and two sensitivity indices, the influence of the various parameters on the terminal-voltage response;
2. A fine-tuning step, in which the optimal parameter-set was identified using different fitting techniques (to extract some properties from specific tests) and optimization techniques (to minimize the differences between simulations and experiments).

The most important merit of the Thesis is the construction of a reliable SPMe model, starting from literature data, experimental tests and fitting/optimization methods. This approach, based on the solid Sensitivity-Analysis, allowed one to select the crucial model's parameters for the estimation/refinement, leaving the less sensitive ones fixed at Mohtat's values.

The primary approach to assess the model was the usage of Root-Mean-Square-Error (RMSE), calculated between simulated and experimental terminal-voltage, as an average quantity. The achieved results, at the end of the parametrization, demonstrated the good capability of the model to reproduce the cell response under different charge/discharge currents (through a wide range of C-rates), at the ambient temperature.

The final parameter-set of the SPMe was subsequently validated against experimental data-sets, considering training, adjustment and pure-validation data. The satisfactory agreement, obtained even in this case, confirmed the model robustness under different operating conditions.

This work allowed one to obtain a suitable parameter-set that, through electrochemical model's equations, can forecast the cell's behavior in real conditions. The application of this type of battery models is widespread in automotive, considering the need for a reliable control-system inside the Battery-Management-Systems.

Regarding the further development of more complex electrochemical models (such as DFN models), a series of specific physico-chemical characterization tests are necessary to parametrize those models. The applied techniques vary from cell's teardown, porosimetry or laser diffraction to TGA (thermo-gravimetric analysis) or SEM (scanning electron microscopy).

Another potential future development for modeling activity is represented by thermal and aging additional sub-models. The thermal analysis is necessary to generalize the models at any temperature conditions, with different levels of details, from lumped to one-dimensional thermal models. The aging or degradation phenomena (e.g., SEI-layer formation or capacity-fade) affect the battery performance in terms of deliverable capacity and potential losses.

In conclusion, this Thesis focuses on the experimental characterization of a Li-ion battery cell and on the use of the open-source software PyBaMM to parametrize the corresponding SPMe electrochemical model.

References

[1] Iqbal Husain. *Electric and Hybrid Vehicles - Design Fundamental*. CRC Press, 2021 (Third Edition).

[2] Francesco Sciatti et al. "A comprehensive overview of lithium-ion batteries for electric vehicles: Materials, performance, safety, recycling, and emerging technologies". In: *Journal of Energy Storage* 144 (2026), p. 119694. ISSN: 2352-152X. DOI: https://doi.org/10.1016/j.est.2025.119694. URL: https://www.sciencedirect.com/science/article/pii/S2352152X25044081.

[3] Kokam. *Kokam Li-ion/Polymer Cell (SLPB) - Catalogue 2012*. URL: https://kokam-li-ion-polymer-cell-battery-solutions/.

[4] Chang-Hui Chen et al. "Development of Experimental Techniques for Parameterization of Multi-scale Lithium-ion Battery Models". In: *Journal of The Electrochemical Society* 167.8 (May 2020), p. 080534. DOI: 10.1149/1945-7111/ab9050. URL: https://doi.org/10.1149/1945-7111/ab9050.

[5] Michael J. Lain, James Brandon, and Emma Kendrick. "Design Strategies for High Power vs. High Energy Lithium Ion Cells". In: *Batteries* 5.4 (2019). ISSN: 2313-0105. DOI: 10.3390/batteries5040064. URL: https://www.mdpi.com/2313-0105/5/4/64.

[6] Qi Yao et al. "Study of High-Power and High-Energy Lithium-ion Batteries: From Parameter Analysis to Physical Modeling and Experimental Validation". In: *WCX SAE World Congress Experience*. 2025.

[7] Bowen Zheng et al. "A comprehensive review of lithium-ion battery modelling research and prospects: in-depth analysis of current research and future directions". In: *Applied Energy* 401 (2025), p. 126688. ISSN: 0306-2619. DOI: https://doi.org/10.1016/j.apenergy.2025.126688. URL: https://www.sciencedirect.com/science/article/pii/S0306261925014187.

[8] F Brosa Planella et al. "A continuum of physics-based lithium-ion battery models reviewed". In: *Progress in Energy* 4.4 (July 2022), p. 042003. DOI: 10.1088/2516-1083/ac7d31. URL: https://doi.org/10.1088/2516-1083/ac7d31.

[9] Marc Doyle, Thomas F. Fuller, and John Newman. "Modeling of Galvanostatic Charge and Discharge of the Lithium/Polymer/Insertion Cell". In: *Journal of The Electrochemical Society* 140.6 (June 1993), p. 1526. DOI: 10.1149/1.2221597. URL: https://doi.org/10.1149/1.2221597.

[10] Thomas F. Fuller, Marc Doyle, and John Newman. "Simulation and Optimization of the Dual Lithium Ion Insertion Cell". In: *Journal of The Electrochemical Society* 141.1 (Jan. 1994), p. 1. DOI: 10.1149/1.2054684. URL: https://doi.org/10.1149/1.2054684.

[11] Scott G. Marquis et al. "An Asymptotic Derivation of a Single Particle Model with Electrolyte". In: *Journal of The Electrochemical Society* 166.15 (Nov. 2019), A3693. DOI: 10.1149/2.0341915jes. URL: https://doi.org/10.1149/2.0341915jes.

[12] G. Richardson et al. “Generalised single particle models for high-rate operation of graded lithium-ion electrodes: Systematic derivation and validation”. In: *Electrochimica Acta* 339 (2020), p. 135862. ISSN: 0013-4686. DOI: https://doi.org/10.1016/j.electacta.2020.135862. URL: https://www.sciencedirect.com/science/article/pii/S0013468620302541.

[13] Peyman Mohtat et al. “Differential Expansion and Voltage Model for Li-ion Batteries at Practical Charging Rates”. In: *Journal of The Electrochemical Society* 167.11 (July 2020), p. 110561. DOI: 10.1149/1945-7111/aba5d1. URL: https://doi.org/10.1149/1945-7111/aba5d1.

[14] Valentin Sulzer et al. “Python Battery Mathematical Modelling (PyBaMM)”. In: *Journal of Open Research Software* (June 2021). DOI: 10.5334/jors.309.

[15] PyBaMM team. *PyBaMM Official Web-site*. URL: https://pybamm.org/.

[16] Madeleine Ecker et al. “Parameterization of a Physico-Chemical Model of a Lithium-Ion Battery: I. Determination of Parameters”. In: *Journal of The Electrochemical Society* 162.9 (June 2015), A1836. DOI: 10.1149/2.0551509jes. URL: https://doi.org/10.1149/2.0551509jes.

[17] Madeleine Ecker et al. “Parameterization of a Physico-Chemical Model of a Lithium-Ion Battery: II. Model Validation”. In: *Journal of The Electrochemical Society* 162.9 (June 2015), A1849. DOI: 10.1149/2.0541509jes. URL: https://doi.org/10.1149/2.0541509jes.

[18] Johannes Schmalstieg et al. “Full Cell Parameterization of a High-Power Lithium-Ion Battery for a Physico-Chemical Model: Part I. Physical and Electrochemical Parameters”. In: *Journal of The Electrochemical Society* 165.16 (Dec. 2018), A3799. DOI: 10.1149/2.0321816jes. URL: https://doi.org/10.1149/2.0321816jes.

[19] Johannes Schmalstieg and Dirk Uwe Sauer. “Full Cell Parameterization of a High-Power Lithium-Ion Battery for a Physico-Chemical Model: Part II. Thermal Parameters and Validation”. In: *Journal of The Electrochemical Society* 165.16 (Dec. 2018), A3811. DOI: 10.1149/2.0331816jes. URL: https://doi.org/10.1149/2.0331816jes.

[20] Paul Gasper. *Awesome Battery Data*. URL: https://github.com/pauljgasper/awesome-battery-data.

[21] W. Weppner and R. A. Huggins. “Determination of the Kinetic Parameters of Mixed-Conducting Electrodes and Application to the System Li3Sb”. In: *Journal of The Electrochemical Society* 124.10 (Oct. 1977), p. 1569. DOI: 10.1149/1.2133112. URL: https://doi.org/10.1149/1.2133112.

[22] Anup Barai et al. “A comparison of methodologies for the non-invasive characterisation of commercial Li-ion cells”. In: *Progress in Energy and Combustion Science* 72 (2019), pp. 1–31. ISSN: 0360-1285. DOI: https://doi.org/10.1016/j.pecs.2019.01.001. URL: https://www.sciencedirect.com/science/article/pii/S0360128518300996.

[23] Alberto Broatch et al. “A generalized methodology for lithium-ion cells characterization and lumped electro-thermal modelling”. In: *Applied Thermal Engineering* (2022). URL: https://www.sciencedirect.com/science/article/pii/S1359431122011048.

[24] Cyril Truchot, Matthieu Dubarry, and Bor Yann Liaw. “State-of-charge estimation and uncertainty for lithium-ion battery strings”. In: *Applied Energy* 119 (2014), pp. 218–227. ISSN: 0306-2619. DOI: https://doi.org/10.1016/j.apenergy.2013.12.046. URL: https://www.sciencedirect.com/science/article/pii/S0306261913010556.

[25] Mathias Petzl and Michael Danzer. “Advancements in OCV Measurement and Analysis for Lithium-Ion Batteries”. In: *Energy Conversion, IEEE Transactions on* 28 (Sept. 2013), pp. 675–681. DOI: 10.1109/TEC.2013.2259490.

[26] Jeffrey Belt. “Battery Test Manual For Plug-In Hybrid Electric Vehicles”. In: (Jan. 2010). DOI: 10.2172/1010675.

[27] Hans-Georg Schweiger et al. “Comparison of Several Methods for Determining the Internal Resistance of Lithium Ion Cells”. In: *Sensors* 10.6 (2010), pp. 5604–5625. ISSN: 1424-8220. DOI: 10.3390/s100605604. URL: https://www.mdpi.com/1424-8220/10/6/5604.

[28] Sadegh Mehranfar et al. “Practical Mixed Parameter Obtention Framework for Li-Ion Battery Electrochemical and Degradation Models Based on Parameter Classification and Physical Measurement”. In: *17th International Conference on Engines and Vehicles*. SAE International, 2025.

[29] Erwan Tardy et al. “3D Electrothermal Model for Internal Temperature Distribution in Lithium-Ion Battery Cell and Module”. In: *ECS Meeting Abstracts* MA2023-02.7 (Dec. 2023), p. 948. DOI: 10.1149/MA2023-027948mtgabs. URL: https://doi.org/10.1149/MA2023-027948mtgabs.

[30] Hamid Hamed et al. “Experimental Investigation of a 64 Ah Lithium-Ion Pouch Cell”. In: *Journal of The Electrochemical Society* 171.2 (Feb. 2024), p. 020510. DOI: 10.1149/1945-7111/ad24c2. URL: https://doi.org/10.1149/1945-7111/ad24c2.

[31] Sara Sepasiahooyi and Shu-Xia Tang. “Sensitivity Analysis of Lithium-Ion Battery SoH Indicators: An Analytical Study”. In: *2024 American Control Conference (ACC)*. 2024, pp. 1971–1976. DOI: 10.23919/ACC60939.2024.10644676.

[32] IonWorks Team. *Battery Parameter Estimation for Research and Development Teams*. URL: https://ionworks.com/blog/battery-parameter-estimation.

[33] Peyman Mohtat et al. “Towards better estimability of electrode-specific state of health: Decoding the cell expansion”. In: *Journal of Power Sources* (2019).

[34] Liqiang Zhang et al. “Parameter Sensitivity Analysis of Cylindrical LiFePO4 Battery Performance Using Multi-Physics Modeling”. In: *Journal of The Electrochemical Society* 161.5 (Mar. 2014), A762. DOI: 10.1149/2.048405jes. URL: https://doi.org/10.1149/2.048405jes.

[35] Weihan Li et al. “Parameter sensitivity analysis of electrochemical model-based battery management systems for lithium-ion batteries”. In: *Applied Energy* 269 (2020), p. 115104. ISSN: 0306-2619. DOI: https://doi.org/10.1016/j.apenergy.2020.115104. URL: https://www.sciencedirect.com/science/article/pii/S0306261920306164.

[36] Jue Chen et al. “Global sensitivity analysis towards non-invasive parameterization of the electrochemical-thermal model for lithium-ion batteries”. In: *Advances in Applied Energy* 18 (2025), p. 100221. ISSN: 2666-7924. DOI: https://doi.org/10.1016/j.adapen.2025.100221. URL: https://www.sciencedirect.com/science/article/pii/S2666792425000150.

[37] Enhui Liu, Leo Sun, and Paul Ziehl. “A systematic method for Li-ion battery simplified electrochemical model parameter sensitivity ranking and optimization”. In: *Journal of Energy Storage* 109 (2025), p. 115118. ISSN: 2352-152X. DOI: https://doi.org/10.1016/j.est.2024.115118. URL: https://www.sciencedirect.com/science/article/pii/S2352152X24047042.

[38] Shichang Ma et al. “Sensitivity analysis of electrochemical model parameters for lithium-ion batteries on terminal voltages and anode lithium plating criterion”. In: *Journal of Energy Storage* 71 (2023), p. 108127. ISSN: 2352-152X. DOI: https://doi.org/10.1016/j.est.2023.108127. URL: https://www.sciencedirect.com/science/article/pii/S2352152X23015244.

[39] Alexander P. Schmidt et al. “Experiment-driven electrochemical modeling and systematic parameterization for a lithium-ion battery cell”. In: *Journal of Power Sources* 195.15 (2010), pp. 5071–5080. ISSN: 0378-7753. DOI: https://doi.org/10.1016/j.jpowsour.2010.02.029. URL: https://www.sciencedirect.com/science/article/pii/S0378775310002740.

[40] D.C. Montgomery. *Design and Analysis of Experiments*. Wiley, 2017. URL: https://books.google.it/books?id=xJBEDwAAQBAJ.

[41] M. Mckay, Richard Beckman, and William Conover. “A Comparison of Three Methods for Selecting Values of Input Variables in the Analysis of Output From a Computer Code”. In: *Technometrics* 21 (May 1979), pp. 239–245. DOI: 10.1080/00401706.1979.10489755.

[42] J.C. Helton and F.J. Davis. “Latin hypercube sampling and the propagation of uncertainty in analyses of complex systems”. In: *Reliability Engineering and System Safety* 81.1 (2003), pp. 23–69. DOI: https://doi.org/10.1016/S0951-8320(03)00058-9. URL: https://www.sciencedirect.com/science/article/pii/S0951832003000589.

[43] Rainer Storn and Kenneth V. Price. “Differential Evolution – A Simple and Efficient Heuristic for global Optimization over Continuous Spaces”. In: *Journal of Global Optimization* 11 (1997), pp. 341–359. URL: https://api.semanticscholar.org/CorpusID:5297867.

[44] J. A. Nelder and R. Mead. “A Simplex Method for Function Minimization”. In: *The Computer Journal* 7.4 (Jan. 1965), pp. 308–313. DOI: 10.1093/comjnl/7.4.308. URL: https://doi.org/10.1093/comjnl/7.4.308.